

# **AN INVESTIGATION OF THE METALLURGICAL MATERIAL FROM PEUN BAOLO AND THONG NA NGUAK, LAOS**

ELŻBIETA WĄTROBA

---

Dissertation submitted in partial fulfilment of the requirements for the degree of  
MSc in the Technology and Analysis of Archaeological Materials  
of University College London in 2012

UCL INSTITUTE OF ARCHAEOLOGY

## Abstract

The archaeological excavations in the area of a currently operating copper and gold mine in the Sepon region, Laos revealed a rich archaeological assemblage related to the Iron Age copper production. In the current studies several categories of finds: crucible fragments, slag pieces, mineral samples and one copper ingot discovered during the first fieldworks season in 2008 at Peun Baolo and Thong Na Nguak, two sites situated within the mining district, were examined in order to explain to which aspect of metal production they are related and to examine the details of the operation. In total 35 finds were sampled and analysed with the use of mainly microscopic methods (optical and electron microscopy) supported by chemical analyses conducted with the ED system attached to the SEM. The investigation confirmed the existence of the developed copper production in the second half of the first millennium BC in the Sepon region. The manufacturing process evidenced in the assemblage comprised the whole sequence of operations from the smelting of copper ore to bronze foundry. According to the present initial interpretation copper smelting was based on the furnace technology while refining of impure copper and its alloying was conducted in open crucibles.

## Contents

1. Introduction	6
1.1. Objectives	6
1.2. Peun Baolo and Thong Na Nguak	6
1.3. Geological setting	9
1.4. Assemblage	9
2. Methodology	11
2.1. Approach	11
2.2. Sampling plan	11
2.3. Analytical methods	11
3. Results of analyses: characterisation of the finds	12
3.1. Copper minerals	12
MINERALOGICAL IDENTIFICATION	12
SUMMARY	21
3.2. Crucibles	23
COMPOSITION OF FABRICS	25
HEAT TREATMENT	38
3.3. Crucible slag	44
COMPOSITION AND MICROSTRUCTURE OF INNER SLAG LINING	45
COMPOSITION AND MICROSTRUCTURE OF EXTERNAL SLAG	49
3.4. Separate slag	51
COMPOSITION AND MICROSTRUCTURE	52
3.5. Copper ingot	56
4. Interpretation of the results: reconstruction of metallurgical process	60
4.1. Nature of the process	60
4.2. Primary copper production at PB and TNN: pyrometallurgical specifics	63
TYPE OF ORE AND COMPOSITION OF A CHARGE	63
BEHAVIOUR OF SEPARATE SLAG AND REDOX CONDITIONS	68
SMELTING INSTALLATION	70
POSSIBLE PRODUCTS OF SMELTING AND THE COPPER INGOT	71
4.3. Role and performance of crucibles	73
PRODUCTION OF CRUCIBLES	73

FUNCTION OF CRUCIBLES	75
4.3. Secondary production	77
CASTING	77
BRONZE MANUFACTURE	78
5. Conclusions	79
Appendix 1: analytical equipment and its working conditions	81
Appendix 2: analyses of non-technical ceramics	85
Appendix 3: crystalline and non-crystalline phases within the crucible slag	88
Appendix 4: crystalline and non-crystalline phases within the separate slag	101
References	112

### Acknowledgements

I would like to acknowledge the following people:

Dr Marcos Martín-Torres and Professor Ian Freestone for their advice and support throughout the year; Dr Nigel Chang and Dr Thomas Oliver Pryce for the opportunity to study the material from Laos, the generous access to the excavation reports, and all of the useful information they provided me; Harriet White, Kevin Reeves and Dr Patrick Quinn for their technical guidance in the labs.

Thanks are also due to The Association for Cultural Exchange for the financial support.

And to Kiwi and Synek, for everything.

# 1. Introduction

## 1.1. Objectives

The dissertation presents the results of a research project in which the artefacts associated with metal production discovered at two sites in Laos, Peun Baolo and Thong Na Nguak, were examined. The objective of the research is the reconstruction of the metallurgical operations practised at the sites with the use of several analytical methods specified in the next chapter. The most accurate and informative technological reconstruction is a primary aim of the current work and constitutes the vast majority of its content.

Furthermore, the technological reconstruction might be later employed in the archaeological interpretation in order to enable better understanding of the issues such as relations between Peun Baolo and Thong Na Nguak communities, functions and organisation of the sites. Some preliminary remarks on these points are presented in the last chapter.

Another important outcome of the project is the enlargement of the body of archaeometallurgical data available for Southeast Asia. It seems to be especially significant since the new data come from the region the prehistoric metallurgy of which had been completely unknown so far. The proposed picture of the prehistoric metallurgy of the Sepon area may be compared to the results of the archaeometallurgical projects based on the finds from Thailand what gives a broader perspective and provides the wider interpretative approaches with the new evidences.

## 1.2. Peun Baolo and Thong Na Nguak

The archaeological sites concerned in the dissertation, Peun Baolo (hereafter PB) and Thong Na Nguak (TNN), are located in the Sepon region of Savannakhet Province, south-eastern Laos (Chang, Sayavongkhamdy, Cawte, & Souksavtdy, unpublished) (Fig. 1). They are both situated within the area of Lane Xang Minerals Limited's current mining works.

The rich history of the Sepon region was initially recognised during the surveys carried out in 2000 and 2006 by the staff of the Department of Museums and Archaeology, Lao PDR. As their results many artefacts were collected and several archaeological sites were identified. The first archaeological excavation in the region took place in 2008 at PB and TNN as a joint project of the Lao Department of National Heritage, James Cook University, and LXML (Chang & Sayavongkhamdy, unpublished).

The works at TNN were suspended after the first season in order to focus on the areas most threatened with distraction. In 2009 over 130 individual circular shafts were identified and excavated within the adjacent to TNN site modern mining pit Khanong (Chang, unpublished). The excavation at PB have been continued until present (Chang, unpublished 2).

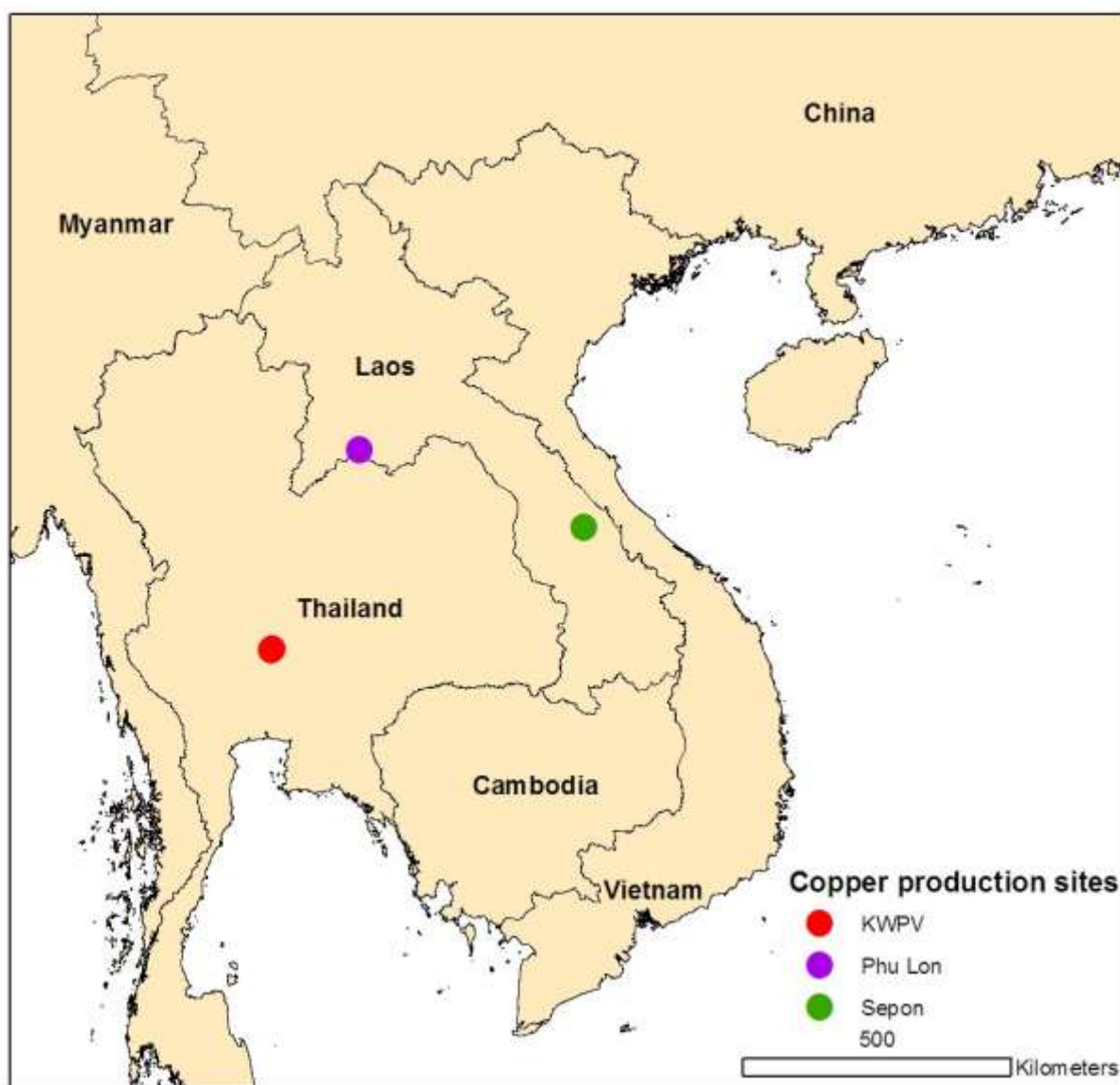


Fig. 1. Map of Southeast Asia, showing the sites mentioned in the text; KWPV - Khao Wong Prachan Valley.

During the excavation at PB series of 1-8m deep shafts were documented. They contained a high number of artefacts associated mostly with metal production: slagged crucible fragments, slag, pieces of ore and copper, discarded rock, sandstone ingot mould as well as domestic pottery. During the 2010-2011 seasons, potential grave locations were identified. The excavated burials were richly equipped with metal objects (11 copper bowl-tie ingots, copper axe and large dagger axe in the largest grave) and other goods such as pottery, white ceramic earrings and bracelet, jade beads (Chang, unpublished 2).

At TNN in a shallow anthropogenic deposit similar artefacts related to metal production were identified (crucibles, slag, vitrified pieces of ceramic). In addition, three low cone artefacts, called ingots, were discovered in association with large vessels of possibly mortuary function. During the construction of the fence around the site further copper cone ingots, bronze objects and over 4000 of beads (glass, shell, ceramic and cornelian) were found within burial jars (Chang, unpublished 2). The overall number of recorded copper ingots from the area around the sites is around 50, included 3 from the excavate context (N. Chang pers. comm.).

The shafts discovered within the Khanong mining pits were dug 14-25 m below the ground surface and had diameter around 2.5m. There were lined with wooden framing and matting. No artefacts were discovered inside the shafts. It is not clear what they were constructed for although the presence of the cooper deposit mined currently by LXML is evocative (Chang, unpublished).

Several radiocarbon dates were obtained from PB and TNN (Table 3). They are all around 2000-2200 BP and fall within the Southeast Asian Iron Age according to the chronology based on the most recent radiocarbon determination for the sites situated on the Khorat Plateau of Northern Thailand (Higham & Higham, 2009) (Fig. 2).

Type of material measured for carbon isotope	Date obtained (calibrated)	
<b>Thong Na Nguak</b>		
charcoal extracted from burial jar (associated with cone ingots)	2126 +/- 28 BP	c. 170 BC
<b>Khanong pit</b>		
small diameter wood	1889 +/- 38 BP	c. 60 AD
bamboo	2142 +/- 39 BP	c. 190 BC
<b>Peun Baolo</b>		
charcoal within mining pit (associated with metallurgical waste)	2261 +/- 29 BP	c. 320 BC

Table 1. Radiocarbon dates for PB, TNN and shafts within Khanong pit (after Chang, unpublished 2).

According to N. Chang (pers. comm.), the co-director of the excavation at PB and TNN, the graves from PB containing a rich copper-base metal assemblage may be dated back to the Bronze Age due to the character of artefacts (no glass, no iron) and stratigraphy (under the layer of mining and smelting detritus).

Cultural period	Date in calibrated radiocarbon years (BC)
Flexed burials	1750-1050
Neolithic 1	1650-1250
Neolithic 2	1250-1050
Bronze Age 1	1050-1000
Bronze Age 2	1000-900
Bronze Age 3	900-800
Bronze Age 4	800-700
Bronze Age 5	700-420
Iron Age 1	420-100
Iron Age 2	200-AD 200
Iron Age 3	AD 200-400
Iron Age 4	AD 300-500
Early Historic	500-

Fig. 2. Chronology of the upper Mun Valley (Thailand) (after Higham, 137, Tab.2); in colour periods evidenced in Sepon by the radiocarbon dates: red-PB, blue-TNN.

Sepon is the third region recognised in Southeast Asia with the abundant evidences of prehistoric copper mining and production (Pryce et al., 2011). The first two areas, Phu Lon



and the Khao Wong Prachan Valley (Fig. 1), were identified and excavated by the Thailand Archaeometallurgy Project in 1980' (Pigott, Natapintu, & Theetiparivatra, 1992; Pigott, Weiss, & Natapintu, 1997). The excavations at situated in northeast Thailand Phu Lon revealed extensive copper mining evidence dated back to the first millennium BCE and a much less clear indicator of local copper extraction (Pryce et al., 2011). In the Khao Wong Prachan Valley in central Thailand two main smelting sites were discovered: Non Pa Wai (c. 500-300 BCE) and Nin Kham Haeng (c. 300 BCE-500CE). At both sites extensive smelting debris up to 4-6 m deep was recognised (Pryce, Pigott, Martín-Torres, & Rehren, 2010, p. 239).

### 1.3. Geological setting

The Sepon region is situated along the Truong Son Fold Belt, a NW-trending track of folded Palaeozoic sedimentary rocks with major granite intrusion which occupies north-centre of Laos and extends eastward into central Vietnam (Workman, 1997, p. 496). The style of mineralisation in the Sepon district and its mining potential was recognised in 1990 when copper and gold lodes covering a variety of primary and secondary types were first documented (Manini & Albert, online).

Three main hypogene mineralisation styles were recognised comprising distal sedimentary rock hosted gold, proximal skarn (Cu, Au) and central porphyry (Cu-Mo). There are epigenetic in their origin, involving magmatic and minor metamorphic fluids, and occur along the faults and/or veins cutting all of the Palaeozoic sedimentary rocks (Cromie, 2010; Workman, 1997). Common sulphide minerals in the Sepon mineral district are pyrite, arsenic-rich pyrite, chalcopyrite, minor sphalerite, galena, bornite and stibnite (Workman, 1997).

Gold mineralisation occurring as fine dissemination is predominantly hosted by highly altered calcareous shale (Manini & Albert, online).

The supergene copper enrichment derived from the weathering of a replacement style massive sulphide deposits developed in carbonate rocks was discovered at three deposits, namely Khonong, Thengkham North and Thengkham South (Workman, 1997). Among them the Khonong lode is the biggest and richest one. Copper minerals present are mainly chalcocite, with minor covellite, malachite, azurite and same native copper (Baxter, Dreisinger, & Pratt, online)

Above the enrichment zone there is a well-developed lateritic profile which forms a leached cup to the supergene copper mineralisation and comprises gossan, ironstone boulders and red ferruginous clay soils. It is generally assumed that copper is leached away from the laterite (Baxter et al., online).

### 1.4. Assemblage

The assemblage under examination consists of 223 pieces of artefacts discovered exclusively during the first excavation seasons at PB (159 pieces) and TNN (64 pieces) in 2008. It was selected from much more numerous collections of similar finds and submitted for analysis to the UCL Laboratory where some part of it (crucibles) was initially examined by H. Cawte (unpublished).

The group of artefacts from PB consists of pieces of separate slag, fragments of crucibles with slag lining or vitrified surface, pieces of copper minerals found in

archaeological context, fragments of domestic pottery, not associated with the metallurgical operations.

The collection from TNN is represented by separate slag pieces, fragments of crucibles with slag lining or vitrified surface, pieces of clay chunk probably partly fired with unknown relation to the metallurgical processes and one out the three copper cone ingots found in association with 'mortuary' vessel.

Each type of artefacts present in the assemblage belongs to the common finds at both sites (pers. comm. N. Chang). It is especially true in the case of PB where the artefacts related to metal production has been found in a large quantity during the following seasons. At TNN the metallurgical waste was less abundant, what is reflected in the smaller proportion of the finds from the site in the collection under examination. Due to the temporal stoppage of the excavations at the site the nature of this situation awaits explanations.

All artefacts were found in the excavated context. Several factors, however, hinders their stratigraphic interpretation. Firstly, due to the serious degree of erosion noted at both sites, many artefacts were discovered under thin layer of earth. Most of the finds from PB comes from the rubble pits which may contain all materials present at the surface during their infilling (long-term washing away or intentional in-filling). They are, therefore, not necessarily contemporary what is showed by two possibly Neolithic sherds inter-mixed with the debris (Chang & Sayavongkhamdy, unpublished).

The radiocarbon determination which may be related to the assemblage in question are around 2260 BP for metallurgical waste from PB and 2120 BP for the copper ingot from TNN. The sandstone mould from PB matching the shape of ingot from TNN may suggest the chronological or cultural link between the sites.

## **2. Methodology**

### **2.1. Approach**

The project is based on a simple assumption that a detailed characterisation of artefacts may make the recognition of their function possible. Moreover, the character of the assemblage, consisting of several groups of artefact which seem to represent different ingredients of the same process, stimulates hope for quite detailed reconstruction of the operation.

Characterisation of the artefacts involves firstly their visual investigation as hand specimens, which is assumed to be an integral part of the examination and is aimed to maximise the amount of information about the assemblage as a whole, and secondly recognition of the microstructure and chemical composition of the selected artefacts with the use of the analytical techniques. Full record on this step is provided in the chapter 3.

In the second step, the author will try to infer as much information as possible about activities and choices of the inhabitants of both sites from the collected data. For this reason some basic concepts of chemistry, particularly thermodynamics, as well as a wide range of methods, results and explanations provided by archaeometrical investigations carried out worldwide are employed.

### **2.2. Sampling plan**

The first step of sample selection was done at the sites during the fieldworks. Through the communication with the site director Nigel Chang it was ensured that the submitted collection contains the most common types of metallurgical waste found at both sites and it is quite safe to base on it the current examination.

Each artefact has been macroscopically analysed and its potential for further studies has been assessed. The sample selection was the subject of a personal assessment of the author without application of any systematic sampling procedure. The artefacts were prioritised according to a few simple rules shown in order of growing importance: 1) artefacts bringing the highest amount of information about the metallurgical process involved; 2) artefacts providing technical details about the metallurgical operations; 3) artefacts offering the information allowing the juxtaposition of the sites; 4) artefacts helpful in contextualisation of the results. The artefacts were sampled gradually and their choice was influenced by the results of the foregoing analyses. Ultimately, 35 artefacts were sampled. 30 of them were prepared as polished blocks and 11 as thin sections.

### **2.3. Analytical methods**

Two analytical techniques were employed in the analysis of the artefacts: scanning electron microscope with an energy dispersive spectrometer (SEM-EDS) and optical microscopy (reflected light microscopy and thin section petrography). All analyses were carried out in the Wolfson Archaeological Science Laboratory at the UCL Institute of Archaeology. For full record on the equipment used and working conditions, see Appendix 1.

### 3. Results of analyses: characterisation of the finds

#### 3.1. Copper minerals

The group of around 20 small finds initially defined as copper minerals and ore fragments was included into the assemblage sent to London. They were all found in archaeological context together with other objects associated with metal production. Most of them come from PB.

According to the preliminary visual investigation four types of mineral aggregates were distinguished and sampled (numbers of samples given in brackets): A) several small pieces of green mineral, most likely malachite (PB-41); B) an aggregate of green minerals associated with rusty earthy material (PB-45); C) a reddish earthy globule with black and green core (PB-38); D) an object with green corrosion products on the surface and a black and purple core (PB-42).

#### MINERALOGICAL IDENTIFICATION

(A)– sample PB-41 – malachite

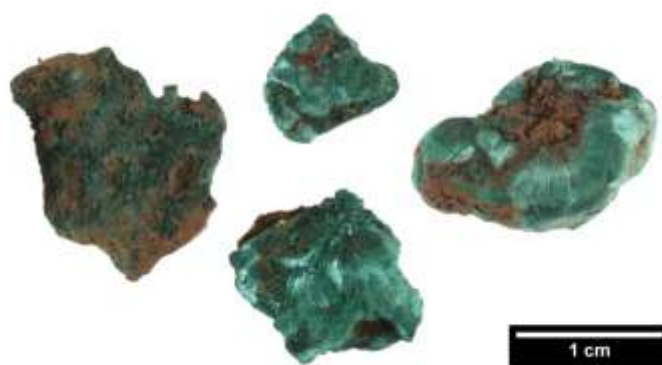


Fig. 3. Malachite pieces found at PB. The one above the scale was sampled (PB-41).

Four small (1cm<sup>2</sup>) pieces of green brittle mineral were submitted for analysis (Fig. 3). Their macroscopic features, such as botryoidal bonded appearance, light green surface and streak as well as fibrous irregular fracture strongly suggest copper carbonate mineral, malachite ( $\text{Cu}_2\text{CO}_3(\text{OH})_2$ ). Reflected light microscopy study (Fig. 4) as well as SEM-EDS results confirmed this identification (Table 2).

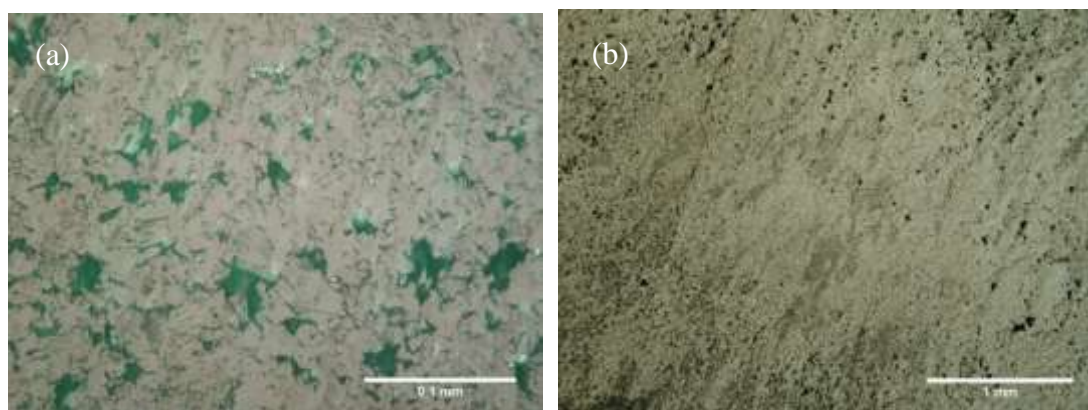


Fig. 4. Reflected light micrographs of PB-41, PPL: (a) Grey malachite showing strong green internal reflection; (b) Malachite forms radiating crystal aggregates seen as light and dark grey streaks. Its natural porosity was probably increased by polishing (note the often triangular oriented in one direction polishing pits).

	CuO	CO <sub>2</sub>	H <sub>2</sub> O	total	Cu/O
Average composition of PB-41, n=4					
mean	67.2	nm	nm	86.8*	1.8
σ	1.0	-	-	0.8	<0.1
Model composition of malachite					
malachite	71.95	19.9	8.15	100	1.6

Table 2. EDS results for the single phase in the sample PB-41 (wt%), not normalised. Malachite composition (webmineral, 2012) given for comparison. Cu and O amounts in the sample are slightly depleted in comparison to malachite but it can be considered as an effect of analytical error. The excess of the oxygen detected is probably bonded to C and H not measured by EDS what contributed to lower totals regularly determined as c. 87%. \*analysed all elements; n-number of analyses included in the average; nm – not measured; σ – standard deviation

The only mineral pieces derived from TNN are represented by two tiny probably malachite aggregates attached to the fragments of rock or earthy material (Fig. 5). Some indications of heating seem to be also visible on the finds (TNN-12).

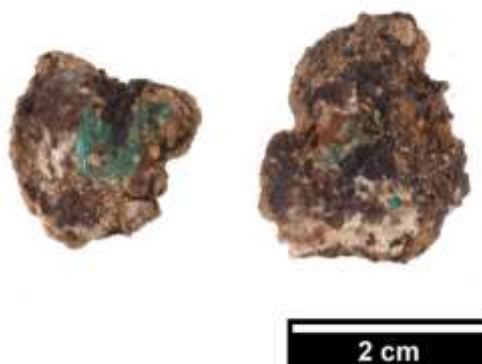


Fig. 5. Malachite bits attached to partly vitrified material from TNN. Black vitrified residue on the surface may suggest that the objects were subjected to heat.

(B) – sample PB-45 – malachite and oolitic iron ore



Fig. 6. Mineral aggregate from PB (PB-45). On the left its section prepared for polished block.

The aggregate is composed of two main phases: copper carbonate (malachite) which is intergrown with oolitic iron oxide minerals (Fig. 7).

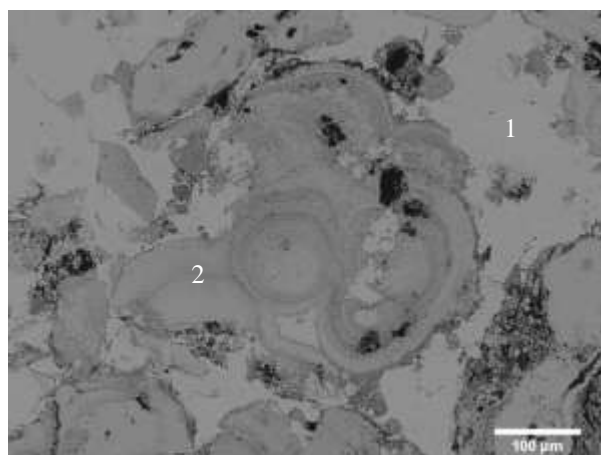


Fig. 7. Backscattered electron image showing two main phases in PB-45: 1) fine-grained massive malachite (white); and 2) iron oxide ooids (grey).

	CuO	FeO	CO2	H2O	total <sup>a</sup>	Cu/O				
Composition of phase 1 in PB-45 <sup>b</sup> , n=3										
highest	69.5	4.1	nm	nm	89	1.9				
lowest	68.9	nd	nm	nm	86.6	1.8				
mean	69.2	2.5	nm	nm	87.7	1.8				
Model composition of malachite										
malachite	71.95		19.9	8.15	100	1.6				
	Fe2O3	SiO2	CuO	ZnO	MgO	P2O5	total <sup>d</sup>	total <sup>a</sup>	Fe/O ratio	
Composition of phase 2 in PB-45 <sup>c</sup> , n=6										
highest	93	5.3	3	0.8	0.6	1.1	88.6	98.1	1.6	
lowest	91	4.5	1.6	nd	nd	nd	85.7	93.0	1.5	
mean	92.1	4.8	2.2	0.1	0.1	0.6	87.1	96.2	1.6	
Composition of phase 3 in PB-45 <sup>c</sup> , one single-spot analysis										
	91.7	4.6	2.7	nd	nd	1.0	91.5	96.9	1.6	
Model Fe/O (wt%) ratio for iron oxides and iron carbonate										
FeO										3.54
Fe3O4										2.8
Fe2O3										2.33
Fe(CO)3										1.16

Table 3. Composition of the phases visible in the Fig. 7; SEM-EDS results (wt%). Fe/O ratios for iron oxides and carbonates as well as model composition of malachite are provided for comparison. The high amount of oxygen detected in the phase 2 may suggest: 1) that iron occurs as Fe<sup>3+</sup> ions; 2) that some elements are missing (C, H). Most likely both factors are true and the phase 2 represents a mixture of limonite and hematite, and some amorphous phases. <sup>a</sup> all elements measured; <sup>b</sup> not normalised; <sup>c</sup> normalised; <sup>d</sup> total of oxides; n - number of analyses included in the average; nm – not measured.

Malachite appears as massive agglomerates cumulated into layers or growing between iron oxide aggregates (Fig. 8a). Iron oxide forms circular aggregates of fine crystals. Mineralogical affiliation of iron oxide is uncertain. The optical properties seen in reflected light (quite high reflectance, grey-white colour with bluish tint, reddish internal reflection) as well as oolitic form of aggregate seem to indicate hematite of sedimentary origin (Fig. 8b).

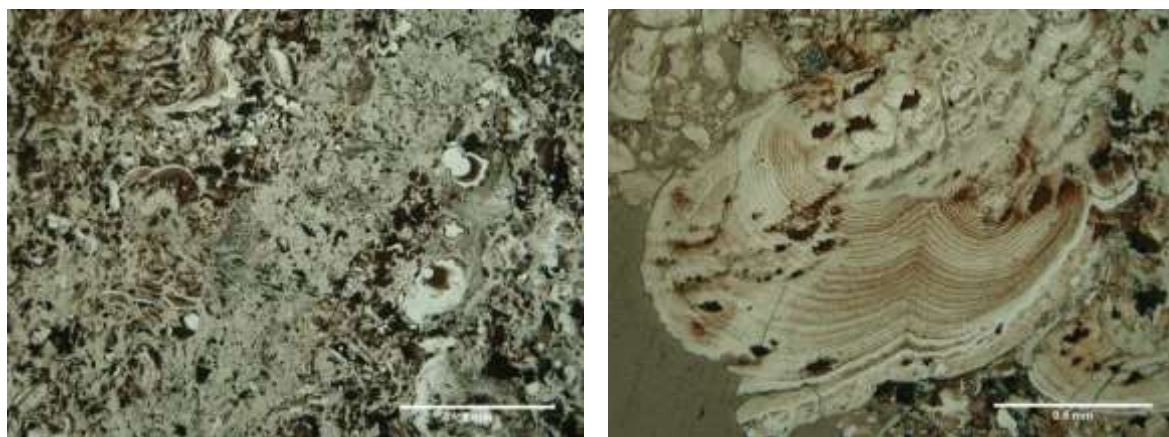


Fig. 8. Reflected light micrographs of PB-45: (a) grey malachite forms a vein in a centre of the image and occurs scattered among spherical agglomerates of iron oxide (white with bluish tint, high reflectance); (b) in a centre oolitic agglomerates of fine-grained iron oxide minerals, probably mostly hematite (grey-white, higher reflectance) which exhibits reddish internal reflection; occurrence of bonded limonite is very likely but was not confirmed; in the left lower corner massive malachite (grey, lower reflectance); malachite intergrown with hematite ooids is also visible in the left upper corner.

However, chemical analyses revealed higher amount of oxygen expected from a simple hematite as well as minor content of  $\text{SiO}_2$ . It suggests, together with a low amount of  $\text{P}_2\text{O}_5$  detected, that the phase present in the sample is more complex and exposes evidences of further weathering. The phase is probably a mixture of iron oxides (sedimentary hematite and magnetite) and hydroxides (limonite), which commonly exhibits bright rusty colour showing by the specimen, as well as amorphous iron oxides.

The habit of iron oxide confirms its pseudomorphic character and indicates that it was formed by the precipitation of iron from the iron-rich solution. That may also shed light on the presence of minor amount of iron oxide in malachite phase. Within the iron oxide phase, several dense nodules were noticed. Their nature is not clear but it may be suggested that they represent iron-minor copper carbonate impregnation of the oolites (Fig. 9) what also would indicate the presence of iron-rich, and carbonated, solution in the environment.

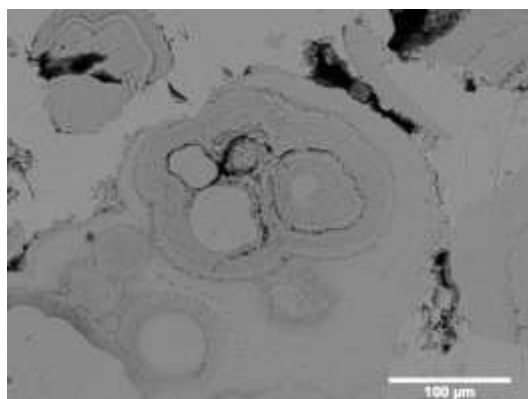


Fig. 9. Dense circular nodules within phase 2. They have the same composition as phase 2. The higher brightness may be explained by their higher density. The character of the phase 3 is arguable. Their association with the process of precipitation is likely.



(C) – sample PB-38 – mixed copper secondary mineralisation in lateritic sediments



Fig. 10. Mineral aggregate from PB (sample PB-38). On the left its section prepared for polished block.

The core of the rusty earthy globule was identified as a mixture of copper oxide and hydroxide minerals (malachite, tenorite and cuprite) and iron oxides. Some native copper was also recognised (Fig. 11).

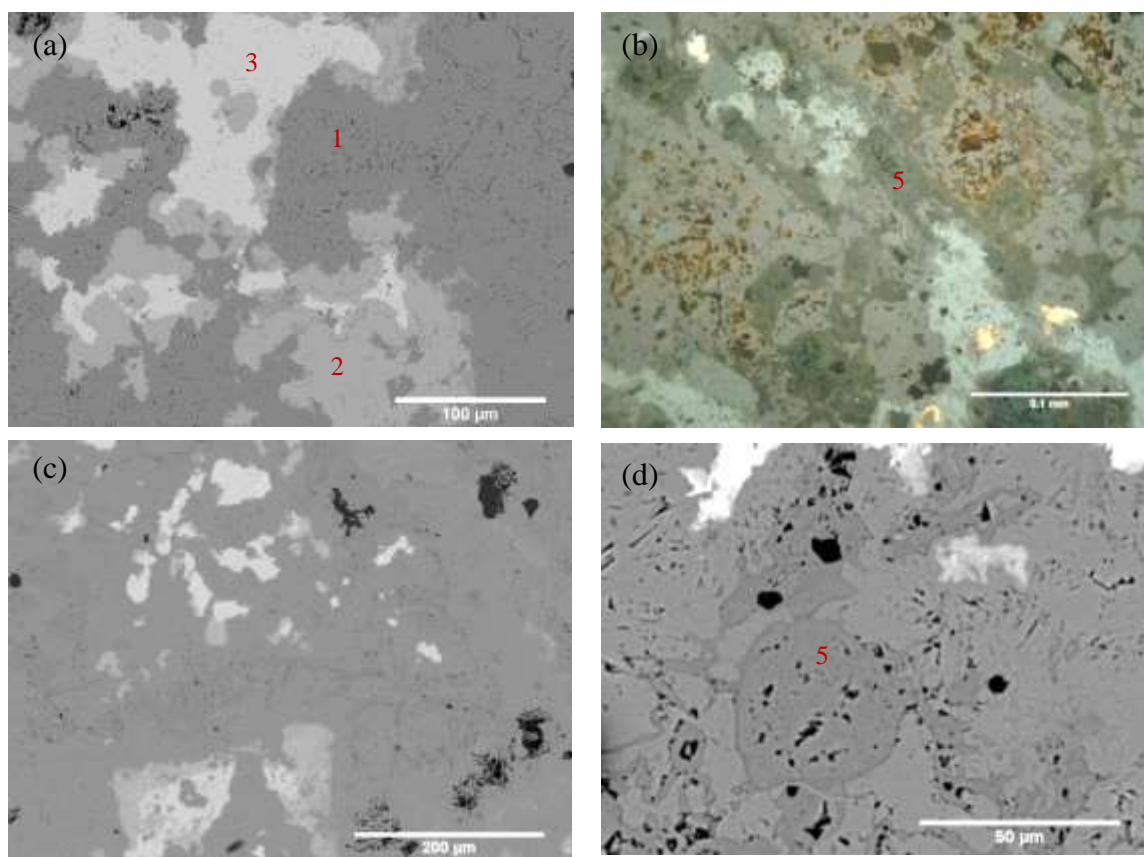


Fig. 11. Microstructure of the core of the sample PB-38: (a) Backscattered electron image showing three-phase structure: 1) fine-grained massive malachite (darker grey); 2) tenorite (?) which forms circular aggregates in some parts; 3) cuprite (white). Within cuprite in left upper corner there is several brighter spot of native copper are visible. (b) Reflected light micrograph, PPL. The yellow phase with highest reflectance is native copper. It occurs usually within cuprite (light grey with bluish tint). The main phase (medium grey) is malachite which is partially replaced by iron-rich corrosion products (phase 5; dark grey/greenish). (c) Backscattered electron image showing phases 1-3 and 5. Note irregular pattern of corrosion (phase 5, darker grey) developing within malachite. (d) Backscattered electron image showing iron-rich corrosion layer (phase 5, darker grey).



All copper-bearing phases seem to be affected by weathering through percolation and precipitation of iron-rich solution what is shown by minor amount of iron oxide detected (Table 4). The identification of the phase 2 of composition similar to tenorite is not clear. It may represent an amorphous product of weathering. Phase 5 is composed mainly of ferric iron oxide and contains several per cent of copper oxide. Its formation is probably connected with weathering of copper minerals by leaching away of copper ions and with precipitation or driftage of secondary silica and possibly iron numerously present in the surrounding lateritic environment.

	Cu	CuO	Cu <sub>2</sub> O	FeO	SiO <sub>2</sub>	Fe	O	Total <sup>a</sup>	Total <sup>b</sup>	Total <sup>c</sup>	Cu/O <sup>d</sup>
Composition of phase 1 in PB-38 <sup>e</sup> , n=7											
highest	56.1	70.2		5.2	nd			74.8		90.3	1.9
lowest	52.5	65.7		2.4	nd			66.4		81.9	1.8
mean	54.2	67.8		3.2	nd			70.5		85.8	1.8
Composition of phase 2 in PB-38 <sup>e</sup> , n=2											
analysis 1	72.5	90.7		0.4	1.8			92.9		95.4	3.3
analysis 2	70.8	88.6		nd	nd			88.6		94.0	3.1
mean	71.7	89.7		0.2	nd			90.1		94.7	3.2
Composition of phase 3 in PB-38 <sup>e</sup> , n=4											
highest	91.7	114.8	103.2	2.3	nd			116.8	105.2	104	8.6
lowest	86.8	108.7	97.8	0.6	nd			108.7	97.8	97.4	7.6
mean	89.4	112.0	100.7	1.6	nd			113.2	101.9	101.4	8.2
Composition of phase 4 in PB-38 <sup>f</sup> , one single-spot analysis											
	98.6				nd	0.7	0.7			100.4	
Model Cu/O (wt%) ratio for copper oxide minerals											
cuprite	88.82		100								7.9
tenorite	79.89	100									4.0
malachite	57.48	71.95									1.6
	Fe <sub>2</sub> O <sub>3</sub>	CuO	SiO <sub>2</sub>	Al <sub>2</sub> O <sub>3</sub>	SO <sub>3</sub>			Total <sup>a</sup>	Total <sup>c</sup>	Fe/O ratio <sup>d</sup>	
Composition of phase 5 in PB-38 <sup>f</sup> , n=4											
highest	93.1	11.9	5.7	0.8	0.7			88.6	99.6	1.6	
lowest	82.4	5.5	1.4	0.7	0.7			82.5	92	1.4	
mean	87.9	8.3	3.1	0.8	0.7			85.6	95.1	1.5	
Model Fe/O (wt%) ratio for iron oxides and iron carbonate											
FeO										3.54	
Fe <sub>3</sub> O <sub>4</sub>										2.8	
Fe <sub>2</sub> O <sub>3</sub>										2.33	
Fe(CO) <sub>3</sub>										1.16	

Table 4. Composition of phases 1-5 in PB-38, SEM-EDS results (wt.%). Cu/O ratios for copper minerals and Fe/O ratios for iron oxides and carbonate are given for comparison. <sup>a</sup> total of oxides with CuO; <sup>b</sup> total of oxides with Cu<sub>2</sub>O; <sup>c</sup> all elements measured; <sup>d</sup> wt.%; <sup>e</sup> not normalised; <sup>f</sup> normalised; n - number of analyses included in the average; nd – not detected.

The rich in copper core is coated with lateritic soil containing high amount of iron oxide and silicate minerals (Fig. 12).

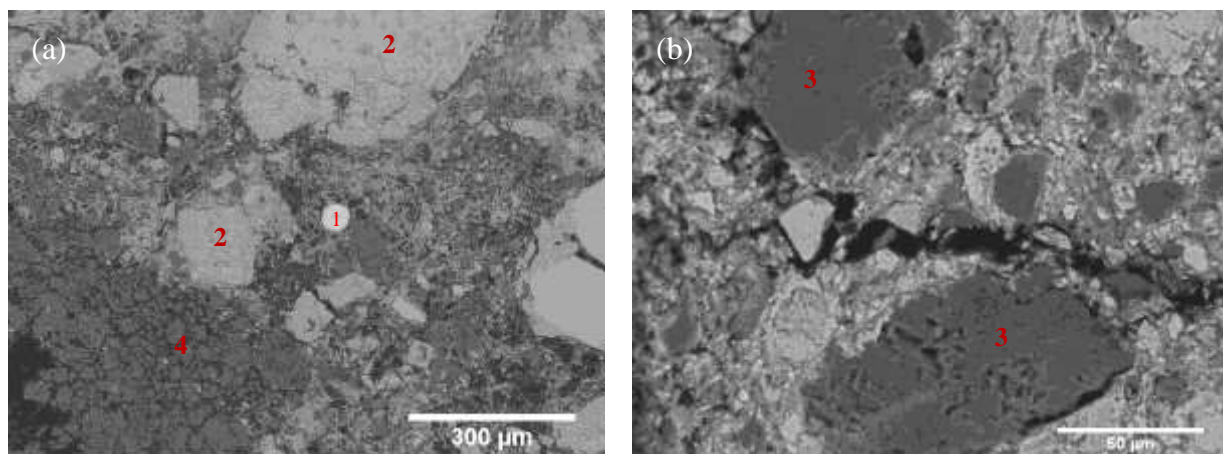


Fig. 12. Backscattered electron images of reddish sediment forming surface of the sample PB-38 showing its main phases: (a) 1) zircon, 2) iron oxide, 4) quartz; (b) 3) lumps of clay of mostly kaolinitic composition. See compositional data for the phases and for the fine-grained matrix in Table 5.

It represents highly weathered sediment containing mainly silica, alumina and iron oxides, i.e. the most stable oxides. Iron oxide occurs probably in the form of hematite and iron hydroxide, for instance limonite. It forms big grains as well as appears as a main component of fine-grained matrix. Such silicates as quartz, zircon as well as high-alumina and silica agglomerates of possibly phyllosilicates (based on kaolinite) were recognised.

	MgO	Al <sub>2</sub> O <sub>3</sub>	SiO <sub>2</sub>	K <sub>2</sub> O	CaO	FeO	Fe <sub>2</sub> O <sub>3</sub>	CuO	ZrO <sub>2</sub>	total <sup>a</sup>	total <sup>b</sup>
Composition of phase 1, one single-spot analysis											
	nd	nd	32.8	nd	nd	1.1		nd	66.2	102.5	101.6
Composition of phase 2, n=3											
mean	nd	0.8	4.1	nd	nd		90.2	4.9	nd	84.8	93.4
σ	nd	0.7	1.1	nd	nd		3.4	1.6	nd	1.6	1.1
Composition of phase 3, three separate single-spot analyses											
a	14.8	38.7	42.3	nd	nd	3.2		1.0	nd	85.9	93.0
b	4.2	40.4	51.3	0.4	nd	3.2		0.6	nd	87.8	96.0
c	nd	40.5	55.1	2.7	nd	1.8		nd	nd	90.3	98.9
Fine-grained matrix of the lateritic sediment, n=2											
mean	2.3	7.0	16.1	nd	1.4		68.5	4.6	nd	79.3	81.0
σ	0.4	3.2	3.1	nd	0.6		7.3	0.02	nd	1.9	6.1
Bulk composition of the lateritic sediment, n=2											
mean	2.0	7.6	31.8	nd	nd		55.5	3.1	nd	87.9	89.0
σ	0.4	3.3	1.8	nd	nd		2.0	0.1	nd	2.6	4.2

Table 5. Composition of the rusty sediment on the surface of PB-38, SEM-EDS results (wt.%), normalised. <sup>a</sup> total of oxides; <sup>b</sup> all elements measured; nd – not detected; n - number of analyses included in the average

(D)- sample PB-42 – mixed ore of copper oxides and relict sulphides



Fig. 13. Mineral aggregate from PB (PB-42). On the left its section prepared for polished block.

The object PB-42 measures 4 x 2.5 cm. It has irregular shape and triangular section. Its rough surface is covered with light green corrosion products (patina) which is a mixture of copper carbonate in various stages of hydration. The object is dense and does not contain any earthy inclusions.

The black and bluish core with a weak metallic lustre is composed primarily of copper oxide minerals, cuprite (phase 1) and tenorite (phase 2), as well as sporadic copper carbonate/hydroxide (phase 3). Native copper is present within cuprite phase (Fig. 14).

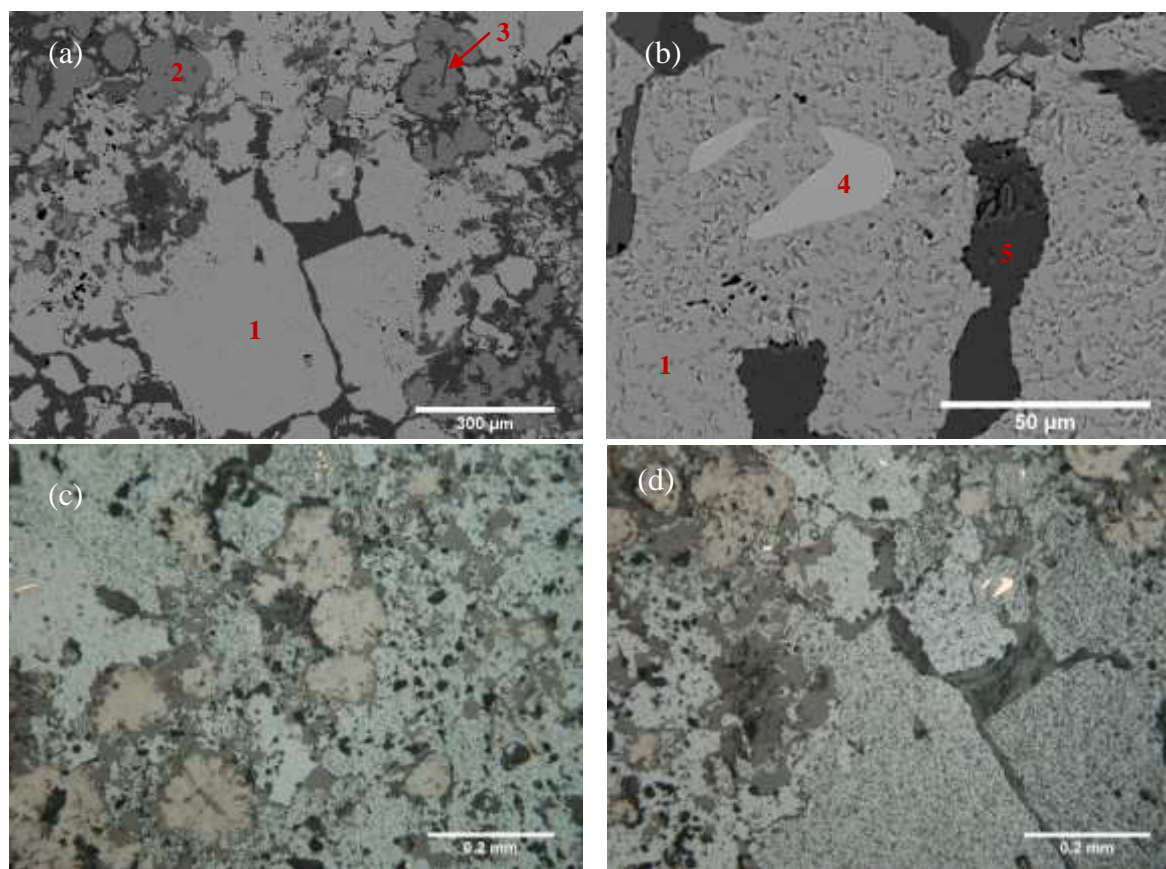


Fig. 14. Microstructure of PB-42: (a) Backscattered electron image of main phases: 1) cuprite (white), 2) tenorite (grey circular grains), 3) copper hydroxide (phase 3), vein of oxidised sulphide (phase 5; dark grey); (b) Backscattered electron image showing native copper (phase 4) within cuprite (phase 1) and sulphur-bearing phase 5; (c) Reflected light micrograph showing cluster of spherical tenorite (phase 2, grey with yellowish tint) growing within cuprite (phase 1, grey with bluish tint), phase 5 (grey) occurring on the edges of tenorite; (d) Reflected light micrograph showing native copper (phase 4, yellow, high reflectance).

Massive cuprite is a main phase. Tenorite, which usually presents no visible crystalline affinities (mindat, 2012), here occurs as circular aggregated of radiating crystals. The habit suggests that tenorite preserved the form of the replaced mineral. It could be malachite which is often found in botryoidal clusters of radiating crystals and is known to lose water at 315°C leaving tenorite. Some acicular grains of composition similar to malachite (phase 3) were found in the centre of circular cluster of tenorite (Fig. 15).

	<b>Cu</b>	<b>O</b>	<b>total<sup>a</sup></b>	<b>CuO</b>	<b>Cu<sub>2</sub>O</b>	<b>Cu/O</b>
Composition of phase 1 in PB-42 <sup>b</sup> , n=4						
Mean	89.0	11.0	86.9	111.4	100.2	8.1
σ	0.6	0.6	25.0	0.7	0.6	0.5
Composition of phase 2 in PB-42 <sup>b</sup> , n=4						
Mean	79.7	20.3	103.7	99.8		3.9
σ	1.1	1.1	15.0	1.4		0.3
Composition of phase 3 in PB-42 <sup>c</sup> , n=2						
Mean	59.4	31.9	91.3	71.3		1.9
σ	2	0.7	2.8	2.5		0.02
Composition of phase 4 in PB-42 <sup>d</sup> , n=3						
Mean	99.5	0.8	98.6			
σ	0.5	0.0	14.8			
Model Cu/O (wt%) ratio for copper oxide minerals						
Cuprite	88.82	11.18	100		100	7.9
Tenorite	79.89	20.11	100	100		4.0
malachite	57.48	42.52	100	71.95		1.6
	<b>CuO</b>	<b>SO<sub>3</sub></b>	<b>Cl</b>	<b>total<sup>e</sup></b>	<b>total<sup>a</sup></b>	
Composition of phase 5 in PB-42 <sup>f</sup> , n=7						
Mean	80.1	19.9	nd	89.4	93.6	
σ	0.7	0.7	nd	9.5	8.5	
Composition of phase 6 in PB-42 <sup>f</sup> , n=3						
Mean	81.7	nd	18.3	100.9	108.0	
σ	0.9	nd	0.9	7.9	9.4	

Table 6. Composition of the phases 1-6 in PB-42, SEM-EDS results (wt.%). <sup>a</sup> all elements measured; <sup>b</sup> Cu and O amounts normalised, calculation of copper oxide based on normalised amount of copper; <sup>c</sup> Cu and O amounts not normalised, calculation of copper oxide based on not normalised amount of copper; <sup>d</sup> Cu and O amounts normalised; <sup>e</sup> total of oxides; <sup>f</sup> normalised; n - number of analyses included in the average; nd – not detected.

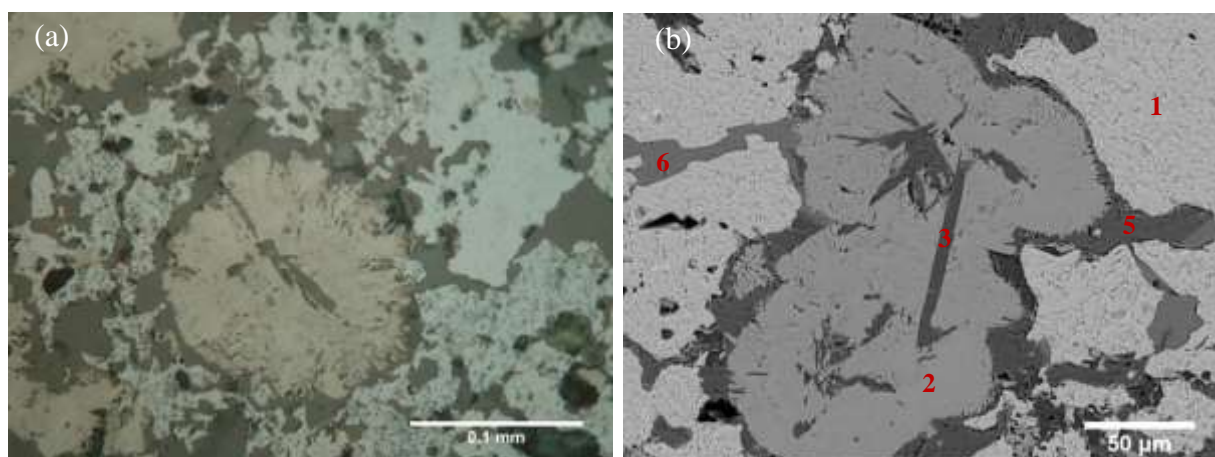


Fig. 15. Tenorite in PB-42: (a) Reflected light micrograph showing spherical agglomerate of radiating crystals of tenorite (phase 2) within cuprite (phase 1, light grey with bluish tint), the tenorite grain is surrounded by sulphate (phase 5, darker grey), in the centre of the grain acicular crystals of copper hydroxide (phase 3); (b) Backscattered electron image of tenorite (phase 2, medium grey), phase 3 and 5. Corrosion layer (phase 6) replacing phase 5 visible within cuprite.

In a few places a residual phase containing c. 19% of  $\text{SO}_3$  were recognised (phase 5). It usually occurs on edges of circular aggregates of tenorite as well as in veins between agglomerates of cuprite. It seems that it represents remains of sulphides, which were gradually oxides and replaced by cuprite and malachite(?)/tenorite. Phase 6 is a corroded phase 5.

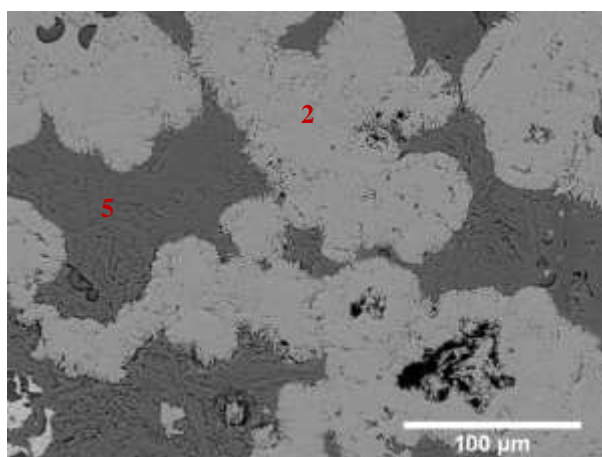


Fig. 16. Backscattered electron image of tenorite (phase 2, light grey) growing within copper sulphate phase (phase 5). Phase 5 usually occurs in PB-42 in small veins or on the edges of tenorite (see Fig. 14 and Fig. 15). Only in the place showing in the image it is more abundant.

## SUMMARY

All of the mineral specimens analysed are related to the supergene enrichment zone of massive sulphide deposits within the Truong Son Fold Belt. They comprise secondary copper minerals (malachite, tenorite, cuprite) and iron oxides and hydroxides (hematite and limonite). Some native copper was also observed. As copper occurs primarily as oxides, its high amount in a range of 30-76 wt.% shown by the bulk composition is not surprising (Table 7). No sulphide minerals, such as covellite or chalcocite which occurs commonly in the enrichment zone, have been recognised. Only in the sample PB-42 small amount of sulphur, average 3.7 wt.%, has been detected. It appears as highly weathered detritus of copper sulphide.

The second most abundant oxide is iron oxide. It appears as both gangue material associated with secondary copper mineralisation (surface of sample PB-38 and sample PB-45) and corrosion products (core of sample PB-38).

	<b>Cu</b>	<b>CuO</b>	<b>FeO</b>	<b>SiO2</b>	<b>SO3</b>	<b>MnO</b>	<b>P2O5</b>	<b>Cl</b>	<b>total<sup>a</sup></b>	<b>total<sup>b</sup></b>
Bulk composition of PB-41 <sup>c</sup> , n=4										
mean	56	67.2	nd	nd	nd	nd	nd	nd	67.2	86.8
σ	0.8	1	nd	nd	nd	nd	nd	nd	1	0.8
Bulk composition of PB-45 <sup>d</sup> , n=3										
mean	30.4	46.1	49.9	3.4	nd	0.3	0.3	nd	70.2	84.8
σ	2.7	4.4	4.0	0.3	nd	0.6	0.4	nd	3.6	4.4
Bulk composition of PB-38 (only core) <sup>d</sup> , n=5										
mean	52.9	79.0	18.5	3.1	nd	nd	nd	nd	70.7	84.5
σ	9.5	15.0	12.9	2.1	nd	nd	nd	nd	8.0	6.8
Bulk composition of PB-42 <sup>d</sup> , n=3										
mean	75.9	94.3	0.7	nd	3.7	nd	nd	2.8	99.6	99.2
σ	4.6	2.0	1.0	nd	1.4	nd	nd	3.7	13.2	16.6

Table 7. Bulk composition of mineral samples, SEM-EDS results (wt.%). <sup>a</sup> total of oxides; <sup>b</sup> all elements measured; <sup>c</sup> not normalised; <sup>d</sup> normalised; n - number of analyses included in the average; nd – not detected.

The occurrence of exclusively copper oxide minerals in the samples as well as their coexistence with iron oxides and lateritic sediments indicate that at least three (PB-38, 41, 45) of the analysed specimens represent minerals associated with the top part of enrichment zone, from which copper is gradually leached and where the process of concentration of iron oxide takes place. The so-called leached cap is generally considered as devoid of larger deposits of copper. All three specimens may be quite safe considered as natural minerals without any evidence of treatment.

The case of the object PB-42 is more complex. On the one hand, it may be identified as a weathered copper sulphide mineral and be assigned to the same zone as other specimens. On the other, however, its quite peculiar shape and the presence of well-crystallised tenorite pseudomorphs may indicate some processing operations, such as mechanical removing of gangue material or roasting at 400-500°C which would convert malachite to tenorite and enhance removing of sulphur as SO<sub>2</sub>. In this case, the mineral agglomerate PB-42 would contained copper sulphides before the possible treatment and may be associated with the deeper rich in chalcocite enrichment zone.

Considering the mineral aggregates as associated with the lateritic oxidation zone, it is difficult to verify if their presence in the archaeological features dug into the laterite is a result of immediate geology or human activity.



### 3.2. Crucibles

About 100 small fragments of crucibles (c. 52 from PB, c. 47 from TMM) were included in the assemblage sent for analysis.

Among the sherds, rim and probably body and base fragments were recognised. Most of the pieces are difficult to relate with a particular part of a vessel due to their small size and large heat-damage. For the same reason the full reconstruction of a crucible shape is not possible. However, a sole complete vessel was found at PB and its characteristics, such as shape of the rim (simple, straight with rounded top), thickness and curvature (slightly convex) of the walls seem to match the attributes of the best-preserved fragments (Fig. 17). It is a conical bowl 8 cm high with a wide mouth (15 cm in diameter). It has a slightly pointed thick base and walls progressively thin (less than 1 cm at the rim level).



Fig. 17. (a) Complete crucible from PB after reconstruction. Photo by N. Chang (Pryce et al., 2011); (b) Rim fragment (PB-17a) and (c) undefined fragment of crucible (PB-5) from PB. The thinning of the rim noticeable in the complete example may partially result from the heat-damage (inner surface of the crucible was molten and incorporated into the melt which solidified at the bottom). Similar effect was noticed on the analysed fragments.

The most distinctive features of the vast majority of the sherds are their light creamy colour, extreme brittleness, roughness and high porosity. All these characteristics seem to be at least to some extent enhanced by the corrosion processes and the way they were used. Many fragments show grey core, usually fading toward the exterior (Fig. 17b). One sherd (PB-15) has an intensively black brittle core and thin light red external zones (Fig. 18c).

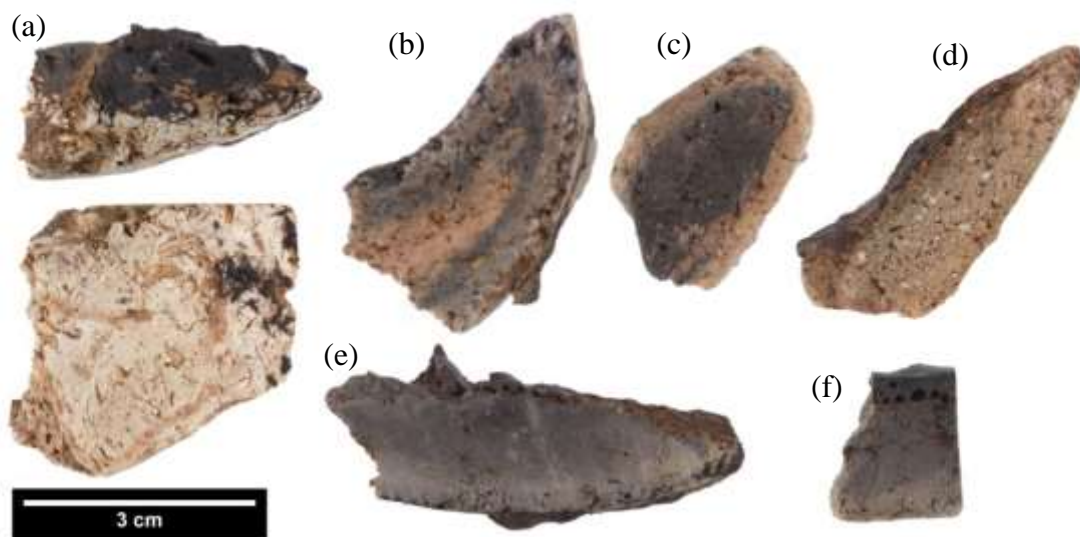


Fig. 18. Fragments of crucibles from PB (a,c-f) and TNN (b): (a) PB-3: note light rough surface of the sherd and advanced slag penetration; (b) TNN-13: three-colour section reflects thermal gradient: the vitrified edges (white/grey) and the non-vitrified red core. Note the slag spilling out of the crucible; (c) PB-15: the sample shows the lowest heat-damage from the whole assemblage; (d) PB-16: note the thin slag lining on the exterior surface, coarse white inclusion and the thin tip of the rim; (e) PB-9: the dark grey zone developing from the interior, slaggy layer visible also on the exterior; (f) PB-17b: grey core and slag layer with smooth upper surface on the inner wall.

Most of the sherds show clear evidence of use (Fig. 19). Almost all the fragments have their inner surface covered with a layer of slag ranging in thickness from less than mm up to 1.5 cm. The three sherds which seem to be less altered are the light red ones (Fig. 18b-d).

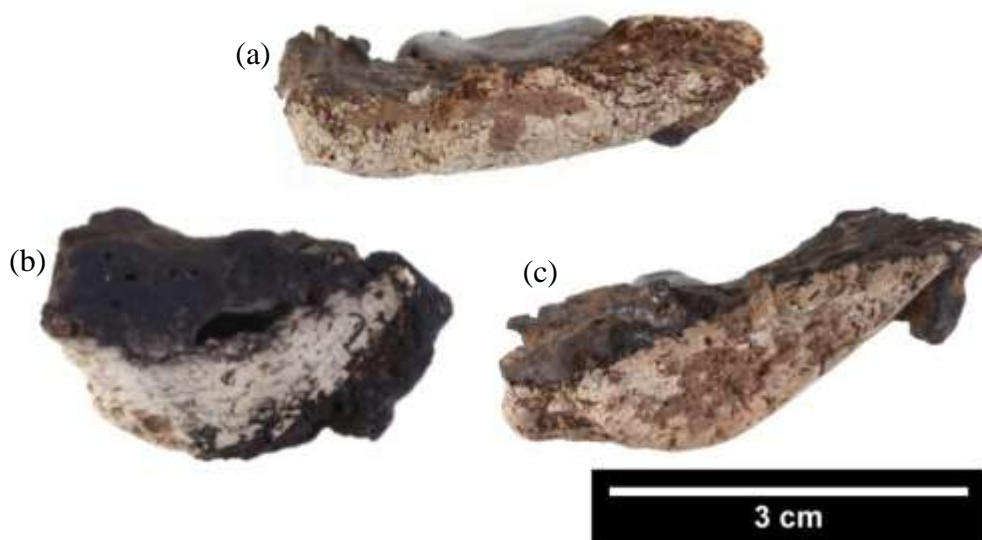


Fig. 19. Slag lining on the inner walls of the crucibles from PB: (a) PB-14: note a high degree of heat damage; (b) PB-13: part of the inner wall was probably fused forming slag; (c) PB-14: note slag spilling out of the crucible.

In most of the fragments no macroscopically visible inclusion was noticed. The only exceptions are white sand grains, most likely quartz, up to 1.5 mm which are, however, visible only in the light red, less damaged sherds (Fig. 18d).

There is no clear evidence of forming technique and surface treatment. The walls of crucibles are very rough and shattered.



## COMPOSITION OF FABRICS

Nine crucible fragments were sampled and analysed with the SEM-EDS, 6 from PB and 3 from TNN. Thin sections for ceramic petrography studies were prepared from 7 sherds (Table 8).

The recognition of the original composition of the crucible fabrics is obscured by two factors, 1) post-deposition alterations increased by intense chemical weathering in humid tropical climate; and 2) to a lesser extent, by contamination with the material from a melt. The second issue, although recognised in a few cases, is not considered as seriously affecting the results.

The process of weathering, in turn, was recognised as especially harmful since it largely changed the ratio of alumina to other oxides in the clay matrix by selective leaching of more mobile ions. The processes which have to be taken into consideration are the weathering of non-clay silicate minerals, such as feldspar, and the desilication of clay minerals (Keller, 1964). They are most clearly demonstrated by the enrichment in alumina of the clay matrix, especially high in parts of the sherds less vitrified, thus more porous and more prone to weathering (Fig. 20).

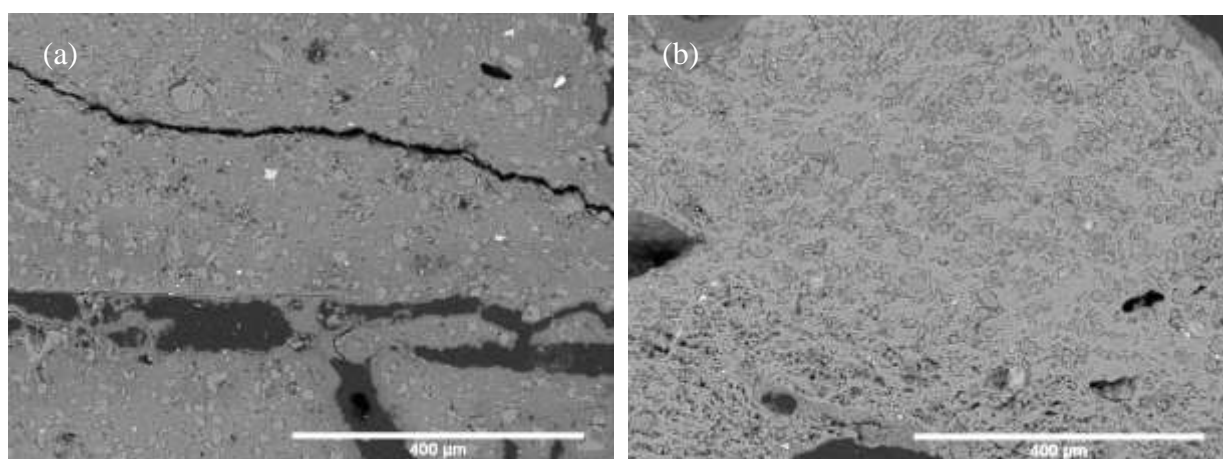


Fig. 20. Backscattered electron images of the sample TNN-13: (a) core and (b) outer zone. The fabrics in both areas show similar textures and inclusion (fine moderately sorted quartz, occasional rutile and zircon (both bright) indicating the same paste). The clay matrices, however, differ quite significantly in appearance and composition. The clay matrix in the core is darker and much higher in alumina (see Table 9: TNN-13 mean 1). This, along with the minor amount of phosphorous, suggests its corrosion (post-depositional weathering). The brighter matrix in outer zone seems to be less affected by weathering what is probably associated with its higher degree of vitrification. Its composition (Table 9: TNN-13 mean 2) may be considered as closer to the original one. In the outer zone between the areas more vitrified, dark weathered spots are also visible (Table 10: TNN-13 analysis 1).

The corrosion is also visible in a peculiar fragmented structure of the clay matrix in which brighter and darker (more weathered, higher in alumina) areas are interlaced (). In addition to weathering this effect is also associated with the fragmented vitrification of the matrix, which formed isolated areas of glass more resistant to corrosion, and less sintered regions more prone to corrosion (Fig. 21). The tendency of less vitrified areas to corrode more intensively was illustrated by the research on deposition of phosphate (Freestone, Meeks, & Middleton, 1985).  $P_2O_5$  is concentrated in the phases less sintered in which porosity is sufficient to allow access for soil solutions (*ibid*, p. 165). Although the amount of  $P_2O_5$  in the presently analysed samples is much lower than reported by Freestone et al., it is higher than the concentration considered as normal in soil and clays, 0.5% (*ibid*, 161) and consistently detected in the dark rich in alumina phase.

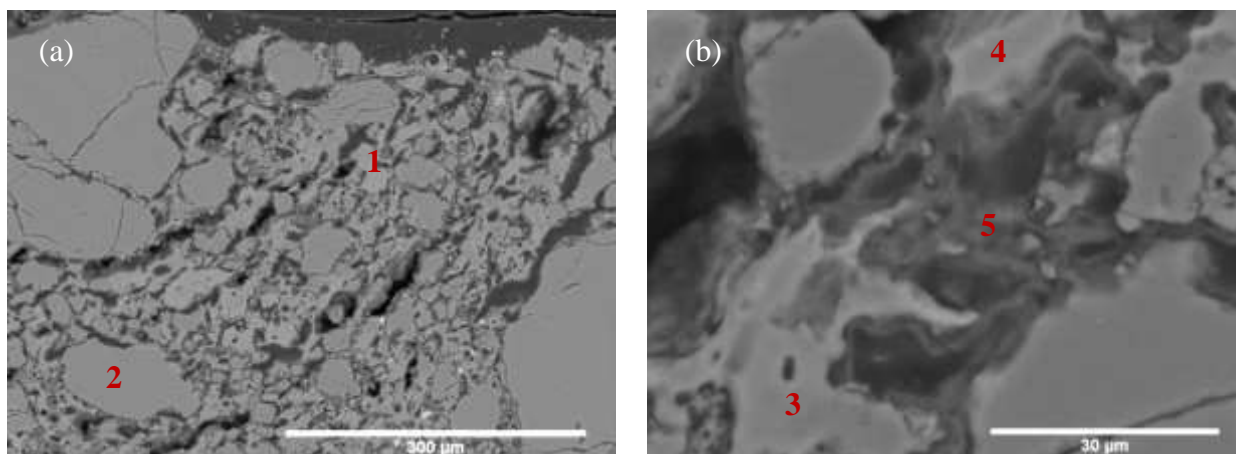


Fig. 21. Backscattered electron images of the sample PB-15 close to the inner surface: (a) General view on 1) fragmentary vitrified matrix (lighter grey areas trending to right corner) and 2) quartz inclusion (darker grey); (b) Fragmented vitrification of the clay matrix at higher magnification: 3) initial vitrification of the clay matrix, less weathered area (Table 10: PB-15 analysis 1); 4) initial vitrification of the clay matrix, less weathered area (Table 10: PB-15 analysis 2); 5) dark corroded region (Table 10: PB-15 mean); note the black holes which may partly resulted from plucking of weathered clay matrix during polishing.

Consequently, it is not possible to eliminate the uncertainty on a degree of alteration of the fabric and the accordance of the results to the composition of a paste actually used for crucible preparation. All analyses of clay matrix are, therefore, assessed carefully and the ones reflected the less weathered areas are tried to be selected (Fig. 22).

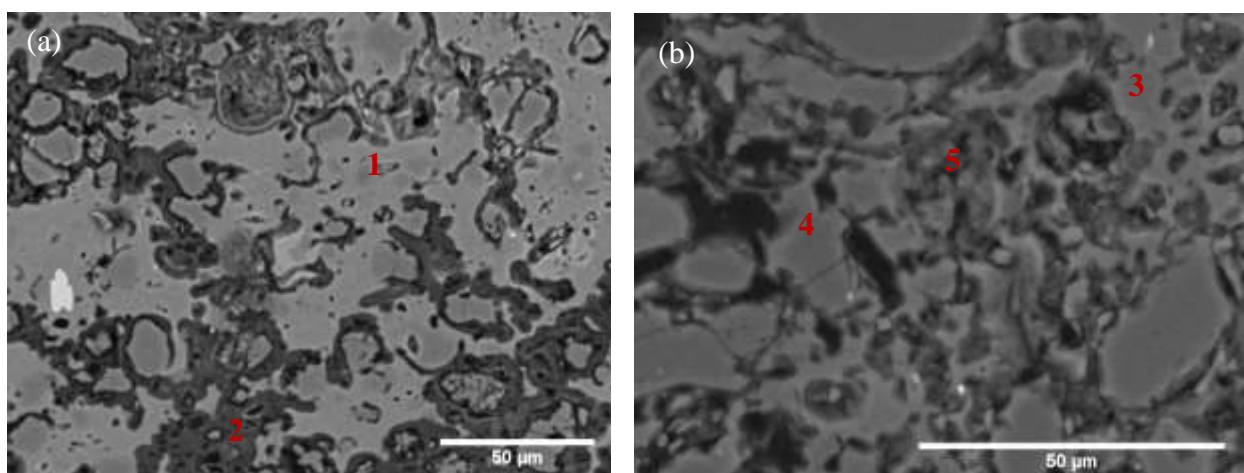


Fig. 22. Backscattered electron images showing the fragmented texture of the crucibles as a result of partial vitrification and weathering processes: (a) sample TNN-13 in outer zone: 1) fresh vitrified areas (light grey), see its composition in (Table 10: TNN-13 mean 2), 2) non-vitrified corroded area (dark grey) see its composition in (Table 10: analysis 1); note how corrosion is developing around large inclusion (ergo along the voids); (b) sample PB-3, note the fragmented texture consisting of 3) separated vitrified areas (lighter grey), 4) partly reacted quartz and 5) corroded non-vitrified regions (dark grey). The determination of less corroded areas is based on the brighter and fresher look as well as the composition (amount of alumina lower than silica, free of  $P_2O_5$ , potash  $\geq 3\%$ ).

\*\*\*

All analysed samples were made of non-calcareous highly weathered clays. Its origin in highly weathered deposits is demonstrated by a very low amount of other ingredients than quartz, presence of weathered potassium feldspar and minerals considered, aside from quartz, as the most resistant ones (rutile, zircon) (Pettijohn, Potter, & Siever, 1973, p. 305). It seems to be also indicated by the composition of the clay matrix originally probably quite rich in high-alumina minerals.

In most cases, clay matrix is light brown in PPL and dark, optically inactive in XP (Fig. 23). It constitutes approximately 40-60% of the paste (excluding pores and inclusion).

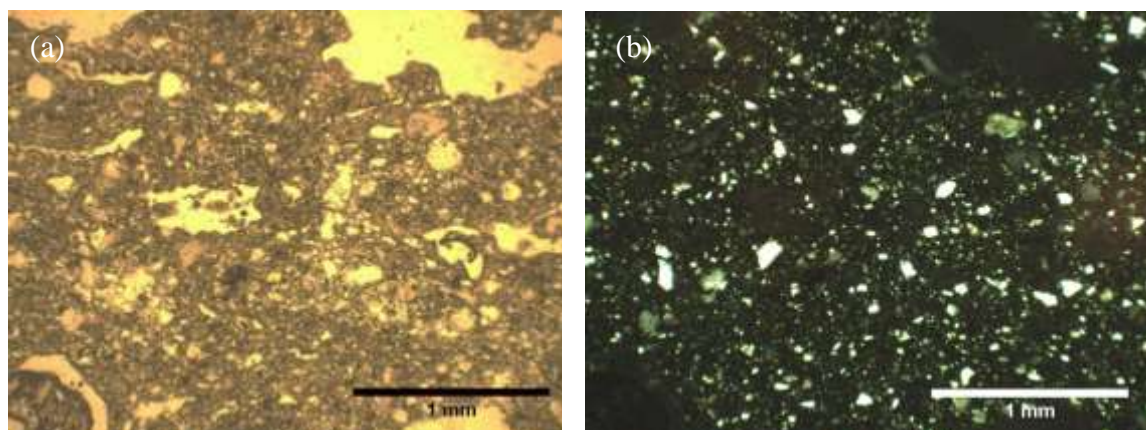


Fig. 23. Optical micrographs of sample PB-9 (a) in PPL and (b) in XP showing evenly distributed fine quartz grains in optically inactive clay matrix. Note randomly distributed elongated crenulated voids in the upper part of the image.

The main mineral inclusion observed in all samples is quartz (Fig. 24). It occurs in a high abundance ranging from 20 to 30%. It mainly consists of evenly distributed very fine grains (below 0.1 mm across). In most of the samples (excepting TNN-2b and TNN-13) coarser, usually 0.2-0.7 mm, quartz grains occur as well. They are less abundant (1-5%) and poorly distributed. Quartz usually shows sub-angular or sub-rounded shape and medium to low sphericity usually considered as indicators of low textural maturity of quartz. Fracture pores observed in large grains, however, seem to indicate the advanced chemical weathering.

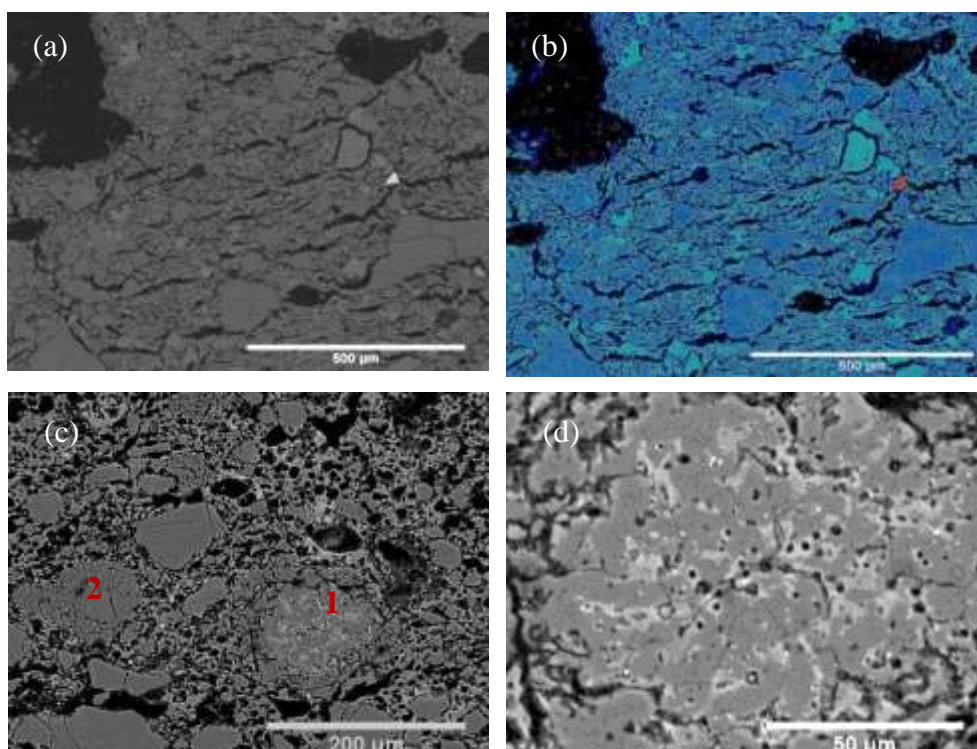


Fig. 24. Quartziferous nature of the crucible paste: (a) Backscattered electron image of the sample PB-3 and (b) its coloured version. Note a high quantity of quartz (dark blue), rarer weathered potassium feldspar (light blue) and occasional rutile (yellow) and single zircon (red); (c) Backscattered electron image of the sample PB-17a showing shattered quartz grains (1-2); (d) grain no. 1 under higher magnification. Note fracture pores (dissolution features?) in which clay was deposited (bright)

Sample	Type of sample		Type of inclusion and its characteristics					
	Polished block	Thin section	Quartz	Potassium feldspar	Rutile	Zircon	Elongated crenulated voids	Iron oxide concentration (red mottling, slag etc.)
TNN-2b	✓	×	Common, moderately sorted Very fine (<0.1): 20% Medium (up to 0.2mm): 1%	Not observed	Very rare (<0.5%) ≤ 20µm	Very rare (<0.5%) < 40µm	Not observed	Fe prills in glassy area
TNN-5	×	✓	Common, moderately sorted Very fine (<0.1): 25-30% Medium (up to 0.6mm): 1%, some polycrystalline	Not observed	Not observed	Not observed	Few (5-15% of the volume) up to 1mm long, not evenly distributed	Not observed
TNN-9	✓	×	Common, moderately sorted Very fine (<0.1): 25% Medium (up to 0.5mm): 1%	Not observed	Rare c. 0.5%, silts size ≤ 30µm	Very rare (<0.5%) < 20µm	Few (5-15% of the volume) up to 1mm long, not evenly distributed	Concentration of fine-grained FeO in glassy area
TNN-13	✓	✓	Common, moderately sorted Very fine (<0.1mm): 15-20% Fine (up to 0.15mm): 1%	Not observed	Very rare (<0.5%) ≤ 20µm; some porous (weathered?)	Not observed	Common (15-20% of the volume) up to 1mm long, not evenly distributed	1) Red mottling 2) Fe prill in glassy areas?
PB-3	✓	✓	Common, moderately sorted Very fine (<0.1): 20% Medium (up to 0.5mm): 3%, some polycrystalline	Rare 1%, up to 0.1mm, weathered and bloated	Very rare (<0.5%) < 10µm	Very rare (<0.5%) ≤ 40µm	Few (5-15% of the volume) up to 1mm long, not evenly distributed	Not observed
PB-5	✓	×	Common, moderately sorted Very fine (<0.1): 20% Medium (up to 0.5mm): 1%	Rare (0.5-2%), up to 0.2mm, weathered and bloated	Rare c. 0.5%, silts size ≤ 50µm	Not observed	Few (5-15% of the volume) up to 1.5mm long, not evenly distributed	Not observed
PB-9	×	✓	Common, moderately sorted Very fine (<0.1mm): 15% Medium (up to 0.3mm): 2%	Not observed	Not observed	Not observed	Few (5-15% of the volume) up to 1mm long, not evenly distributed	Not observed
PB-13	✓	×	Common, moderately sorted Very fine (<0.1mm): 20% Medium (up to 0.3mm): 2%	Rare 2%, up to 0.3mm, weathered and bloated	Rare c. 0.5%, silts size < 50µm	Not observed	Few (5-15% of the volume) up to 1mm long, not evenly distributed	Not observed
PB-15	✓	✓	Common, poorly sorted, bimodal grain size distribution Very fine (<0.1mm): 20% Medium (up to 0.8mm): 3%	Not observed	Very rare (<0.5%) Silt size < 20µm	Not observed	Few (5-15% of the volume) up to 2mm long, not evenly distributed	1) Lump of lateritic soil with quartz inclusion 2) Metallic iron
PB-16	✓	✓	Common, poorly sorted Very fine (<0.1mm): 25% Medium (up to 0.5mm): 5% Coarse (up to 1.5mm): <1%, polycrystalline	Not observed	Very rare (<0.5%) Fine silt < 10µm	Not observed	Few (5-15% of the volume) up to 1mm long, not evenly distributed	Glassy slaggy chunk
PB-17a	✓	✓	Common, poorly sorted Very fine (<0.1mm): 25% Medium (up to 0.5mm): 5% Coarse (up to 1.5mm) <1%, polycrystalline	Not observed	Rare c. 0.5%, silts size < 40µm; some porous (weathered?)	Very rare, 30µm, anhedral	Few (5-15% of the volume) up to 2mm long, not evenly distributed	1) Glassy slaggy chunk 2) White substance in voids (weathering?)

Table 8. Characterisation of the inclusion in the crucible samples. Frequency of particular minerals was roughly estimated with the help of abundance estimation charts.



Among other silicates recognised in the samples there are: weathered feldspar showing evidences of vitrification (coarse bloating pores), very rare sometimes porous (weathered?) rutile and zircon (Fig. 25).

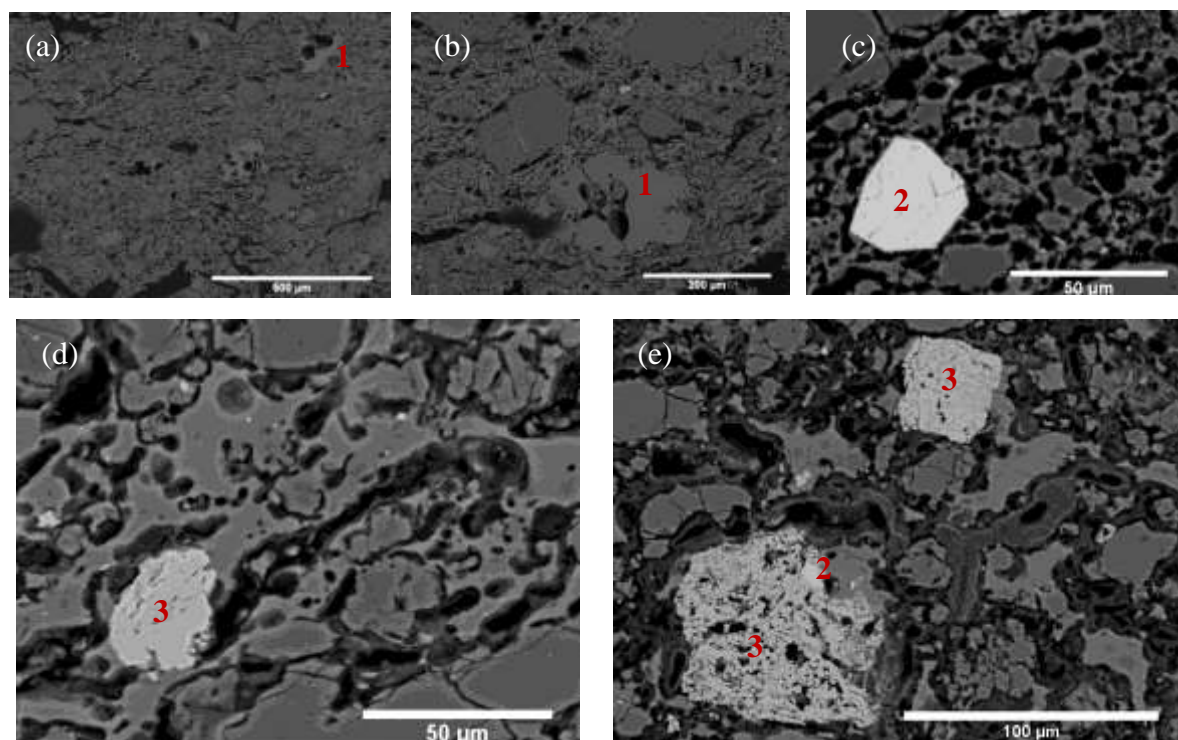


Fig. 25. Backscattered electron images of the crucible samples showing main type of mineral inclusion: (a) and (b) sample PB-13: weathered potassium feldspar with bloating pores (1-slightly lighter grey); (c) sample PB-17a: zircon (2-bright); (d) sample PB-9: rutile (3-bright); (e) sample TNN-9: porous (weathered?) rutile (3) and small zircon grain (2-brightes within rutile).

In the samples less affected by heat, red mottling was noticed under the polarising microscope (Fig. 26a). It may be identified as iron oxide. The iron oxide concentrations were also observed in the glassy areas of the samples under the SEM (Fig. 26b). In the sample PB-15 lump of lateritic clay with quartz inclusion was recognised (Fig. 26c).

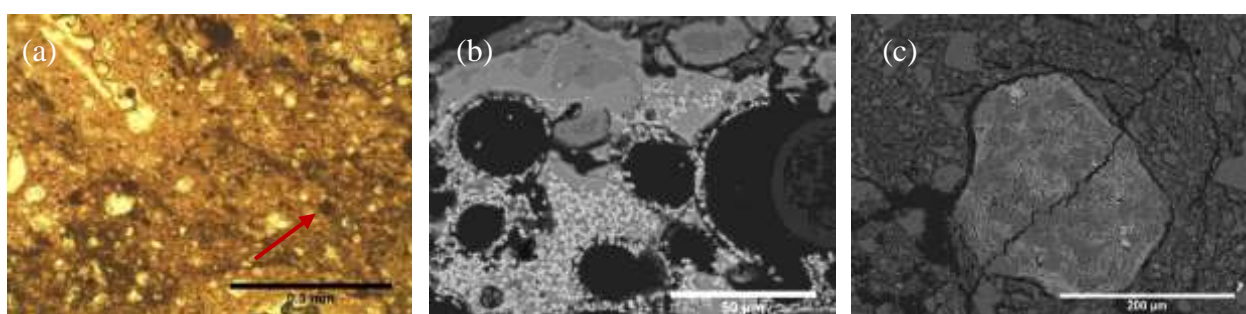


Fig. 26. Concentration of iron oxide in the crucible fabric: (a) Optical micrograph of the sample TNN-13. Note dark red mottling (arrow); (b) Backscattered electron image of the sample TNN-9 showing fine iron oxide (bright) within the glassy area (light grey); (c) Backscattered electron image of the sample PB-15 with a lump of lateritic clay (bright) with quartz inclusion (grey).

The porosity of the samples is quite high. Aside from macro cracks and pores resulted most likely from mechanical damage, neglected paste preparation and burning off the organic inclusion, there is a high abundance of micro pores which make the appearance of the fabric under the SEM fragmentary and unclear. The microporosity constitutes round bloating pores visible in the more vitrified areas, shrinkage voids around large inclusion and open pores part

of which were probably formed due to removing of matrix pieces and inclusion during sample polishing (Fig. 27).

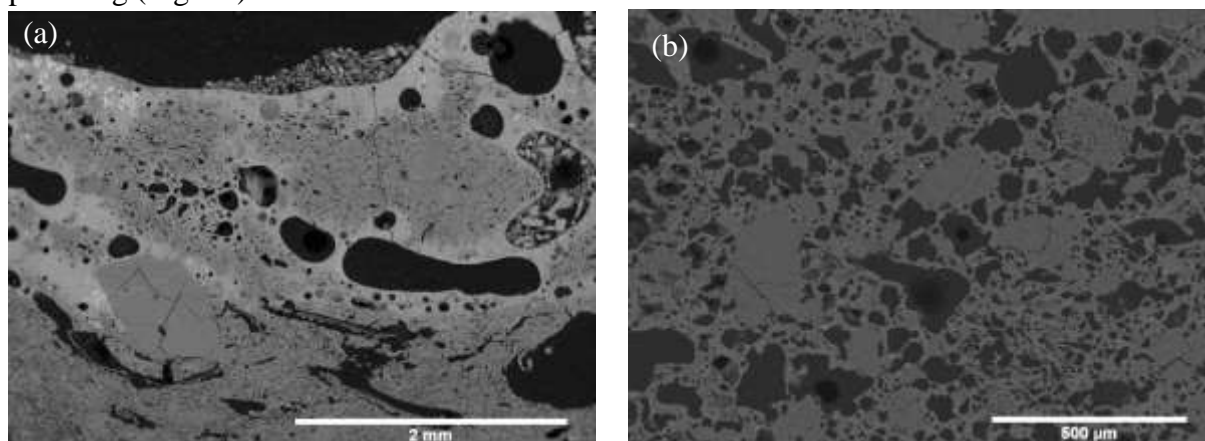


Fig. 27. Porosity in the crucibles, both backscattered electron images: (a) coarse bloating pores developed in glassy areas close to the inner edge of the sample PB-13. Gas bubbles are formed due to giving off the structural water by clay minerals and rapid freezing of the melt. (b) heavily vitrified and bloated fabric just below the slag lining on the inner wall of the sample PB-16; some of the large irregular pores may have contained originally clay matrix which was weathered and/or plucking out during sample polishing (note removing of resin-black areas in the centre of the voids and compare with Fig. 25e). Shrinkage voids mentioned in the text can be observed around the lateritic inclusion in Fig. 26c and quartz and weathered feldspar grains in Fig. 24a-b).

The original arrangement and the quantity of pores are difficult to define since they were largely altered by heat-damage (Fig. 21a). The elongated parallel to the walls shrinkage cracks, constituent most likely the original component of microporosity, may be observed in a few better preserved areas of the samples (Fig. 28).

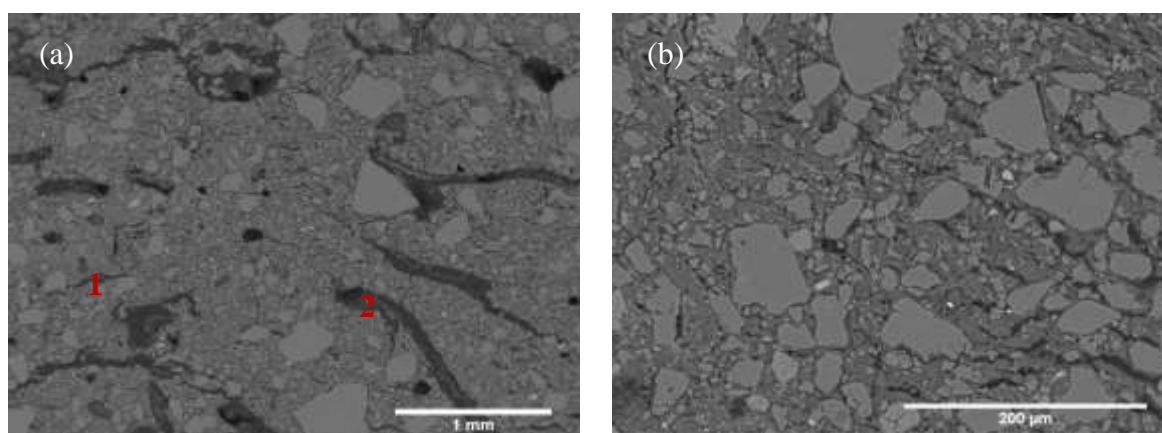


Fig. 28. Backscattered electron images of the core of the sample PB-15 showing: (a) fine shrinkage cracks in the centre (1; see similar in Fig. 24a) and rice-husk voids (2); (b) fine shrinkage cracks at higher magnification. Compare the arrangement of the pores with the Fig. 21a showing the same sample but in the vitrified outer zone. The orientation, size and shape of the void were altered during heating.

In most of the samples the characteristic elongated voids with wavy edge were noticed (Fig. 29). They were identified as burnt rice husks on the basis of comparison to the detailed studies on this type of temper (Lippi, Gonnelli, & Pallecchi, 2011; Tomber, Cartwright, & Gupta, 2011). They are unevenly distributed and randomly oriented. Their amount is much lower than in the analysed fragment of domestic pottery from PB (Appendix 2, PB-19).

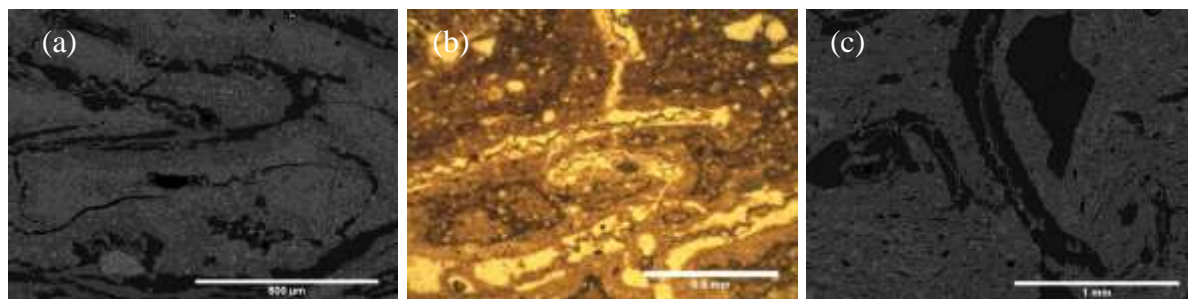


Fig. 29. Rice-husk voids in the crucible fabrics: (a) Backscattered electron image and (b) Optical micrograph of the sample TNN-13 showing concentration of the voids; (c) Backscattered electron image of the sample PB-16. Note varied orientation of the voids.

The average bulk compositions of the samples seem to indicate several differences between crucibles from PB and TNN (see average bulk composition in Table 9). First of all, the silica to alumina ratio is lower in the examples from TNN. The samples from TNN are also richer in FeO. All other oxides are at similar low levels.

The average bulk composition cannot be, however, considered as reliable since the variation between particular samples is too large (note the high amount of iron in the contaminated sample TNN-2b and highly varied contents of silica and alumina across the samples). Assuming that the types of inclusion present in all samples are similar, what was evidenced above, the variability may result from 1) different composition of the clay matrix (what seems to be, at first sight, indicated by average results in Table 10); 2) varied amount of particular types of inclusion, particularly quartz and weathered feldspar; 3) different degree of weathering; and 4) uncontrolled plucking out the pieces of the soft non-vitrified matrix during polishing. The author believes that the first two factors are crucial and their detailed explanation may improve understanding of the crucible making traditions at both sites.

Considering the clay matrix, the results presented in Table 10 show a wide distribution and lack of consistency (Fig. 30). The measurement fluctuation reflects the normal mineralogical heterogeneity of the clay relative to small, due to the attempt to avoid weathering region even of spot-size, analytical areas.

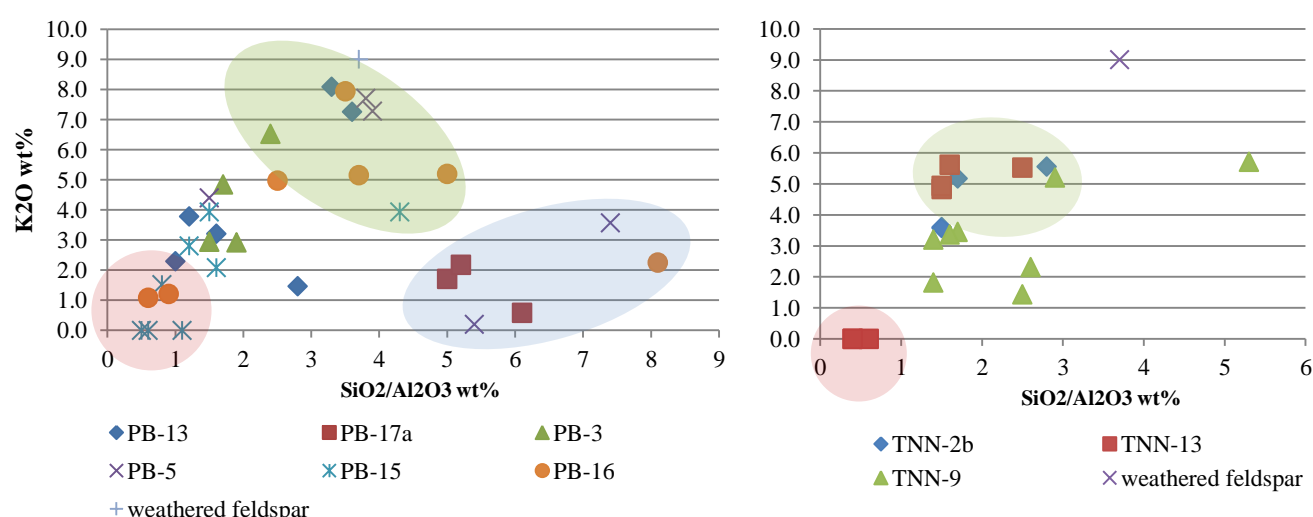


Fig. 30. Scatter charts plotting the amount of potash and silica to alumina ratio in the single analysis of the fine-grained fraction in crucible fabrics from PB and TNN; SEM-EDS results, normalised (wt%) Note the wide variations in both parameters indicating the lack of compositional homogenisation of the fabric due to firing and the fact that phases of different mineralogical origin were analysed.



The partial vitrification made the appearance of the fine-grained fraction uniform making difficult to decide when the vitrified area being analysed represents relict clay matrix (consisting for instance of kaolinite, fine-grained sericite, illite) and when mainly sintered or melted coarser minerals (such as very fine quartz, weathered feldspars) (Fig. 31). The duration of firing was, however, insufficient to homogenise the fabric compositionally by interdiffusion and the analyses may be considered as representing the relict phases of the original raw material (Tite, Freestone, & Wood, 2012, p. 40). The original character of these phases is tried to be guessed on a basis of their composition, in particular SiO<sub>2</sub>/Al<sub>2</sub>O<sub>3</sub> ratio.

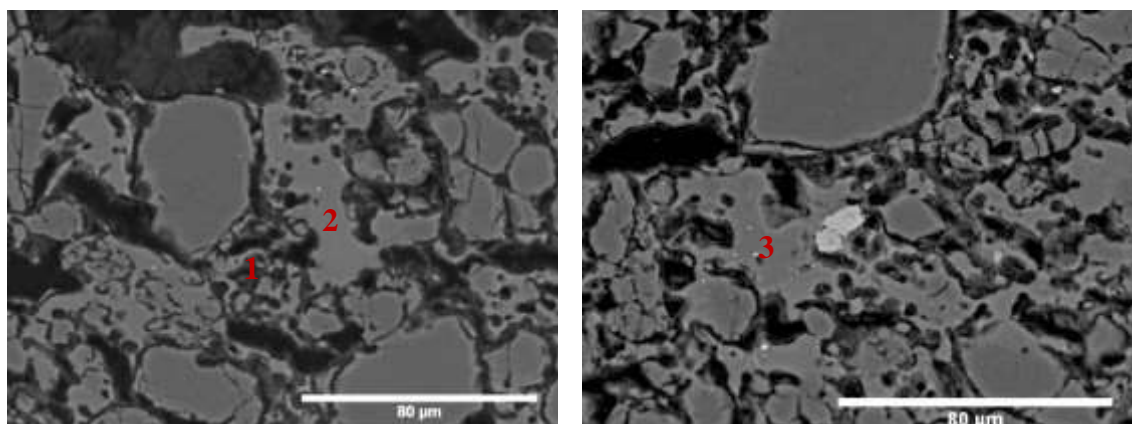


Fig. 31. Backscattered electron images of the fine-grained fraction in the sample PB-5. In order to avoid analysing of weathered dark grey areas (1), small vitrified region were analysed (2, 3). They produced, however, varied compositional results, low (2-full results see Table 10: PB-5 mean) and high (3, Table 10: PB-5, analysis 1) in alumina. They must be, therefore, considered as a sintered fine-grained fraction (clay and silt size) of varied components (see text below).

The results with the SiO<sub>2</sub>/Al<sub>2</sub>O<sub>3</sub> ratio above 4 suggest the large contribution of quartz sintered with the surroundings to the analyses (Fig. 30, blue circle; Fig. 33) and, in the case of the measurements high in potash (above 3-4%), of the weathered feldspar (Fig. 32), secondary mica or illite (Fig. 30, green circle). The results with alumina above 30% may be considered as analyses of a vitrified mixture of predominantly kaolinitic clay minerals with fine-grained impurities (sericite?). The results especially high in alumina, originating from dark in BSE areas often containing P<sub>2</sub>O<sub>5</sub>, are classified as a corroded clay matrix which originally may have consisted of high-alumina clay minerals (kaolinite) (Fig. 30, red circle).

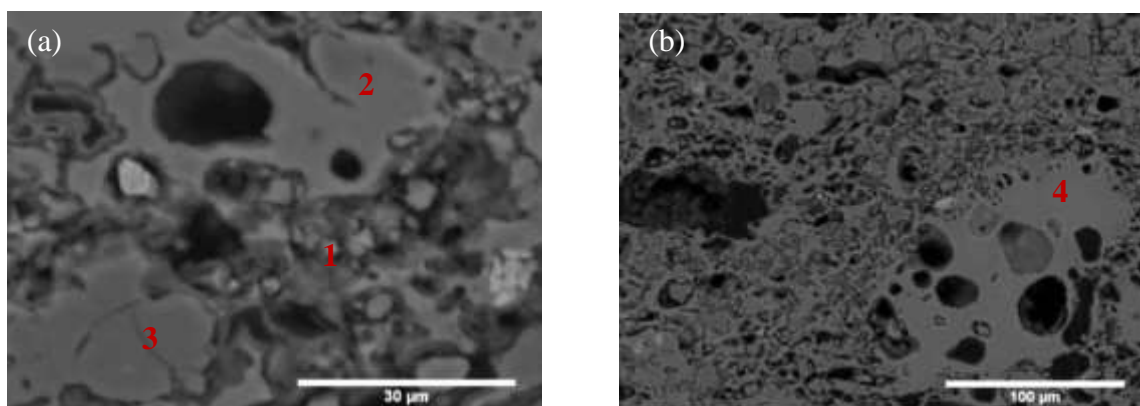


Fig. 32. Backscattered electron images of the sample PB-13: (a) Fine-grained fraction. Note dark non-vitrified probably weathered areas (1, see its composition in Table 10: PB-13 analysis 1) and vitrified bloated region composed probably mostly of molten, weathered feldspar (2, see its composition in Table 10: PB-13 mean 2), quartz (3); (b) Bloated weathered feldspar (4) with the composition almost exactly the same as the vitrified phase, marked in Fig. 30. Note how the feldspar grain is melted away and fused with the surrounding.



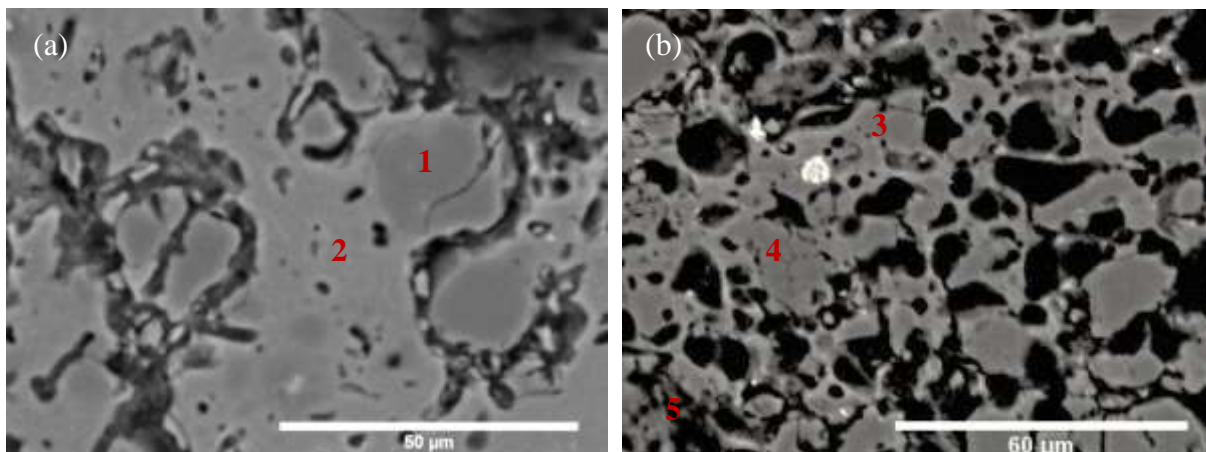


Fig. 33. Backscattered electron image of: (a) outer zone of the sample TNN-13: quartz grains (1) fused with the matrix rich in alumina (2); (b) heavily bloated matrix of sample PB-17a: the vitrified area analysed (3) was identified as composed of fine quartz fluxed by the surroundings ( $\text{SiO}_2$ -81%,  $\text{Al}_2\text{O}_3$ -13%,  $\text{FeO}$ -3%,  $\text{TiO}_2$ -2% ; $\text{K}_2\text{O}$ -0.6,  $\text{MgO}$ -0.6); note the shattered quartz (4). Where is the clay matrix? One of the possible explanations is that some of the voids (for instance in the area 5) contained clay minerals but they were removed (weathering, polishing, melted away).

The clay fraction of the paste used in the crucible manufacture may have contained predominantly high-alumina clay minerals. The clay was, however, impure and quite heterogeneous containing varied amount of fine weathered potassium feldspar and possibly secondary mica stimulating the vitrification. The patchy character of the clay and incomplete vitrification may be partly explained by the compositional variability of the clay: when some part of the paste were already melted, another, more refractory, remained unaffected, therefore more prone to post-depositional weathering which enhanced the fragmentary character of the artefacts and their brittleness, the distinctive features of the crucibles noticeable at first sight (Fig. 34).

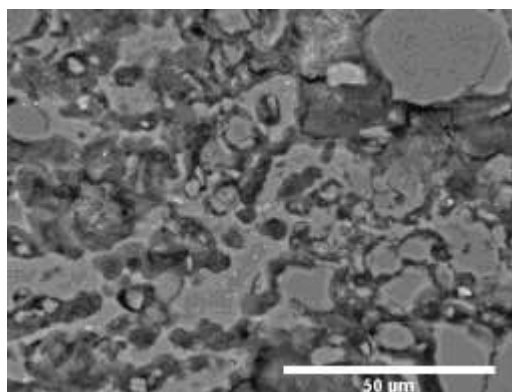


Fig. 34. Backscattered electron image of the sample PB-5. Note patchy nature of the fabric probably originated from incomplete vitrification and weathering.

To conclude, the precise determination of the raw material used in crucibles is not possible at present. The author inclines to believe that most of the analysed crucibles were made of quartziferous impure kaolinitic clay. The main compositional differences result from a varied proportion of clay matrix and quartz in the particular samples (and sometimes in the scan areas analysed) and a different degree of clay impurity. The issue such as degree of preservation, heat-damage and contamination during use made also a contribution.

Table 9. SEM-EDS results, normalised wt%, for bulk composition of the crucible fabrics; ‘contamination’ – due to the use; n - number of analyses included in the average;  $\sigma$  – standard deviation.

Sample	Degree of weathering	Contamination	MgO	Al2O3	SiO2	P2O5	K2O	CaO	TiO2	FeO	CuO	Cl	total
TNN-2b													
mean (n=2)	partly weathered (dark-bright patches)	yes	0.3	35.8	46.9	0.5	2.0	0.5	1.6	12.3	nd	nd	87.3
σ			0.5	0.1	6.2	0.7	0.3	0.05	0.2	5.9	nd	nd	30.4
TNN-9													
mean (n=3)	partly weathered (dark-bright patches)	no	nd	21.0	72.4	nd	2.0	nd	1.0	3.5	nd	0.2	62.0
σ			nd	0.6	1.1	nd	0.2	nd	0.2	0.4	nd	0.3	6.2
TNN-13													
mean 1 (n=2)	weathered (less vitrified core)	no	0.9	40.3	52.4	nd	0.5	0.2	0.3	5.1	nd	0.3	68.1
σ			0.1	0.6	0.7	nd	0.3	0.3	0.4	0	nd	0.4	9.3
mean 2 (n=3)	relative unweathered (vitrified)	no	0.8	29.0	63.2	nd	3.0	nd	0.3	3.6	nd	nd	88.7
σ			0.04	0.5	1.2	nd	0.2	nd	0.3	0.3	nd	nd	1.8
PB-3													
mean (n=3)	partly weathered (dark-bright patches)	no	0.3	21.0	74.7	nd	2.2	0.2	0.4	1.2	nd	nd	76.8
σ			0.3	0.9	0.7	nd	0.1	0.3	0.4	0.1	nd	nd	6.2
PB-5													
mean (n=4)	partly weathered (dark-bright patches)	minor	0.4	20.5	73.8	0.3	2.0	0.3	1.2	1.4	0.2	nd	76.5
σ			0.1	1.5	1.7	0.3	0.1	0.2	0.2	0.2	0.3	nd	8.0
PB-13													
mean (n=4)	partly weathered (dark-bright patches)	no	0.5	25.5	67.3	nd	2.8	nd	0.6	1.8	1.4	0.1	70.5
σ			0.4	1.0	1.4	nd	0.2	nd	0.4	0.3	0.5	0.2	8.1
PB-15													
mean 1 (n=5)	partly weathered (dark-bright patches)	no	0.1	16.8	78.7	nd	0.8	nd	0.9	2.6	nd	0.1	68.2
σ			0.2	1.0	0.8	nd	0.9	nd	0.2	0.4	nd	0.1	8.0
analysis	weathered (less vitrified lower edge)	no	nd	25.4	66.6	1.2	3.1	nd	0.0	3.7	nd	nd	70.3
PB-16													
mean (n=2)	relative unweathered (vitrified)	no	nd	16.4	77.4	nd	2.4	nd	0.6	3.1	nd	nd	67.5
σ			nd	1.6	3.3	nd	0.3	nd	0.0	1.1	nd	nd	1.3
PB-17a													
mean (n=6)	relative unweathered (vitrified)	no	0.5	14.4	78.1	nd	1.2	0.5	1.1	4.2	nd	nd	72.9
σ			0.2	0.8	1.5	nd	0.1	0.03	0.5	0.3	nd	nd	11.8

Sample	Degree of weathering	Contamination	MgO	Al <sub>2</sub> O <sub>3</sub>	SiO <sub>2</sub>	P <sub>2</sub> O <sub>5</sub>	K <sub>2</sub> O	CaO	TiO <sub>2</sub>	FeO	CuO	Cl	total
<b>Bulk composition of crucibles from TNN (excluding highly weathered areas)</b>													
mean (n=8)			0.4	27.7	62.6	0.1	2.4	0.1	0.9	5.8	nd	0.1	78.4
σ			0.4	6.3	10.9	0.4	0.6	0.2	0.6	4.6	nd	0.2	18.1
<b>Bulk composition of crucibles from PB (excluding highly weathered areas)</b>													
mean (n=23)			0.3	18.8	75.2	0.1	1.7	0.2	0.9	2.5	0.3	0.0	72.2
σ			0.3	4.0	4.3	0.2	0.8	0.3	0.4	1.2	0.6	0.1	8.6

Table 10. SEM-EDS results, normalised (wt%), for composition of the fine fraction in the crucible fabrics; n - number of analyses included in the average;  $\sigma$  – standard deviation.

Sample	Description	MgO	Al2O3	SiO2	P2O5	K2O	CaO	TiO2	FeO	CuO	Cl	total
TNN-2b												
mean (n=4)	fresh, vitrified, round bloating pores	1.2	31.6	55.8	nd	4.5	nd	1.0	5.6	0.3	nd	109.1
σ		0.1	7.5	7.3	nd	1.1	nd	0.2	1.4	0.6	nd	0.8
TNN-9												
mean 1 (n=3)	fresh, vitrified, higher in alumina	0.7	32	60.1	0	3	0	0.8	3.4	0	0	99.6
σ		0.7	5.3	6.4	0	0.6	0	0.2	0.5	0	0	14
mean 2 (n=2)	fresh, vitrified, lower in alumina	0.8	18.5	71.2	0	5.5	0	0.6	3.4	0	0	104.4
σ		0.1	6.2	6	0	0.4	0	0.2	0.3	0	0	3.4
mean 3 (n=3)	weathered, dark porous areas incorporated	0.3	32.2	55.1	0.8	2.1	0.5	1.7	7.3	nd	0.2	74.8
σ		0.5	6.3	10.3	0.8	0.9	0.4	1.0	6.4	nd	0.3	14.9
TNN-13												
mean 1 (n=2)	weathered dark core	1.3	60.7	31.2	1	nd	0.2	nd	5.4	nd	nd	82
σ		0.4	4.0	5.7	0.3	nd	0.2	nd	2.1	nd	nd	6.0
analysis 1	weathered dark area in outer zone	1.89	65.35	28.58	nd	nd	nd	nd	3.57	nd	0.61	56.1
mean 2 (n=3)	fresh, vitrified outer zone	1.2	35.2	55.1	nd	5.1	nd	nd	3.4	nd	nd	100.9
σ		0.3	0.7	1.0	nd	0.4	nd	nd	1.2	nd	nd	3.1
analysis 2	fresh, vitrified outer zone, lower in alumina	1	26	64.7	nd	5.5	nd	nd	2.9	nd	nd	103.2
PB-3												
mean (n=3)	fresh, vitrified	0.8	32.9	59.3	nd	4.8	0.5	nd	1.8	nd	nd	91.3
σ		0.3	5.9	3.5	nd	1.8	0.4	nd	0.2	nd	nd	12.7
analysis 1	partly weathered	1.0	31.9	61.1	0.9	2.9	0.0	nd	2.1	nd	nd	86.0
PB-5												
mean (n=4)	fresh, vitrified, fine round bloating pores, lower in alumina	0.8	15.6	76.1	0.1	4.7	0.8	nd	1.8	0.1	nd	98.2
σ		0.4	3.1	8.1	0.3	3.5	0.7	nd	1.2	0.2	nd	8.4
analysis 1	fresh, vitrified, fine round bloating pores, higher in alumina	0.8	36.2	55.9	nd	4.4	0.7	nd	2.0	0.0	nd	96.2
PB-13												
analysis 1	weathered dark area incorporated	1.0	45.2	44.6	1.5	2.3	0.6	0.8	2.4	1.7	nd	81.3
mean1 (n=2)	fresh, vitrified, higher alumina	0.7	38.6	55.1	nd	3.5	nd	0.4	1.6	nd	0.1	89.3
σ		0.3	5.0	3.8	nd	0.4	nd	0.5	0.5	nd	0.2	18.7

mean 2 (n=2)	fresh, vitrified, lower alumina	0.8	19.9	69.1	nd	7.7	nd	nd	1.4	1.1	nd	101.1
$\sigma$		0.1	0.8	1.8	nd	0.6	nd	nd	0.3	0.2	nd	0.8
<b>Sample</b>	<b>Description</b>	<b>MgO</b>	<b>Al2O3</b>	<b>SiO2</b>	<b>P2O5</b>	<b>K2O</b>	<b>CaO</b>	<b>TiO2</b>	<b>FeO</b>	<b>CuO</b>	<b>Cl</b>	<b>total</b>
<b>PB-15</b>												
mean (n=6)	weathered dark areas	0.6	47.2	43.2	1.3	1.1	0.2	0.5	5.5	0.2	0.2	71.1
$\sigma$		0.5	8.5	10.2	0.8	1.2	0.4	0.7	2.2	0.5	0.3	11.3
analysis 1	fresh, vitrified inner edge, lower in alumina	0.53	17.53	75.64	nd	3.93	0.71	nd	1.65	nd	nd	96.5
analysis 2	fresh, vitrified inner edge, higher in alumina	0.92	35.75	54.41	nd	3.93	0.95	0.69	3.36	nd	nd	96.5
<b>PB-16</b>												
mean 1 (n=3)	weathered, outer less vitrified zone	1.7	49.8	37.5	1.8	1.1	nd	nd	7.6	nd	0.4	65.1
$\sigma$		0.3	4.9	4.7	0.2	0.1	nd	nd	0.2	nd	0.1	3.5
mean 2 (n=2)	fresh, vitrified, lower in alumina	0.8	18.0	72.3	nd	6.1	0.2	nd	2.7	nd	nd	103.0
$\sigma$		0.3	2.1	4.9	nd	1.6	0.4	nd	1.1	nd	nd	7.8
analysis 1	fresh, vitrified, higher in alumina	0.8	25.5	62.6	nd	5.0	nd	0.7	5.4	nd	nd	105.0
analysis 2	fresh, vitrified, quartz incorporated	nd	10.6	85.7	nd	2.3	nd	nd	1.4	nd	nd	98.6
<b>PB-17a</b>												
mean (n=3)	fresh, vitrified	0.7	14.6	79.1	nd	1.5	0.6	0.9	2.7	nd	0.0	96.1
$\sigma$		0.1	1.2	1.3	nd	0.8	0.5	0.9	0.4	nd	0.0	5.8
<b>Average composition of clay matrix of the crucibles from TNN</b>												
mean (n=13)		1.0	30.1	59.7	nd	4.5	nd	0.6	4.1	0.1	nd	103.9
$\sigma$		0.4	7.0	7.3	nd	1.1	nd	0.5	1.5	0.3	nd	7.2
<b>Average composition of clay matrix of the crucibles from PB</b>												
mean (n=19)		0.8	24.4	66.7	nd	4.8	0.5	0.3	2.4	0.1	nd	97.3
$\sigma$		0.2	9.4	9.1	nd	2.2	0.5	0.5	1.0	0.4	nd	8.6

## HEAT TREATMENT

Crucibles, as reaction vessels used in high-temperatures processes, may be submitted to heat basically in two different situations, at the manufacturing step when they are prepared for the use by pre-firing, what however is not obligatory, and during the use. All of the crucibles examined are characterised by the presence of slag lining on their walls, described in the next section, which is a clear indicator that they were actually used. It means also that the texture of fabrics observed under the microscope represents the state after the use what largely limits the possibility to investigate the pre-use heat treatment.

Some of the features evidencing the heat treatment had been already mentioned when weathering and lack of compactness in the crucibles were tried to be explained. Here they are clarified and summarised.

The majority of the analysed crucibles show a consistent heavy heat alteration throughout the sample. They all exhibit white or grey colour in a hand specimen and fragmentary vitrification on a macroscopic scale. The fragmentary vitrification is characterised by the occurrence of isolated or in part interconnected (at a further step of vitrification) vitrified areas together with the non-vitrified spots. The vitrified segments often show fine or medium bloating pores. The distinguishable grains of weathered feldspar are always heavily vitrified and bloated. They appear to diffuse the alkalis into the matrix. Large quartz remained unreacted or partly reacted on the edges. The fine quartz grains are often sintered to the matrix (Fig. 35).

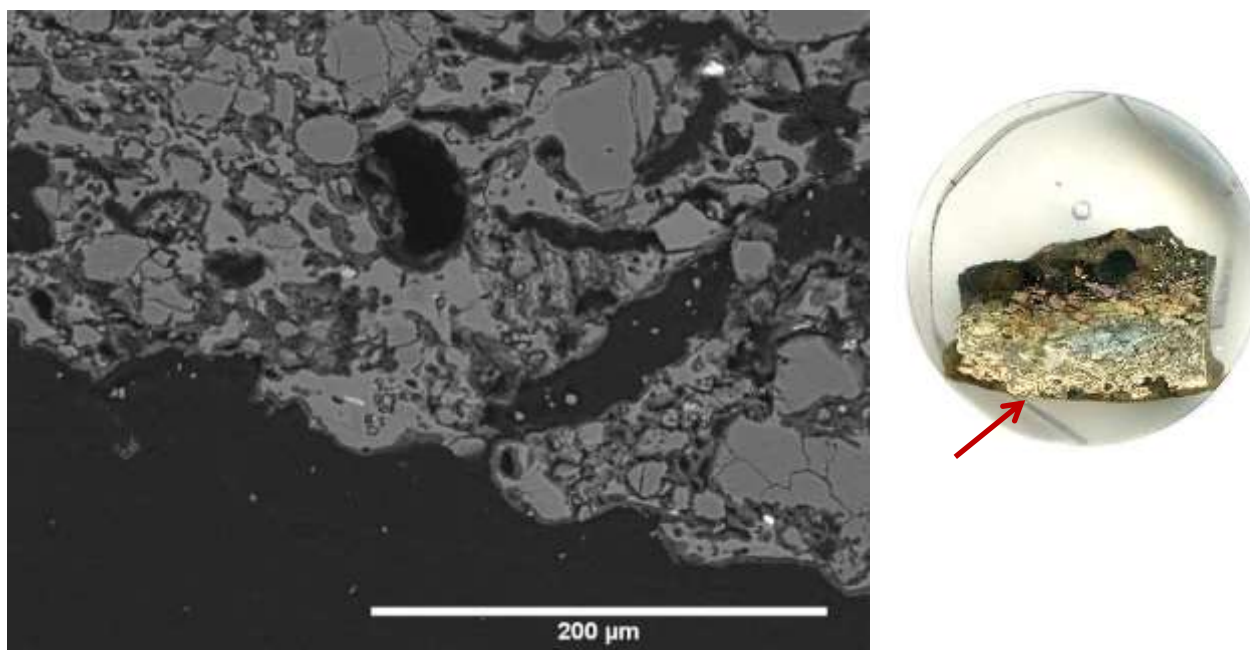


Fig. 35. (a) Backscattered electron image of the outer edge of the sample PB-5 showing partially vitrified fabric. Note: vitrified areas with rare fine bloating pores (1, light grey); dark non-vitrified regions (2, dark grey); large unreacted quartz grains (3), some of them shattered maybe due to thermal stress (4); fine quartz fused with the surroundings (5, more clear examples see in Fig. 33). Compare with the Fig. 25, Fig. 31, Fig. 32, Fig. 34. Bloated grains of weathered feldspar see also in Fig. 25a-b, Fig. 32b. (b) Sample PB-5 mounted in resin with the place from which BSE image was taken marked. Note the thick slag layer on the interior wall and high degree of contamination of the fabric due to use.

In a few samples (PB-15, PB-16, TNN-13) a clear thermal gradient from a lack of vitrification up to intense bloating may be observed. They all differ significantly in appearance from the samples described above. The red colour visible in hand specimens appears to be associated with the lower degree of heat alteration. It is most clear in the sample TNN-13 in which the red core does not show any sign of vitrification on the contrary to the white and grey external zones (Fig. 36).

In the samples PB-15 and PB-16 respectively initial and advance limited to the zone just below the slag layer vitrification was developed exclusively on the inner walls of the crucibles (i.e. containing residues) (Fig. 37 and Fig. 38).

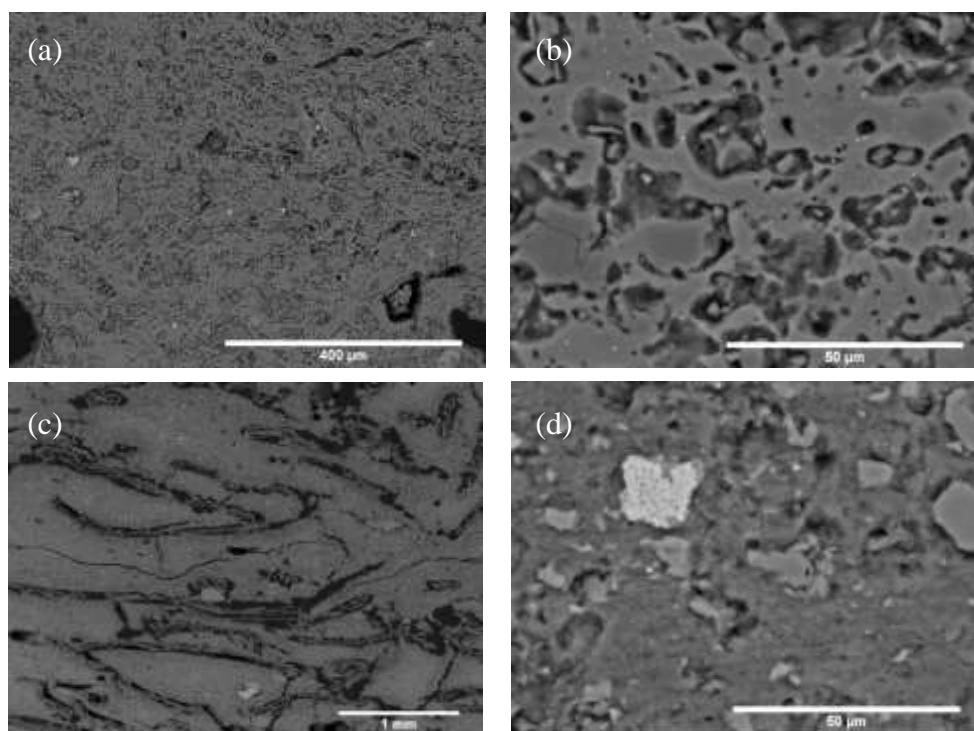


Fig. 37. Backscattered electron images of the sample PB-16: (a-b) inner wall just below the slag layer; (c-d): the exterior.

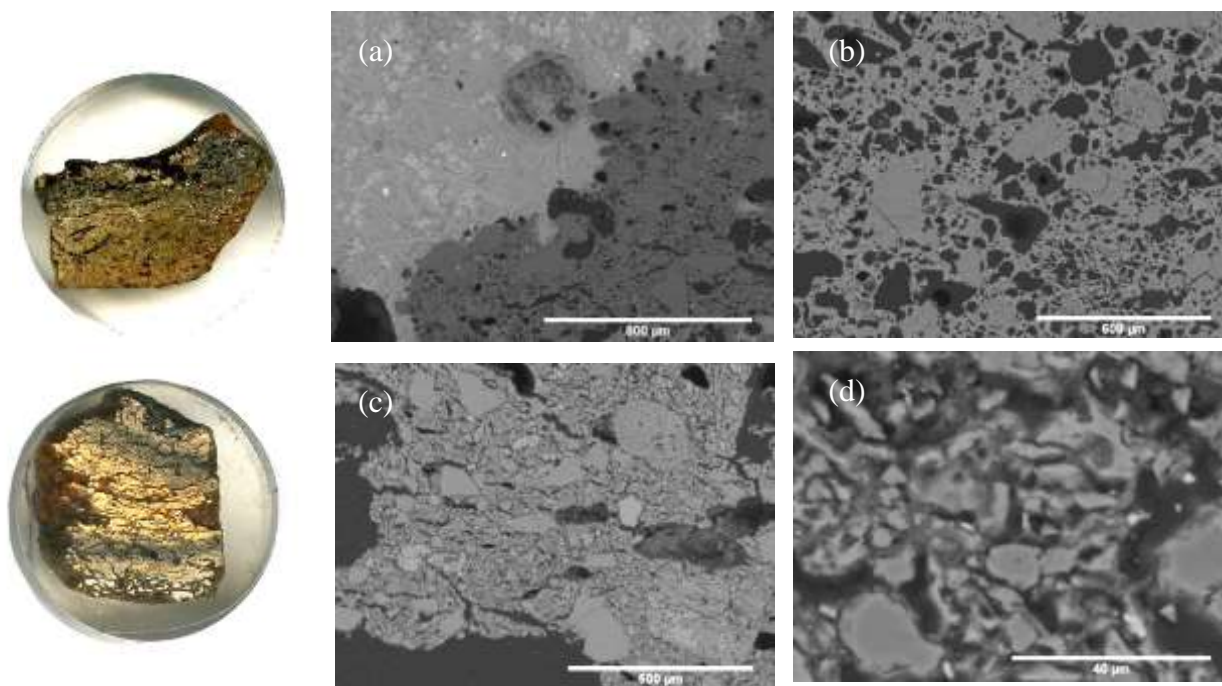


Fig. 36. Thermal gradient in the sample TNN-13: (a) sample TNN-13 mounted in resin; (b-c) Backscattered electron images of the upper edge. Note vitrification of the clay matrix, very fine bloating pores ( $< 10\mu\text{m}$ ), shrinkage cracks and fused fine quartz. (c-d) (b) Backscattered electron images of the core. Note lack of signs of vitrification of clay matrix and very fine unreacted quartz inclusion embedded in the clay matrix (light grey), white grain is rutile.



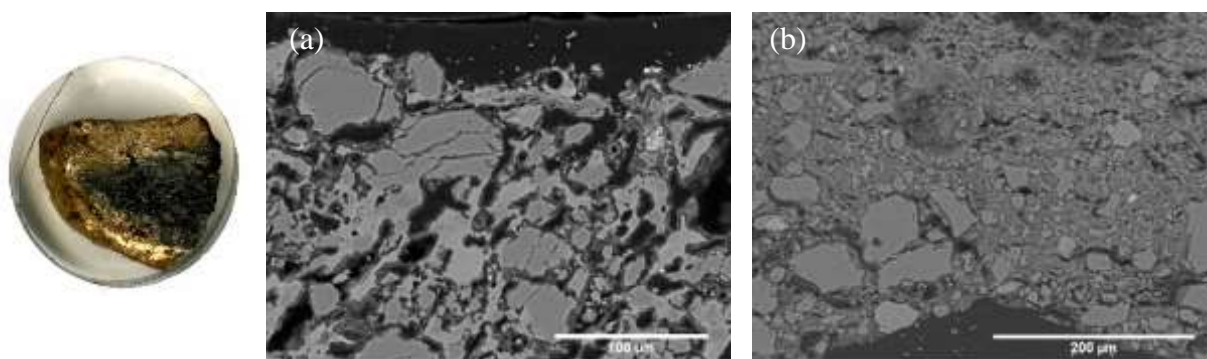


Fig. 38. Backscattered electron images of the sample PB-15: (a) inner wall; (b): the exterior of the vessel.

The temperature to which the crucibles were heated may be roughly estimated from the composition of vitrified phases. The same regards the temperature required to melt the slag adhering to crucible walls which will be considered in the next chapter. As no experimental studies were conducted, the estimation is based exclusively on the comparisons between composition of the vitrified phases observed in the samples and the data provided in the paper by Freestone and Tite. (1986).

The heavily bloated areas observed in the sample PB-16 and PB-17a have compositions similar to the medieval crucibles from London (Table 11). The characteristic features of the London ware are a high content of quartz as well as a low amount (usually below 5-10%) of the major fluxes, CaO, MgO, K<sub>2</sub>O (Freestone & Tite, 1986, p. 50). Both characteristics are commensurate with the samples from PB. The refiring experiments indicated that ceramic of this composition bloats around 1100°C exhibiting fine bloating pores. The medium pores, seen in the sample PB-17a (Fig. 39b), appear at temperature of 1200°C. The massive bloating observed in the sample PB-16 (Fig. 39a) may indicate that this part of the crucible was subjected to the temperature above 1200°C.

In several samples phases with much higher silica/alumina ratio show vitrification and fine bloating (e.g. Fig. 31b, Fig. 33a). Their SiO<sub>2</sub> and Al<sub>2</sub>O<sub>3</sub> contents are quite similar to the composition of the Stamford ware which shows fine bloating around 1200°C (Table 11). The examples from Laos are, however, higher in at least one of the flux oxides, FeO or K<sub>2</sub>O, which could significantly lower the melting temperature of these phases (Fig. 39c-d).

The weathered feldspar (Fig. 32b) melts, estimating from the SiO<sub>2</sub>-Al<sub>2</sub>O<sub>3</sub>-K<sub>2</sub>O phase diagram, at temperature around 1200°C which, however, may be modified by other elements present in the weathered phase (Table 11).

	MgO	Al <sub>2</sub> O <sub>3</sub>	SiO <sub>2</sub>	K <sub>2</sub> O	CaO	TiO <sub>2</sub>	FeO	CuO	Cl	Bloating	Fig.
London ware bulk	0.7	15.8	77.5	1.8	0.8	0.7	1.7	nd	nd	1100 FB	
London ware matrix	0.0	25.3	66.7	2.5	1.3	0.8	2.1	nd	nd	1200 MB	
PB-16	nd	17.5	75.1	2.6	nd	0.6	3.9	nd	0.31	VCB	
PB-17a	0.6	15.3	75.7	1.2	0.5	2.2	4.5	nd	nd	CB	
Stamford ware bulk	0.5	32.7	61.6	0.1	1.0	1.9	1.8	nd	nd	1200	
Stamford ware matrix	0.3	36.6	57.1	0.2	1.1	2.3	1.8	nd	nd	V/FB	
PB-3	1.0	34.7	57.4	4.9	0.6	nd	1.5	nd	nd	FB	
TNN-2b	1.6	31.6	53.3	5.2	nd	1.0	7.3	nd	nd	FB	
PB-5	0.8	36.2	55.9	4.4	0.7	nd	2.0	nd	nd	FB	
PB-13 weathered potassium feldspar	0.5	18.4	68.8	9.0	0.9	nd	0.8	1.6	nd	VCB	

Table 11. Composition of the vitrified phases mentioned in the text and the fabrics to which there were compared (after Freestone & Tite, 1986, pp. 42–43, 45, Tabs. IV-V). Terminology from Freestone & Tite, 1986: V-intermediate vitrification, FB-bloating pores<10μm, MB-10-40μm, CB-40-100μm, VCB>100μm



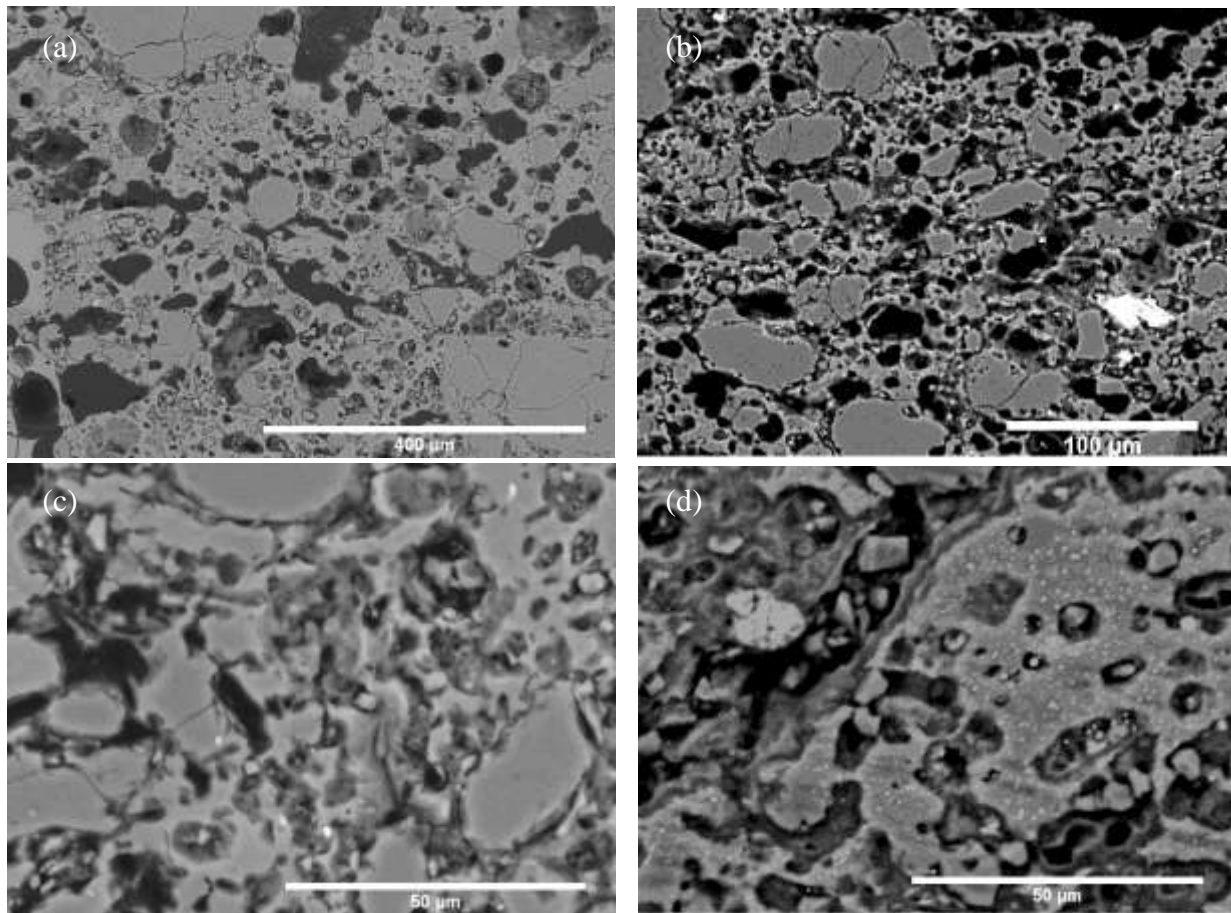


Fig. 39. Backscattered electron images of bloated, vitrified areas; the regions analysed with EDS and reported in Table 11 marked: (a) PB-16 just below the slag layer: coarse bloating pores, see also in Fig. 37; (b) PB-17a: medium bloating pores; (c) PB-3, fine bloating pores; (d) TNN-2b; fine bloating pores, note bright spots, probably precipitated iron.

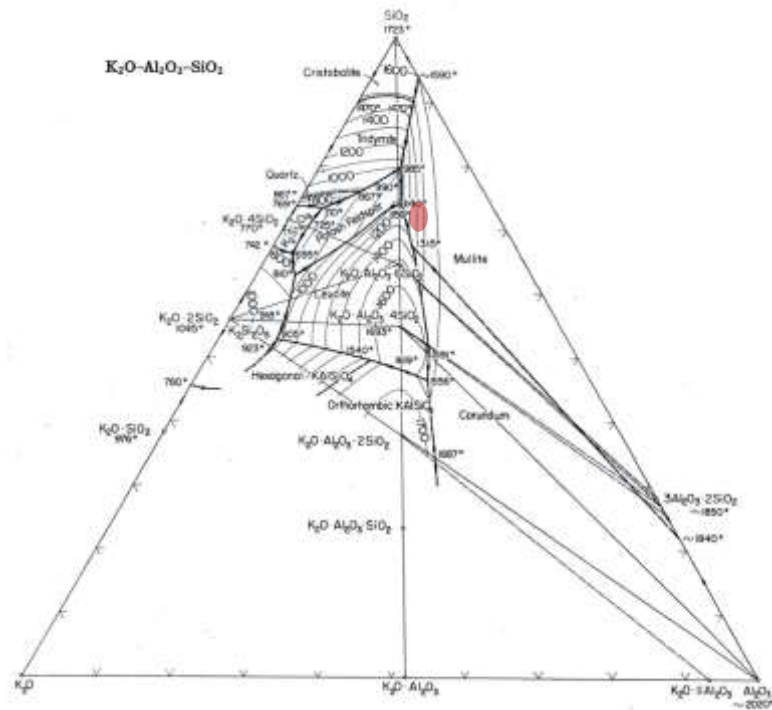


Fig. 40.  $K_2O-Al_2O_3-SiO_2$  phase equilibrium diagram (after Levin, McMurdie, & Hall, 1956). Composition of weathered feldspar marked.

The second, aside from temperature, factor influencing a charge of a crucible and the crucible itself during heating is the amount of oxygen available for the process. As mentioned above, the crucibles contained rice husk inclusion which was burnt out. The colour of the samples and a redox gradient visible on a few of them indicate that at least for some time crucibles were heated under oxidizing condition allowing removal of carbon originating from the charring of the organic matter. In the case of sample PB-15 (Fig. 18c; Fig. 38) the black core indicates that the absorbed by the fabric carbon was not removed due to the insufficient amount of available oxygen or too short duration of firing making impossible to oxygen to penetrate inside the vessel walls. The grey zone visible in many samples (Fig. 16e,f) which usually tend to fade towards the exterior seems to originate from absorption of carbon from the melt inside a crucible and partly by reduction of ferric iron to ferrous.

In several samples precipitation of metallic iron was recognised (Table 12; Fig. 41a-d). It confirms the formation of locally very reducing conditions within the crucibles due to the presence of organic matter. The same effect was observed in crucible used in making wootz steel and in an 18<sup>th</sup>-century steelmaking Hantsman crucible (Freestone & Tite, 1986, pp. 54–56).

An opposing effect of iron concentration on the crucible fabric may be observed in the sample TNN-9. The high amount of iron oxides cumulated in a sole area caused continuous vitrification of this zone massive bloating and, probably, terminal melting seen as a large hole above the melted away material. Iron appear to have crystallised from a melt as iron oxide which indicate more oxidising conditions than observed in the aforementioned iron-bearing features.

	MgO	Al2O3	SiO2	K2O	TiO2	MnO	FeO	Fe	Cu	P	total
TNN-2b											
glassy matrix	1.0	18.5	49.0	2.8	1.0	3.4	24.2				108.0
prill								95.1	4.0	0.8	113.0
TNN-9											
iron oxide	1.2	26.8	9.6	0.7	0.6	0.5	60.2				102.5
glassy matrix	0.5	24.1	63.7	4.4	0.5		6.8				101.4
	Mg	Al	Si	K	Fe	O	total				
TNN-13											
matrix	0.7	18.2	26.9	3.6	2.2	48.5	121.2				
prill	0.8	15.3	19.5	2.2	24.7	37.5	116.5				
matrix <sup>a</sup>	1.0	19.7	25.2	2.9	2.8	48.4	77.5				
prill <sup>b</sup>					100						
	Fe	Cu	total								
PB-15											
phase 1	97.4	2.6	101.3								

Table 12. Composition of metallic phases in crucible samples, SEM-EDS results (wt.%), normalised. (a) assumed composition of the background incorporated to the analysis of the prills, normalised after subtraction of 22.5% of iron; (b) possible composition of the prill alone.

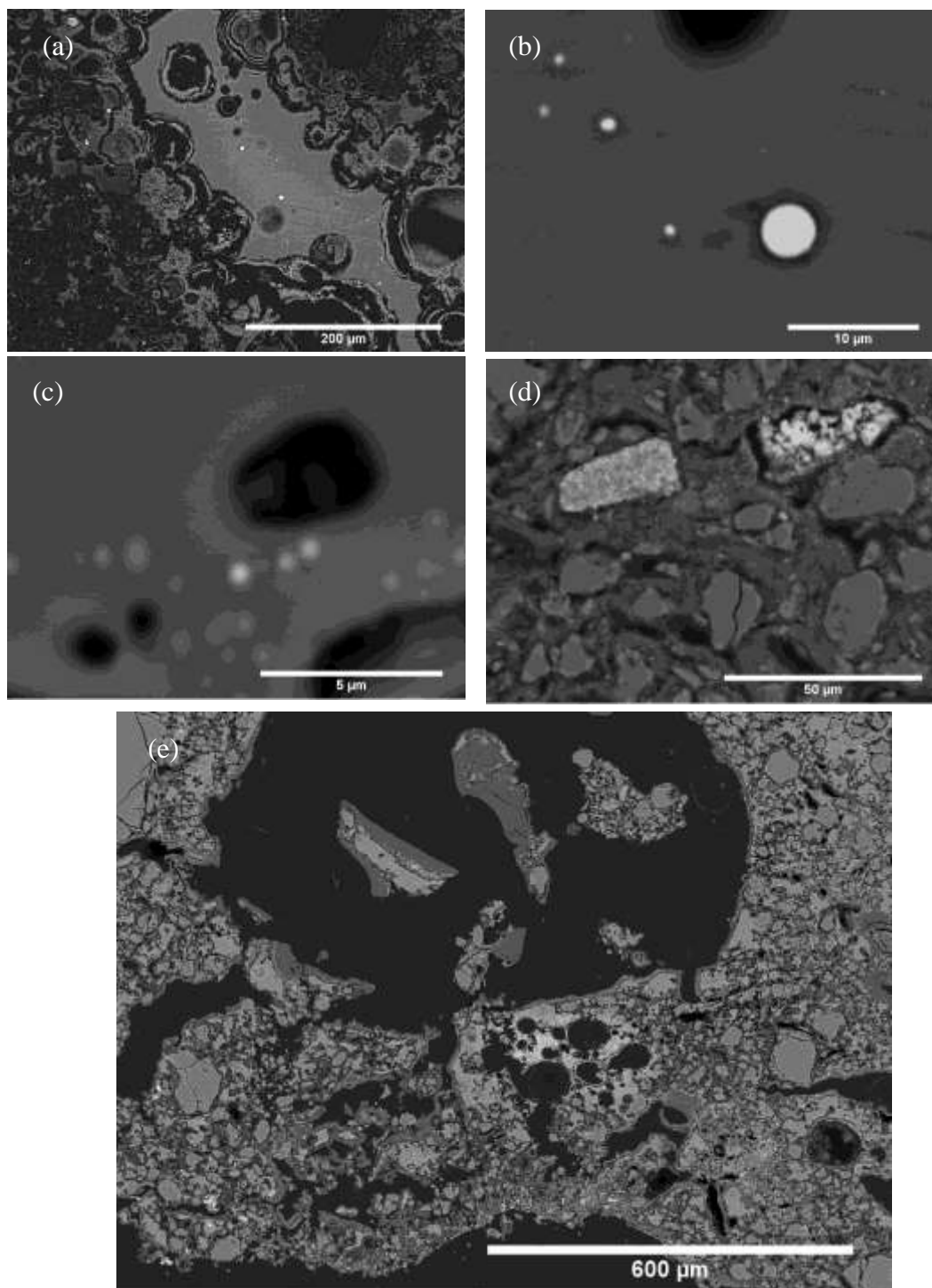


Fig. 41. Effects of iron oxide concentration in the samples, backscattered electron images: (a-b) TNN-2b: droplets of metallic iron (white) precipitated in glassy area; (c) TNN-13: less than 1 μm precipitation of metallic iron, see at lower magnification in Fig. 36b; (d) PB-15, metallic iron (1) probably reduced from an aggregate of iron oxide. Note shape (similar to neighbouring particle of TiO<sub>2</sub> and FeO, 2) and porosity suggesting decrease in volume (due to removing of oxygen); (e) TNN-9: concentration of iron oxide in heavy vitrified area, see at higher magnification in Fig. 26b.

### 3.3. Crucible slag

A characteristic feature of nearly all of the crucible fragments selected for analysis is a distinct slag layer covering their walls (e.g. Fig. 19). This vitrified material is a clear indicator of the use of the vessels in a high-temperature operation and a rich source of information about the nature of the process.

In seven samples it is apparent, basing on the observation of the wall curvature, which the slag residues adhere to the internal side of the crucibles. In the case of the sample TNN-2b and TNN-9 the position of the lining cannot be determined due to their small size and a large heat-damage (Fig. 42). The results of their analyses will be discussed together with the inner slag lining. In the samples PB-13 and PB-17a the continuous vitrification was also developed on the exterior of the crucibles. In the case of the sample PB-17a, however, it was recognised in a very limited area.

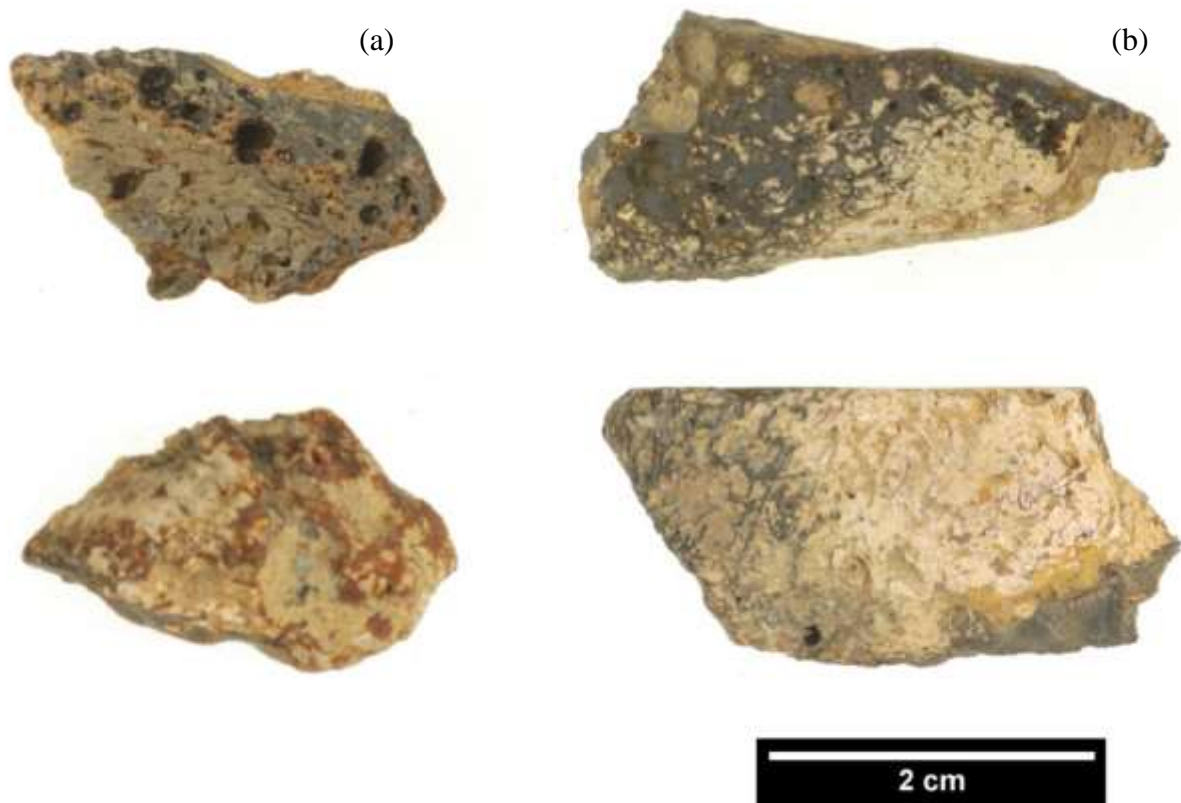


Fig. 42. Slag adhering to pieces of ceramic: (a) sample PB-2b and (b) PB-9. According to the examination, the ceramic fabrics in both samples are commensurate with the rest of the analysed crucible fragments what seems to confirm their association with this group of finds. Their small size and damage, however, do not allow for any further interpretation which is possible in the case of better preserved fragments (compare with Fig. 19).

## COMPOSITION AND MICROSTRUCTURE OF INNER SLAG LINING

The bulk chemical analyses indicate that the most abundant oxides in all inner slag samples are SiO<sub>2</sub>, FeO and Al<sub>2</sub>O<sub>3</sub> (Table 13). Their contents make up nearly 90% or above of the slag composition. The concentrations of SiO<sub>2</sub> and FeO are widely varied in particular samples as well as within the same sample what confirms the heterogeneity of the slag demonstrated also by its microstructure. The content of alumina in particular samples varies between 4 and 17.7% with the average value around 8. The slag with higher content of silica appears to contain more alumina as well (Fig. 43).

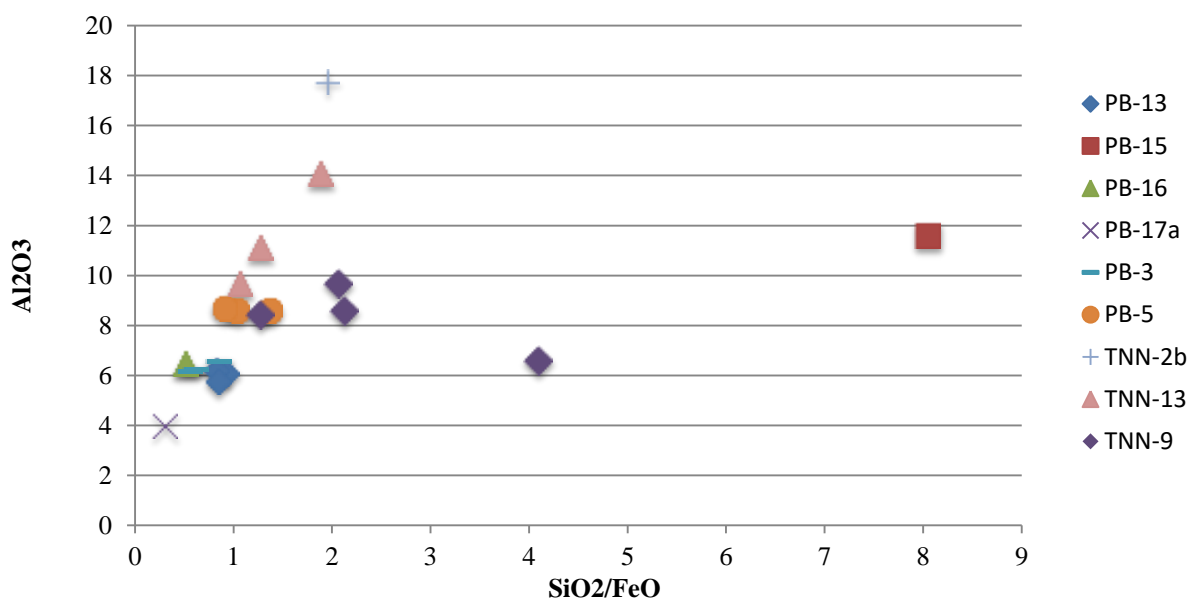


Fig. 43. Scatter chart showing SiO<sub>2</sub>/FeO ratio plotted with concentration of Al<sub>2</sub>O<sub>3</sub> (wt.%) in particular samples (results from Table 13); SEM-EDS results, normalised. Note a quite wide distribution of the SiO<sub>2</sub>/FeO ratios resulting from the varied proportion of these two oxides in the samples. Most of the analyses show a slight correlation between silica and alumina (variables are directly proportional). Two exceptions are the results for the sample PB-15 which generally appears to stand alone from other samples and one measurement for TNN-9 which is related to the analysis of a large area including the unreacted material.

The minor oxides determined in nearly all samples are K<sub>2</sub>O, CuO, TiO<sub>2</sub>, CaO, MgO and MnO. Their amounts is quite varied in particular samples, however, often do not exceed 1% each (Fig. 44). A few samples appear to stand alone due to their higher content of particular oxide or occurrence of a component not detected in other samples. The sample PB-15 has to be named here first. It contains an elevated amount of CuO (6.2%) and potash (4.6%) and as the only one proved the presence of SnO<sub>2</sub>. The microstructure (see below) and the appearance of the sherd PB-15 (residue not visible microscopically and no heat-damage) differentiate the sample from other as well. Composition of the sample TNN-9 is also particularly interesting showing an elevated content of TiO<sub>2</sub> (mean 7.3%) associated with ZrO<sub>2</sub> (mean 2.6%), the oxide detected only in this sample. These two different components are clearly reflected in the characteristic microstructure of the slag.

Table 13. Bulk composition of the crucible slags, SEM-EDS results (wt%), normalised; n - number of analyses included in the average; σ – standard deviation.

	Description	MgO	Al2O3	SiO2	P2O5	SO3	K2O	CaO	TiO2	MnO	FeO	CuO	ZnO	SnO2	BaO	ZrO2	total
TNN-2b (2-5mm thick)																	
mean (n=3)	glassy, fayalitic slag also present but not included into the bulk analysis	0.8	17.7	48.0	nd	nd	3.0	0.2	0.9	3.4	24.6	1.3	nd	nd	nd	nd	98.7
σ		0.1	0.1	0.8	nd	nd	0.1	0.3	0.1	0.3	1.0	0.3	nd	nd	nd	nd	20.3
TNN-9 (1-5mm thick)																	
mean (n=4)	inner slag 1 and 2 plus area rich in unreacted materials	0.3	8.6	52.4	nd	nd	1.9	0.6	7.3	nd	24.7	1.7	nd	nd	nd	2.6	93.5
σ		0.3	1.5	9.5	nd	nd	0.5	0.5	3.0	nd	7.0	0.6	nd	nd	nd	0.8	21.2
inner slag 1 (n=2)	glassy	0.5	9.7	52.2	nd	nd	1.9	1.0	5.2	nd	25.3	2.2	nd	nd	nd	2.0	105.3
σ		0.05	0.5	1.4	nd	nd	0.02	0.4	0.8	nd	2.3	0.1	nd	nd	nd	0.5	2.1
inner slag 2	glassy with white pattern	0	8.5	41.0	nd	nd	1.2	0.6	11.4	nd	32.3	1.7	nd	nd	nd	3.3	101.3
general	large area including unreacted material	0	6.6	64.1	nd	nd	2.5	nd	7.2	nd	15.7	0.9	nd	nd	nd	3.1	61.9
TNN-13 (2mm thick)																	
mean (n=3)	inner slag 1 and 2	2.4	11.1	46.7	nd	nd	1.8	0.4	0.4	0.2	36.7	0.0	nd	nd	0.4	nd	80.5
σ		0.4	3.0	6.2	nd	nd	0.7	0.3	0.3	0.3	9.4	0.0	nd	nd	0.7	nd	7.0
inner slag 1 (n=2)	fayalitic	2.5	9.7	43.7	nd	nd	1.4	0.6	0.3	0.3	41.0	nd	nd	nd	0.6	nd	76.5
σ		0.4	2.2	4.7	nd	nd	0.5	0.2	0.4	0.4	8.0	nd	nd	nd	0.9	nd	1.8
inner slag 2	glassy	2.13	14.1	52.76	nd	nd	2.42	nd	0.59	nd	28	nd	nd	nd	nd	nd	88.4
PB-3 (up to 1 cm thick)																	
mean (n=4)	inner slag 1 and 2	nd	6.3	33.9	1.5	nd	0.8	0.3	0.6	nd	54.9	1.7	nd	nd	nd	nd	95.3
σ		nd	0.3	4.5	0.3	nd	0.3	0.6	0.1	nd	4.8	0.6	nd	nd	nd	nd	17.2
inner slag 1 (n=3)	fayalitic	nd	6.2	31.7	1.6	nd	0.6	nd	0.6	nd	57.3	2	nd	nd	nd	nd	93.3
σ		nd	0.3	0.4	0.3	nd	0.1	nd	0.02	nd	0.3	0.2	nd	nd	nd	nd	20.4
inner slag 2	glassy, partly reacted quartz not included	nd	6.6	40.7	1.1	nd	1.2	1.2	0.5	nd	47.7	1	nd	nd	nd	nd	101.2
PB-5 (5 mm thick)																	
mean (n=3)	inner slag 1 and 2	1.3	8.6	41.8	0.3	nd	1.2	0.9	0.2	1.7	40.4	3.4	0.2	nd	nd	nd	101.9
σ		0.05	0.1	2.5	0.3	nd	0.2	0.1	0.2	0.2	6.7	4.1	0.3	nd	nd	nd	1.7
inner slag 1 (n=2)	fayalitic	1.3	8.7	40.4	0.3	nd	1.1	0.9	0.1	1.7	44.3	1	0.3	nd	nd	nd	102.8
σ		0.1	0.1	0.5	0.4	nd	0.2	0.1	0.2	0.2	0.6	0,01	0.4	nd	nd	nd	0.7
inner slag 2	glassy, partly reacted quartz not included, in close relation to the crucible fabric	1.3	8.6	44.7	0.4	nd	1.4	0.8	0.4	1.5	32.7	8.1	nd	nd	nd	nd	100



Description		MgO	Al2O3	SiO2	P2O5	SO3	K2O	CaO	TiO2	MnO	FeO	CuO	ZnO	SnO2	BaO	ZrO2	total
<b>PB-13</b> ( 9mm thick)																	
mean n=6	inner slag 1 and 2 plus area rich in partly reacted quartz	0.8	6.1	39.2	nd	nd	0.9	0.8	0.1	1.2	42.2	8.7	nd	nd	nd	nd	97.4
σ		0.1	0.4	6.2	nd	nd	0.1	0.1	0.2	0.2	5.9	6.8	nd	nd	nd	nd	2.4
inner slag 1 (n=3)	fayalitic	0.8	6.2	38.8	nd	nd	0.9	0.8	0.1	1.4	47.1	3.9	nd	nd	nd	nd	98.5
σ		0.1	0.3	1	nd	nd	0.1	0.1	0.2	0.04	1.1	1.3	nd	nd	nd	nd	3.2
inner slag 2 (n=2)	glassy, partly reacted quartz not included	0.9	5.8	34.4	nd	nd	0.8	1.0	nd	1.2	40.7	15.4	nd	nd	nd	nd	96.2
σ		0.04	0.05	0.5	nd	nd	0.01	0.04	nd	0.1	1.9	2.6	nd	nd	nd	nd	0.1
<b>PB-15</b> (0.2mm)																	
mean (n=3)	small glassy area	0.9	11.6	62.8	0.4	nd	4.6	1.7	0.3	nd	7.8	6.2	nd	3.1	nd	nd	99.5
σ		0.2	1.2	2.9	0.4	nd	1	0.2	0.3	nd	2.7	1.5	nd	1.5	nd	nd	3
<b>PB-16</b> (1mm)																	
mean (n=2)	fayalitic	0.9	6.5	29.3	0.4	nd	0.8	1.5	0.2	1.3	57.1	0.6	1.3	nd	nd	nd	94.8
σ		0.1	0.03	1.4	0.6	nd	0.2	0.2	0.3	0.2	3.3	0.9	0.1	nd	nd	nd	5.3
<b>PB-17a</b> (0.5mm)																	
mean (n=4)	fayalitic	nd	4	22.2	0.2	nd	0.1	0.2	nd	nd	72.6	0.8	nd	nd	nd	nd	95.1
σ		nd	0.5	5.4	0.4	nd	0.2	0.3	nd	nd	5.7	1	nd	nd	nd	nd	17

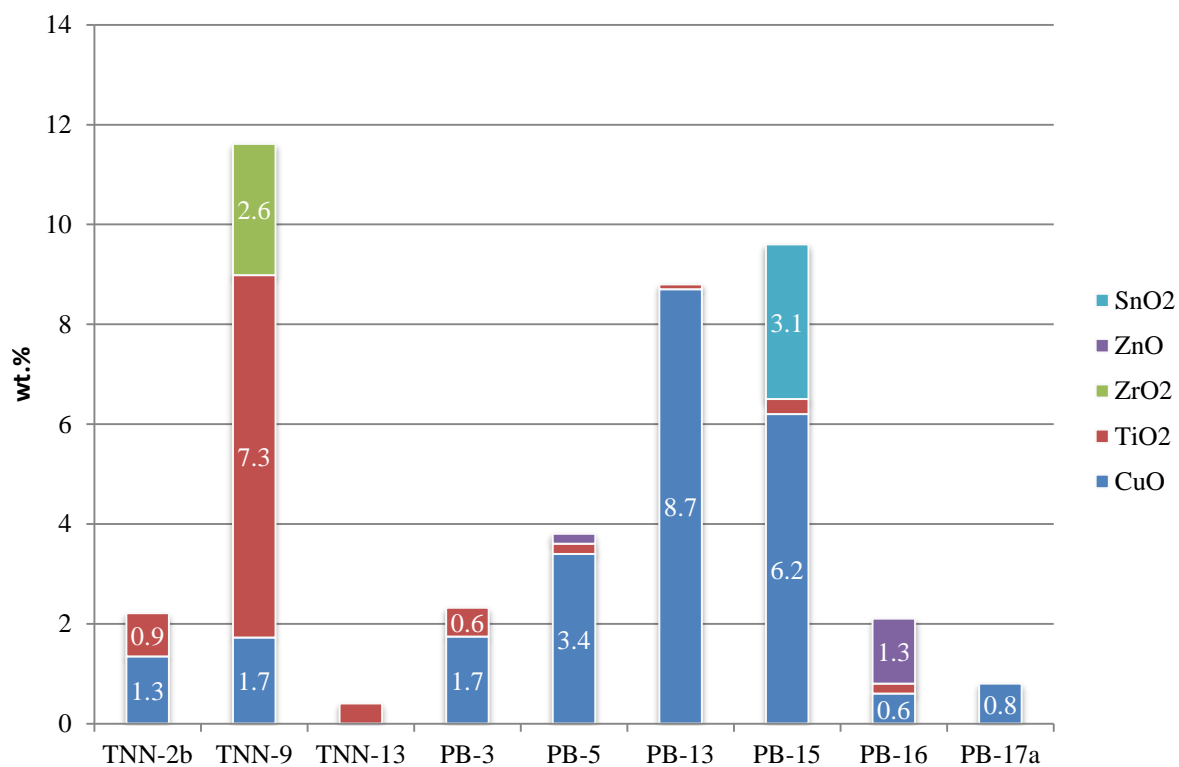
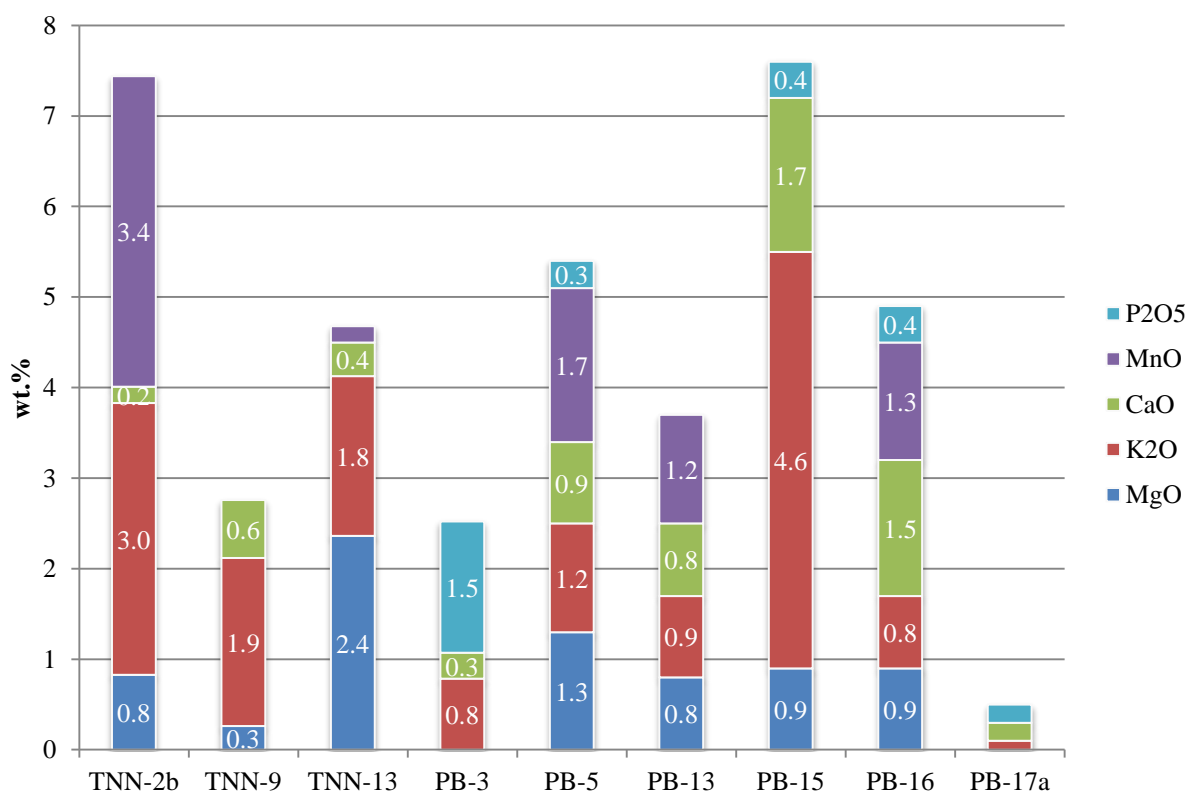


Fig. 44. Cumulative bar charts showing minor oxide contents in the crucible slags.

Basically, the microstructure of the slag lining is quite heterogeneous varying from the well-reacted areas, representing one or two of the types described below, to the mixed regions with a lot of relict, unreacted or partly reacted, material present. Among the well reacted areas, i.e. being largely a fluid during the heating process, two types of microstructure were recognised: 1) well-crystallised structure constituting essentially olivine crystals tightly packed with spinel crystals and metallic or sulphidic prills in a matrix of minor interstitial glass, hereafter referred to as a fayalitic slag; 2) structure with glass as a main phase in which spinel and metallic or sulphidic prills are embedded, named below a glassy slag. In both cases the glassy phase shows initial crystallisation in some parts. These two different microstructures are not limited to the particular samples and may coexist within the same sample forming, in a few cases, distinct layers. They are also not clearly related to the thickness of the slag.

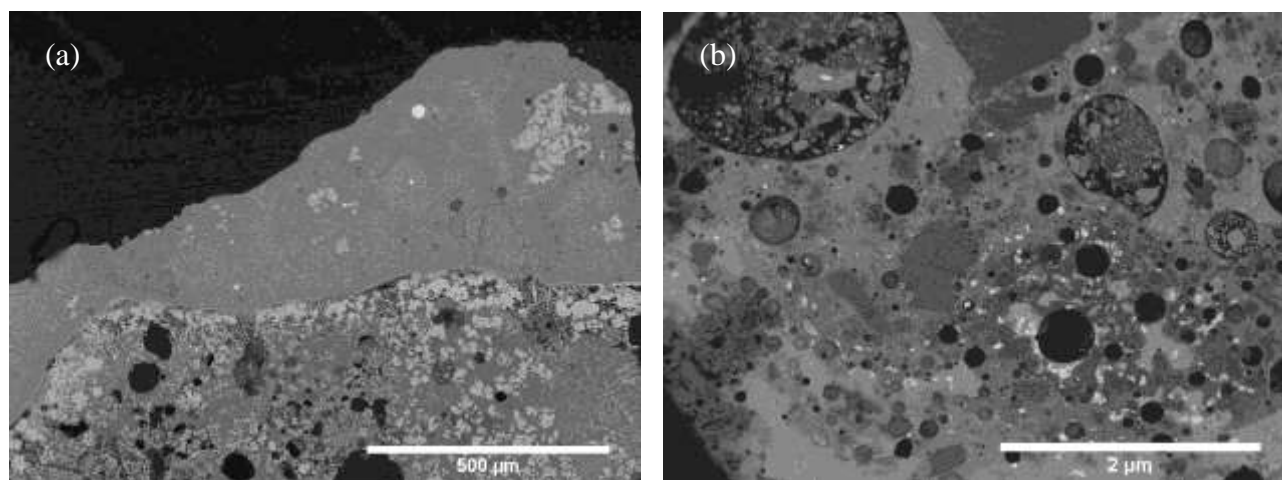


Fig. 45. Backscattered electron images of the crucible slag samples showing the variability of the microstructure in the crucible lag: (a) sample PB-13: in the upper layer fayalitic slag, in lower glassy slag; (b) TNN-9: cluster of partially reacted materials.

The description of particular phases within the slag lining and their relevance to the chemical composition of the samples are presented in the Appendix 3.

#### COMPOSITION AND MICROSTRUCTURE OF EXTERNAL SLAG

On surface of two samples from PB vitrified material was noticed also on the external side of crucible sherd. In the case of the sample PB-13, the slaggy layer is apparent in a hand specimen and seems to result from spilling of the melt over the sides. The slag consists of glassy matrix and iron oxide crystals (Fig. 46a-b). It is rich in silica, alumina and iron oxide with, however, a significant depletion in amount of the third one relative to the inner slag (Table 14).

The slag on the exterior of the sherd PB-17a forms a small vitrified area containing quartz grains and minute copper prills (Fig. 46c-d). The glassy phase consists primarily of silica, alumina and copper oxide with a minor contribution of potash (Table 14).

Sample	MgO	Al <sub>2</sub> O <sub>3</sub>	SiO <sub>2</sub>	K <sub>2</sub> O	CaO	TiO <sub>2</sub>	MnO	FeO	CuO	total
PB-17a	1.13	16.18	58.04	3.62	1.52	0.71	nd	4.13	14.68	94.7
PB-13	0.8	11.6	54.7	2.8	1.2	0.2	0.7	28.1	nd	102

Table 14. Composition of the external slag layer, SEM-EDS results (wt%), normalised.

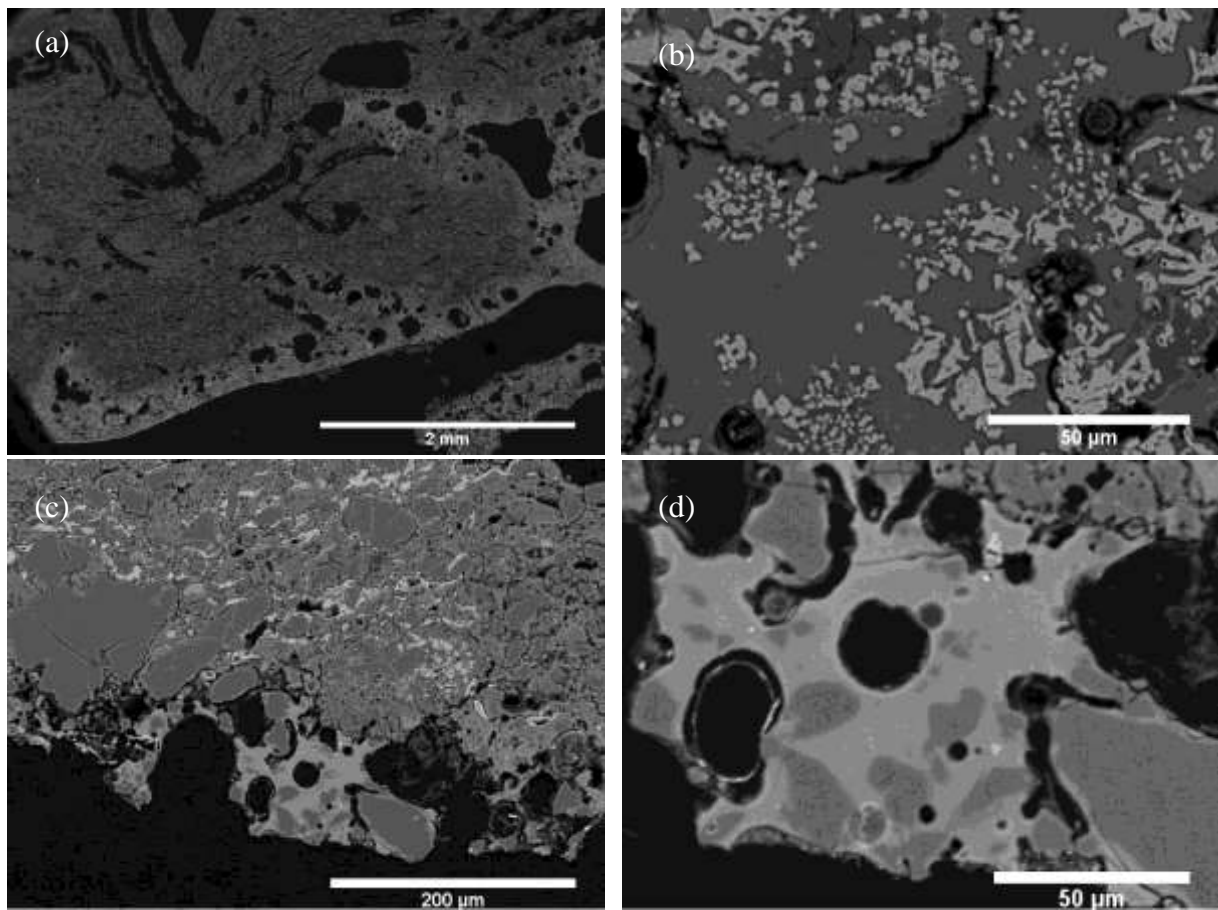


Fig. 46. Backscattered electron images of the external slag layers: (a-b) PB-13; (c-d) PB-17a.

### 3.4. Separate slag

62 (55 from PB and 7 from TNN) pieces of separate, i.e. not adhering to the crucible fragments, slag were submitted for analysis. They are all quite small (usually 2-4 cm across, 5-43g), compact, black with brownish rust visible in few cases. Most of the slag fragments have homogeneous, dense texture. In a few examples some inclusion, such as sand grains and ceramic pieces, are observed. 9 samples of separate slag from PB and 5 from TNN were chosen for optical and chemical investigation. In terms of their morphology they were divided into several types:

- **thin platy slag** (Fig. 47a); it is one of the most distinctive type of slag found at PB, it is characterised by small thickness (0.2-0.5cm), high homogeneity and density and flat, rather smooth upper and lower surfaces; on the surface which appears to be the upper one fine wrinkles are often observed; it is always fragmented in small angular pieces (2-3cm or less). Samples PB-24g, 25a, 31, 34a and 35a belongs to this type;
- **thin porous slag** (Fig. 47b) found at TNN; thin (c. 0.3 cm) small irregular pieces of slag with rough porous bottom; represented by samples TNN-16a, 16b, 17b;
- **thick platy slag** (Fig. 48a-b); 1 cm thick homogeneous, dense slabs with rounded thinner rim and flat and smooth faces; some gas holes apparent on one or both of their faces. Two pieces of slag from PB represent this type (PB-24b and PB-26a).
- **lumpy slag** (Fig. 48c-d); irregular lumps of slag varied in size (1-4 cm across) and shape without any flat face; sometimes earthy, ceramic or sandy inclusion visible. Samples PB-24a and TNN-17d belong to this class.
- **coarse flat slag** (Fig. 48e-f); irregular slabs with at least one flat surface; top usually smooth, bottom smooth or rough and porous with the impression of soil particles; represented by sample PB-23 and TNN-17d.

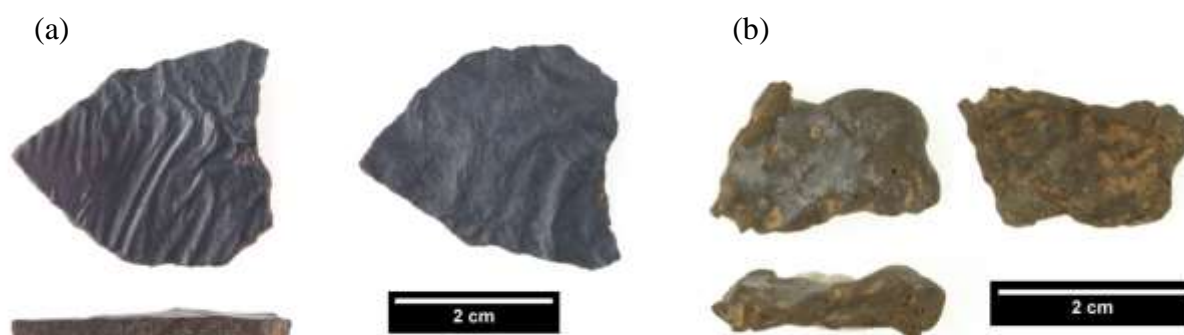


Fig. 47. (a) Thin platy slag from PB, both surfaces and side; (b) thin porous slag from TNN.

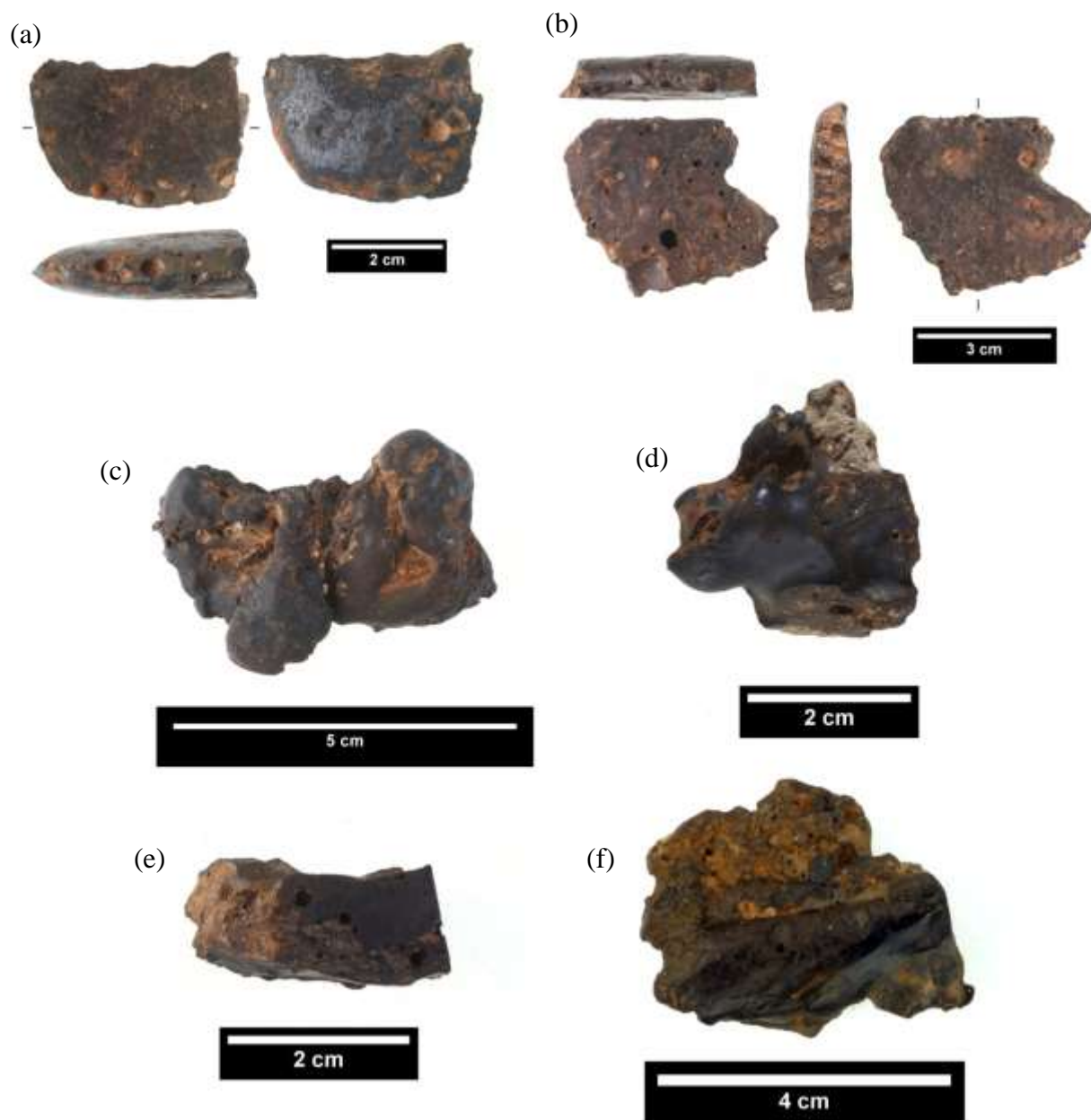


Fig. 48. (a-b) Thick platy slag from PB; (c) Lumpy slag from PB and (d) TNN; (e) Coarse flat slag from PB and (f) TNN.

#### COMPOSITION AND MICROSTRUCTURE

All of the slag samples examined are characterised by high contents of silica, alumina and iron oxide (Table 15). The three main components are, therefore, the same as documented in the crucible slag. Much less variability, however, was noticed within the composition of separate slags as regards content of major and minor oxides in particular samples.

The main differences between slag samples from TNN and PB are higher amount of FeO and SiO<sub>2</sub>/Al<sub>2</sub>O<sub>3</sub> ratio in the samples from PB and larger amount of MnO and ZnO<sub>2</sub> in the case of the slag from TNN. These differences are clearly shown in the mean values (Fig. 49) and confirmed by comparing of the particular samples (Fig. 50).



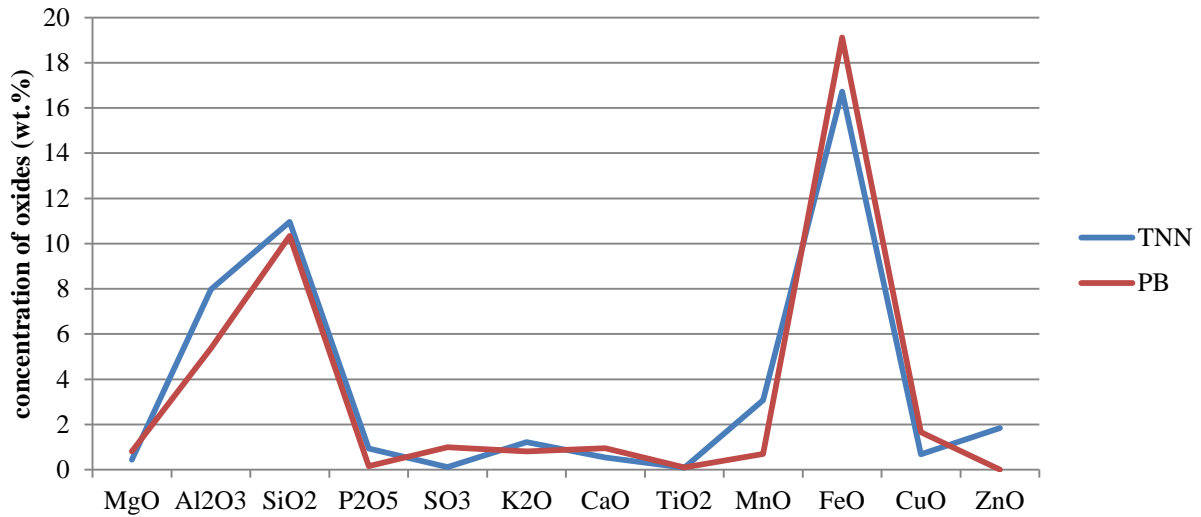


Fig. 49. Line chart showing the comparison between mean bulk composition of the separate slags from TNN and PB, SEM-EDS results (wt%), normalised; FeO and SiO<sub>2</sub> values are divided by 3.

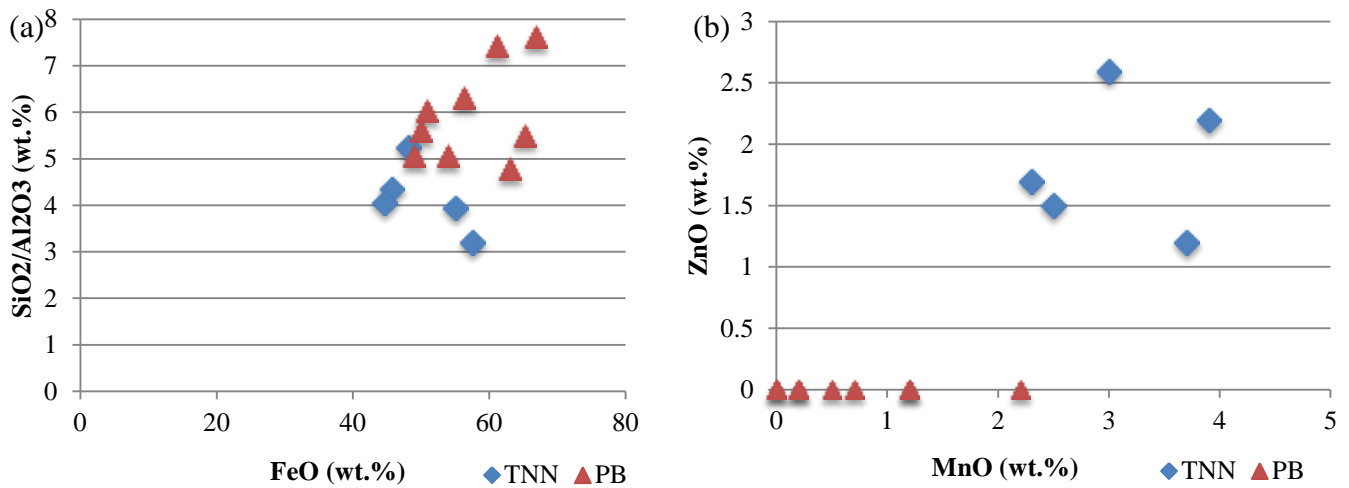


Fig. 50. Scatter plots showing the comparison between: (a) SiO<sub>2</sub>/Al<sub>2</sub>O<sub>3</sub> ratios and amount of FeO in the separate samples from TNN and PB and (b) amount of ZnO and MnO. SEM-EDs results (wt%), normalised.

The content of sulphur and copper oxides in the samples from both sites is quite low. The bulk analysis seems to indicate that the slag from PB is slightly enriched in these components.

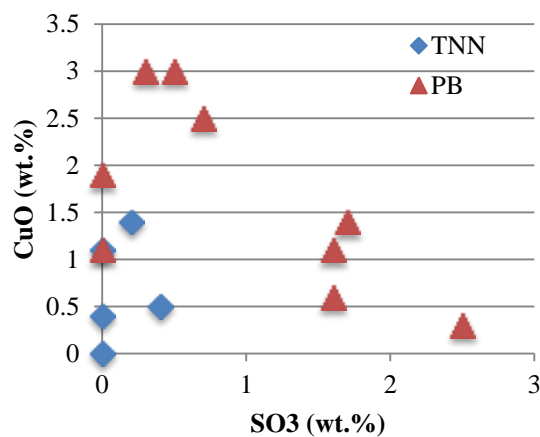


Fig. 51. Scatter plot showing the amounts of CuO and SO<sub>3</sub> in the separate slag samples from TNN and PB.

Table 15. Bulk composition of the separate slag samples, SEM-EDS results (wt%), normalised; ; n - number of analyses included in the average;  $\sigma$  – standard deviation.

Sample		Type	MgO	Al2O3	SiO2	P2O5	SO3	K2O	CaO	TiO2	MnO	FeO	CuO	ZnO	total
TNN-16a	mean (n=3)	thin porous slag	nd	7.8	30.8	1.1	nd	0.9	0.4	nd	2.3	55	nd	1.7	92.8
	σ		nd	0.7	1.9	0.2	nd	0.2	0.3	nd	0.3	1.4	nd	0.4	1.1
TNN-16b	mean (n=2)	thin porous slag	0.3	8.2	35.7	1	nd	1.6	0.8	nd	3	45.7	1.1	2.6	98.7
	σ		0.4	0.6	0.05	0.2	nd	0.2	0.2	nd	0.1	0.8	0.4	0.3	9.3
TNN-17b	mean (n=3)	thin porous slag	0.2	7.9	25.3	1.4	0.4	0.3	0.2	0.2	3.9	57.5	0.5	2.2	94.4
	σ		0.3	0.3	1.4	0.3	0.3	0.3	0.3	0.3	0.1	1.8	0.5	0.1	4.9
TNN-17a	mean (n=8)	coarse flat slag	1.5	6.6	34.6	0.1	0.2	1.4	1.1	nd	3.7	48.1	1.4	1.2	83.5
	σ		0.2	0.6	1.6	0.3	0.3	0.1	0.1	nd	0.4	1.4	0.8	0.6	18.7
TNN-17d	mean (n=3)	lumpy slag	0.2	9.4	38.1	1.1	nd	1.9	0.2	0.2	2.5	44.6	0.4	1.5	97.4
	σ		0.4	0.3	0.3	0.2	nd	0.1	0.3	0.3	0.1	0.7	0.6	0.2	9.2
min			nd	6.6	25.3	0.1	nd	0.3	0.2	nd	2.3	44.6	nd	1.2	83.5
			1.5	9.4	38.1	1.4	0.4	1.9	1.1	0.2	3.9	57.5	1.4	2.6	98.7
			0.4	8.0	32.9	0.9	0.1	1.2	0.5	0.1	3.1	50.2	0.7	1.8	93.4
PB-24g	mean (n=2)	thin plate slag	nd	3.4	25.9	nd	1.7	0.9	nd	nd	nd	66.8	1.4	nd	81.4
	σ		nd	0.3	0.7	nd	0.1	0.1	nd	nd	nd	0.2	0.7	nd	6.6
PB-25a	mean (n=4)	thin plate slag	0.4	5.5	26.3	nd	1.6	1	0.6	0.2	0.7	63	0.6	nd	98.3
	σ		0.3	0.1	0.3	nd	0.2	0.3	0.1	0.2	0.1	1.4	0.4	nd	6.1
PB-31	mean (n=3)	thin plate slag	1.2	6.8	34.4	nd	0.3	1.2	1.6	0.5	2.2	49	3	nd	92.7
	σ		0.1	0.2	0.9	nd	0.4	0.1	0.1	0.1	0.1	0.5	0.8	nd	7.9
PB-34a	mean (n=12)	thin plate slag	0.3	4	29.7	1.1	1.6	0.7	nd	nd	0.2	61.1	1.1	nd	101.2
	σ		0.2	0.4	2.1	0.2	0.4	0.2	0.1	0.0	0.3	2.7	0.6	nd	12.8
PB-35a	mean (n=14)	thin plate slag	nd	5.3	33.4	nd	2.5	1	0.6	nd	0.5	56.3	0.3	nd	105.9
	σ		nd	0.3	0.4	nd	0.3	0.03	0.1	0.1	0.1	0.4	0.4	nd	2.5
PB-24b	mean (n=4)	thick plate slag	0.7	6.3	38	0.3	nd	0.8	0.6	0.2	1.2	50.8	1.1	nd	104.8
	σ		0.1	0.1	0.3	0.4	nd	0.1	0.2	0.2	0.2	0.1	0.3	nd	1.9
PB-26a	mean (n=4)	thick plate slag	0.5	6.6	36.9	nd	0.5	0.7	0.6	nd	1.2	49.9	3	nd	106.9
	σ		0.4	0.5	1.1	nd	0.6	0.1	0.1	nd	0.1	1.4	2.0	nd	21.4
PB-23	mean (n=3)	coarse flat slag	nd	4.6	25.3	nd	0.7	0.7	0.5	nd	nd	65.2	2.5	nd	97.2
	σ		nd	0.1	3.6	nd	0.7	0.1	0.1	nd	nd	2.6	1.0	nd	1.9
PB-24a	mean (n=5)	lumpy slag	4.2	5.8	29.4	n	nd	0.3	4.1	nd	0.2	53.9	1.9	nd	90.9
	σ		0.5	1.1	2.4	nd	nd	0.3	1.2	nd	0.3	2.8	0.9	nd	12.9
min			nd	3.4	25.3	n	nd	0.3	n	nd	nd	49	0.3	nd	81.4
			4.2	6.8	38	1.1	2.5	1.2	4.1	0.5	2.2	66.8	3	nd	106.9
			0.8	5.4	31.0	0.2	1.0	0.8	1.0	0.1	0.7	57.3	1.7	nd	97.7

The differences in content of main oxides between slags from both sites are associated with the fact that only at PB thin plate slag was found which is enriched in FeO and have lower SiO<sub>2</sub>/Al<sub>2</sub>O<sub>3</sub> ratio in comparison to other samples (Fig. 52). It shows also higher content of sulphur (Table 15).

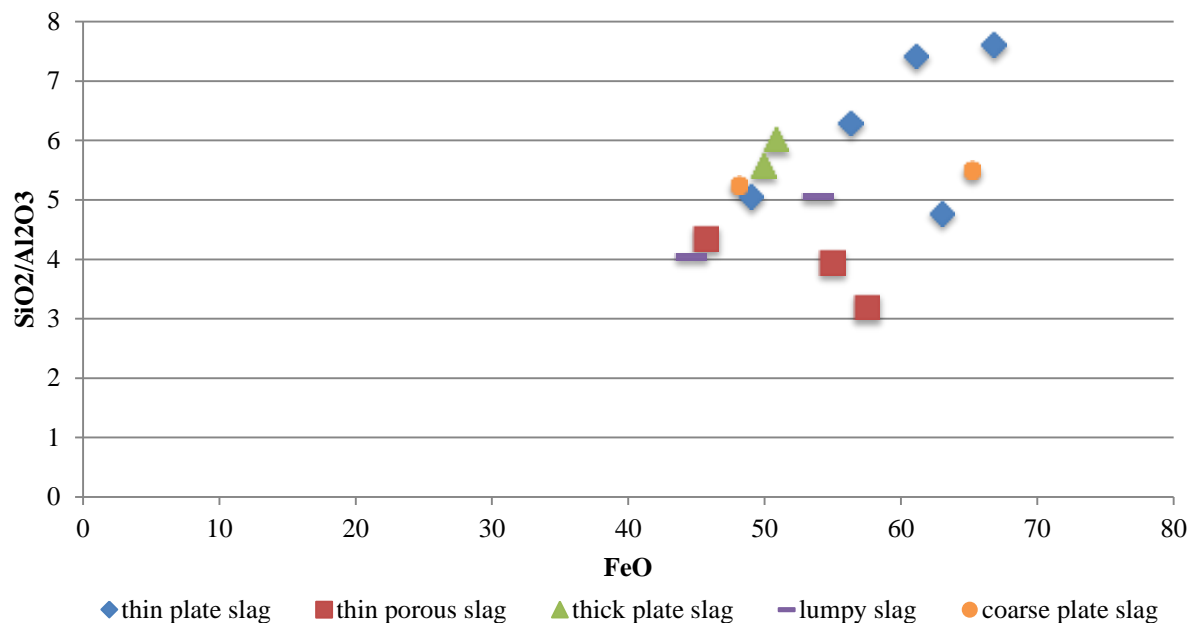


Fig. 52. Scatter plot showing the amount of FeO and SiO<sub>2</sub>/Al<sub>2</sub>O<sub>3</sub> ration according to the morphological types of the separate slag. SEM-EDS results (wt%), normalised.

The slightly higher FeO/SiO<sub>2</sub> ratio in the regular platy slag samples may be also observed (Fig. 53).

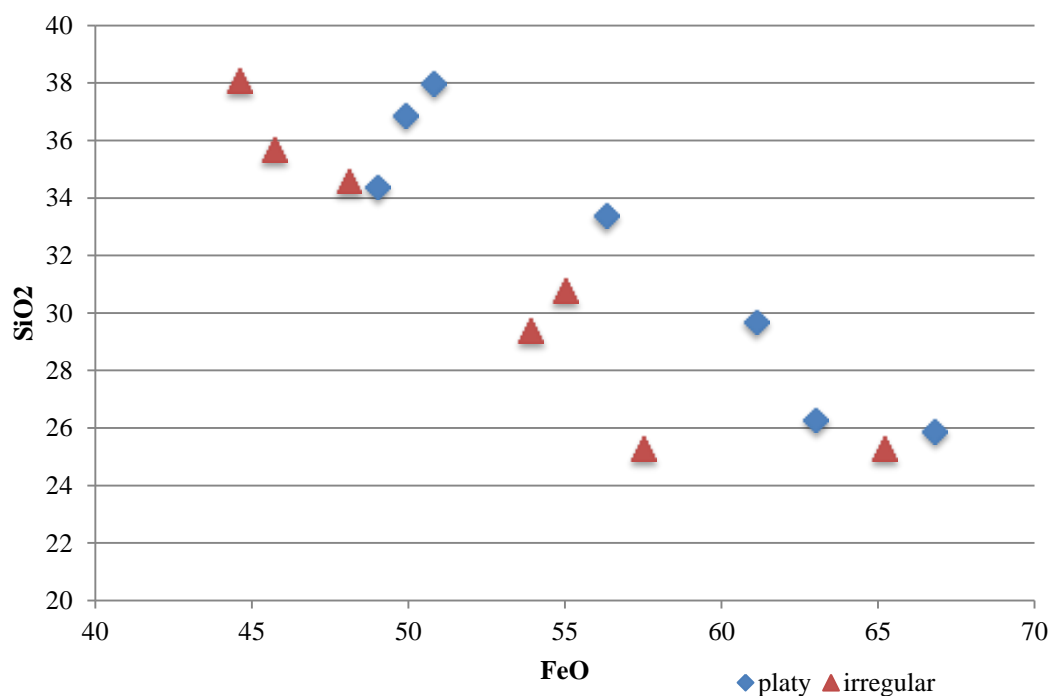


Fig. 53. Scatter plot showing the amount of SiO<sub>2</sub> and FeO in platy homogenous slags (thin and thick platy slag types) and in more porous and less regular ones (lumpy, thin porous, coarse flat slag).

The microstructure of the separate slag is very similar to the arrangement and the composition of phases observed in the crucible slag of fayalite type. Iron-rich olivine is also here the main phase occurring in all of the samples. The second common crystalline phase is iron oxide. These two phases coexist with metallic and sulphidic prills in the glassy matrix. The pieces of separate slag contain also partly unreacted materials and phases associated with corrosion process. They all are described in details in Appendix 4.

Basically, the separate slag may be considered as well reacted and homogenous. The microstructure of particular pieces appears to be consistent throughout the sample. The element of irregularity is introduced by corrosion of the more prone to deterioration glassy matrix occurring intensively in the areas close to the surfaces and rarer within the core.

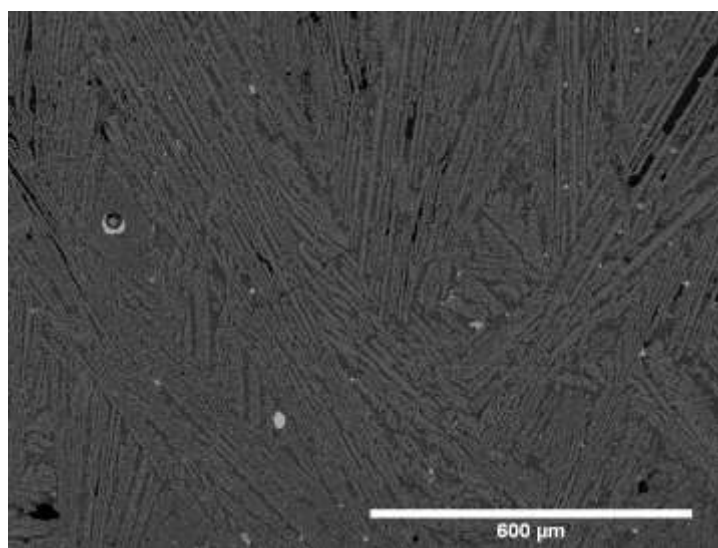


Fig. 54. Backscattered electron image of the sample PB-35a (thin platy slag) showing general feature of the microstructure of the separate slag samples: predominance of fayalite, some sulphidic prills (white) and black corrosion developed mainly in the glassy matrix.

### 3.5. Copper ingot

One of the copper ingots found at TNN was cut in half, embedded in resin and examined with the reflected light microscope and the SEM-EDS. It was previously analysed for lead isotopes as a part of the Southeast Asian Lead Isotope Project (Pryce et al., 2011). The results indicate the correlation between the lead isotopes in the ingot and in slag pieces from both Sepon sites.

The analysed object is a slightly asymmetrical 1.4 cm high cone with flat and nearly circular base 3.1-3.4 cm in diameter. It weighs 27.7g. The surface of the object is covered with green patina (Fig. 55).

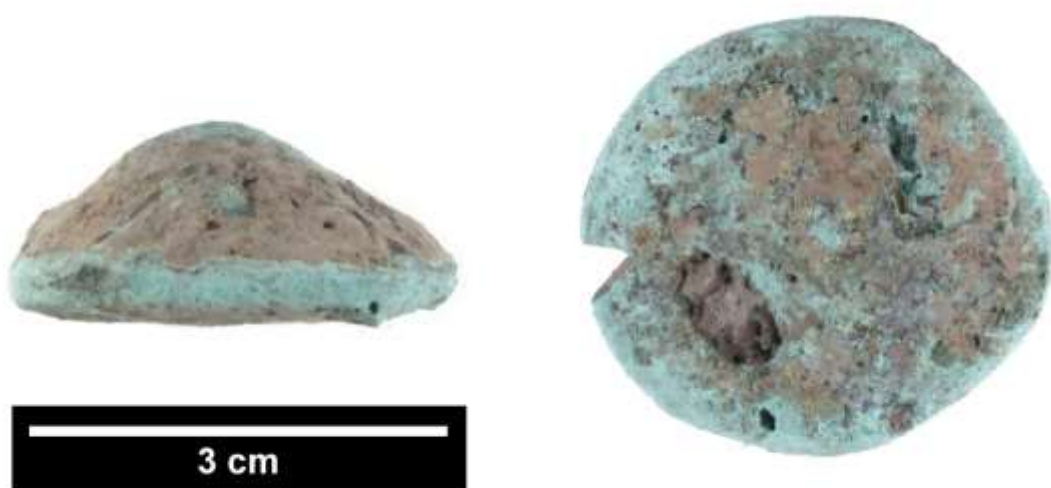


Fig. 55. Cone-shaped ingot from TNN.

The core of the object was found to be more complex than it was anticipated. It consists of metallic phase surrounded by corrosion layer and a piece of pottery (Fig. 55).



Fig. 56. The core of the ingot from TNN.

The bulk analyses of the metallic phase show on average 98.4% of copper and over 1% of sulphur (Table 16). The copper groundmass contains no other than sulphur impurities on a detectable in a bulk analysis level (c. 0.2%). Sulphur is segregated into globular sulphides of nearly chalcocite composition. Lead, although in an amount too low to be detected in bulk analyses, appears as globular segregates (Fig. 57).

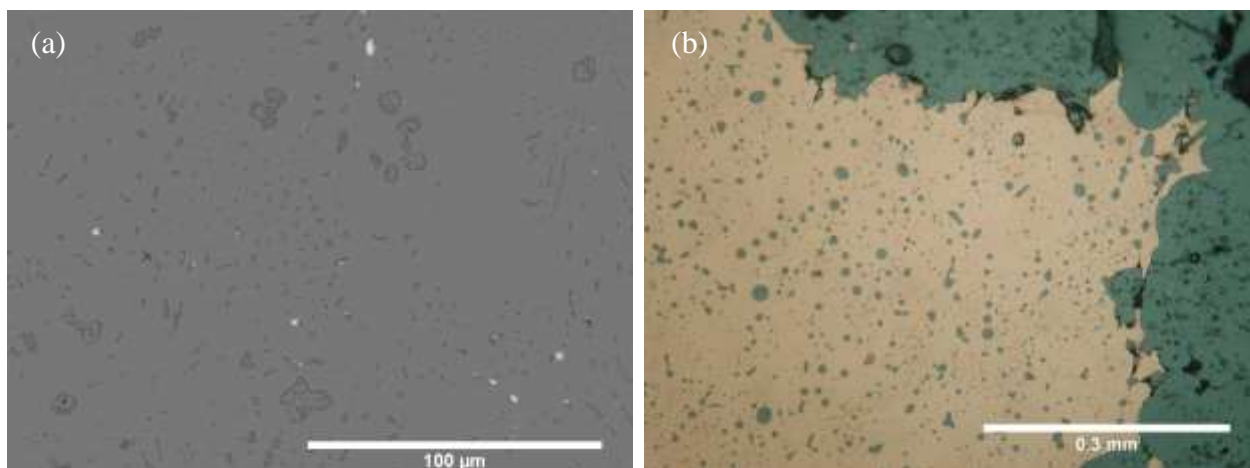


Fig. 57. Metallic part of the ingot: (a) Backscattered electron image showing metallic copper background (light grey) in which sulphur (dark grey) and lead segregates (white) are present; (b) Reflected light micrograph showing yellow copper matrix and blue sulphides.

		Cu	S	Fe	O	total
bulk	mean (n=3)	98.4	1.4	0	0.2	96.6
	$\sigma$	0.3	0.1	0	0.3	3.1
copper sulphide segregates	mean (n=3)	79.7	17.6	0.1	0.2	96.9
	$\sigma$	4.0	1.8	0.2	0.4	3.7
		Cu	Pb	Cl	O	total
lead segregates	single	14.5	93.5	1.4	1.7	113.4

Table 16. Composition of the phases recognised within the mostly metallic part of the ingot, SEM-EDS results (wt%), normalised.

Corrosion was developed through the hole in the protective rust on the bottom and progressed along the porous pottery fragment. Green surface layer is composed of mixture of copper carbonates and sulphides. The blue under the reflected light microscope phase surrounding the metallic copper is a partially oxidised copper in proportion Cu/O similar to cuprite (Table 17).

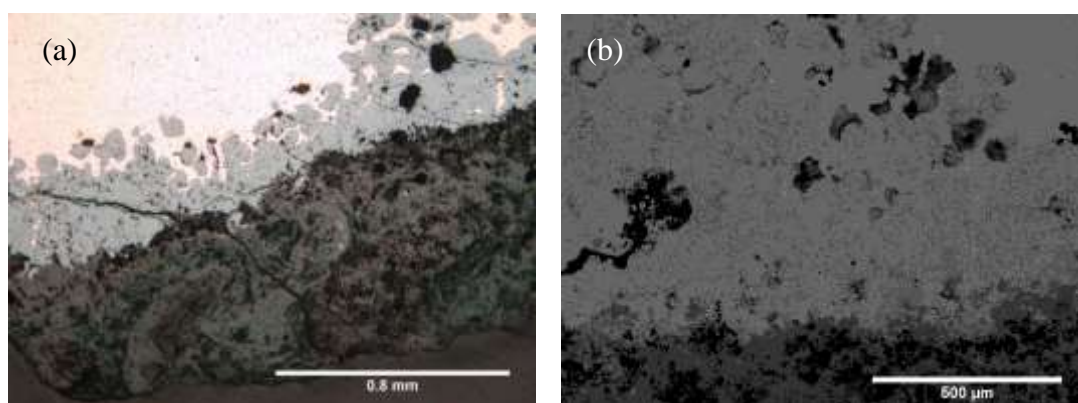


Fig. 58. Corrosion products in the ingot: (a) Reflected light micrograph: patina (1), oxides copper (2) and metallic copper (3); (b) Backscattered electron image: the same numbering as in (a).

	Cu	S	O	total
blue	86.08	1.3	10.17	98.7
green	47.59	4.1	32.67	87

Table 17. Composition of corrosion products, SEM-EDS results (wt%), normalised.



A small 0.6 cm thick piece of pottery was introduced to the object probably during casting. The shape and composition of the ceramic piece suggest that it is a fragment of vessel wall. The sherd is composed of fine rich in quartz paste. Bulk analyses showed high silica (around 70%) and alumina (15%) contents (Table 18). The elevated amount of copper oxide (11.6%) results probably from the corrosion of copper ingot and accumulation of leached copper ions in the porous ceramic body. The low contents of alkali and alkaline earth elements may indicate that the original clay matrix consisted primarily of kaolinite. Angular fine or very fine poorly sorted quartz (grain up to 0.3 mm) is a main inclusion (Fig. 59b). It occurs also as silt-sized particles evenly distributed in the paste. Sparse very fine rutile (5µm) and pallets of lateritic soil with quartz inclusion were also observed (Fig. 59a). The body contains elongated cavities recognised as voids left by burnt off rice husk (Fig. 59c). The fabric does not show any evidence of overheating such like bloating voids. No shrinkage voids developed in continuous clay matrix or around the quartz grains were observed.

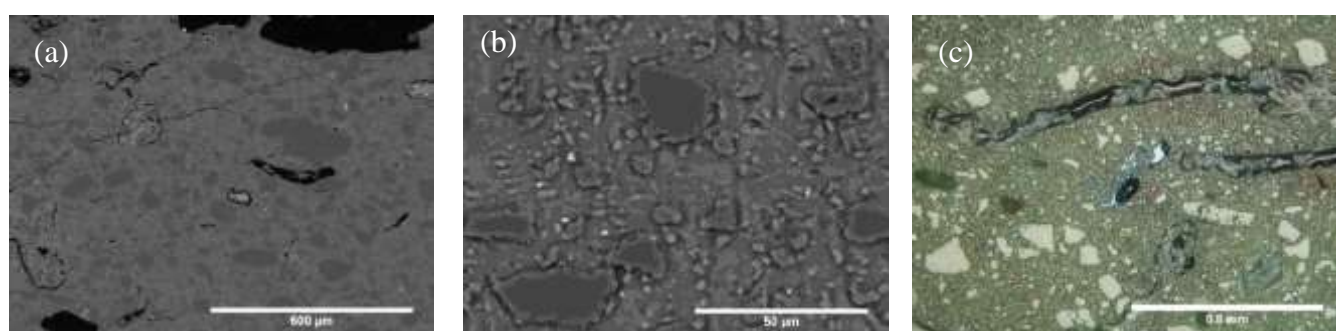


Fig. 59. C ceramic piece within the copper ingot: (a) Backscattered electron image of the body: dark grey quartz grains and pallets of lateritic soil with shrinkage void; (b) Backscattered electron image of the fine fraction: dark grey angular quartz grains and minute rutile; (c) Reflected light micrograph: rice husk void with wavy edge, white quartz grains whitening the stained green clay matrix.

		MgO	Al <sub>2</sub> O <sub>3</sub>	SiO <sub>2</sub>	K <sub>2</sub> O	TiO <sub>2</sub>	CaO	FeO	CuO	P <sub>2</sub> O <sub>5</sub>	V <sub>2</sub> O <sub>5</sub>	total
bulk	mean (n=3)	0.4	15.0	70.5	0.4	0.6	nd	1.5	11.6	nd	nd	90.8
	σ	0.3	0.5	0.3	0.1	0.1	nd	0.2	0.8	nd	nd	3.3
matrix	mean (n=6)	0.9	29.7	44.6	0.2	0.1	0.6	6.1	17.4	0.3	nd	88.0
	σ	0.3	4.3	7.5	0.3	0.2	0.9	10.0	9.4	0.6	nd	10.1
laterite pallets	single	nd	16.6	33.8	nd	4.1	nd	40.4	4.1	nd	1.0	94.2

Table 18. Composition of the piece of pottery within the copper ingot, SEM-EDS results (wt%), normalised.

## 4. Interpretation of the results: reconstruction of metallurgical process

### 4.1. Nature of the process

The compositional data of all types of the artefacts examined strongly indicate that they are all related to the copper-based production what is commensurate with the Sepon geology and previous studies (Cawte, unpublished; Pryce et al., 2011).

The analysed mineral aggregates may be easily linked to the first stage of copper production, smelting, and may have been used as a copper source. They all represent rich oxidised ore. Pieces of malachite (sample PB-41) and aggregate of copper oxides (PB-42) may be easily smelted to metallic copper by heating them with charcoal. The reaction would generate, however, no or very little slag (Gale, Kayafa, & Stos-Gale, 2009, p. 166). The charge composed of exclusively copper oxide is, therefore, rather unlikely in the context of the rest of finds (the heavily slagged crucibles and separate slag) and the composition of other two mineral samples which contain iron oxide as a gangue component which must be slagged away. The way, considered as the easiest one, to do it is the generation of fayalitic slag by adding of, in the case of iron-rich ore, silica to a charge. Formation of fayalitic slag is well-evidenced in the assemblage from both sites (the crucible slag of fayalite type and all separate slag samples). The core of sample PB-38 is surrounded by lateritic soil in which FeO/SiO<sub>2</sub> ratio (1.75) is very close to one of the eutectics in the FeO-SiO<sub>2</sub> binary system and falls within the range of composition represented by all of the samples from PB and TNN as well as generally most of ancient metallurgical slag (Tylecote & Boydell, 1978, p. 40, fig. 14) (Fig. 60). A preliminary assumption may be, therefore, made that removing the gangue of this composition during beneficiation would not be necessary and it could act as a facilitator during the process.

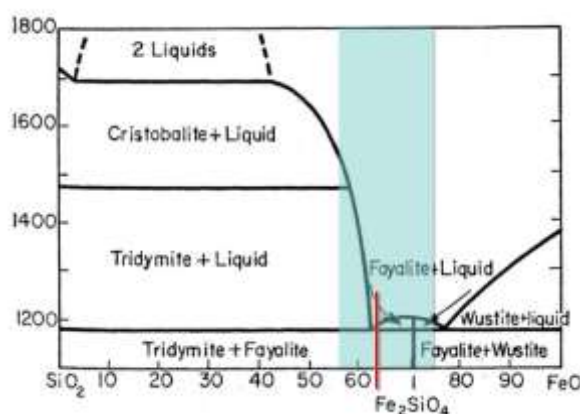


Fig. 60. System FeO-SiO<sub>2</sub> (after Levin et al., 1956, fig. 80); in blue the range of composition of the separate slag from Sepon; red line – FeO/SiO<sub>2</sub> ratio for laterite in the sample PB-38.

Several issues must be considered while investigating the function of the crucibles. Firstly, if the use of the term *crucible* in their context is correct. Due to their heat-damage and slaggy residues of repetitive composition, it is quite apparent that they were used in high-temperature operation locally reaching even the temperature above 1200°C as indicated in Table 11. Their shape (rim, curvature of the wall) and similarity to the complete vessel from PB, fulfil the second requirement of a crucible definition (Bayley & Rehren, 2007, p. 46), being a potentially moveable container. The consistent occurrence of elevated amount of copper in the slag lining is clear evidence of their association with some aspect of copper metallurgy. The

question is, therefore, in which, and if in only one, step of the production process they were employed: smelting, refining, melting or alloying. To explain this issue, a composition of a charge, i.e. a type of material which was heated in the crucibles, was tried to be inferred from the compositional data for the crucible fabric and slag residues. In all, except PB-15, samples the highly elevated content of iron oxide in the inner crucible slag indicates the incorporation of this element to the crucible slag from an external source (Fig. 61). The same may be stated about other elevated components: Cu, sometimes Mn, K, Ca and, in the case of TNN-9, Ti and Zr. The occurrence of all of these ingredients seems to exclude the secondary processes such as melting and alloying from the possible operations being practised in the crucibles. Smelting of copper ore or refining of raw low-grade copper are the most likely alternatives. This topic is broadly discussed below to make the comparison with the already interpreted material possible.

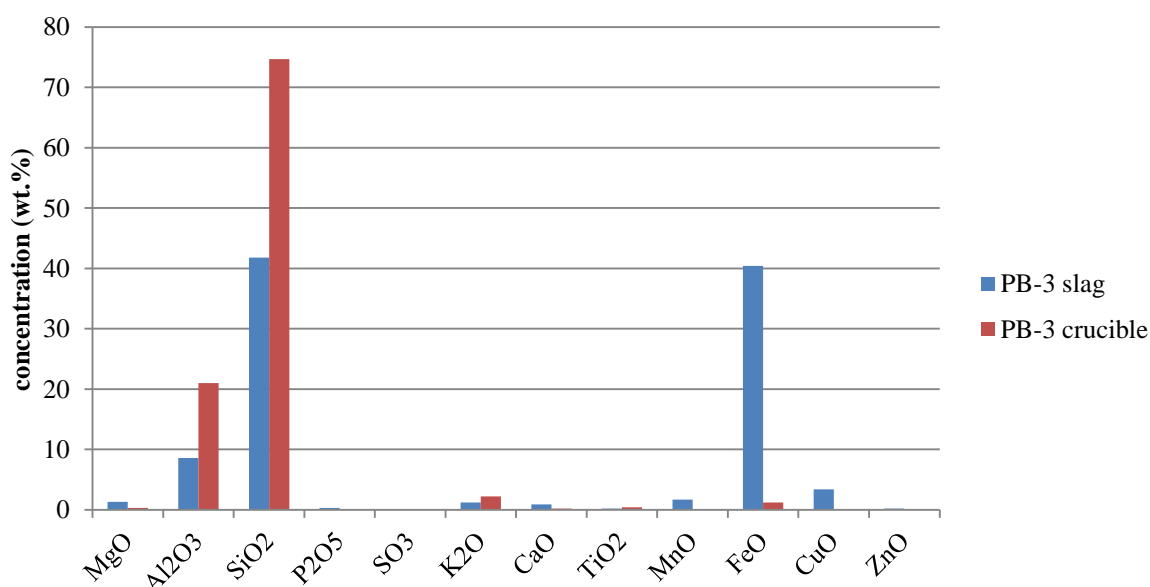


Fig. 61. Bar chart showing the comparison between the composition of the slag on the inner wall of the crucible PB-3 and its fabric; SEM-EDS results (wt%), normalised.

Slag occurring on the inner surface of the sample PB-15 has a different character and origin. It corresponds compositionally to the crucible fabric indicating that it may have originated mostly from the vitrification of crucible wall under high temperature without incorporation of nearly none external material (Fig. 62). Tin and copper was most likely loaded into the crucible and processed. Their co-occurrence may suggest several processes related to production of tin bronzes: melting of bronze (recycling), alloying of copper and tin, co-smelting of copper and tin minerals, cementation of tin minerals with metallic copper (Murillo-Barroso, Pryce, Bellina, & Martín-Torres, 2010, p. 1769). They will be discussed further this chapter.

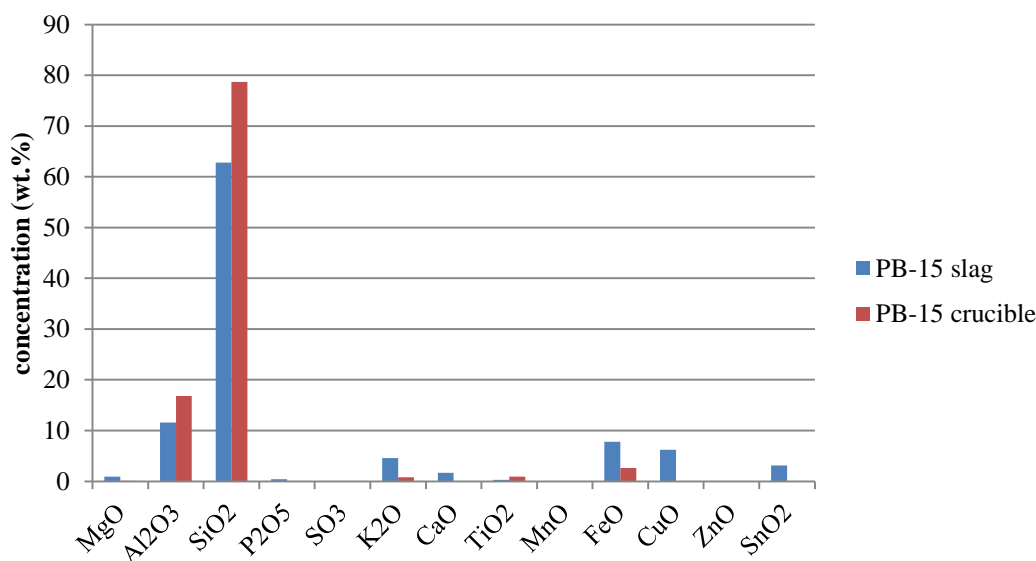


Fig. 62. Bar chart showing the comparison between the composition of the slag on the inner wall of the crucible PB-15 and its fabric; SEM-EDS results (wt%), normalised.

All the separate slag samples are similar in terms of their compositions presenting the peaks in amounts of iron oxide, silica and alumina and the microstructure limited to the slag of fayalite type. These characteristics, although valuable in the reconstruction of the original composition of a charge, firing parameters or behaviour of hot slag, are not very instructive for understanding of a type of metal which have been processed since a similar slag may be generated during iron, copper, tin smelting (Bachmann, 1982; for iron see e.g. Humphris, Martín-Torres, Rehren, & Reid, 2009; for copper see Maldonado & Rehren, 2009, p. 2002) what results from prevalence of iron and silica in all kinds of ore (Craddock, 1995, pp. 23–24). The best evidence that slag from PB and TNN is related to copper production is regular occurrence of low amounts of copper in all samples which is not usually detected in iron (Iles & Martín-Torres, 2009, p. 2321, tab. 2) or tin slag (Chirikure, Heimann, & Killick, 2010, p. 1659). Furthermore copper is the sole transition metal occurring in metallic form in the samples. The separate copper slag may be formed at several stages of copper production starting from smelting of ore minerals and ending with remelting of existing copper metal. The slag pieces discovered at PB and TNN are most likely associated with the process of copper extraction due to their high contents of transition metals other than copper as relict components of ore (iron, in TNN also manganese, zinc) (Radivojević et al., 2010, p. 2777) as well as the well-reacted morphology suggesting separation of gangue from copper by liquidation rather than just melting of a part of heating installation, such as reaction vessels, what may create larger piece of slag during secondary copper production. The shape of slag and its working parameters (see details below) also indicate the conditions suitable for copper smelting and its good segregation.

The copper ingots found across the mine and the mould from PB indicate that copper was cast at the sites after smelting. The composition of the ingot, i.e. the undetectable level of iron, indicates the application of refining of the crude copper before casting into a mould.

To sum up, all artefacts from both sites are associated with copper production (Table 19). Nearly all represent the primary stage of manufacture (smelting and refining to be considered). The interpretation of slag residue on the sample TNN-13 is impossible since it does not contain

any distinctive ingredients. One crucible sample from PB (PB-15) shows evidence for secondary copper production (bronze manufacture).

		Basic recognition of process	Further questions
Primary copper production			
Minerals	PB-41 and PB-42	smelting by reduction of copper oxides and carbonates with no or little production of slag	actually used or accidentally in archaeological deposits?
	PB-38 and PB-45	smelting with slagging away the gangue minerals	"
Crucibles	TNN-2b, 9; PB-3, 5, 13, 16, 17a	smelting and/or refining of copper	refining practised? relation to separate slag; mode of operation;
	TNN-13	process involving heating	
Separate slag	TNN-16a, 16b, 17a, 17b, 17d; PB-24a, 25a, 31, 34a, 35a, 24b, 26a, 23, 24a	smelting of copper	parameters of process; composition of a charge; where preformed; one or several stages?
Secondary copper production			
Crucible	PB-15	production of tin bronze	alloying of metallic Cu and Sn or tin added as oxide?

Table 19. Summary of the possible operations represented by the particular types of artefacts.

#### 4.2. Primary copper production at PB and TNN: pyrometallurgical specifics

##### TYPE OF ORE AND COMPOSITION OF A CHARGE

The first question, which is tried to be answered when reconstructing of the details of copper smelting at Sepon sites, is what types of ore were used in the process responsible for generating of separate slag discovered at both sites. To approach this issue the possible function and origin of each components of slag and composition of a smelting charge is considered.

The main components of a copper smelting charge are an **ore** containing copper-bearing minerals and often also unwanted compounds (gangue), **fluxes** which are a deliberate ingredient added to facilitate the slag formation and metal separation as well as **charcoal** added as fuel and burnt into ash which may contribute to the composition of the slag (Tylecote, Ghaznavi, & Boydell, 1977). Linking this basic set-up with the composition and microstructure of separate slag from Sepon several conclusions may be drawn.

The two main components of the slag, iron oxide and silica, are responsible for the formation of a workable low-melting slag of fayalite type which cleanly separated copper<sup>1</sup>, from the impurities occurring in the ore. They both, therefore, were acting as facilitators of the process by fluxing each other. Another issue is, however, if they were added deliberately to a charge as fluxes or entered the system together with other component or accidentally. Among the artefacts analysed there are several possible sources of silica and iron oxide. For iron oxide they are: secondary iron minerals associated with malachite (PB-45) and iron rich lateritic sediments (surface layer of PB-38); for silica the walls of firing installation made of siliceous fabrics from which the melt may have drawn a needed material during smelting (Th. Rehren et al., 2007, p.

<sup>1</sup> See low composition of copper in the bulk analyses of the slag (Table 15).

214) and the lateritic sediments PB-38 containing also silica. Lateritic soil as a source of both, silica and iron oxide, as well as alumina, the third most abundant element in the slag, seems at first sight to be a perfect match; especially that it occurs in close association with secondary copper minerals and does not contain any other oxides in high amounts which also correspond to the composition of the slag (Fig. 63, Table 5). Composition of the laterite, here represented just by one sample, may be, however, quite varied in the amount of silica, alumina and iron oxide. This could, on the one hand, explain a quite wide range of proportions of these elements detected in the separate slag, on the other makes the signature of the laterite indistinctive and the theory impossible to confirm at the moment. The occurrence of copper sulphide prills in the unreacted cluster of quartz in the sample PB-24b (Fig. 104b) suggests that at least part of silica may have entered a charge together with copper, i.e. within the ore, such as for instance represented by the laterite-bearing sample PB-38.

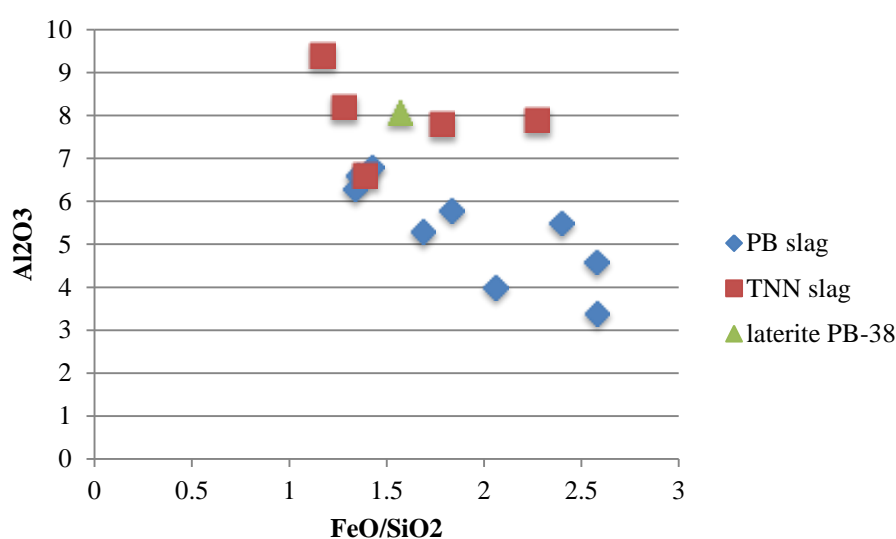


Fig. 63. Scatter plot showing the comparison between amount of alumina and FeO/SiO<sub>2</sub> ratio in the separate slag samples and in lateritic deposits in the sample PB-38.

The character of the heating installations will be mentioned again latter. Now just initial ideas are brought up. Several partially vitrified chunks of clay which may have been parts of a furnace were included into the assemblage from TNN. Unfortunately, as they were not analysed nothing more can be said about their role at the moment. Another possible type of heating installation are crucibles which are sometimes, also in the Southeast Asian context, considered as smelting reaction vessels (Bourgarit, Mille, Burens, & Carozza, 2005; Pryce et al., 2011). This complex issue will be discussed in one of the next chapters. If this was a case, however, together with silica in the form of quartz abundantly occurring in the paste, other elements of the crucible fabric would be fused with a melt, i.e. alumina and minor oxides. The quite low amount of CaO, MgO and K<sub>2</sub>O both in the slag and crucible fabric is in agreement with this suggestion (Fig. 64). The proportion of alumina to silica, which could make a good argument, varies widely in crucibles making any definite answer impossible. At the moment it seems that most of the separate slag samples tend to contain less alumina relative to silica that it is observed in the crucibles.



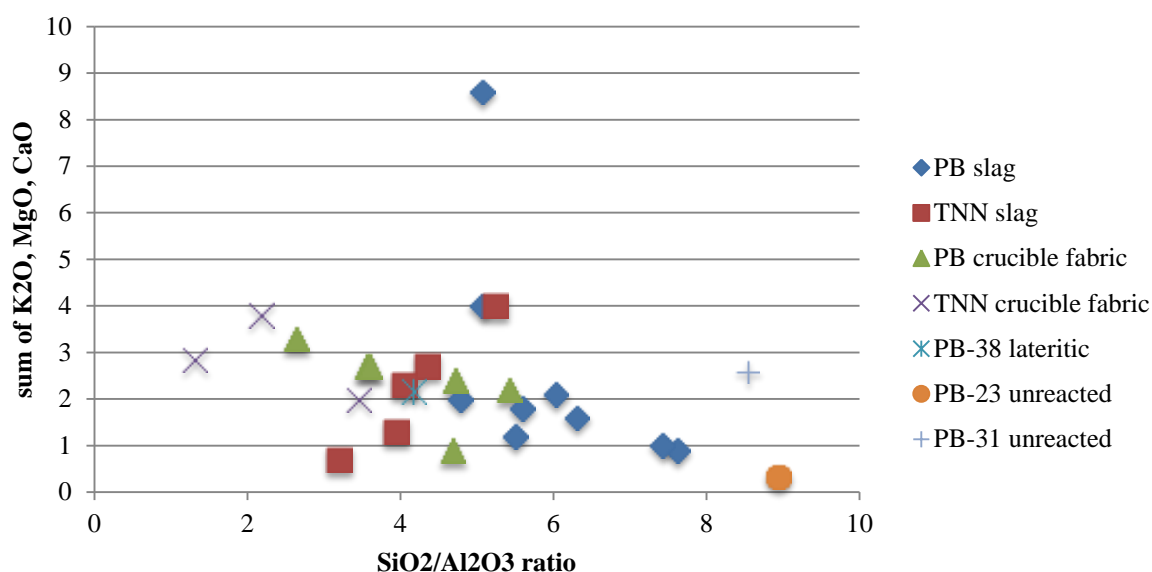


Fig. 64. Scatter plot showing amount of minor oxides and SiO<sub>2</sub>/Al<sub>2</sub>O<sub>3</sub> ratio in the separate slag samples as well as in the crucible fabrics, in laterite and unreacted phases; SEM-EDS results (wt%), normalised.

Two unreacted pieces from the bottom part of the sample PB-23 and centre of PB-31 match neither crucible nor lateritic sediment in silica/alumina ratio (Fig. 98). They represent the small part of the smelt not being in equilibrium with the bulk and less prone to melting. As far as lateritic sediments may easily vary in amount of quartz sand<sup>2</sup>, its distribution in the crucible paste was assessed as regular and no areas with such low amount of alumina relative to silica was detected in many scan analyses. Due to this fact and the occurrence of, common also in laterite layer of PB-38, iron oxide grains within the unreacted phases, they may be tentatively identified as rather remains of lateritic deposits, or other material not evidenced in the assemblage, than crucible fragments.

The concentration of residual iron oxide in the sample PB-24a together with copper sulphide (Fig. 107b) points out at possibility that some of the iron oxide occurred in the ore.

Manganese and zinc occurring in a content of 1-3% in the samples from TNN are most likely associated with the ore. In the case of zinc, it seems to be confirmed by the residual phases present in the sample TNN-16a containing this element (Table 34). Zinc and manganese seem to differentiate the TNN slag from PB pieces pointing out, at least on a scale of a few samples analysed, at some minor differences existing in the ore smelted.

Sulphur regularly occurs as copper sulphide prills and lumps in all separate slag samples. It may be traced back to the ore, predominantly to its copper-bearing part. The amount of sulphur in bulk analyses is low, usually below 0.5-1%. The only exceptions are four thin platy slag samples from PB showing 1.6-2.5% of SO<sub>3</sub>. The presence of sulphur in the slag cannot be considered as evidence of smelting of predominantly sulphide ores (Gale, Papastamaki, Stos-Gale, & Leonis, 1985, p. 86). The oxide ores from the enrichment zone may contain low amounts of sulphur<sup>3</sup> which, as experimental studies showed (Tylecote et al., 1977), will be, due to high affinity of sulphur to copper, transferred into a raw copper<sup>4</sup> or slag as copper sulphide

<sup>2</sup> See the concentration of quartz in left corner of Fig. 12a.

<sup>3</sup> Compare the composition of Rio Tinto ore in (Tylecote, Ghaznavi, & Boydell, 1977, p. 314) and of the sample PB-42.

<sup>4</sup> See composition of the copper ingot

during reduction smelting. On the other hand, however, a rich in sulphides ore require a different approach to obtain metallic copper, which may result in the same low-sulphur slag (Table 20).

Pathways in smelting of sulphidic ores		
I Two-stage operation		
1. Roasting: removing of most of the sulphur content by oxidation and decomposition of sulphur compounds	Experiments: Tylecote et al. (1977): as reported, easily and successfully made at 850°C for 5 hours, result: small residual sulphur content of 1.3%; Rostoker (1975): at 400-550°C for up to 8 hours, at higher temperature unwanted fusing into lumps, result: reducible roasted ore Doonan (1994): several roasting experiments at 700-800°C; results: small reduction in sulphur (from 11 to 9.5%), slight concentration of copper (from 11.6 to 16%)only top of the bed oxidised	Remains: slag containing low amount of sulphur associated with copper (copper and sulphide prill, sulphide lumps), raw copper containing sulphide inclusions
2. Reduction smelting of the roasted ore: reduction of cooper oxide to metal, slagging away of impurities into silicate slag	Experiments: Tylecote et al. (1977): separation to copper with low amount of impurities (S-0.35; Fe-0.45) and slag containing only 0.13% of sulphur Rostoker (1975): successful separation of copper into lump and slag but only when the crucible heated to high temperature of 1300°C; at lower temperatures small copper pieces dispersed throughout the slag; fluxes may help lower viscosity of slag at lower temperature	
II Co-smelting		
Charge composed of mixed oxide and sulphide ore resulted from disseminated occurrence of mixed oxide and sulphide ores in the nature and lack of their segregation by smelters (Rostoker, Pigott, & Dvorak, 1986) or from partial roast (Hanks & Doonan, 2009) is heated in a mildly oxidising environment.	Experiments Rostoker et al. (1986): recovering of copper from chalcopyrite and reducing of copper oxide to metal possible in one-stage operation due to acting of sulphide as reducing agent for CuO $5\text{CuO} + \text{CuFeS}_2 \rightarrow \text{FeO} + 2\text{SO}_2 + 6\text{Cu}$	”  Amount of sulphur in slag depends on the control over amount of oxygen in the system and proportion of oxide to sulphide minerals
III Matte-smelting		
Multi-stage operation involving: liquid separation of matte from gangue, remelting of matte to drive FeO into silicate slag and to gravity-separate of Cu-enriched matte, roasting of copper sulphides (Rostoker et al., 1986, p. 72).		???  Many possibilities also as above

Table 20. Possible pathways in smelting of sulphidic ores.

The presence of sulphur lost in the matte, occurring as prills and lumps in the slag, indicates that the environment in which the reaction was taking place was not oxidising enough to remove it and that probably sulphur and carbon were competing for oxygen. The issue if the paucity of oxygen results from the fact that the process was basically reduction smelting of oxide ores with spare accidental sulphides or from the excess of sulphide over oxide minerals in a co-

smelt or from any other mixed process or its one of the steps cannot be decided on a basis of the composition of the slag.

The only phases which may be considered as relict ore components were recognised in the sample TNN-16a in the form of barite, probably gangue mineral, and possibly as a piece of secondary mineral transformed/corroded to pseudomorphic compound containing iron and copper oxides (Fig. 108).

The contribution of fuel ash to the slag is low since nearly all of the samples examined contain small amount of oxides of the alkali and alkaline earth metals which are common components of charcoal ash (Tylecote et al., 1977, p. 311).

The summary of possible original components of a smelt and their sources is presented in Table 21.

Possible source		Slag component	Evidence and options	Questions
Ore	Ore minerals	Copper oxide minerals (tenorite, cuprite), carbonates (malachite) and native copper	- their presence in mineral samples found at PB; - piece of copper-rich probably relict phase in TNN-16a presenting secondary (associated with precipitation) structure (Fig. 108a-b); - metallic copper was for sure produced in the process and all known paths to metallic copper are bases on copper oxides (occur as such or transformed by previous stages)	Proportion of oxide-sulphide smelt is difficult to estimate. Possibilities: - assuming the mineral samples are representative, the charge would be mostly oxidic with relic amount of sulphide not removed (just heated and melted) during reduction smelting - mixed smelt: some sulphide oxidised stimulating the process, copper oxides reduced - mostly sulphidic charge would require several stages; was the slag into question produced during operation resulting in matte or metallic copper?
		Copper sulphide	- presence of sulphide phase in the slag samples and in a small amount in the mineral sample PB-42;	
	Gangue minerals	Barite, zinc and manganese compounds	- zinc and manganese occur in the slag samples from TNN; - barite relic minerals in the sample from TNN;	Differences between sites?
		Iron oxide	- recognised in two mineral samples from PB, included lateritic soil; - composition of lateritic soil is commensurate with slag and may give workable slag; - unreacted material in slag samples PB-24b, 23 and 31 could be residual pieces of laterite;	Self-fluxing ore?
		Silica	- occurrence in lateritic gangue in PB-38	
Fluxes		Iron Silica	- well-reacted slag of consistent fayalite structure as evidence of the control over the composition and deliberate addition of fluxes? - silica may added as sand; iron as hematite – difficult to confirm;	Slag liquid below 1300°C extends in FeO/SiO <sub>2</sub> ratios significantly (1.5-5.65) what means FeO content may vary from 60 to 85% relative to silica. This fact, plus the fluxing influence of other components on a slag, may limit somewhat the necessarily of precision in creating a workable fayalite slag.
Fuel ash		Little amount of calcia, magnesia, potash	- these oxides may be derived also from different sources; - in the sample TNN-17a locally higher amount of potash resulted in formation of leucite-local contact with fuel? - no charcoal relict in the slags;	What is a reason of small contribution of fuel ash, especially calcia, to the composition of the slag? Little physical contact? Type of fuel?
Heating installation		Silica and alumina	- crucibles commonly found – but silica/alumina ratio difficult to assess - from a wall of smelting pit dug in laterite soil common at both sites?	Where was smelting conducted?
		Iron	- from a wall of smelting pit dug in laterite soil common at both sites?	

Table 21. Summary of the components of the slag and their possible source and role during the process.

## BEHAVIOUR OF SEPARATE SLAG AND REDOX CONDITIONS

The microstructure of the separate slag pieces indicated that bulk of the slag was molten during the process and a vast majority of the crystalline phases was newly-formed. This assumption allows plotting of the compositional data on the ternary diagram of the FeO-Al<sub>2</sub>O<sub>3</sub>-SiO<sub>2</sub> system to roughly estimate the working temperature of the slag samples. As indicated in the Fig. 65 all separate slag samples fall precisely within the fayalite formation region around 1100-1200°C. The small amount of minor metal oxides, for instance manganese regularly occurring in the samples from TNN, may have brought this temperature even more down by an estimated 50°C, significantly in the context of fluidity of the slag, important for clear slag/metal separation.

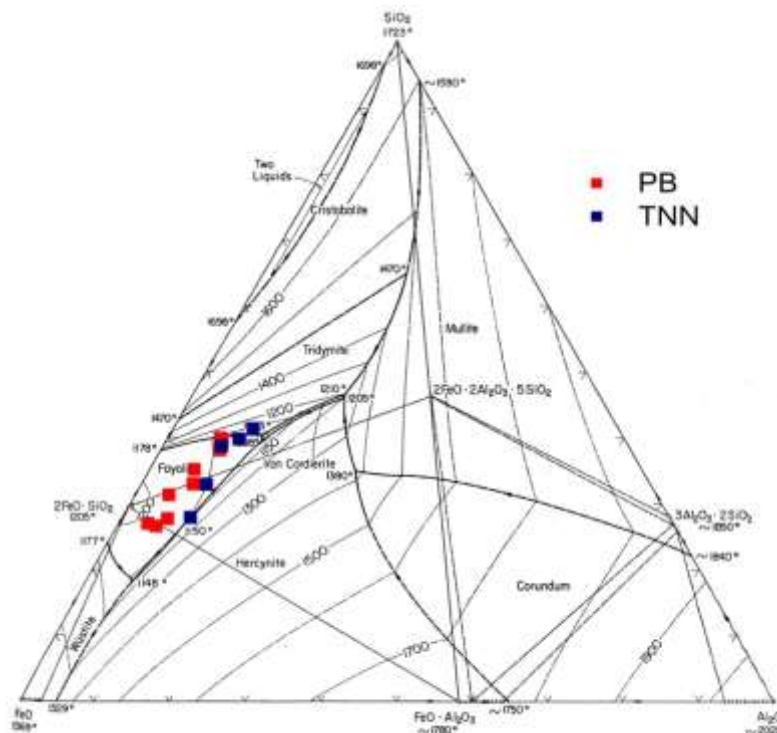


Fig. 65. Bulk composition of the slag samples plotted on the ternary equilibrium diagram of a FeO-Al<sub>2</sub>O<sub>3</sub>-SiO<sub>2</sub> system (Levin et al., 1956, p. 241, fig. 696).

In most of the samples, FeO/SiO<sub>2</sub> ratio falls within a range of 1.5-2.5 what lowers the viscosity of slag in comparison to richer in silica slags. Amount of alumina below 8-10% affects positively slag behaviour bringing liquidus temperature down (Park, Park, & Sohn, 2011, fig. 10). As alumina seems to be associated more with silica than with iron, the increase in silica amount entails growth in amount of alumina, which significantly improves the behaviour of liquid slag with lower FeO/SiO<sub>2</sub> ratio (around 1) (Fig. 66b).

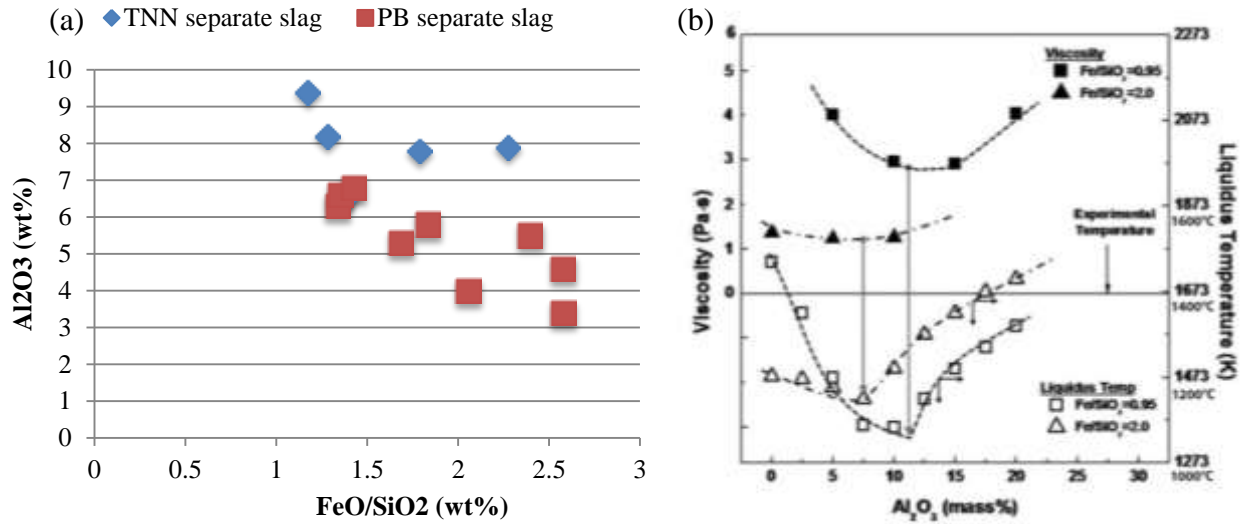


Fig. 66. (a) Scatter plot showing amount of alumina and FeO/SiO<sub>2</sub> ratio in the separate slag. SEM-EDS results (wt%), normalised; (b) Graph showing the relationship between 1) viscosity and liquidus temperature (y axis) and 2) amount of alumina in the system (x axis) (after ). Note that system with higher amount of silica (FeO/SiO<sub>2</sub> = 0.95) has higher liquidus temperature and viscosity which may be improved by the appropriate amount of alumina. The decrease of both parameters falls within the range of alumina contents detected in slags.

The magnetite lines were recognised in the samples PB-34a (thin platy slag) and TNN-17b (thin porous slag) (Fig. 98e-f). They are usually considered as evidence of tapping, removing of liquid slag from a furnace during smelting (Georgakopoulou, Bassiakos, & Philaniotou, 2011, p. 130). They are certainly indicators of full liquidation of the slag, its low viscosity and the fact that it was in motion during some part of the process. It seems that temperature may have reached even well above 1200°C to provide overheating necessary for full melt. The crystallisation of magnesia-rich olivine in the sample PB-24a also indicates reaching of very high temperature since this phase forms well above 1300°C (Bowen & Schairer, 1935, p. 156, tab. Ic). However, so high temperatures were most likely local and temporal phenomena.

The predominance of fayalite in the slags indicates that most of the iron in the melt was bivalent pointing out at the reduction condition during the process (Lutz, Pernicka, & Wagner, 1994). The presence of magnetite, on the other hand, indicates that the conditions were not wholly reducing since the fayalite/magnetite ratio is mostly controlled by redox conditions (Zhang, Zhang, Wang, & Sui, 2005, p. 942). The formation of magnetite may be influenced not only by the oxygen entering the system but also by the oxide/sulphide mineral proportion in the initial ore (Bourgarit et al., 2005). The slag from both sites contains little magnetite. The abundance of magnetite was noticed only in one separate slag sample (PB-23) and in the slag lining of the sample PB-13. In both cases higher than average amount of copper was detected what confirms the detrimental effect of magnetite on slag viscosity and metal or matte/slag separation (Bourgarit et al., 2008, p. 7). Basically, the fayalite/magnetite ratio, although quite difficult to estimate with the methods used in the project, seems to be well controlled during the formation of slags from both sites. It must have been attained by the regulation of amount of gaseous oxygen entering the smelt as well as probably by the quite stable proportion of malachite to sulphide minerals.

Considering the shape of regular platy slags (thick and thin ones), their flat regular surface indicates that they solidified while floating on a liquid phase, most likely on a pool of

molten copper. The shape of the edge of the sample PB-26a reminds a meniscus of a pool of molten metal (Hanks & Doonan, 2009) (Fig. 48b). The platy slag is probably derived from a cake, rim of which was recognised in several pieces. It was not possible, however, to estimate its shape, size or diameter since the pieces are too small. The slag PB-24b seems to have a rectangular quite regular outline which may point out the possibility of slag remelting and casting (?) (Fig. 48a).

The flat coarse slag probably solidified on a rough earthy surface. In the piece TNN-17a flow of a new portion of slag is well visible. The pieces of lumpy slag may represent portions of slag which were entrapped in the colder parts of the firing installation what explained their higher viscosity.

#### SMELTING INSTALLATION

At both Sepon sites the heavily slagged crucibles were found together with the pieces of separate slag in the same context. As indicated above, both types of slag may be related to some aspects of primary copper production, i.e. to treatment of ore or impure copper. The close association of both types of artefacts and the tradition of crucible-based smelting known from Khao Wong Prachan Valley (Bennett, 1989; Pryce et al., 2010) suggest considering the crucibles as smelting reactors. However, the present examination of separate slag pieces indicates that at least part of them was generated during furnace smelting what is based on the following facts:

- On the occurrence of fully reacted and homogenous platy slag with flow marks on its surface Fig. 67. This type of slag, German Plattenschlacke, is usually associated with furnace smelting (Craddock, 2001; Maldonado & Rehren, 2009) and is considered, in the case of ancient European and Near East metallurgy, as an indicator of the technological progress observed in Early Bronze age copper production relative to Chalcolithic period (Bourgarit et al., 2008, p. 7).



Fig. 67. Fragments of thin platy slag from PB.

- On the magnetite lines observed in two samples which indicate draining of some of the slag outside the smelting installation during the operation; in other words tapping associated with furnace technology.

The magnetite line was noticed in one of the thin platy slags which is characterised also by flat regular bottom suggesting the solidification on a liquid phase. Tapping of metal out of the furnace is against the principle of tapping (separation of slag and metal with the use of a difference in their density). It may be, therefore, suggested that in the case of this type of slag three different immiscible phases were produced: copper metal remaining in the base of a furnace as well as slag and matte being tapped out. Similar



process was observed in smelting of noble metal ores in Renaissance Austria (Mongiatti, Rehren, Martín-Torres, & Cech, 2009). Slag produced during this operation is very similar in appearance to the one from PB. Copper, matte and slag were observed also during experimental co-smelting of sulphide and oxide minerals (Rostoker et al., 1986, p. 74, fig. 3). This interpretation could be a clue for the slightly higher amount of sulphur detected consistently in the thin platy slag. The formation of matte may have resulted from higher sulphide/oxide minerals ratio in a particular smelt and may not have been a part of each operation what is evidenced by the presence of probably tapped slag without a characteristic flat bottom. No example of matte was found at Sepon. It is not surprising though since this rich in copper material would certainly be reprocessed.

- On the presence of the vitrified or slagged pieces of ceramic which may have been parts of furnace (Fig. 68a); one of them is reminiscent of an aperture, for instance for a nozzle (Fig. 68b). None of them was examined.

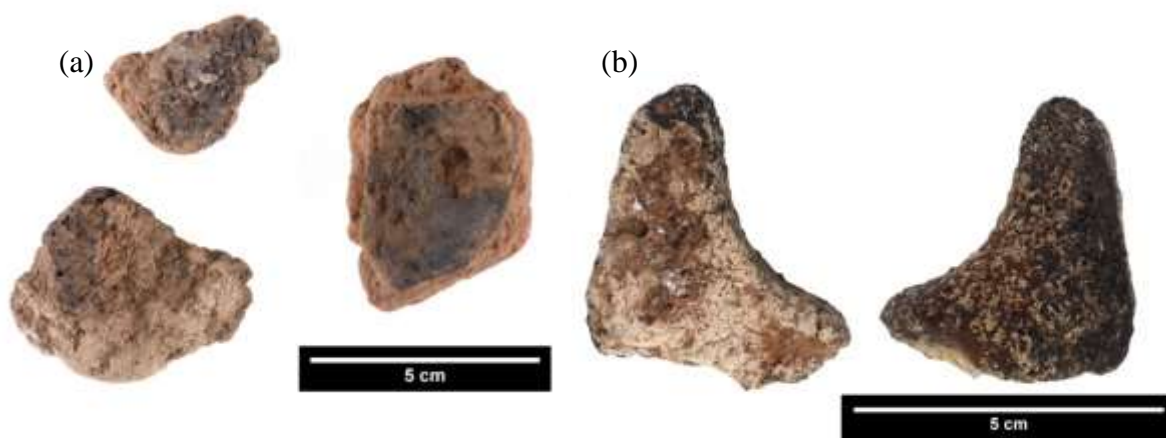


Fig. 68. (a) Irregular pieces of ceramic from TNN slightly vitrified or slagged on the surface; (b) Vitrified piece of clay from PB with a hole (?).

This theory has also several weak points and does not explain all features of the separate slag. They are as follows:

- Absence of large pieces of slag with weight in a range of kilograms and lack of slag heaps which usually are encountered when furnace smelting is considered (Maldonado & Rehren, 2009);
- Lack of tuyeres often found as a sole or major furnace remain (Bourgarit et al., 2008; Hein, Kilikoglou, & Kassianidou, 2007);
- Shape of the slag PB-24b which seems to have solidified in a kind of mould, what would require the hot liquid manipulation in a portable container. Slag casts were recorded at Nil Kham Haeng, one of the Khao Wong Prachan Valley site (Pryce et al., 2010).

#### POSSIBLE PRODUCTS OF SMELTING AND THE COPPER INGOT

The conditions evidenced in the samples were suitable for copper smelting what is confirmed by the presence of metallic copper entrapped into the slags. They occur as prills with their diameters between nearly 5 and 300  $\mu\text{m}$ . Most of them contains a quite high level of iron on average 3%. The highest determinations (above 3%) are most likely related to the measurement of the iron- rich background together with a prill. The amount of iron in the prills above 50 $\mu\text{m}$

should be, however, quite reliable (below 1-2%). The dendritic segregation of iron has not been noticed in any prills what also suggests a lower amount of iron than showed by small prills (Tylecote & Boydell, 1978). It was observed that iron may remain in solid solution with copper without formation of a distinct phase even in amount as high as 2.5% (Hauptmann, 1989, p. 130). The parameters of the slag indicate an efficient (low Cu amount in the slag) fully liquid process during which an extensive absorption of iron by copper is very likely. At 1200°C around 6% of iron may be dissolved in molten copper (Craddock & Meeks, 1987, p. 130). The resulted raw copper may have contained several per cent of iron which degrades formability and casting qualities of metal (Rostoker & Sadowski, 1980, p. 38).

Copper obtained during the process evidenced at PB and TNN contained most likely also a few per cent of sulphur, which, if not removed by roasting carried out prior to smelting, accompanies the metallic copper throughout the smelting process.

The bulk analysis of the copper ingot from TNN showed 1.4% of sulphur as a sole detectable impurity. Neither iron and nor slag inclusion were detected. Sulphur appears as copper sulphide segregates with the level of sulphur similar to sulphide phase in slag, however with much lower amount of iron (minimum detectable level). The very low amount of iron (below detection limit and for sure lower than detected in the copper prills in slag) indicates that the ingot was made of purified copper what confirms the process of refining practised at the Sepon sites, or at least at TNN. Remelting crude copper in an open crucible may have removed the excess of iron. In this process content of sulphur does not change significantly what results from preference of copper to bond with sulphur (Thilo Rehren, Boscher, & Pernicka, 2012, p. 1723). The experimental studies showed also that lead, which is visible as segregates in the ingot matrix, is not removed so efficiently as iron and a little amount of it may be retained in refined copper (Tylecote et al., 1977, p. 324).

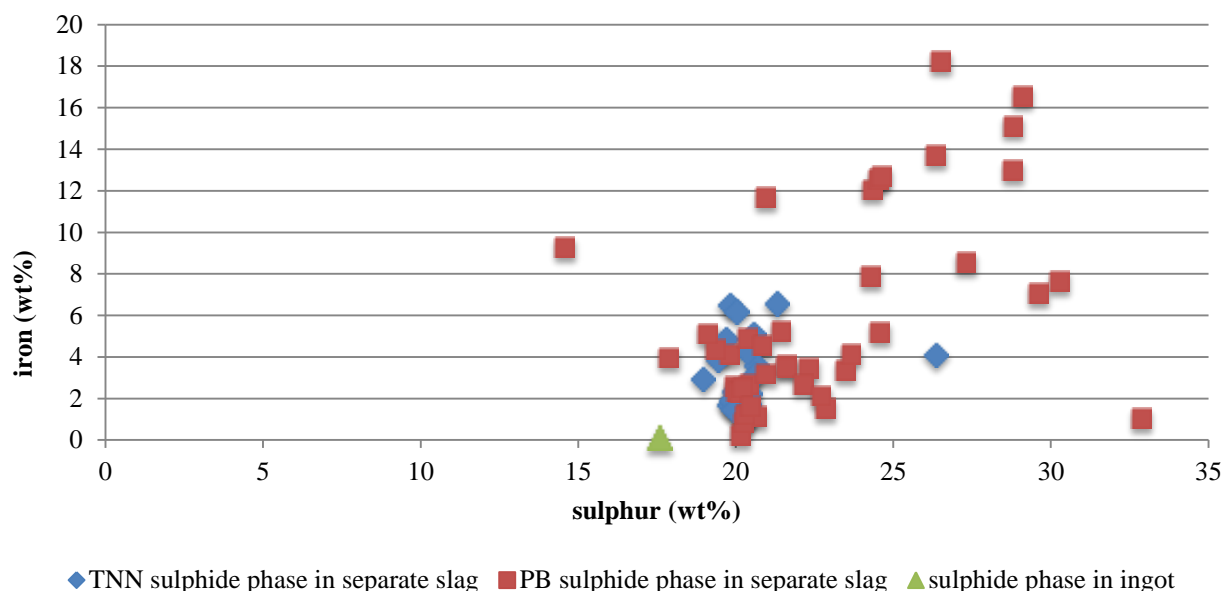


Fig. 69. Scatter plot showing the amount of iron and sulphur in the sulphidic phases (prills and lumps) in the separate slag pieces as well as in the copper ingot from TNN; SEM-EDS results (wt%), normalised.

### 4.3. Role and performance of crucibles

#### PRODUCTION OF CRUCIBLES

The clay used in the manufacture of the crucibles probably originated from deeply weathered acidic igneous rocks<sup>5</sup>. The original deposit contained primarily quartz widely varied in size, what reflects the progressive process of chemical and mechanical disintegration of rocks, clay, residual feldspar and some mica. The source of clay may be, therefore, compared in its composition and origin to the clays used in south China in the production of stoneware and porcelain (compare with Tite et al., 2012, pp. 38–39).

In terms of clay preparation techniques, several observations were made. Firstly, the most common inclusion, quartz, does not seem to be a deliberately added temper. Its wide grain size distribution from very fine silt to medium sand (0.004–0.5 mm) and angular shape suggest the chemical erosion as a main factor in its origin what is commensurate with the character of a possible clay source proposed above. Lavigation may have been used to remove coarse grains and impurities not observed in the crucible paste but noticed (large up to 1–2 mm granite fragments) in one of the pottery samples analysed characterised by basically similar to crucibles bulk composition (Appendix 2, sample PB-20).

In all samples voids left by rice husk were noticed. The practice of tempering clays with rice husk is common in the region (Vincent, 2003, pp. 52–58) and known from the domestic pottery found at PB (Appendix 2, sample PB-19). In the case of the crucible paste, the rice husk temper occurs in smaller quantity than in the pottery sherd and is unevenly distributed what suggests poor paste preparation (little homogenising by kneading) and again the occurrence of quartz, which is equally distributed through the fabric, as a natural inclusion.

The composition of the paste used in the manufacture of crucibles does not differ significantly from the fabric of non-technical ceramics found at the PB. Mineralogical investigation did not indicate any bigger differences between them either. Thus it seems that the clay for crucibles was not carefully selected because of its exceptional properties, for instance refractoriness. The heavily vitrified walls of the crucibles also suggest that they were not able to remain chemically and microstructurally stable during the heating process they were used for what one can expect from refractory materials. However, the low amount of major flux oxides, CaO, K<sub>2</sub>O, MgO, and high amount of silica in the clay put the crucible fabrics ahead of non-technical ceramics and other ancient ceramics used in high temperature operations (Fig. 70). Therefore, it may be concluded that the heavy alteration of the crucibles may be related to the composition of the melt (very reactive toward the siliceous fabric) and the high temperatures reached (as indicated above for sure above 1100°C). The locally accessible clays may have been adjusted to the role of reaction vessels by simple techniques of clay preparation (coarse feldspar grains were removed) and shape design (thicker walls and base) since the paste itself provided a quite suitable baseline.

---

<sup>5</sup> Based on the occurrence of particular heavy minerals, zircon, rutile (Pettijohn, Potter, & Siever, 1973, p. 304, tab. 8-2).

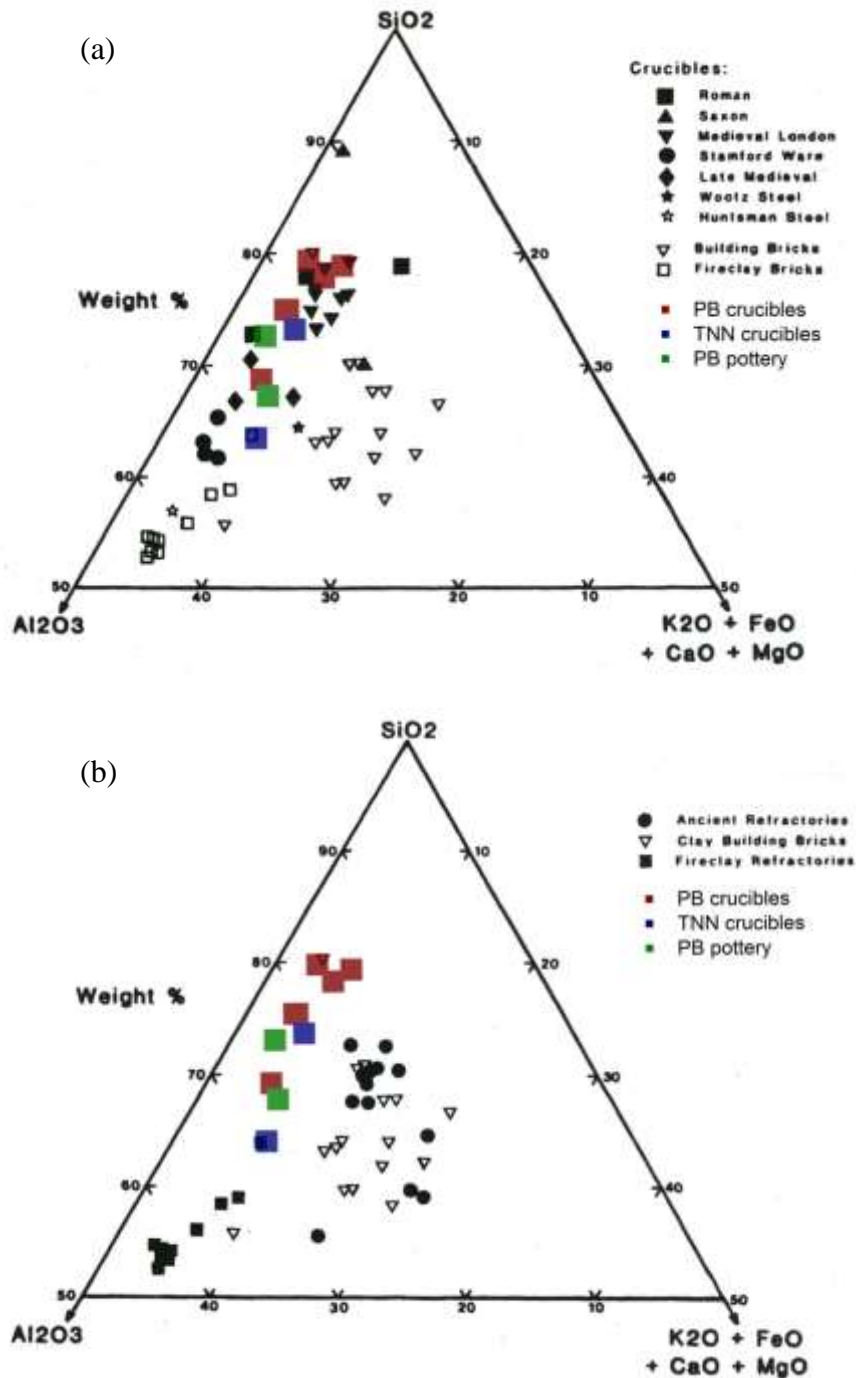


Fig. 70. Composition of crucible and domestic pottery fabrics from Sepon plotted on the triangular diagrams showing different types of ancient and modern ceramics (after Freestone & Tite, 1986, p. 57, figs. 21-22); (a) ceramic fabrics from Sepon straggling along the compositions of Roman and Medieval crucibles; (b) the amount of major flux oxides is much lower in the ceramics from Sepon than in ordinarily building clay and in other ancient refractories.

The question of pre-firing of crucibles before the use cannot be answered satisfactorily. The examination of several less altered during metallurgical operation pieces indicate, however, that they were not fired at a very high temperature (no sign of vitrification except the inner wall). During the use, crucibles probably still contained organic inclusion or its carbonised form which enhanced reducing condition within the fabric what resulted in precipitation of iron observed in several samples. Temperature at which carbon is efficiently eliminated is estimated around 600-750°C (Rice, 1987, p. 88). These parameters seem to match the conditions of firing evidenced in

properties of domestic pottery (softness, dark core with carbonised inclusion, optically active clay matrix). Obviously, a duration of possible prefiring has to be taken into consideration as a factor considerably influencing the qualities of a fabric and not easy (almost impossible) to estimate. The fragmented microstructure of the clay matrix of crucibles may, however, indicates that the soaking time was short (Tite et al., 2012, p. 46).

The vitrification gradient observed on the crucible walls indicate that the vessels were heated from above during the use. There is no clear evidence of a heat directed on the external walls except slaggy layer on the samples PB-13 which, however, is a result of slag spilling out of the crucible what is clear in the hand specimen as well as on the external wall of the sample PB-17a which got probably in contact with hot copper what might confirm using crucible to move and pour metal (Fig. 70).

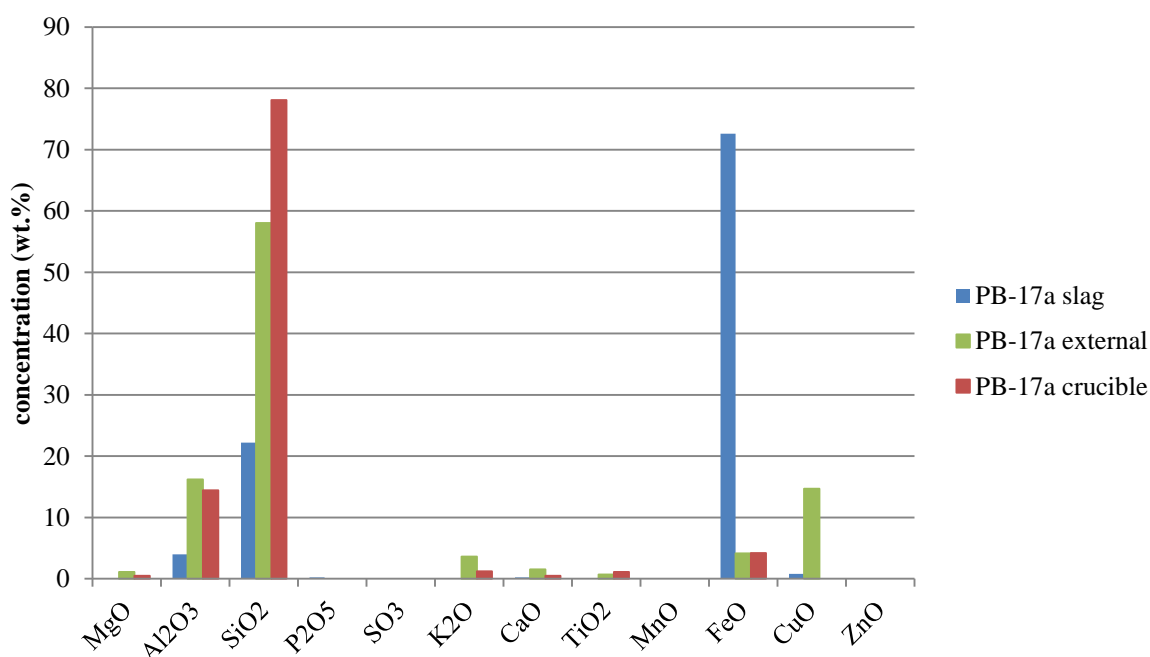


Fig. 71. Bar chart showing the comparison between compositions of inner and external slag as well as ceramic fabric of the crucible PB-17a.

#### FUNCTION OF CRUCIBLES

Reconsidering the function of crucible in the context of other artefacts from Sepon, several initial conclusions may be drawn. Firstly, several important differences may be noticed in the composition of separate and crucible slags from TNN: 1) regular occurrence of zinc in separate slag in contrast to its absence in crucible lining; 2) phosphorus and manganese much more visible in the separate slags (Fig. 72b). As all of these elements are likely to originate from gangue part of the ore and are passed mostly to the slag during smelting (Tylecote et al., 1977, pp. 316–317), it seems that refining as a practise carried out in the crucibles may be confirmed. The lower amount of iron oxide in the crucible slag might be also interpreted in accordance with that (Fig. 72a).

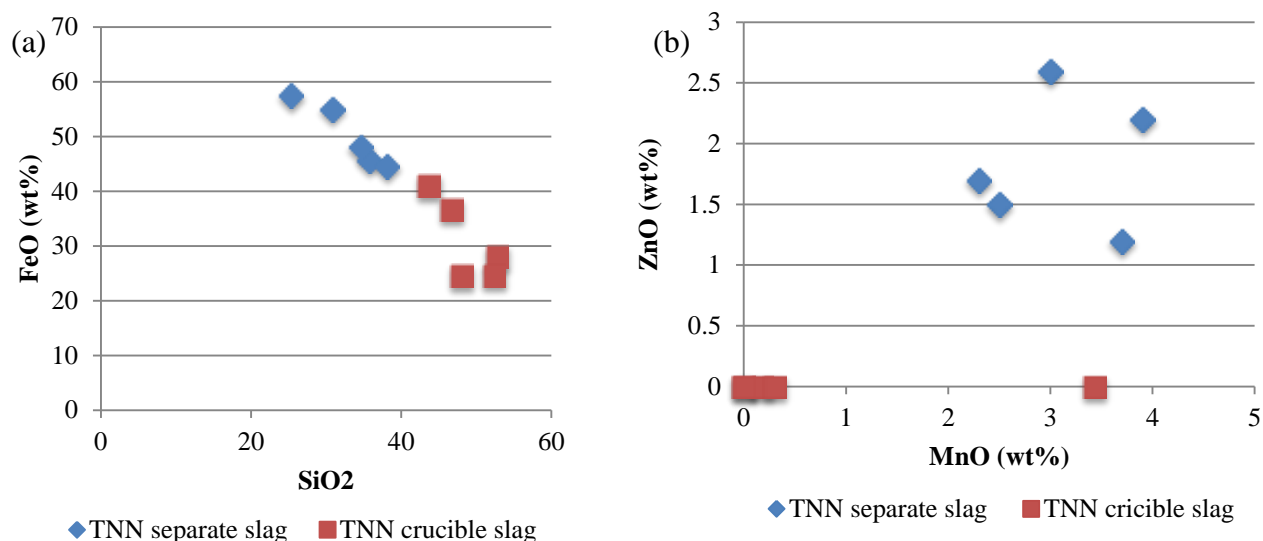


Fig. 72. Scatter plots showing the amounts of (a) ZnO and MnO; (b) FeO and SiO<sub>2</sub> in the separate and crucible slags from TNN.

The case of PB is more difficult to explain due to the lack of distinctive elements in the slag. Manganese occur both in the separate and crucible slag samples but inconsistently.

As refining is employed to remove iron from copper, it may be expected that metallic and sulphidic phases in the refining slag contains less iron than in the smelting slag. This trend can be observed only in the sulphidic phases (Fig. 90, Fig. 101). The copper metal prills in the crucible slag seem to contain more iron than, however, must be considered in the context in their much smaller sizes affecting the analyses.

Another issue which requires an explanation is the presence of additional silica in several samples of the crucible slag. The comparison of SiO<sub>2</sub>/Al<sub>2</sub>O<sub>3</sub> ratios in slag lining and crucible fabrics revealed much higher silica amount relative to alumina in most of the slags what may indicate the addition of silica from outside of the system (unrelated to alumina).

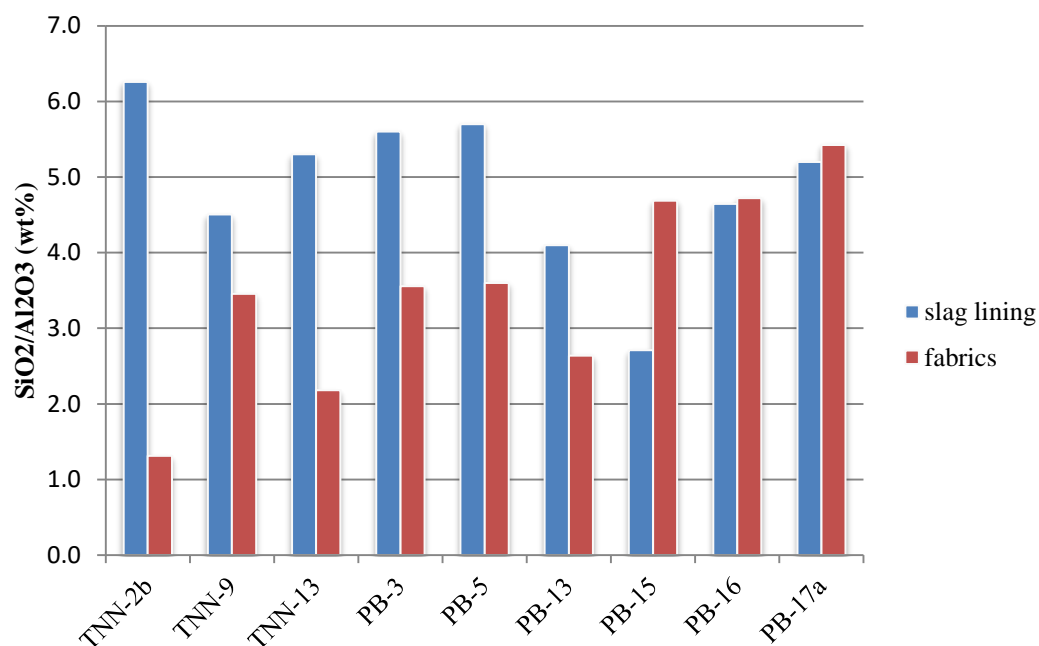


Fig. 73. Bar chart showing the comparison between SiO<sub>2</sub>/Al<sub>2</sub>O<sub>3</sub> ratios in the crucible slag and crucible fabric, SEM-EDS results (wt%).



It may be partially explained by the fact that in a lump of smelted impure copper inclusion of slag may be present what is shown by the metallographic examination of the copper oxhide ingots from Uluburun shipwreck (Hauptmann, Maddin, & Prange, 2002). The addition of sand to facilitate the process and to protect the integrity of crucibles is also possible. This practice seems to be evidenced in the sample TNN-9 (Fig. 74) where high amount of titanium and zirconium (much higher than detected in any of the separate slag samples) may indicate the admixture of rich in heavy minerals sand. The addition of quartz neutralising highly reactive iron-rich melt may have saved a crucible enabling pouring out the copper securely.

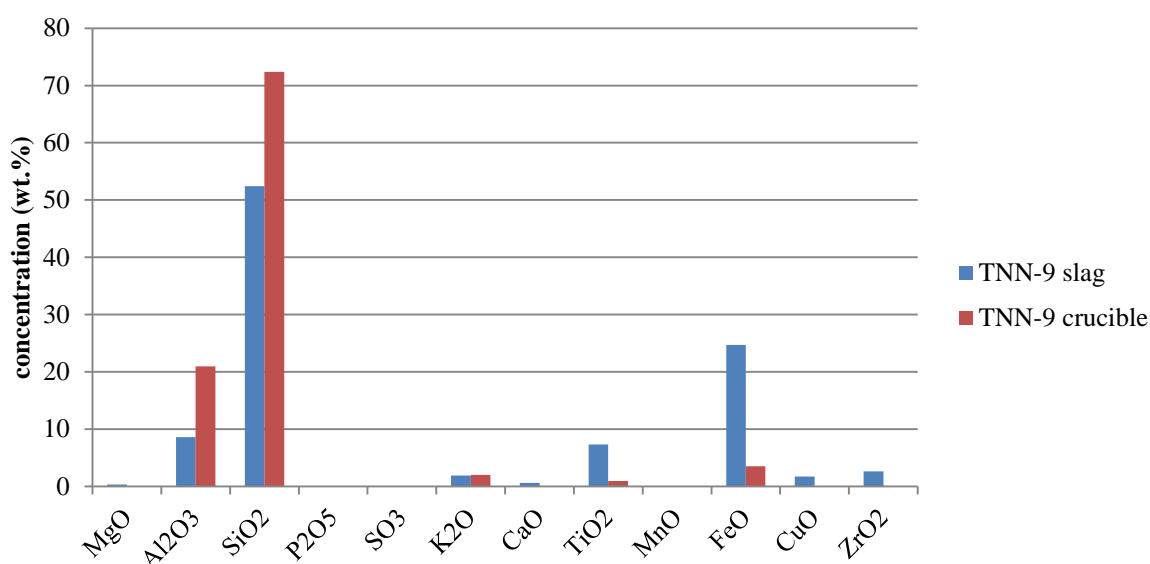


Fig. 74. Bar charts showing the comparison between the crucible fabric and crucible slag in the sample TNN-9, SEM-EDS results (wt%), normalised.

It would seem, in conclusion, that refining of raw copper was an important part of the production sequence at Sepon sites. The smelted copper was remelted in the crucibles to remove iron and other impurities by their preferential oxidation. The presence of fuel inside the pot, evidenced by the vitrification pattern on the crucibles, may have hampered the oxidation of impurities. Stirring with the stick during the process would, however, considerably facilitate the oxygen access (Bourgarit et al., 2005). The high temperature of the process, documented in the crucibles, much higher than the melting point of copper (1084°C) would improve slag-copper separation (Rostoker, 1975). The process of poling, on the other hand, could be a remedy for oxidation of copper (Craddock, 1995, p. 204). The practice of copper purifying at primary production sites was confirmed at Late Bronze Age Timna where a crucible furnace for refining of copper was discovered (Rothenberg, 1972, pp. 78–80).

#### 4.3. Secondary production

##### CASTING

Although the sample was not etched, casting as a sole method of shaping may be indicated by the round sulphide inclusion, which does not show any elongation observed when an object is subjected to cold-working (Modlinger, 196). The mould discovered at PB confirms the casting operation was carried out at Sepon sites.

An interesting issue is the presence of the piece of ceramic inside the ingot. As ceramic has much slower density than copper metal, the piece of sherd would float at the surface of an

ingot if no special technique was applied to keep it in a core. In the case of the copper bun ingots stuffed with a chunk of slag from al-Aqir it was suggested that firstly a slag ingot was cast and then it was covered with copper in at least two steps good documented in the ingots' morphology (Weisgerber & Yule, 2003). In the ingot from TNN no heterogeneity was noticed suggesting pouring the metal in two portions. It must be, however, verified with metallographic examination on an etched specimen. It is possible that a bit too big chunk of pottery got stuck in the mould when it was shoved. It also could have been held with tongs during pouring of metal. In the first case the piece of pottery would be visible on the surface of copper objects which may be concluded from the cross section of the ingot (Fig. 56, right side). Recently, a number of corroded copper cone-shaped ingots with visible piece of pottery was discovered at TNN (N. Chang pers. comm.).

Because the function of the so-called ingots is not certain, the interpretation of the fact that ceramic pieces were intentionally regularly put into them is difficult. If the interpretation of the objects as ingots is correct, what is based on its repetitive shape<sup>6</sup> and high frequency of occurring, they may be considered as fakes. The fact that the ceramic piece may have been visible casts some doubt on this idea, although the possibility of unsuccessful fakes must be taken into consideration as well. Anyway, two things are undisputable; a piece of ceramic set into an object saves the quantity of metal used for casting and significantly deteriorates its remelting abilities.

#### BRONZE MANUFACTURE

One fragment of crucible, PB-15 (Fig. 18c), exhibits evidence of bronze manufacture in a form of small vitrified zone on the inner surface of the vessel containing tin and copper. Concerning the specifics of the operation, very low amount of components in the slag which may originate from gangue minerals and presence of metallic copper seem to argue against co-smelting. According to Rovira (Murillo-Barroso et al., 2010, p. 1769) nodular cassiterite appearing in clusters, documented in the sample PB-15 (Fig. 75), may indicate cassiterite cementation with metallic copper. In this case copper would be, however, fluid during tin diffusion since the copper prills indicating liquidation were observed (Fig. 93). The possibility of alloying of metallic copper and tin cannot be ruled out since metallic tin would have been oxidised prior copper giving presumably similar effect as noticed in the sample.

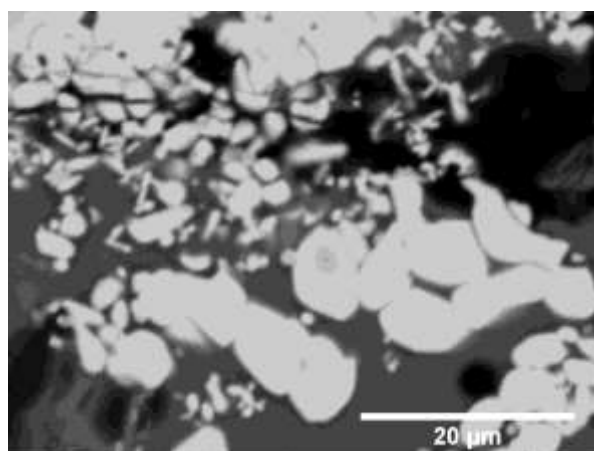


Fig. 75. Backscattered electron image of the residue on the inner wall of the crucible PB-15.

<sup>6</sup> The author is not sure about the ingots' consistency in the weight.

## 5. Conclusions

The current studies confirmed the existence of the developed multi-stage copper production during the second half of the first millennium BC in the Sepon area.

The examination of the metallurgical waste discovered at Peun Baolo and Thong Na Nguak enabled for the initial differentiating of several stages of production:

- 1) Smelting of copper ores probably carried out in furnaces what is evidenced by the morphology and composition of the separate slag discovered at both sites;
- 2) Refining of iron-rich copper in the open crucibles;
- 3) Casting of pure copper;
- 4) Manufacturing of tin bronze by melting the metallic copper with tin in the crucibles.

Thus the whole sequence from the copper minerals occurring in the nature to the copper ready to be used was confirmed with some evidence of production of bronze objects. At each stage some interesting issues and question arose.

Considering the smelting process, the analyses of the slag samples indicate the systematic process in which slag was cleanly separated from metal by full liquidation. The slag pieces are almost free of relict charge components and low in copper. They present qualities pointing out at the good control over the process: quite regular composition, low viscosity, relatively low liquidus temperature consistent fayalite/magnetite ratio. All these parameters assured good copper separation but also encouraged the absorption of iron by copper.

Copper containing high amount of iron needed purification what seems to be documented in the crucible slag. The process of copper refining requires high skills to control the amount of oxygen entering the system. The operation may sometimes fail what seems to be evident in some of the slag layers with very high amount of copper. The copper ingot shows that the process was effective lowering the content of iron below 0.2 wt%.

In the case of bronze manufacture, it has to be mentioned that its evidence is at the moment very tiny, literally tiny in a form of glassy spot in a size of 0.1 mm documented on one crucible from PB. However, tin and copper is certainly present there together with the strong indication of heating. The further careful assessment of the crucible sherds should, therefore, bring a confirmation and maybe an answer for the question about the form in which tin was introduced to the melt: as metal which was traded or tin oxide sources of which might have been present in the region.

The crucibles are a broad topic and, in opinion of the author, an interesting one which deserves independent systematic well-thought-out investigation. It allows addressing the issues such as the relationship between *potters* and *metallurgists*, brought up by the peculiar (maybe crucible grog?) type of inclusion noticed in one of the pottery sample (Appendix 2, PB-18), or the problem of possible differences in the fabrics used in production of crucible for copper refining and alloying. The detailed studies may also help to decide if the remelting of copper was the only one operation carried out in the heavily slagged crucibles or if crucible-based smelting may be also involved. The conclusions based on the current studies are limited due to the low number of sherd analysed and the unsystematic approach of sampling adjusted for metallurgical reconstruction. It may be, however, stated that they were made of locally accessible clay low in all oxides except silica, alumina and occasionally iron oxide occurring often as nodules. At both sites the same practice of tempering with rice husk was recorded.

The picture of the sophisticated Iron Age copper metallurgy of Peun Baolo and Thong Na Nguak depicted in the present studies correlates well with the recent isotopic investigations pointing out at the Sepon region as one of the most important copper suppliers in the prehistoric Southeast Asia (Pryce et al., 2011). The further excavations at Peun Baolo as well as at the adjacent sites will certainly result in establishing of a reliable chronological sequence of the occupation in the area what would enable investigating the diachronic development of metallurgical techniques. They will provide also new data which will test the preliminary ideas presented in the dissertation.

## **Appendix 1: analytical equipment and its working conditions**

### **SEM-EDS**

SEM-EDS was applied as a main technique in characterisation of both chemical composition of the samples and their microstructure. The SEM-EDS examination was designed to make best use of all of the advantages this method offers. In the case of the current project there were: the permanent availability of the equipment, quickness of analysis and good imaging abilities under high magnification. Obviously, SEM-EDS has also a range of limitations, among which the major are quite low accuracy and precision, high detection limit, unstable beam current and possibility of overlapping of some elements, lead and sulphur, which may have some importance for this studies, included. Although, the limits seem to be quite serious, and for sure for some purposes they would disqualify SEM-EDS as a method of choice, in the case of the present project and its goals the abilities of the technique are considered as fairly enough and its limitations were assessed as not harmful regarding the final results. The operating conditions and research strategy were adjusted to enhance the assets of SEM-EDS rather than to minimise its inherent constrains.

### **Sample preparation**

For SEM analysis, resin-mounted polished blocks were prepared. The selected artefacts were cut perpendicularly to the surface with an abrasive tile cutter in the place of interest. Small, approximately 1-2 cm across, pieces were removed and embedded in epoxy raisin. The block was grounded flat and polished with diamond paste to 1 or 0.25  $\mu\text{m}$  depending on polishing qualities of a material. Before analysing, the samples were coated with thin layer of carbon.

### **Equipment and operating conditions**

The samples were analysed with a Phillips XL30 scanning electron microscope fitted with an energy dispersive spectrometer (Oxford Instrument INCA series) and ZAF-corrections. Calibration of the EDS using a cobalt standard was conducted regularly throughout the analysis.

The analyses were carried out over a span of two months. During this period the SEM-EDS set-up were modified by a main operator of the instrument what resulted in a different values of emission current during the first several session (in a range of 87-93  $\mu\text{A}$ ) and the latter ones (68-73  $\mu\text{A}$ ). Despite these differences, the actual current of the incident beam, so the number of electrons reaching a sample, was kept quite stable by adjustment of the spotsize, i.e. smaller (4) during the first analyses and larger (6.3-6.7) during the latter ones. The construction of the SEM is image-oriented and allows rastering the beam over a quite large area of a sample what was taken advantage of many times in the current research. The mobility of the beam, however, and the necessity to obtain a balance in a vacuum system each time the chamber is reloaded make the current slightly unstable over the time which is clearly demonstrated in totals, sometimes widely varied. The slight changes in current were tried to be recognised by observing a detector deadtime on a cobalt standard for which a target value was in a range of 35-40%. If it dropped, the spotsize was slightly increased.

An accelerating voltage of 20kV and working distance of 10 mm were fixed. Process time was set to 5 giving. Livetime of 50s was set during most analyses. However, in some cases lower value of 30s was also used.

## Accuracy, precision, detection limits

The accuracy of the measurements was assessed using the certified reference material, the U.S. Geological Survey basalt standard (abbreviated BHVO-2). The standard was analysed following the same procedure which was applied in the examination of the sample

The above described equipment and its set-up allows for chemical analysis with accuracy within 5-10% relative error of the expected concentrations for the major oxides (Table 22). It means that the absolute error of each measurement usually did not exceed 0.2-0.5 wt% and in the case of silica 2.5 wt%. Precision, presented as the standard deviation ( $\sigma$ ) of the measurements, was 0.1-0.2 wt%. It gives quite satisfactory relative  $\sigma$  values falling usually in a range of 1-5%. The possibility to improve the precision by extending the lifetime was not used since it entails an undesirable increase in the analysis time.

P2O3 present in the standard in the amount of 0.27wt% was not detected. This sets the detection limits on a level of sensitivity generally accepted for the EDS, around 0.2 for elements with  $Z > Z_{Si}$  (Ciliberto, & Spoto, 2000, p. 410; Pollard & Heron, 1996, p. 52; Potts, 1992, p. 366).

	Na2O	MgO	Al2O3	SiO2	K2O	CaO	TiO2	FeO	total
average	2.0	7.0	12.8	52.4	0.5	11.2	2.9	11.2	117.1
$\sigma$	0.05	0.13	0.12	0.06	0.04	0.12	0.04	0.08	2.08
relative $\sigma$	2.3	1.8	1.0	0.1	7.3	1.1	1.5	0.7	1.8
given	2.2	7.2	13.5	49.9	0.5	11.4	2.7	11.6	
absolute error	0.22	0.23	0.66	-2.46	0.01	0.19	-0.16	0.40	
relative error	9.82	3.15	4.89	4.93	2.69	1.67	5.86	3.48	
average	2.1	7.0	12.9	52.3	0.5	11.2	2.9	11.1	95.3
$\sigma$	0.04	0.10	0.16	0.14	0.04	0.15	0.05	0.04	3.57
relative $\sigma$	1.7	1.4	1.2	0.3	8.2	1.3	1.6	0.4	3.7
given	2.2	7.2	13.5	49.9	0.5	11.4	2.7	11.6	
absolute error	0.10	0.21	0.62	-2.39	-0.01	0.19	-0.13	0.50	
relative error	4.65	2.86	4.62	4.79	1.92	1.67	4.64	4.28	
average	2.0	6.9	12.8	52.2	0.5	11.2	2.8	11.5	100.5
$\sigma$	0.08	0.10	0.10	0.14	0.01	0.09	0.10	0.12	0.55
relative $\sigma$	4.0	1.4	0.8	0.3	2.8	0.8	3.6	1.0	0.5
given	2.2	7.2	13.5	49.9	0.5	11.4	2.7	11.6	
absolute error	0.17	0.33	0.71	-2.28	0.02	0.21	-0.11	0.14	
relative error	7.77	4.50	5.28	4.57	3.85	1.80	4.12	1.16	

**Table 22.** SEM-EDS results (wt%) for the basalt standard (BHVO-2), normalised; nd – not detected;  $\sigma$  – standard deviation; given – certified content in the standard; relative  $\sigma$ :  $\frac{\sigma}{\text{average}} \times 100\%$ ; absolute error: *given minus average*; relative error:  $\frac{\text{absolute error}}{\text{given}} \times 100\%$ .

Considering all the parameters, the result presented in the dissertation may be considered as quantitative. All major and minor elements were measured with quite good accuracy allowing for comparison between the samples. However, differences of less than 0.5-1% and in the case of silica below 3% must be handled carefully.



## **Types of analyses**

Basically, two kinds of chemical analysis were carried out with the SEM-EDS: analysis of single phases and bulk analysis. In both cases some difficulties were encountered and the most suitable solutions were tried to be established. All of them are described below.

### **Bulk analysis**

Bulk analysis was conducted on each type of material by scanning with a beam a selected area of a sample. This method entails several problems. First of all, the SEM-EDS electronics are set up for analysis of a single homogeneous phase. Therefore, when several different phases, such as for instance oxides and metallic prills, are analysed at the same time some slide in accuracy must be taken into consideration. Another concerns were a quite small area which can be scanned each time, limited by the size of area possible to be encompassed in an image and the problems with the geometry of the beam-sample-detector system, and an associated question about the representativeness of the results. On the other hand, however, the opportunity to see what is actually analysed allows assessing each analysis separately and explaining any deviation which possibly occurs. In order to balance the positives and negatives, a strategy for bulk analyses was adopted where the possibly largest, but no bigger than c.  $1\text{mm}^2$ , area is analysed which includes all main phases recognised in a sample and excludes, if possible, large voids and clearly corroded regions. As a result areas of varied size from  $200\text{ }\mu\text{m}$  to  $1\text{ mm}$  across were analysed what, however, is not considered as a drawback. Each sample was analysed at least 3 times and the bulk composition used in the studies is a mean of all scans.

### **Analysis of single phases**

SEM-EDS analysis of single phases with the use of spot mode or small scans was applied as a main method of their chemical and mineralogical identification. With the accelerating voltage of  $20\text{ keV}$ , the actual size of the area analysed falls in a range of  $2\text{-}6\text{ }\mu\text{m}$  in width and depth depending on the average density of sample (Pott 1992, 336-337). Therefore, it was assumed that the phase for which an analysis without contribution of the background may be securely conducted should be at least  $10\text{-}20\text{ }\mu\text{m}$  across. Since most of the phases occurring in the samples are much larger, measurements of their composition may be considered as fully qualitative.

In several cases, however, an attempt was made to recognise the composition of the phases smaller than  $10\text{-}20\text{ }\mu\text{m}$ . In this case only average composition may have been assumed by comparing the chemistry of the phase and its surroundings. This issue was recognised as quite inconvenient in the case of copper prills since the size of the majority of them does not extent  $20\text{ }\mu\text{m}$ . Furthermore, they occur in the iron-rich background so an artificial enrichment in this element was likely. Since the amount of iron in copper prills may be significant in an interpretation, the size of the prill analysed was always recorded considered.

### **Data processing**

As may be easily seen in the tables through the dissertation, the totals of both bulk and single spot analyses are widely varied. There are several reason for that. First of all, the electron beam was diagnosed as quite unstable, what was especially true in the case of the measurements done during the first several sessions. It means that the beam of wide-ranging current streaked the samples generating a varied amount of X-rays. Regarding the low totals for the crucible fabric, they usually result from its high porosity. In the case of both, varied

current and high porosity, normalisation to 100% has been considered as a good solution what was confirmed when results obtained for the standard and artefacts with high and low totals after normalisation were compared (Table 22)

The only situation when normalisation was not applied was when the presence of missing elements were suspected. That was the case when malachite samples were analysed giving consistent totals of c. 87% and during the examination of carbonate phases probably associated with weathering.

Since the EDS system is generally considered as incapable to measure oxygen accurately, the amount of this element was calculated by stoichiometry. In most cases the INCA analysis software was used to calculate oxides by stoichiometry. The software was set up to calculate iron as occurring exclusively in the form of FeO what is obviously a simplification and may cause some minor fluctuation in totals. There were, however several situations where stoichiometry was not used, at least not automatically, or other oxides were calculated. Regarding copper oxide minerals, the results were firstly assessed in a raw format, where copper and oxygen were measured by element. The ratio of these two elements was compared and possibility of the existence of some missing (C, H) elements was considered. Similar procedure was followed in the case of the phases with ion configuration not matching the general rule accepted for stoichiometry calculation.

## OPTICAL MICROSCOPY

### Reflected light microscopy

Before carbon coating the polished blocks were examined under polarised reflected light using a metallurgical microscope Olympus BX60. The examination was carried out in order to initially characterise the microstructure and types of phases in the slag samples as well as to orient the further studies with the SEM-EDS. The images made under the reflected light microscope and included in the dissertation are called in the captions *Reflected light micrographs*.

Unfortunately, none of the samples was etched. The etching may have been very useful in the case on the copper ingot to reveal the features of its microstructure and allow the studies on the techniques used in its manufacture (grain size). It is strongly recommended in the future. The etching of the crucible fabrics may also be used for better understanding of the composition of fine-grained fraction under the SEM-EDS.

### Transmitted light microscopy

The ceramic petrography was applied to examine several crucible and pottery samples. Cross-sections of the samples were fixed to a glass slide and abraded to a standard thickness of 0.03 mm. Thin sections were examined under a Leica polarizing microscope at magnification up to 200x. The images taken under the petrographic microscope are referred to as *Optical micrographs* in the captions.

The technique was applied to check if any of the features of the crucible fabrics was not overlooked in the examination with the SEM-EDS. In the case of the domestic pottery samples it was aimed to recognise their general character and similarity to the clay used in the manufacture of crucibles as well as to assess if further studies with SEM-EDS may be useful.

## Appendix 2: analyses of non-technical ceramics

Three non-technical ceramic pieces from PB were analysed with the petrographic microscope to make the comparison with the crucible fabrics possible. Two of them were also analysed for their chemical composition with the SEM-EDS.

None of the sherds analysed show any evidence of the use in the high-temperature process. On the contrary, the clay matrix of all of them is optically active showing a considerable degree of birefringence (Fig. 76). It indicates the low temperature of firing. The temperature at which most of the clay minerals starts to break down is usually estimated around 800-900°C (Rice, 90; Reedy, 186). It is commensurate with the general impression of advanced brittleness of the pottery, experienced intensively during the sample preparation.

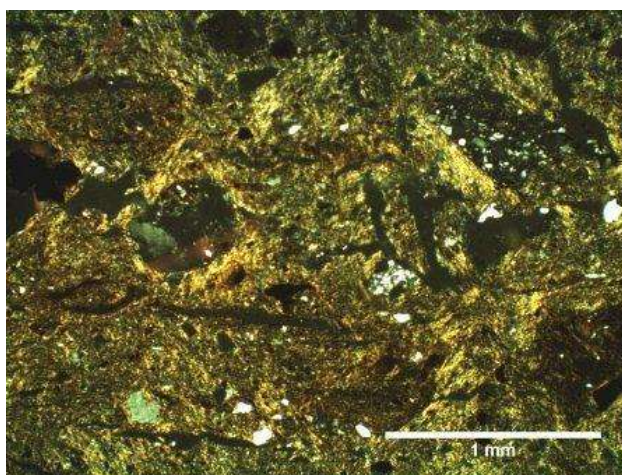


Fig. 76. Optical micrograph in XP showing the fabric of PB-18. Note optical activity of the clay matrix.

Two samples have a similar redox gradient: thin light red oxidised surface layers and black core resulted from charring of organic matter present in the fabrics. The sample PB-20 is greyish.

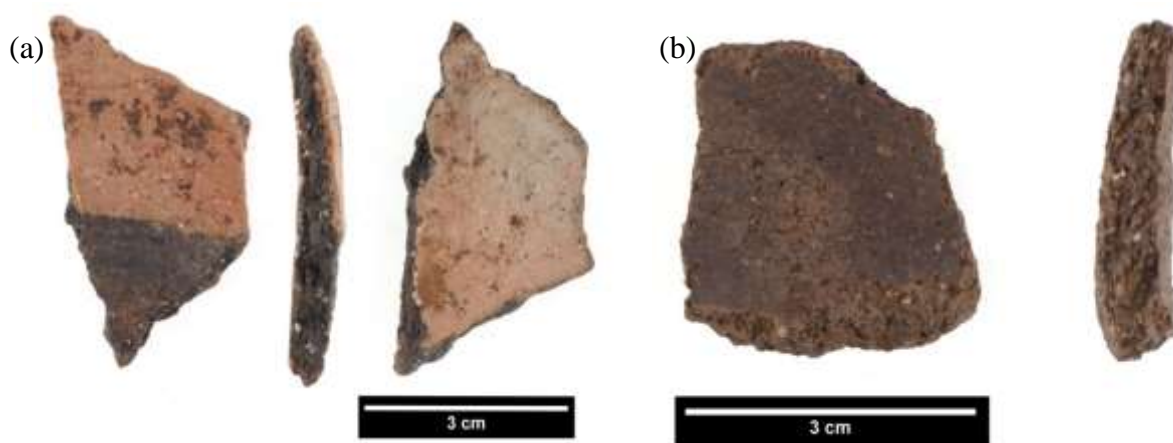


Fig. 77. Domestic pottery from Peun Baolo: (a) PB-18; (b) PB-20.



Fig. 78. Domestic pottery from Peun Baolo: PB-19.

The samples are characterised by different types of predominant inclusions. The sample PB-19 is tempered with a large quantity of rice husk charred in place (Fig. 79b) what suggests reducing conditions of firing (Reedy, 186, fig. 8.3.4.), also inferred from its black soft core. It contains also abundant fine quartz evenly distributed through the paste (Fig. 79a).

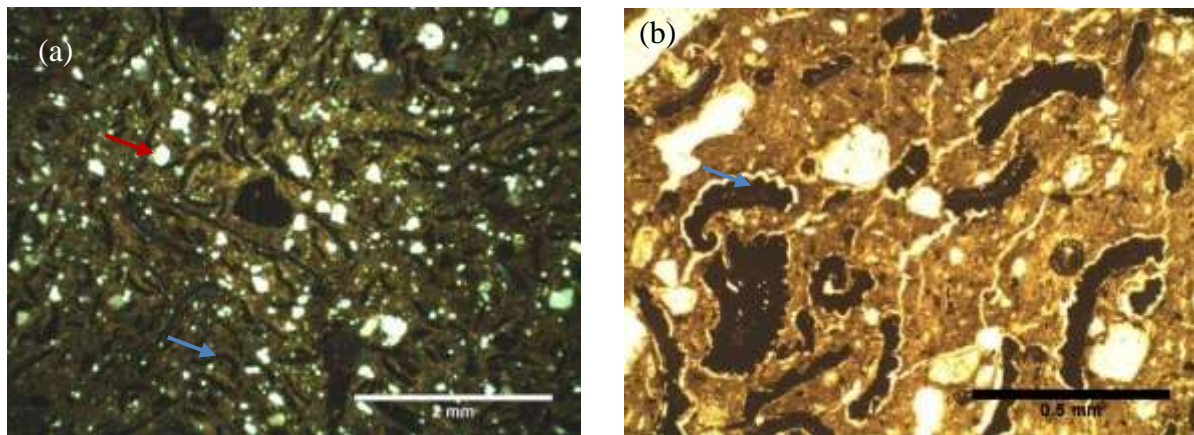


Fig. 79. Optical micrographs showing the sample PB-19: (a) bright fine quartz grains (red arrow) and abundant rice husk temper (blue arrow), XP; (b) details of rice husk temper charred in place, PPL.

The characteristic feature of the sample PB-20 is lithic inclusion occurring as large up to 2 mm grains. It consists of angular to sub-angular fragments of acidic igneous rock (granite) which exhibits evidence of advanced weathering. It does not contain any rice husk.

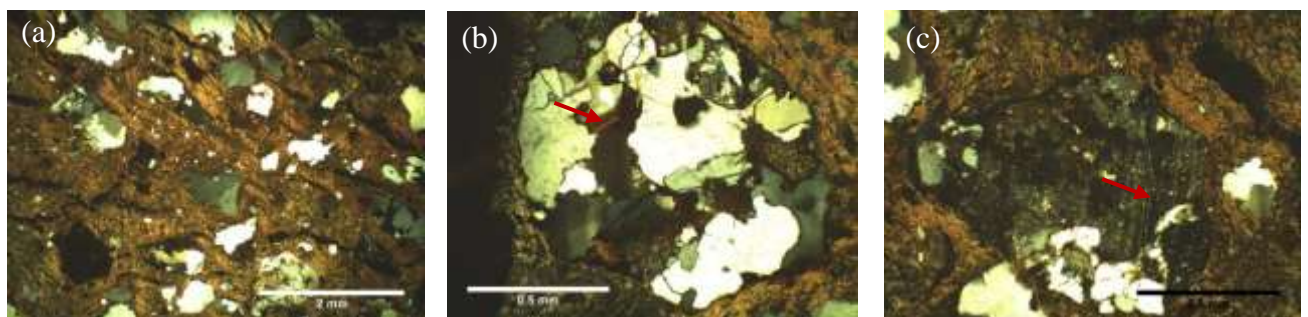


Fig. 80. Optical micrographs in XP showing fabric of the sample PB-20: (a) abundant lithic inclusion in fine optically active clay matrix; (b) granite rock fragment containing mainly potassium feldspar, quartz and biotite mica (arrow); (c) partially weathered rock fragment, on the right side of the grain residual plagioclase feldspar showing multiple twinning (arrow); the untwined alkali feldspar crystals are much more common in the rock fragments and their recognition was confirmed by SEM-EDS analysis.



The fabric of the sample PB-18 is very fine and contain only few microscopically visibly inclusions (Fig. 76). They are tentatively recognised by the author, on a basis of the comparison with the crucible fabric, as a grog inclusion made of finely crushed crucibles. It seems to be indicated by the similar microstructure of the pallets: fine abundant quartz in optically inactive glassy matrix (Fig. 81a-b). Probably a piece of slag was also recognised (Fig. 81c).

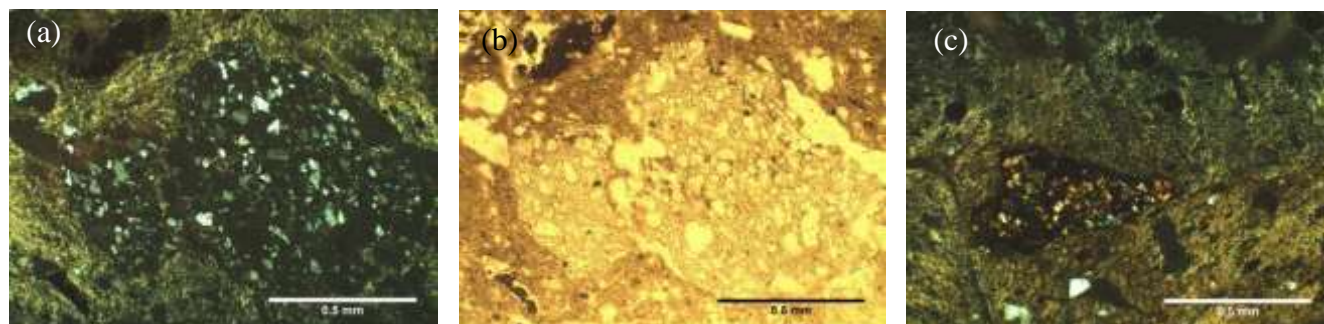


Fig. 81. Optical micrographs of the sample PB-18: (a) grain of grog inclusion, note dark inactive optically matrix in which fine abundant quartz grains are embedded in XP; (b) grain of grog inclusion in PPL; note the glassy matrix; (c) slag inclusion (?) in XP; minute olivine crystals (?) embedded in opaque probably iron-rich matrix.

The chemical composition of two samples analysed with the SEM-EDS is quite similar. They both represent a siliceous quite rich in alumina fabrics containing low amounts of oxides of alkali and alkaline earth metals. Detection of copper oxide in both samples indicates the corrosion of the sherds, visible also in other types of artefacts analysed during the project.

The sample PB-20 contains more iron oxide, which occurs as nodules. The higher amount of potassium results from the high content of potassium feldspar.

	Na <sub>2</sub> O	MgO	Al <sub>2</sub> O <sub>3</sub>	SiO <sub>2</sub>	P <sub>2</sub> O <sub>5</sub>	K <sub>2</sub> O	CaO	TiO <sub>2</sub>	FeO	CuO	total
<b>Clay matrix</b>											
PB-19 (n=2)	0.1	nd	29.9	63.1	1.3	0.8	0.1	1.0	2.6	1.0	79.5
σ	0.23	0.00	6.09	7.39	0.68	0.38	0.25	0.13	0.42	0.35	8.72
PB-20	nd	0.8	34.6	50.2	nd	1.9	0.5	2.8	6.2	3.1	94.6
σ	nd	0.10	0.99	2.30	0.00	0.38	0.04	0.69	1.53	0.02	4.21
<b>Bulk</b>											
PB-19 (n=2)	nd	nd	23.2	71.0	nd	0.6	nd	1.2	2.9	1.1	67.9
σ	nd	nd	0.8	1.5	nd	0.1	nd	0.1	0.1	0.5	7.3
PB-20	nd	nd	25.6	65.7	nd	1.4	nd	1.1	5.0	1.2	74.7

Table 23. Bulk and clay matrix compositions of domestic pottery samples, SEM-EDS results (wt%), normalised.

### Appendix 3: crystalline and non-crystalline phases within the crucible slag

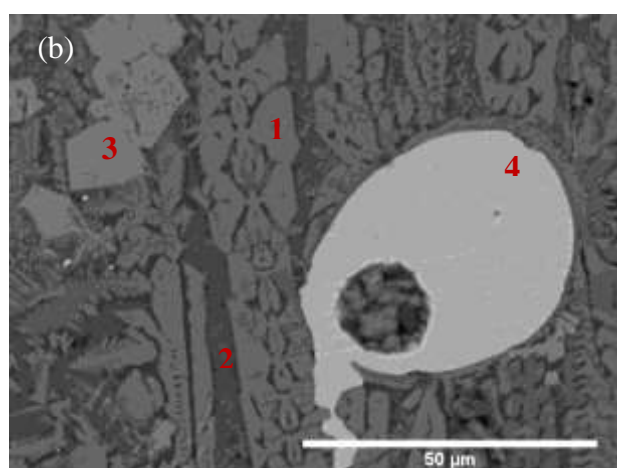
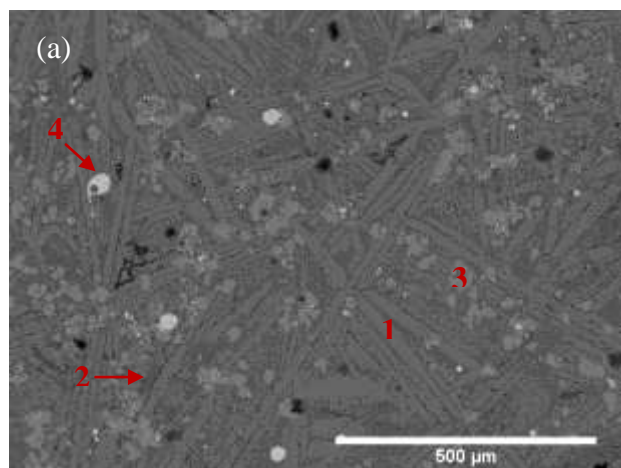
#### 1. Olivine

Crystals of olivine are the main phase in the first type of slag distinguished above. They were recognised in most of the samples examined. The composition of olivine crystals is basically of fayalite ( $\text{Fe}_2\text{SiO}_4$ ) with a minor substitution of  $\text{Mg}^{2+}$ ,  $\text{Mn}^{2+}$ ,  $\text{Ca}^{2+}$  and  $\text{Zn}^{2+}$  for bivalent iron (Table 24). The enhanced concentration of magnesia determined in the bulk analyses of TNN-13 is well reflected in the composition of olivine in this sample.

Sample	MgO	Al <sub>2</sub> O <sub>3</sub>	SiO <sub>2</sub>	K <sub>2</sub> O	CaO	MnO	FeO	ZnO	Total	Near formula
PB-17a	0.9	nd	30.3	nd	nd	nd	68.8	nd	96.3	$\text{Fe}_{1.95}\text{Mg}_{0.05}\text{SiO}_4$
PB-13	1.1	2.03	33.5	0.3	0.4	2.5	60.1	nd	101.7	$\text{Fe}_{1.84}\text{Mn}_{0.08}\text{Mg}_{0.06}\text{Ca}_{0.02}\text{SiO}_4$
PB-3	nd	nd	30.6	nd	nd	0.6	68.9	nd	103.7	$\text{Fe}_{1.98}\text{Mn}_{0.02}\text{SiO}_4$
PB-16	2.5	nd	30.7	nd	nd	2.3	63.1	1.4	103.3	$\text{Fe}_{1.77}\text{Mg}_{0.13}\text{Mn}_{0.07}\text{Zn}_{0.04}\text{SiO}_4$
TNN-13	7.1	nd	32.3	nd	nd	0.6	60.1	nd	105.0	$\text{Fe}_{1.64}\text{Mg}_{0.34}\text{Mn}_{0.02}\text{SiO}_4$

Table 24. Composition of olivine crystals in particular samples, SEM-EDS results (wt.%), normalised. The amount of bivalent ions in the olivine formula is normalised to 2. Results for PB-13 may be contaminated with the background since a very small crystal was analysed (a branch below  $5\mu\text{m}$ ); this explains detection of alumina and potash present in the adjacent glassy matrix. Very fine (below  $10\mu\text{m}$ ) crystals of olivine were also recognised in the sample PB-5 and TNN-2b; however no chemical analysis was done for them.

Olivine crystals occur most commonly in the shapes associated with fast cooling rate: feather and lattice olivine with dendrite fibres below  $10\mu\text{m}$  (Fig. 82c-d) and fine elongate skeletons (chain olivine) up to  $1\text{mm}$  long (Fig. 82); terminology from Donaldson (1976). Chain olivine crystals are usually randomly oriented and tightly packed. A fine-grained dendritic mesh (lattice and feather olivine) occupies thoroughly the space between larger olivine grains.





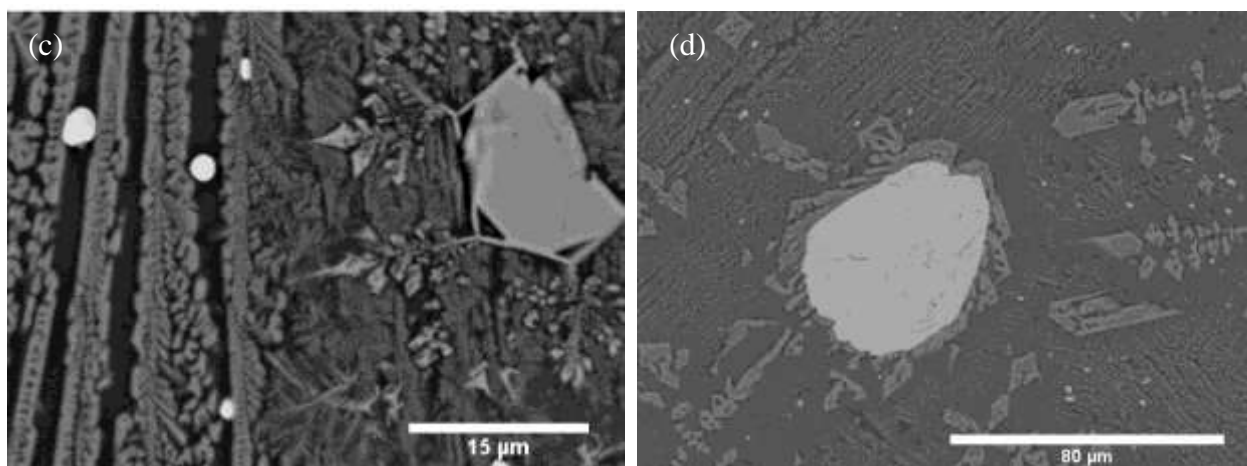


Fig. 82. Olivine crystals in the crucible slag. Backscattered electron images of: (a) sample PB-3: randomly oriented chain olivine crystals (1) in a glassy matrix (2, dark grey) with spinel crystals (3, light grey) and sulphidic prills (4, bright); dark spots are corrosion products developing in the glassy matrix; (b) PB-3: fragment of chain olivine internally skeletal (1), fine feather olivine crystals in the left lower corner, equant spinel crystals in the left upper corner (3); glassy matrix (2) and oval sulphidic prill (4). (c) PB-5: chain olivine crystals on the left and fine-grained feather olivine crystals on the right, small sulphidic prills between the crystals, partly-reacted residual (?) iron oxide with dendritic branches, interstitial glass. (d) PB-2b: matrix almost completely infilled with fine lattice olivine crystals, sulphidic prills in the centre surrounded by spinel crystals visible also on the left.

In two samples, PB-17a and TNN-13, blocky olivine crystals were noticed resembling Donaldson's hooper olivine type (prismatic, some with well-formed faces, usually internally skeletal) which crystallised at slightly slower cooling rate (Fig. 83). The particular forms of olivine crystals coexist often within one type of slag reflecting its varied history of crystallisation.

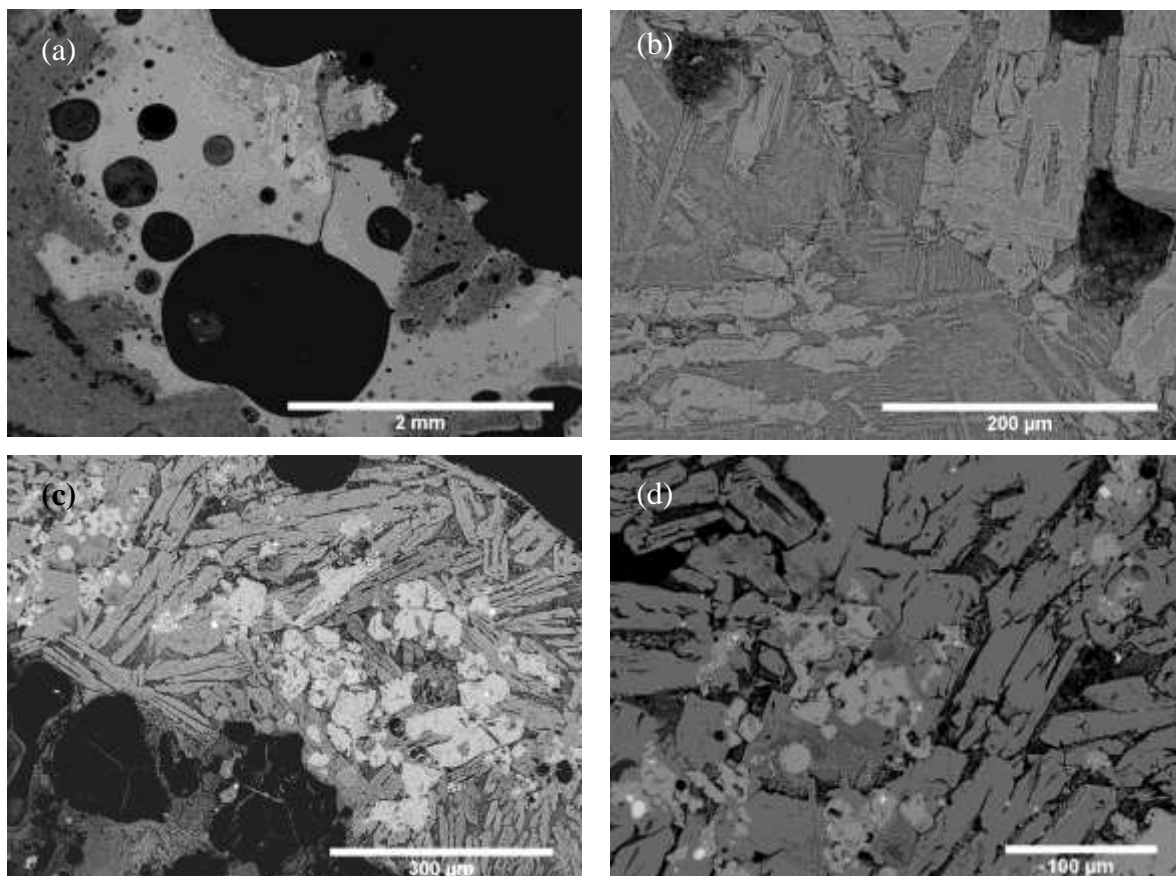


Fig. 83. Backscattered electron images of blocky olivine in the crucible slag: (a-b)TNN-13: small slag residue in the inner surface; fayalite crystals are whitish closest to the edge; (c-d): PB-17a: thin layer of slag on the inner surface, hooper fayalite (light grey), cluster of spinel crystals (whitish)

## 2. Iron oxide

Iron oxide occurs in the crucible slag primarily in the form of magnetite what is determined on a basis of the type of impurities detected in this phase, Mg, Mn, Zn, Ti, Al, Cr which are common substitutes for iron in minerals of a spinel group, as well as of the shape of the crystals (euhedral) (Ineson, 1989, pp. 121–122). The optical properties exhibiting by the crystals under the reflected light microscope, grey colour with brownish tint and moderately low reflectance, also seem to confirm this identification and clearly differentiate this phase from haematite (no bluish like in PB-38, higher reflectance) (Nesse, 2004, p. 305,308; Wells, 1954) (Fig. 84).

Sample	Description	FeO	Al <sub>2</sub> O <sub>3</sub>	TiO <sub>2</sub>	MgO	MnO	CuO	ZnO	Cr <sub>2</sub> O <sub>3</sub>	SiO <sub>2</sub>	K <sub>2</sub> O	total
PB-3	equant crystals within fayalitic slag	94.7	4.3	1.1	nd	nd	nd	nd	nd	nd	nd	95.2
PB-5	cluster of globular crystals within glassy slag	90.3	5.1	0.3	0.9	1.2	0.9	nd	nd	1.3	nd	90.7
PB-5	minute crystals in glassy slag	78.3	8.0	1.1	0.9	0.8	1.5	nd	nd	9.1	0.3	100.2
PB-5	in fayalitic slag	91.9	6.5	0.5	0.6	0.6	nd	nd	nd	nd	nd	94.2
PB-13	in fayalitic slag	95.5	3.9	nd	nd	0.7	nd	nd	nd	nd	nd	91
PB-13	abundant equant crystals in glassy slag	89.2	2.8	nd	1.4	1.9	4.7	nd	nd	nd	nd	91.8
PB-16	equant crystals in fayalitic slag	92.2	4.7	0.5	0.8	0.7	nd	1.11	nd	nd	nd	91.9
PB-17	equant crystals in fayalitic slag	97.2	2.8	nd	nd	nd	nd	nd	nd	nd	nd	97.6
TNN-2b	minute crystals in glassy slag	35.6	47.1	0.5	2.1	2	nd	3.2	2.4	6.4	0.7	75.6
TNN-2b	dendrites in fayalitic slag	84.5	8.8	1.2	nd	3.7	nd	nd	nd	1.7	nd	89

Table 25. Composition of spinel crystals in the crucible slag, SM-EDS results (wt%), normalised.

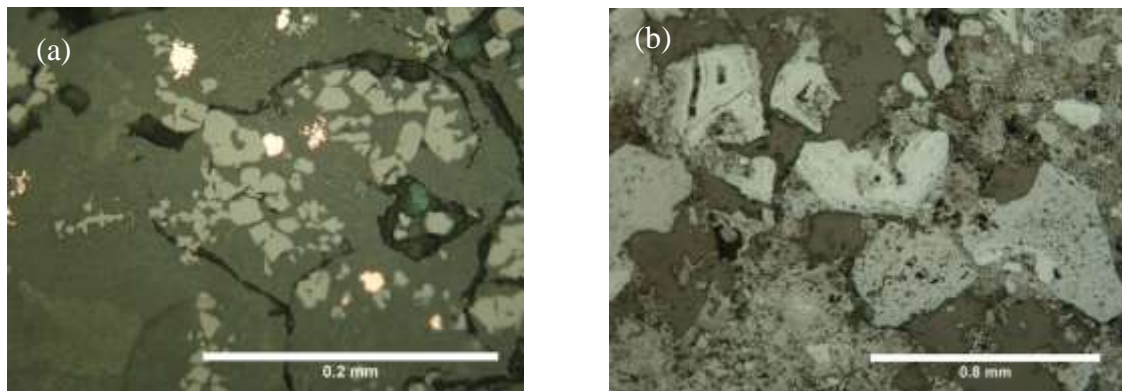


Fig. 84. Optical micrographs (RLM) of: (a) the crucible slag PB-5, magnetite crystals in the centre (light grey), note they brownish tint and lower reflectance in comparison to hematite in (b) PB-38, mineral aggregates containing mostly trivalent iron oxides, light grey with bluish tint crystals are probably hematite.

Magnetite was recognised in both types of well-reacted slag. In fayalitic slag it usually occurs as equant up to 0.1mm across grains unequally distributed within the slag (Fig. 85). The finest magnetite often forms dendritic structure. The angular shape of particular crystals within the branches of dendrites (Fig. 82c) differs from the globular form often reported for dendritic wüstite (Sharp & Mittwede, 2012). The form of crystals, is not, however, a parameter which clearly differentiates the two phases since they both may occur in nearly identical shape (Wells, 1954, p. 716). Magnetite is the second, after olivine, most abundant phase in fayalitic crucible slag.

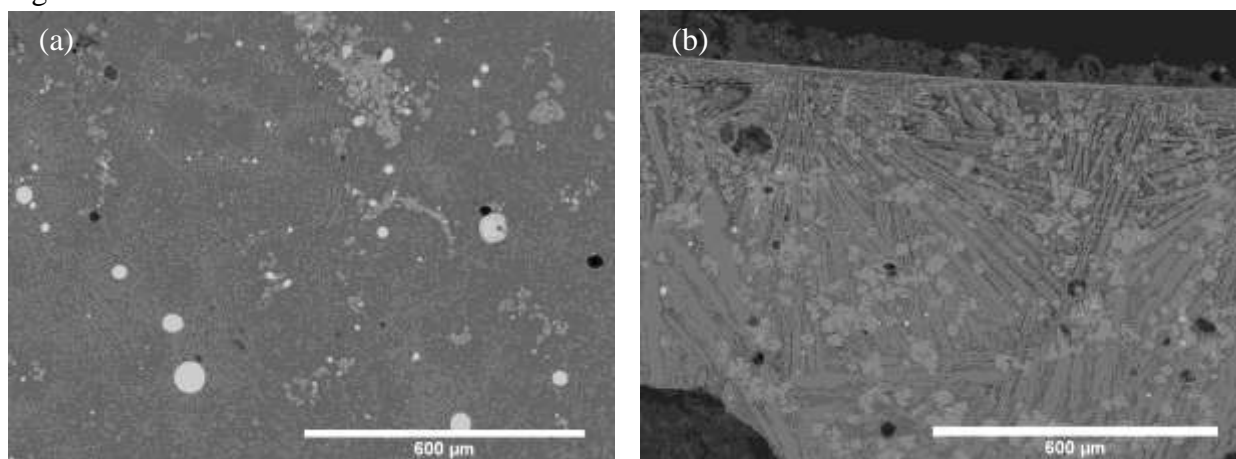


Fig. 85. Backscattered electron images showing magnetite spinel in the crucible slag: (a) PB-13: clusters of magnetite (light grey) in fine-grained fayalitic slag (dark grey); (b) PB-16: abundant magnetite phase (light grey crystals) in the slag of fayalite type.

In glassy slag magnetite is usually the only distinguishable crystallographic phase (PB-3 image). In the sample PB-13 it is particularly abundant (Fig. 86).

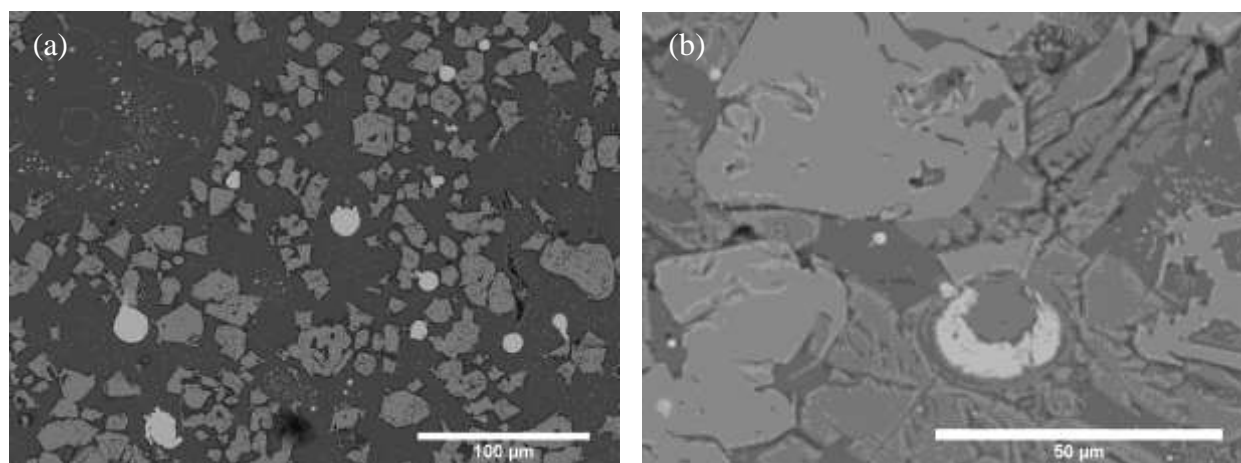


Fig. 86. Backscattered electron images of magnetite crystals in: (a) PB-13 within the glassy slag, (b) PB-16 within the fayalite slag. In these two sample magnetite occurs most abundantly.

In the sample TNN-2b alongside magnetite occurring in the fayalitic slag, very fine hercynite crystals were recognised within the glassy phase (Fig. 87). It is commensurate with the higher amount of alumina detected in this sample. Basically, composition of spinel crystals in fayalitic slag is usually closer to the ideal formula of magnetite than in the case of the grains embedded in the glassy slag what is consistent with the fact that the latter is depleted in iron.

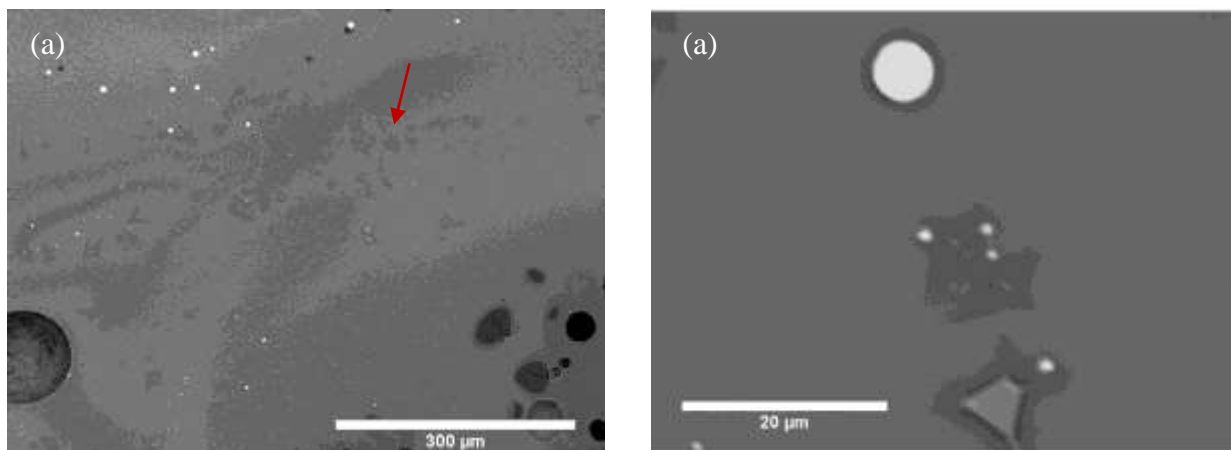


Fig. 87. Backscattered electron images of the crucible slag in the sample TNN-2b: (a) minute hercynite crystals in a glassy matrix; (b) hercynite crystals in the lower part of the image (light grey) and copper prills (white).

### 3. Metallic and sulphidic phases

In nearly all samples examined (excepting TNN-13) metallic or sulphidic phase were recognised. They occur as minute (5-80μm) perfectly circular or less regular oval globules trapped inside the crystal structure of fayalitic slag or embedded in the matrix of glassy slag. The large prills (above 30μm) are limited to fayalitic slag.

In most of the samples both copper and sulphidic (matte) prills were recognised. They usually are closely associated with each other. Copper prills occur inside the matte prills or are rimmed with thin, often irregular sulphidic edge (Fig. 88a-b). In a few samples, PB-3, PB-16 and PB-17a, where only sulphidic prills were detected, copper prills may have corroded (Fig. 88c-d). In two samples, PB-5 and PB-15 only copper prills were recognised.

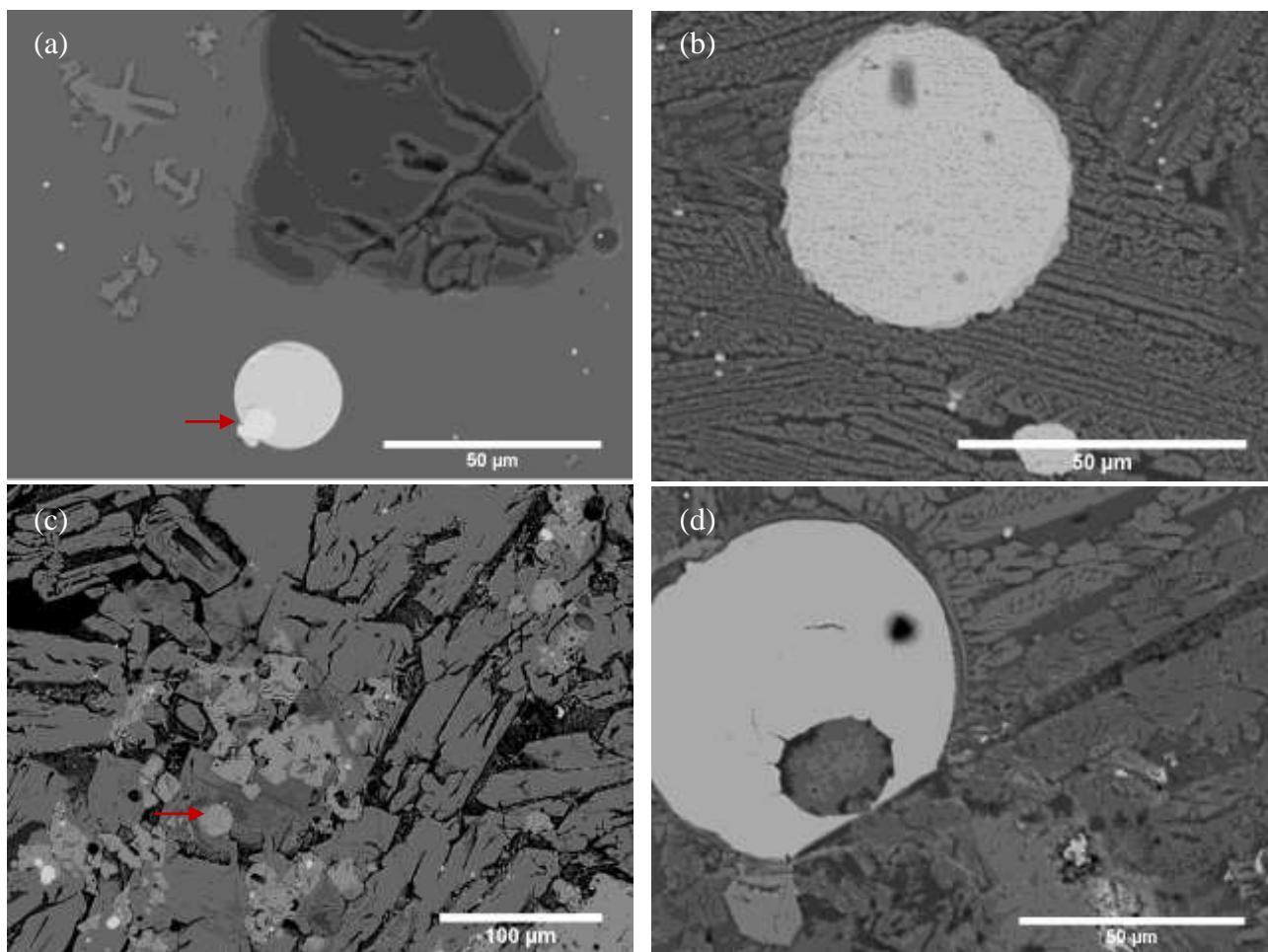


Fig. 88. Backscattered electron images of metallic copper and matte in the crucible slag: (a) sample TNN-2b minute copper prill in a copper sulphide globule; (b) PB-13 copper prill with sulphidic edge; (c) PB-17a: possibly a corroded copper prill (pointed by arrow), bright spots are sulphides; (d) PB-3: a sulphide globule with a hole filled with corrosion product (copper-iron oxide composition) possibly left by a leached away copper prill.

Basically, copper prills contain a high, however quite varied, amount of iron. The content of iron falls in a range 0.3-5% with a mean value of 2.3%. The lowest level of iron was detected in the copper prills within a small vitrified area on the exterior of the sample PB-15 (Fig. 89a). The highest measurements of iron (4-5%) are shown by the smallest prills (below 10μm). It may be related to the problem, observed also by other authors (Georgakopoulou et al., 2011, p. 133), of the simultaneous excitation of the iron-rich background during the spot analysis of minute prills. The correlation between size of the prills and amount of iron is evident (Fig. 90a). It is not, however, clear if it results exclusively from the analytical issue or also from the fact that smaller prills have larger surface area and tend to absorb iron more readily when it is present in the surrounding during their formation. The measurements of iron in the copper prills 20μm or bigger in diameter, constituting usually 1-2%, seem to be reliable (see Appendix 1).



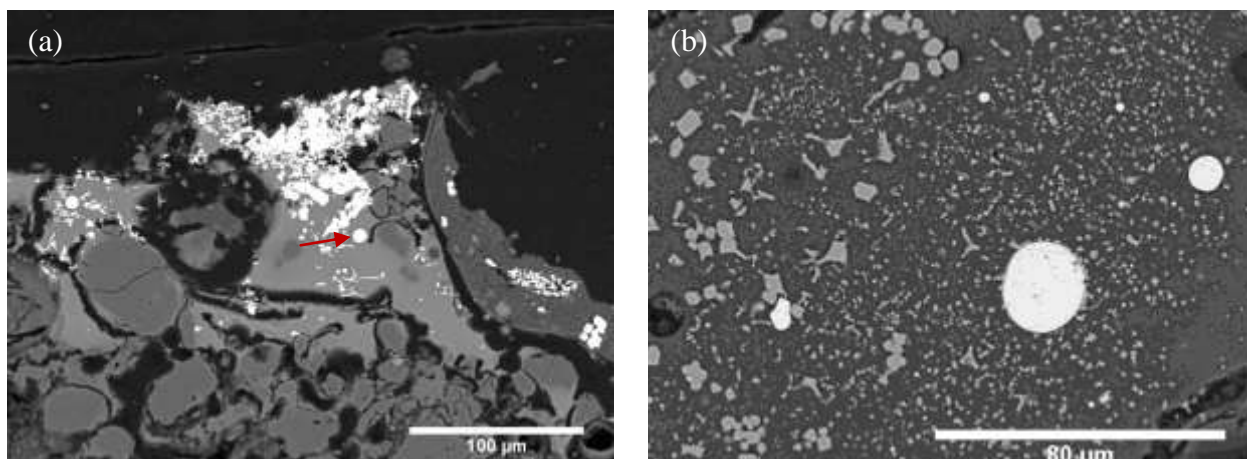


Fig. 89. Backscattered electron image of: (a) sample PB-15 with a low-iron prill pointed with an arrow; (b) PB-5 copper prills in the glassy slag: larger surrounded by iron oxide containing 1.6% of iron (1); smaller with 2.8% of iron detected.

All sulphide prills recognised in the samples are copper-iron sulphides containing 73% of copper on average, 21% of sulphur and several per cent of iron. The content of iron covers a wide range between 1 and 10%. The correlation between iron amount and size of prill is here even more apparent than in the case of copper prills. The largest globules have composition close to chalcocite containing just 1-2% of iron.

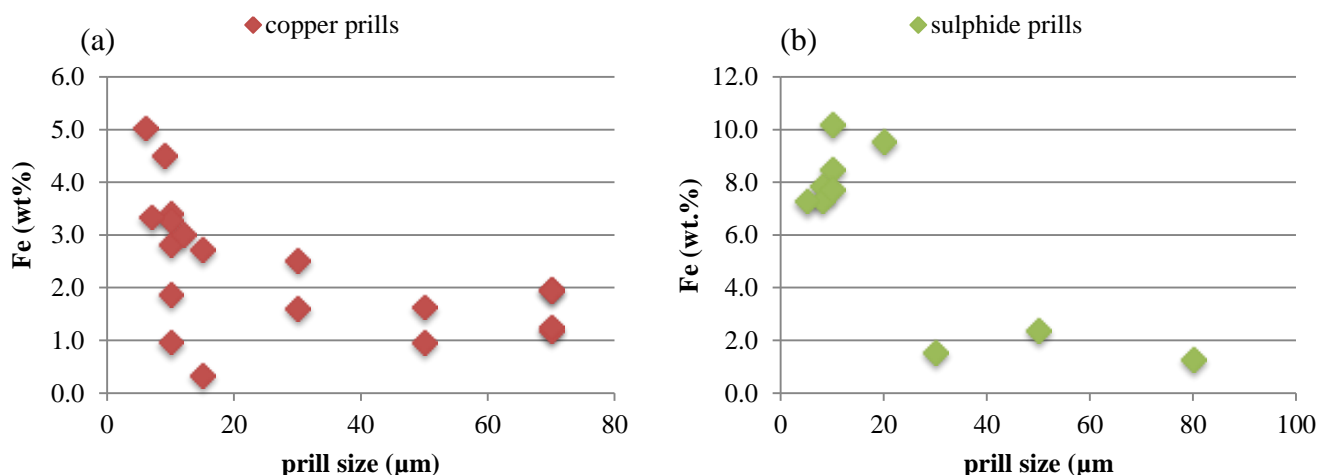


Fig. 90. Scatter plot showing the relation between size of copper and sulphidic globules and their iron contents. Note that the highest determinations are associated with the smallest prills.

	prill size (μm)	Cu	S	Fe	O	total
<b>Copper prills</b>						
max	70	99	19.9	5	2	107.7
min	6	94.9	0	0.3	0	78.7
average	29.2	97.2	0	2.3	0.4	99.1
<b>Sulphide prills</b>						
max	80	78.7	23.9	10.2	2	109.5
min	5	66.6	15.9	1.3	0	98.2
average	23.1	72.7	20.7	5.9	0.2	104.2

Table 26. Average copper and sulphide prill composition in the crucible slag; full results in Table 27.



Table 27. Composition of metallic and matte phases in the crucible slag samples, SEM-EDS results (wt%), normalised; n - number of analyses included in the average;  $\sigma$  – standard deviation.

	Phase	Size	Type of slag	Cu	S	Fe	O	Si	total
TNN-2b									
mean (n=6)	circular and oval copper prills	10-70	fayalitic and glassy	97.7	nd	1.9	0.3	nd	92.0
σ				0.8	nd	0.8	0.4	nd	8.1
single analysis	circular sulphide prill with copper prill inside	30	glassy	78.7	19.7	1.6	nd	nd	104.8
TNN-9									
single analysis	circular copper prill with sulphide rim	15	glassy with minute crystals	96.4	nd	2.7	0.9	nd	107.7
single analysis	sulphide rim			74.0	19.9	3.3	2.0	0.7	106.6
PB-3									
single analysis	circular sulphide prill	20	glassy	66.6	23.9	9.6	nd	nd	103.9
single analysis	circular sulphide prill	80	fayalitic	77.6	21.1	1.3	nd	nd	104.9
PB-5									
mean (n=2)	small circular copper prills	6-9	fayalitic	94.9	0.1	4.8	0.2	0.0	105.6
σ				0.1	0.1	0.4	0.3	0.0	0.6
single analysis	larger circular copper prill	30	fayalitic	97.2	0.3	2.5	nd	nd	103.0
mean (n=2)	small circular copper prills	10	glassy	95.9	nd	3.1	0.7	0.2	102.7
σ				0.1	nd	0.4	0.2	0.2	0.4
single analysis	larger circular copper prill	30	glassy	97.9	nd	1.6	0.5	nd	104.1
PB-13									
mean (n=2)	larger circular copper prill	50	fayalitic	98.3	nd	1.3	0.4	nd	99.5
σ				0.1	nd	0.5	0.5	nd	0.6
single analysis	sulphide rim			76.8	19.4	3.8	0.0	nd	101.3
single analysis	small sulphide prill	5	fayalitic	70.9	15.9	7.3	0.8	0.3	102.9
single analysis	small circular copper prill	10		96.0	nd	3.3	0.7	nd	103.9
single analysis	small circular copper prill	12	glassy	97.0	nd	3.0	nd	nd	100.0
PB-15									
mean (n=2)	copper prills	10-15	glassy	98.7	nd	0.7	0.6	nd	98.7
σ				0.4	nd	0.4	nd	nd	1.6
PB-16									
single analysis	sulphide prill	50	fayalitic	76.7	20.9	2.4	nd	nd	101.9
PB-17a									
mean (n=6)	sulphide prills	8-10	fayalitic	70.7	21.3	7.9	nd	nd	104.8
σ				2.4	0.8	1.6	nd	nd	5.2

#### 4. Glassy matrix

As already mentioned, the occurrence and abundance of the non-crystalline phase in crucible slag is varied. In fayalitic slag it forms a sparse phase which froze at the very end of the slag formation process filling the spaces between fayalite and spinel crystals. The structure of fayalitic slag is usually tightly packed with crystals leaving little space for interstitial glass. At higher magnification in some places within the glass matrix minute, secondary, i.e. crystallised after larger fayalite laths, poorly-formed crystals of fayalite are visible (Fig. 82b-c).

In the second type of well-reacted slag glass forms a main phase in which other constituents are embedded. This type of microstructure appears usually in the areas more closely associated with the crucible fabric. It often contains pieces of unreacted materials and coarse bloating pores (Fig. 91a-b). At high magnification in some parts of the glassy slag initial crystallisation is observed. In the sample TNN-9, characterised by the rich in  $\text{TiO}_2$  and  $\text{ZrO}_2$ -composition, a distinct segregated structure was noticed (Fig. 91c). Composition of the glassy slag is usually higher in silica. It also often contains more copper the most remarkable example of which is the glassy slag in the sample PB-13 which shows highly elevated content of  $\text{CuO}_2$  (glassy matrix-27%; bulk-15%) (Fig. 91d).

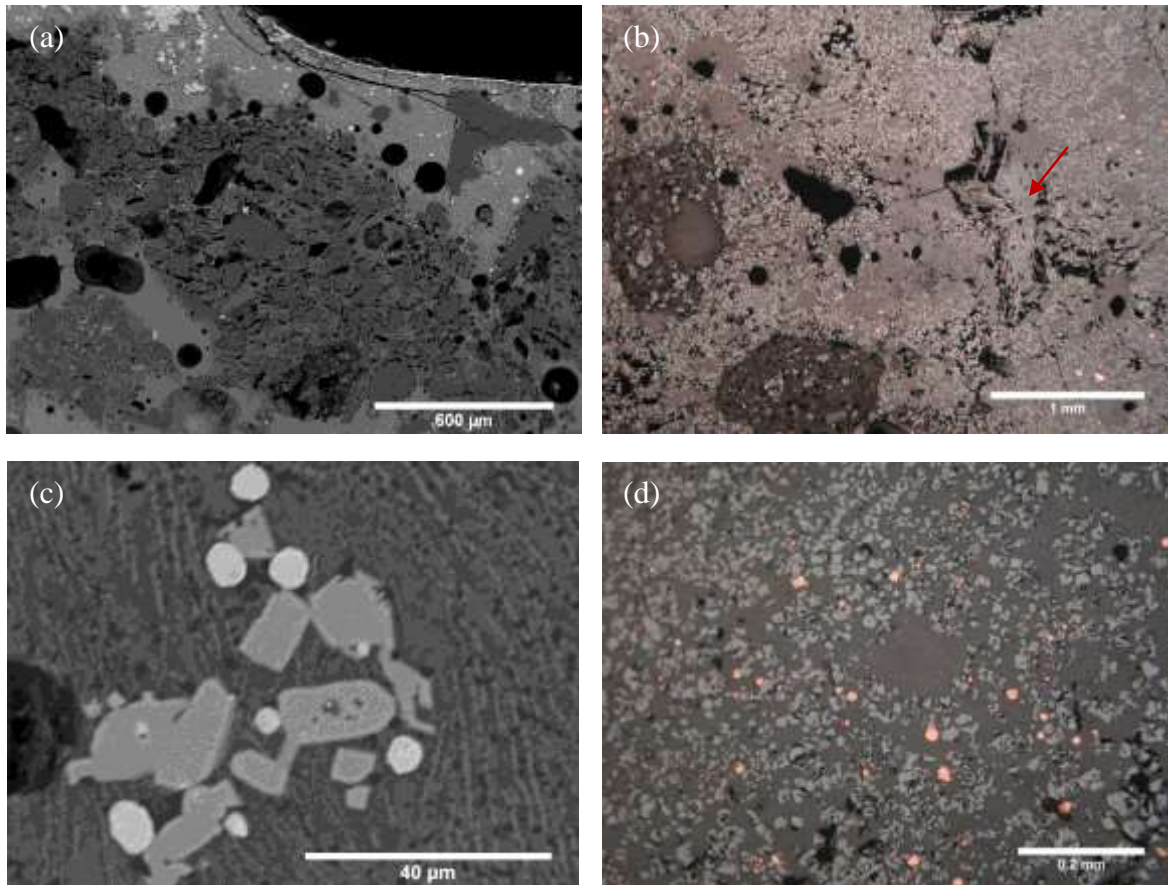


Fig. 91. (a) Backscattered electron images of the inner edge of the sample PB-5: copper and iron-rich glassy slag reacting heavily with the crucible fabric; (b) Reflected light micrograph of the sample PB-13: partially reacted quartz in the glassy slag with high content of copper (yellow prills), magnetite (light grey), probably small cluster of delafossite (arrow); (c) Backscattered electron images of the crucible slag TNN-9: cluster of zircon crystals (light grey) and sulphide prills within high-titanium matrix; (d) Reflected light micrograph of PB-13: note high amount of copper present as minute prill (yellow) and magnetite (light grey crystals).

In two samples, PB-13 and PB-3, two types of slag form distinctive layers, fayalitic slag on the top, glassy on the bottom adhering to the crucible walls.

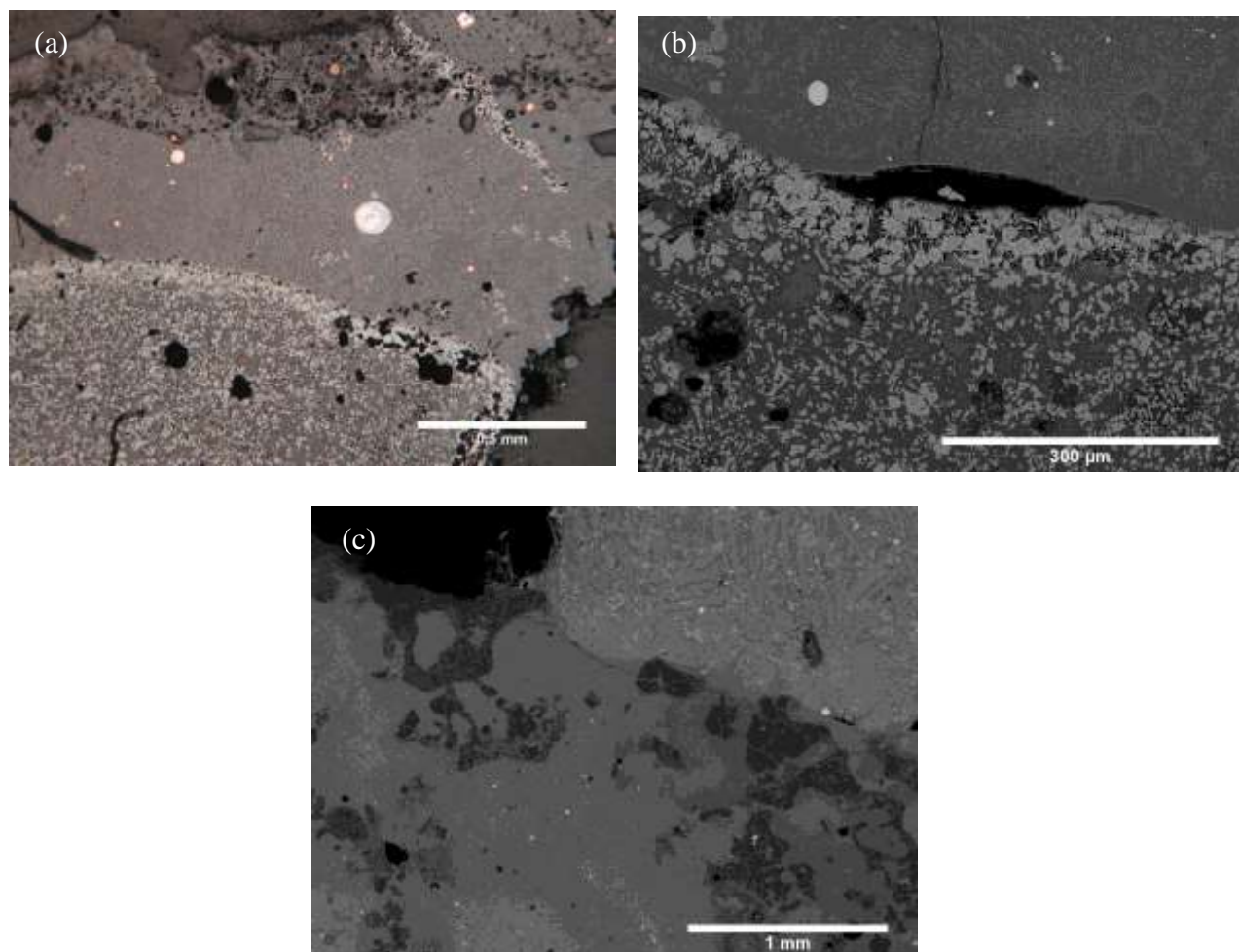


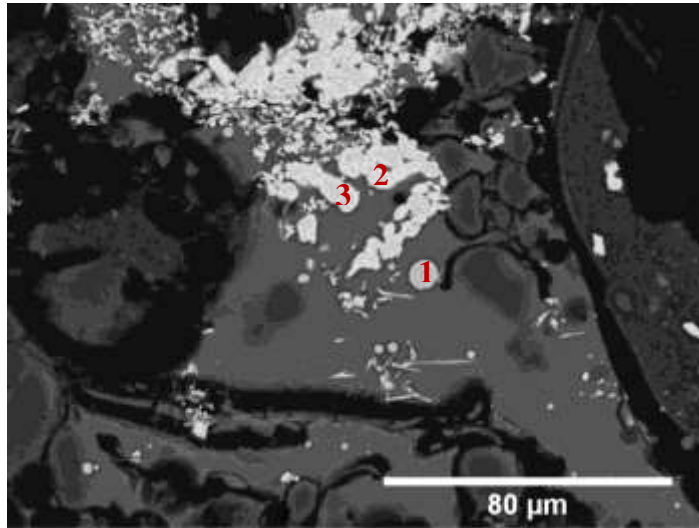
Fig. 92. Backscattered electron images showing layers of slag of different character within the same crucibles: (a) PB-13: upper fayalitic, lower glassy with magnetite as a major phase; (b) PB-13 border between slag layer at higher magnification, note concentration of magnetite and possibly acicular delafossite; (c) PB-3 glassy slag rich in partially unreacted quartz (dark grey) covered with slag of fayalite type.

Table 28. Composition of glassy matrix in the crucible samples, SEM-ES results, normalised, n - number of analyses included in the average.

Sample			MgO	Al <sub>2</sub> O <sub>3</sub>	SiO <sub>2</sub>	P <sub>2</sub> O <sub>5</sub>	SO <sub>3</sub>	K <sub>2</sub> O	CaO	TiO <sub>2</sub>	MnO	FeO	CuO	ZnO	PbO	SnO <sub>2</sub>	BaO	ZrO <sub>2</sub>	total
TNN-2b	glassy slag	mean (n=2)	0.9	18.5	49.4	0	0	3.2	0.3	1.1	2.8	23.1	0.6	0	0	0	0	0	85.6
TNN-9	minor crystals	mean (n=2)	0.6	8.7	50.2	0	0	1.7	1.2	6.5	0	28.1	0.6	0	0	0	0	2.5	106.8
TNN-13	glassy slag	mean (n=2)	0.3	16.8	53	0.9	0	2	1	0.6	0	24.2	0.3	0	0	0	0.9	0	98.1
PB-3	interstitial	single analysis	0	15.3	45.6	2.8	0	1.9	0.6	1.1	0	31.1	1.6	0	0	0	0	0	105
PB-3	minute crystals	mean (n=2)	0.4	6.6	40.9	0.6	0	1.1	0.6	0.6	0	49.2	0	0	0	0	0	0	103.7
PB-5	interstitial	mean (n=3)	1.2	7.2	41.5	0.4	0	0.9	0.7	0	1.7	46	0.3	0.2	0	0	0	0	103.1
PB-5	glassy slag	single analysis	1.1	9.2	56.7	0.5	0	1.7	1.1	0.4	1.4	23.1	4.8	0	0	0	0	0	97.5
PB-13	interstitial	single analysis	0	14.7	51	0	1	1.6	1.7	0.7	0.6	25.6	3.1	0	0	0	0	0	95.9
PB-13	glassy slag	mean (n=2)	0.9	7.6	49.5	0.4	0	1.2	1.5	0.2	1	11	26.6	0	0	0	0	0	100.9
PB-15	glassy slag	single analysis	1	10.6	61.8	0.6	0	4.2	1.6	0.5	0	8.3	7.4	0	0	4.1	0	0	103
PB-16	interstitial	mean (n=2)	0.3	12.2	48.2	1	0	2.5	6.5	0.2	1	24.8	0	1.4	2	0	0	0	102
TNN-17a	interstitial	mean (n=2)	0	13.3	35.3	0.6	1.7	2.8	2.9	1.2	0.2	42	0	0	0	0	0	0	107.7
all samples			max	1.2	18.5	61.8	2.8	1.7	4.2	6.5	2.8	49.2	26.6	1.4	2	4.1	0.9	2.5	107.7
			min	0	6.6	35.3	0	0	0.9	0.3	0	8.3	0	0	0	0	0	0	85.6
interstitial			max	1.2	15.3	51	2.8	1.7	2.8	6.5	1.2	1.7	46	3.1	1.4	2	0	0	107.7
			min	0	7.2	35.3	0	0	0.9	0.6	0	0	24.8	0	0	0	0	0	95.9
			mean	0.3	12.5	44.3	1	0.5	2	2.5	0.6	0.7	33.9	1	0.3	0.4	0	0	102.7
glassy slag			max	1.1	18.5	61.8	0.9	0	4.2	1.6	6.5	2.8	49.2	26.6	0	0	4.1	0.9	106.8
			min	0.3	6.6	40.9	0	0	1.1	0.3	0.2	0	8.3	0	0	0	0	0	85.6
			mean	0.7	11.1	51.6	0.4	0	2.2	1	1.4	0.7	23.9	5.8	0	0	0.6	0.1	99.4

## 5. Other minor phases

In the sample PB-15 within the small glassy region on its inner surface tin compounds were recognised. They form small nodular grains embedded in the glassy matrix and appear in close association with copper prills (Fig. 93a). They were recognised as tin oxide and tin-copper oxide (Fig. 93b).



Phase	Cu	Sn	Fe	O	total
copper prill (1)	99	nd	0.3	0.6	97.7
	CuO	SnO <sub>2</sub>			total
tin oxide (2)	1.2	102.0			109.8
Cu-Sn oxides (3)	27.6	82.2			103.2

Fig. 93. (a) Backscattered electron image of a glassy area on the inner surface of the crucible PB-15: tin oxide nodules (1), copper prill (2); (b) composition of the tin-bearing phases and copper prill within the vitrified area, SEM-EDS results (wt%), normalised.

The slag in sample TNN-9 contains quite abundant crystals of zircon. They occur in well-reacted parts of the slag as randomly distributed crystals of varied shapes (Fig. 94a). They often show well-formed crystal faces and appear to have been crystallised from the melt (Fig. 94b). They are a sole primary crystalline phase within the slag. In the areas containing remains of unreacted materials grains of zircon were also recognised (Fig. 94c). They have often rounded faces and occur in a close association with large (up to 1mm across) grains of quartz. The latter type of zircon may be considered as residual zircon.

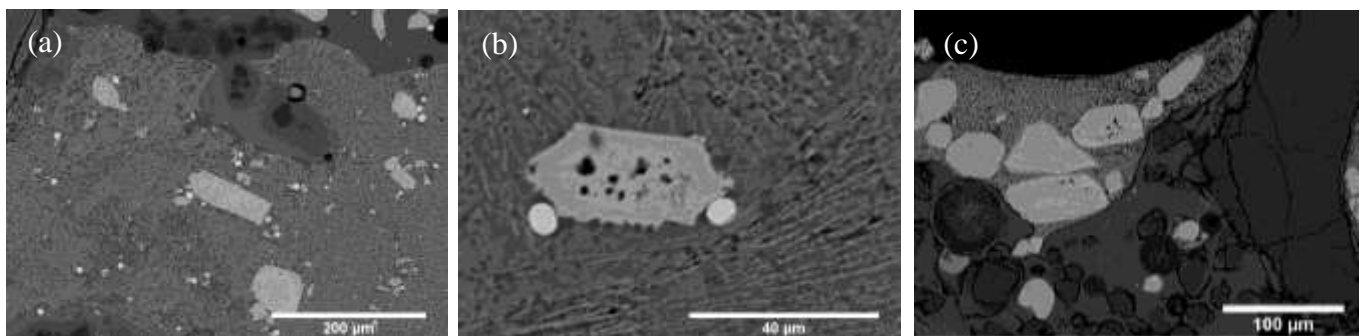


Fig. 94. Backscattered electron images of the crucible slag in TNN-9: (a-b) crystals of zircon probably newly-formed from the melt (light grey), small copper prills (white); (c) probably residual zircon grains (white) in quartz-rich surrounding.



## 6. Residual phases

Residual phases are understood as materials which did not enter the liquid phase during formation of the bulk slag. They remained unreacted or partly reacted preserving some of their original characteristics, such as a shape. They occur much more frequently within the glassy slag, particularly in the areas adjacent to the crucible walls, than in the well-crystallised fayalitic slag.

The most common residual phase recognised in the crucible slag samples is quartz. It is often trapped within the slag as single grains surrounded by amorphous matrix (Fig. 95a-b) or as a part of the crucible fabric incorporated to the melt (Fig. 91a).

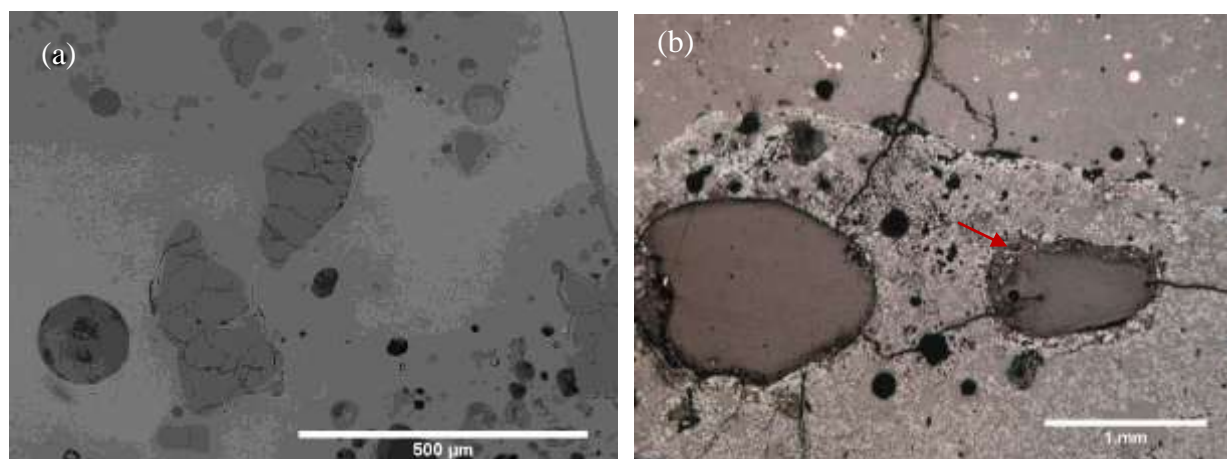


Fig. 95. Backscattered electron images showing partially reacted quartz: (a) sample TNN-2b: dark grey quartz grains partially dissolved in the slaggy residue; (b): PB-13: large quartz grain in the glassy copper and iron-rich slag, note the partial dissolution of quartz on edges (arrow).

Basically, most of the magnetite appears to have crystallised during formation of the slag, i.e. precipitated from the melt together with olivine. In the sample PB-5, however, within the glassy slag close to the upper edge, a cluster of fine anhedral magnetite crystals was recognised (Fig. 96). The cluster seems to retain the shape of the original grain which was trapped into the slag and partly decomposed. Magnetite crystals in the fayalitic slag are often clustered what is, however, a usual effect of slag formation also observed in the synthetic slag prepared from oxide powders (Zhang et al., 2005, p. 940 fig. 3).

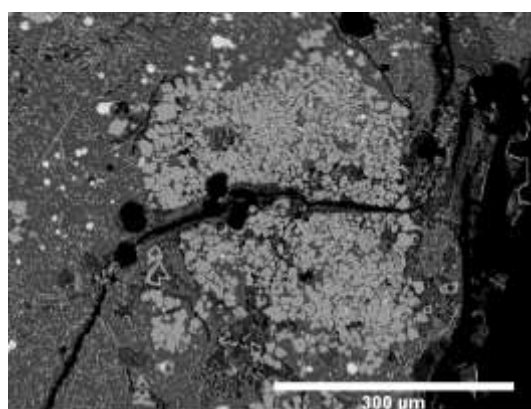


Fig. 96. Backscattered electron image of a possibly residual iron oxide in the sample PB-5.

Residual zircon grains, which also belong to this category, have been described above.

## Appendix 4: crystalline and non-crystalline phases within the separate slag

### 1. Olivine

Olivine of fayalite composition is the main phase observed in all of the samples examined. Some of the iron ions are substituted by Mg, Ca, and, in the case of the samples from TNN with Zn and Mn cations (Table 29). Manganese appears to be mainly bonded to fayalite. In the sample PB-24a cored olivine crystals occur.

Fayalite occurs in several different habits which do not seem to be related to any of the morphological type of the slag. Thin internally skeletal chain and branching crystals up to 1.5 mm long occur most commonly and were observed in each kind of slag (Fig. 97a-b). Their laths are usually randomly oriented, although in limited spaces parallel growing of crystals is also present. In several samples, blocky (polyhedral and hooper types) fayalite crystals with well-formed crystal faces predominate (Fig. 97c-d).

In the sample TNN-16a a band of fayalite crystals was observed (Fig. 97d).

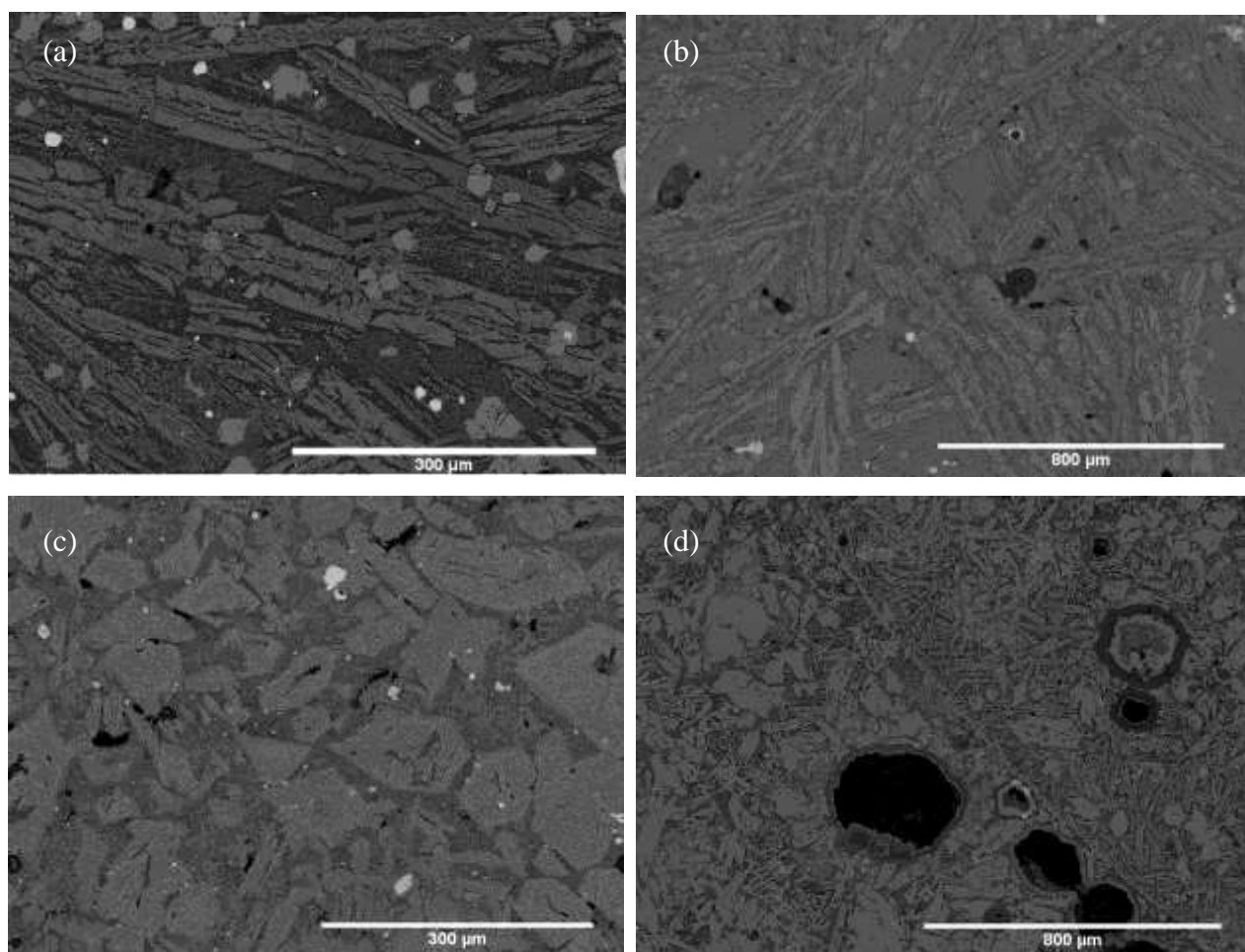


Fig. 97. Backscattered electron images showing habits of olivine crystals in the separate slag samples: (a) PB-26a chain olivine crystals; (b) TNN-17d: highly skeletal chain olivine crystals; (c) PB-34a: blocky olivine; (d) TNN-16a blocky olivine and fayalite line.



Sample	MgO	Al <sub>2</sub> O <sub>3</sub>	SiO <sub>2</sub>	SO <sub>3</sub>	P <sub>2</sub> O <sub>5</sub>	K <sub>2</sub> O	CaO	MnO	FeO	ZnO	CuO	total
PB-24a	4.9	nd	31.3	nd	nd	nd	1.1	0.5	62.3	nd	nd	102.3
PB-24a	20.7	nd	34.0	0.3	nd	nd	nd	0.2	43.0	0.9	nd	104.9
PB-24b	1.7	1.1	31.6	nd	nd	nd	nd	1.7	64.4	nd	nd	104.4
PB-26a	1.1	0.7	33.0	0.1	0.1	0.1	0.1	1.7	62.9	nd	nd	91.7
PB-34a	1.2	1.4	28.6	nd	1.0	nd	0.0	0.5	68.7	nd	nd	103.3
PB-35a	0.4	2.5	32.7	0.2	nd	0.8	0.8	0.5	62.2	nd	0.3	104.9
PB-23	0.6	nd	34.0	nd	nd	nd	nd	nd	65.4	nd	nd	100.9
PB-24g	1.3	nd	30.1	nd	nd	nd	nd	0.6	68.0	nd	nd	104.8
PB-25a	nd	nd	30.6	nd	nd	nd	0.3	1.0	68.2	nd	nd	103.0
PB-31	1.9	nd	30.9	nd	nd	nd	nd	3.2	64.1	nd	nd	103.2
TNN-17a	4.2	0.7	35.5	nd	nd	nd	nd	4.8	52.5	1.2	1.1	81.3
TNN-16a	1.4	nd	31.6	nd	nd	nd	nd	3.3	62.5	1.2	nd	102.5
TNN-16b	1.5	nd	30.5	nd	nd	nd	nd	4.0	61.3	2.7	nd	104.3
TNN-17b	1.0	nd	30.2	nd	nd	nd	nd	5.4	61.4	2.0	nd	104.0
TNN-17d	1.1	nd	33.4	nd	nd	nd	nd	3.4	60.6	1.5	nd	102.0

Table 29. Composition of olivine crystals in the separate slag samples, SEM-EDS results (wt%), normalised.

## 2. Iron oxide

Iron oxide is the second, after ferrous olivine, crystalline phase occurring in the separate slag. Its frequency and proportion relative to fayalite is difficult to estimate on a basis of microscopic examination. It seems, however, that it is generally quite low. In several samples iron oxide does not occur at all in a crystalline form or very sporadically (Fig. 54). It is true mostly in the case of the homogeneous pieces of slag, mainly the thin platy slag. In the sample PB-23, on the other hand, which presents a quite coarse morphology, iron oxide appears very abundant (Fig. 98a).

Iron oxide occurs primarily in the form of magnetite recognition of which is based on the same factors as in the case of the crucible slag (shape, substitutions and optical properties). It forms small-sized (usually 20-50 $\mu\text{m}$ ) euhedral, equant crystals unevenly distributed within the slag (Fig. 97a). It carries small variable amounts of alumina, magnesia, manganese and titania (Table 30). Magnetite in samples from TNN is high in alumina and zinc. Dendrites of magnetite consisting of elongated spin with euhedral arms were also observed (Fig. 98b). In two samples (PB-25a and PB-24g) iron oxide in a characteristic acicular form was noted (Fig. 98d-e).

Magnetite bands were observed in one of the thin platy slag samples (PB-34a) and in porous slag TNN-17b. They run in parallel with the slag faces (Fig. 98e-f).

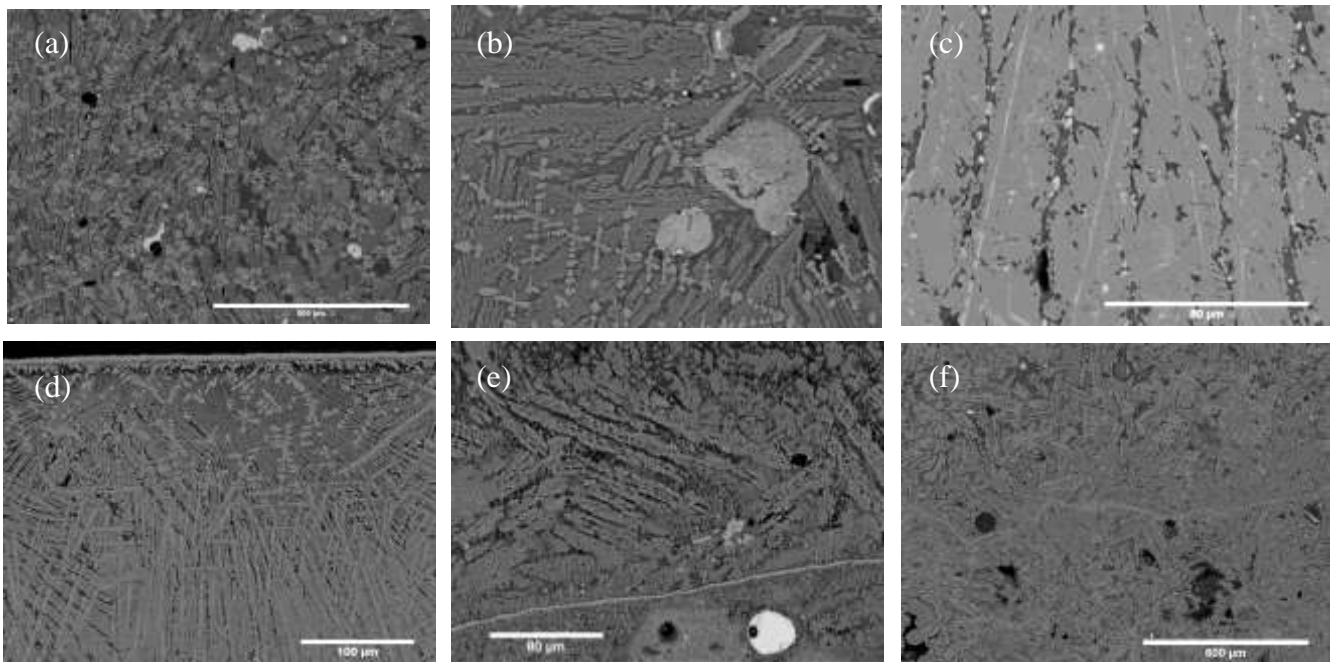


Fig. 98. Backscattered electron images showing magnetite habits: (a) sample PB-23: equant magnetite crystals; (b) sample PB-31: magnetite dendrites; (c-d) PB-25a: acicular magnetite; (e) sample PB-34a and (f) TNN-17b: magnetite bands.

Sample	Description	FeO	Al <sub>2</sub> O <sub>3</sub>	TiO <sub>2</sub>	MgO	MnO	CuO	ZnO	SiO <sub>2</sub>	total
PB-23	euhedral	96.4	2.9	nd	nd	nd	nd	nd	0.8	92.5
PB-23	euhedral	91.7	6.1	1.1	nd	nd	nd	nd	1.1	91.7
PB-24g	euhedral	96.4	2.7	nd	nd	nd	nd	nd	0.9	101.0
PB-24g	euhedral	93.8	5.4	nd	nd	nd	nd	nd	0.8	96.5
PB-24g	acicular	85.6	3.0	nd	nd	nd	nd	nd	11.4	102.3
PB-25a	euhedral	81.9	13.9	2.6	nd	0.5	nd	nd	1.1	98.4
PB-25a	acicular	80.8	2.8	0.6	0.7	0.6	nd	nd	14.6	101.5
PB-31	euhedral	93.5	4.7	0.4	0.8	0.7	nd	nd	nd	95.2
PB-24a	euhedral	87.1	8.3	0.7	2.9	0.1	0.3	nd	0.5	101.5
PB-24a	residual	96.1	0.8	nd	2.5	nd	nd	nd	0.6	96.8
PB-24b	residual(?)	90.6	5.9	1.5	nd	0.5	nd	nd	1.6	95.6
TNN-16a	euhedral	80.7	11.8	2.5	nd	0.9	nd	2.2	2.0	99.6
TNN-16a	euhedral	80.2	13.4	2.3	nd	0.6	nd	1.8	1.7	97.3
TNN-16b	euhedral	84.1	10.1	1.2	nd	1.1	nd	2.7	0.8	96.2
TNN-17d	euhedral	50.4	38.5	1.7	nd	1.0	nd	6.9	1.6	106.0

Table 30. Composition of magnetite spinel crystals in the separate slag samples, SEM-EDS results (wt%), normalised.

### 3. Metallic and sulphidic phases

Metallic copper is the only one metallic phase occurring in the separate slag samples. It was observed as prills ranging in size from less than 5µm up to 300µm. They contain a variable amount of iron which seems, such as in the crucible slag samples, to correlate with the size of a prill (Fig. 101). In one case, within a large copper prill lead separates were recognised (Fig. 99a).

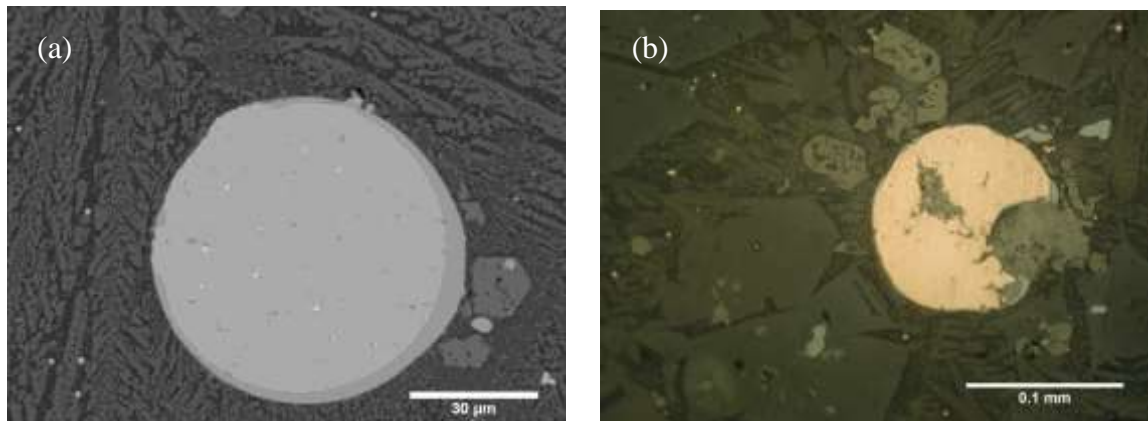


Fig. 99. (a) Backscattered electron image of the copper prill with sulphide rim (light grey) and lead separates (white spots within the prill) in the sample TNN-16b, (b) Reflected light micrograph of the copper prill (yellow) with small sulphide edge (blue) and probably corrosion products (grey) in the sample TNN-17a.

Copper prills always occur in association with sulphidic phases. Sulphide edge may rim a copper prill (Fig. 100a-b) and/or separate sulphide globules or irregular lumps may co-occur in the same sample (Fig. 100c-e). The sulphidic lumps are much more asymmetrical in shape than the copper prills and often cracked. They are frequently adjacent to round voids character of which is not clear. They are usually referred to as gas holes created during sulphur releasing. The close association of the sulphidic phase with copper prills and the presence of much evidence of

copper corrosion (leaching) may, however, indicate that some of the voids may have been left by the leached copper.

In several samples only sulphide phases were recognised with the SEM-EDS analysis (Table 31). The factors just mentioned, the existence of round holes and corroded phases, question, however, this statement. Metallic copper may be present as tiny prills finely dispersed within the slag which were noticed under the reflected light microscope but not analysed with the SEM-EDS. In the case of the sample PB-34a two large probably corroded (cuprite) copper prills were observed (Fig. 98d).

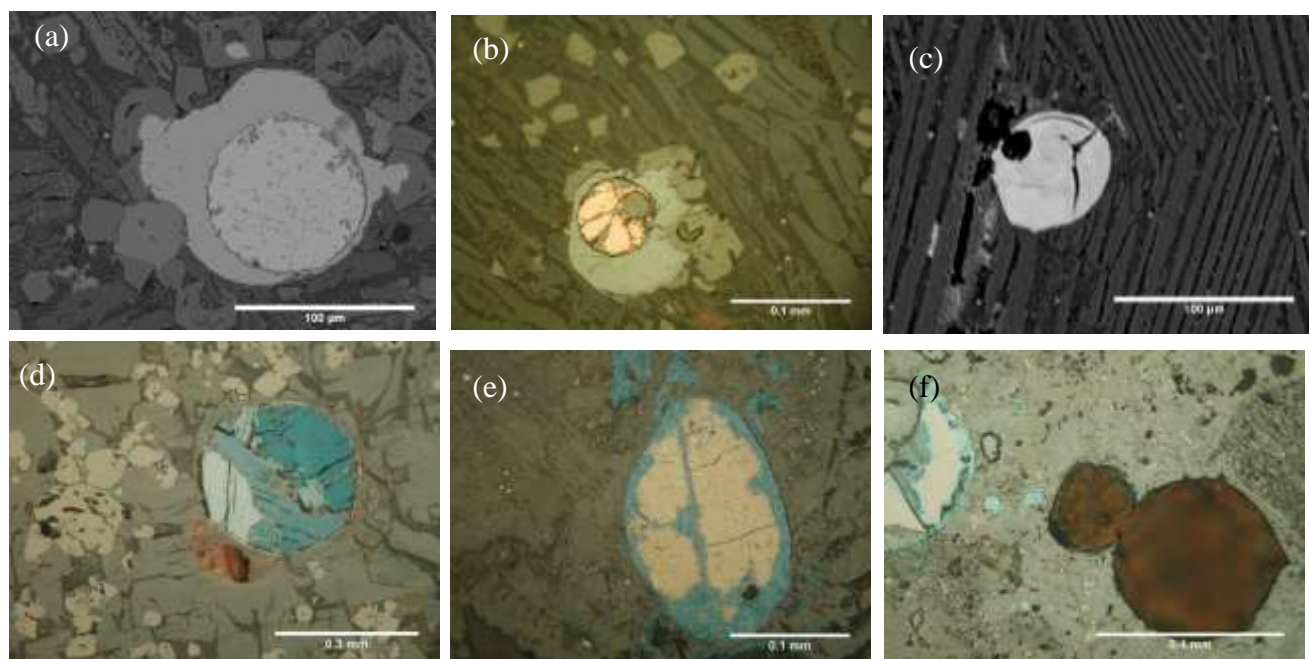


Fig. 100. Sulphide phases in the separate slag samples: (a) Backscattered electron image of a copper prill with sulphide edge in TNN-17d; (b) Reflected light micrograph of a corroded copper prill within sulphide globule in PB-26a; Backscattered electron image of a sulphide prill with a hole in PB-35a; (d) Reflected light micrograph of a sulphide phase in PB-23; (e) Reflected light micrograph of a sulphide phase PB-35a; Reflected light micrograph of possibly two corroded copper prill in PB-34a.

The composition of sulphide phase is much more variably than in the case of the crucible slag (Table 31). The low-iron sulphides compositionally comparable to chalcocite also occur but much more often the elevated amount of iron was detected. The sulphide phases recognised in the sample PB-35a have especially high iron contents reaching even 18%. The amounts of iron and size of lumps do not seem to correlate (Fig. 101).

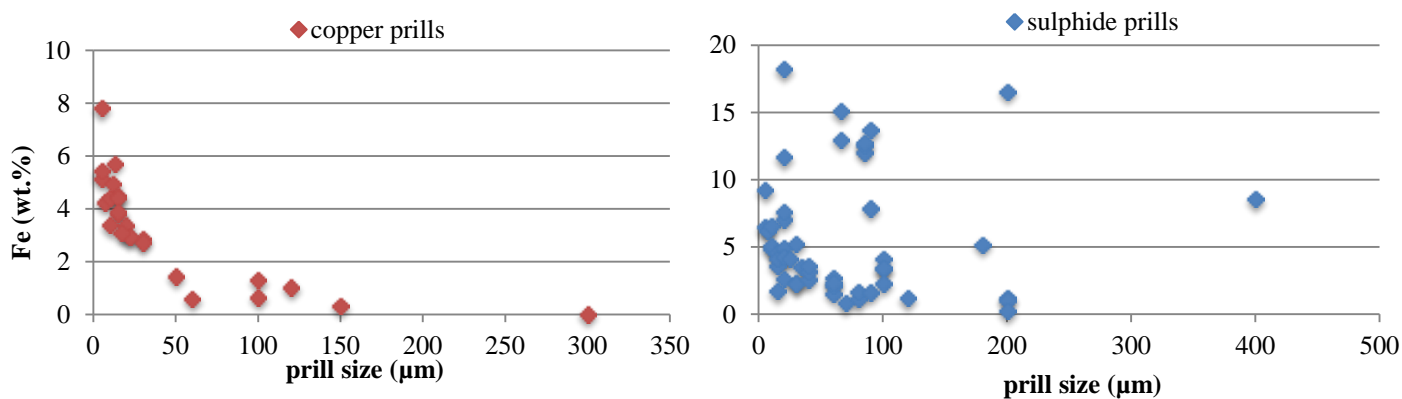


Fig. 101. Scatter plots showing the relation of the size of copper and sulphide prills to their iron contents.

Sample	Phase		prill size (µm)	Cu	S	Fe	O	Si	Pb	total
TNN-17a	copper prill	mean (n=2)	150-300	99.4	nd	0.2	0.4	nd	nd	96.1
TNN-17a	sulphide prill	mean (n=5)	10,80	76.8	20.1	3.2	nd	nd	nd	87.4
TNN-17a	sulphide rim	mean (n=3)		78.0	19.7	2.3	nd	nd	nd	94.6
TNN-16a	copper prill	mean (n=2)	7,15	92.4	0.3	4.1	0.8	nd	2.3	105.7
TNN-16a	sulphide prill	mean (n=2)	15	72.6	23.5	3.9	nd	nd	nd	103.8
TNN-16a	sulphide rim	single analysis		75.7	19.4	3.9	0.9	nd	nd	105.5
TNN-16b	copper prill	mean (n=4)	5-100	96.4	nd	3.0	0.5	nd	nd	103.2
TNN-16b	sulphide rim	single analysis		74.9	20.6	3.2	1.3	nd	nd	104.9
TNN-17b	sulphide prill	mean (n=3)	5,20	73.6	20.5	5.8	nd	nd	nd	103.6
TNN-17d	copper prill	single analysis	100	98.7	nd	1.3	nd	nd	nd	92.6
TNN-17d	sulphide prill	mean (n=2)	7,20	74.2	20.2	4.2	0.7	0.6	nd	106.1
TNN-17d	sulphide rim	single analysis		77.1	19.9	1.5	1.5	nd	nd	97.3
PB-23	sulphide prill	mean (n=5)	25-200	77.6	20.1	2.3	nd	nd	nd	102.8
PB-23	sulphide prill (1)	single analysis		66.1	32.9	1.1	nd	nd	nd	97.3
PB-24a	copper prill	mean (n=5)	10-120	92.7	nd	3.9	3.2	nd	nd	101.4
PB-24a	sulphide prill	mean (n=3)	5,20	72.7	18.6	7.9	0.7	nd	nd	112.9
PB-24b	copper prill	mean (n=3)	17-22	96.2	0.3	3.0	0.5	nd	nd	104.7
PB-24g	sulphide prill	mean (n=3)	100-180	71.9	23.9	4.2	nd	nd	nd	100.3
PB-25a	sulphide prill	mean (n=3)	30-100	74.4	22.2	3.4	nd	nd	nd	101.2
PB-26a	copper prill	mean (n=3)	10,30	95.3	0.1	3.3	0.8	nd	nd	106.6
PB-26a	sulphide prill	mean (n=4)	70,200	78.4	20.2	1.1	0.2	nd	nd	96.1
PB-26a	sulphide rim	mean (n=2)		71.5	18.6	4.2	3.6	1.4	nd	109.2
PB-31	copper prill	mean (n=3)	5,50	95.3	nd	4.2	0.5	nd	nd	105.5
PB-31	sulphide prill	mean (n=3)	20,80	76.2	20.6	3.2	nd	nd	nd	103.5
PB-31	sulphide rim	mean (n=2)		76.1	19.7	3.8	0.4	nd	nd	104.0
PB-34a	sulphide prill	mean (n=8)	15,400	69.8	24.5	5.0	0.7	nd	nd	88.9
PB-35a	sulphide prill	mean (n=11)	10,200	59.0	26.6	13.2	1.2	nd	nd	103.6
copper prills		min	5	86.6	0.0	0.0	0.0	77.6		
		max	300	99.7	0.7	7.8	10.9	111.3		
		mean	46	94.6	0.1	3.2	1.7	101.9		
sulphide prill		min	5	54.3	14.6	0.2	0.0	76.2		
		max	400	78.9	32.9	18.2	3.9	113.1		
		mean	69	72.2	22.1	5.2	0.4	99.1		

Table 31. Composition of copper and matte phases in the separate slag samples, SEM-EDS results (wt%), normalised.

#### 4. Glassy matrix

Glass occurs interstitially to all of the above and below described phases. Its volume depends on the degree of fayalite crystallisation. It may fill dissent-sized sectors between thin fayalite laths or be extremely sparse as in the case of the slag with well-developed blocky fayalite crystals.

The glassy matrix is, in fact, mostly cryptocrystalline showing initial crystallisation. Tiny feather-like and chain fayalite crystals were started to be formed within the amorphous phase (Fig. 102).

The low, relatively to typical glass, in silica and high in alumina and iron oxide glass contains variable amount of particular components carrying the ingredients not incorporated to

the structure of the crystalline phases formed in the first instance. Therefore, the enrichment in potash, calcia and alumina was usually observed (Table 32).

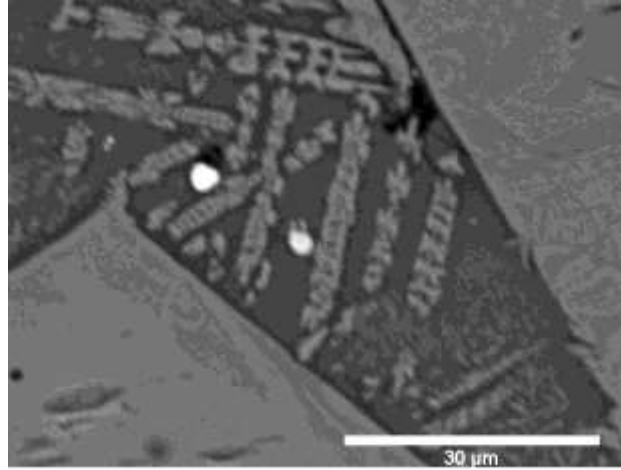


Fig. 102. Backscattered electron image of a glassy matrix with minute fayalite crystals in the sample TNN-17a.

sample		Na2O	MgO	Al2O3	SiO2	P2O5	SO3	K2O	CaO	TiO2	MnO	FeO	CuO	ZnO	BaO	PbO	total
PB-23	single	nd	nd	15.1	50.5	nd	nd	3.3	3.0	nd	nd	28.1	nd	nd	nd	nd	100.9
PB-24a	n=2	nd	0.2	9.4	43.7	nd	nd	1.9	17.6	nd	nd	26.9	0.4	nd	nd	nd	109.4
	σ	nd	0.05	0.8	0.04	nd	nd	0.1	0.6	nd	nd	0.9	0.6	nd	nd	nd	0.8
PB-24b	n=3	nd	nd	13.6	49.2	0.6	nd	1.5	1.7	0.5	0.8	30.7	1.0	0.5	nd	nd	103.6
	σ	nd	nd	1.0	0.4	0.1	nd	0.5	0.2	0.2	0.3	1.2	0.3	0.3	nd	nd	2.8
PB-24g	single	nd	nd	17.4	40.2	0.7	0.7	9.2	2.4	0.8	nd	28.0	0.0	nd	nd	nd	108.0
PB-25a	single	nd	0.6	11.0	38.1	1.5	2.7	4.6	5.3	0.5	0.5	34.6	0.6	nd	nd	nd	104.4
PB-26a	n=2	nd	0.1	14.4	50.0	0.4	0.8	0.9	2.1	nd	1.1	24.7	5.3	nd	nd	0.4	105.9
	σ	nd	0.1	1.4	0.2	0.6	1.1	0.3	0.4	nd	0.5	4.3	6.0	nd	nd	0.6	2.1
PB-31	single	nd	nd	13.2	46.9	0.9	nd	2.1	4.3	0.8	1.8	30.1	0.0	nd	nd	nd	103.5
PB-34a	n=3	nd	nd	11.4	35.5	1.7	2.4	2.7	0.3	0.4	nd	44.6	1.0	nd	nd	nd	100.0
	σ	nd	nd	1.4	0.2	0.6	1.1	0.3	0.4	0.2	nd	4.3	6.0	nd	nd	nd	2.1
PB-35a	n=7	nd	nd	7.5	35.3	nd	2.9	1.4	0.9	0.2	0.3	51.5	0.1	nd	nd	nd	106.1
	σ	nd	nd	3.6	2.2	nd	1.4	0.6	0.5	0.3	0.2	8.0	0.2	nd	nd	nd	1.2
TNN-16a	single	nd	nd	14.8	47.1	2.0	nd	3.7	2.9	nd	1.5	24.9	nd	1.9	1.3	nd	101.2
TNN-16b	single	nd	nd	16.3	43.2	1.4	nd	2.8	1.7	0.7	2.2	27.4	nd	3.1	nd	1.2	102.9
TNN-17a	single	0.5	nd	17.2	43.3	1.2	nd	3.0	3.0	1.3	2.2	26.9	nd	1.5	nd	nd	100.4
TNN-17b	single	nd	nd	22.4	32.1	2.4	nd	5.9	1.5	1.2	1.3	28.8	nd	4.5	nd	nd	103.2
TNN-17d	single	nd	nd	12.8	45.2	2.2	nd	4.5	nd	1.1	1.1	31.6	nd	1.4	nd	nd	102.0

Table 32. Composition of the glassy matrix in the separate slag samples, SEM-EDS results (wt%), normalised.

## 5. Other minor phases

In one sample (TNN-17a) potash reached such level in some places that modal leucite was locally formed (Fig. 103a-b; composition in Table 33). This mineral phase was not observed in any other samples.

In several samples from TNN and PB copper-iron oxide globules occur. They contain iron and copper oxide in similar proportion and a minor, variable amount of silica (Table 33). The globules are characterised by speckled white-grey in BSE texture (Fig. 103a-d). Their identification is uncertain; therefore detailed compositional data of a few of them are presented.



The globules usually occur in association with sulphide phases. They are often, similarly to copper prills, rimmed with a sulphide edge. This implies their identification as corroded copper prills from which some of the copper ions were leached away leaving a corroded copper phase enriched in iron and a space in which additional iron and silica were precipitated. This identification seems to be confirmed by occurrence of Fe-Cu oxide mixture in the cracks within the copper prills and beside the partially corroded copper. The low amount of chloride detected in some of the globules may indicate weathering as well.

The points, which, however, challenge this interpretation, are the consistence of the copper/iron ratio detected in particular globules, extraordinary in terms of corrosion products, and the co-occurrence of other phases difficult to explain (Fig. 103f). The Cu/Fe ratio seems to be consistent with chalcopyrite. It implies another interpretation entailing presence of chalcopyrite which was rusting (heating under oxidation condition) above 750°C. This process would remove sulphur as a gas and make the product largely a spinel  $(\text{Cu,Fe})_3\text{O}_4$  (Rostoker *et al.* 1986).

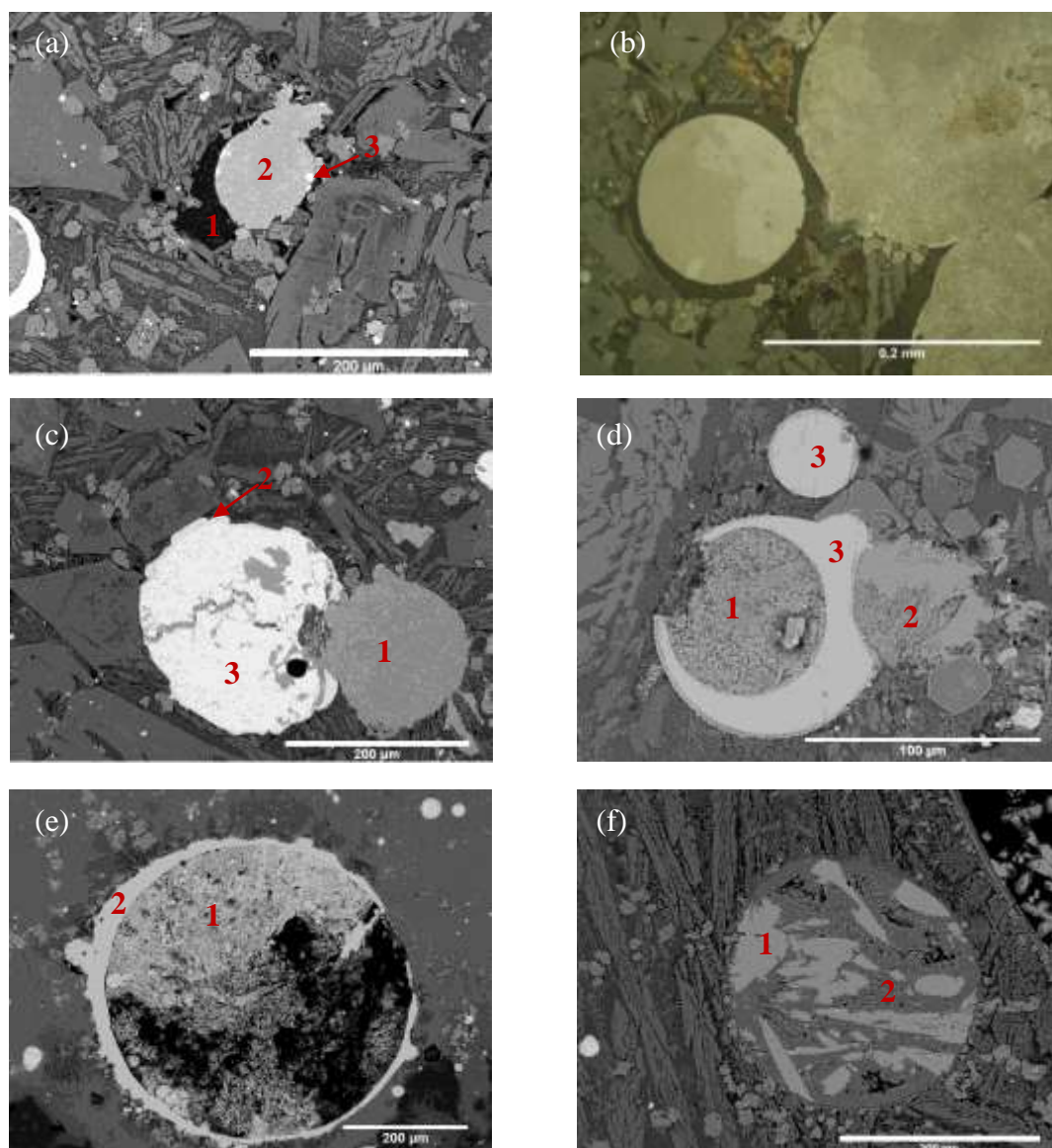


Fig. 103. Minor phases in the separate slag samples: (a) Backscattered electron image showing Cu-Fe oxide phase surrounded by leucite (see composition in Table 33); (b) Reflected light micrograph of Cu-Fe oxide globules (light grey) surrounded by leucite (dark grey) in TNN-17a; Backscattered electron image of: (c) cracked copper prill in TNN-17a, (d) Cu-Fe oxide phases in TNN-17d (Table 33); (e) corroded copper prill in PB-31; (f) Phases of uncertain character in PB-26a.

		Al <sub>2</sub> O <sub>3</sub>	SiO <sub>2</sub>	K <sub>2</sub> O	SO <sub>3</sub>	FeO	CuO	CoO	SrO	BaO	Cl	total
TNN-17a	leucite (a1)	21.0	57.6	19.6	nd	1.2	0.7	nd	nd	nd	nd	78.0
TNN-17a	Cu-Fe oxides (a2)	nd	9.1	nd	nd	40.4	48.8	nd	nd	nd	1.7	110.5
TNN-17a	barite (a3)	nd	nd	nd	34.1	3.7	3.6	0.1	0.9	57.5	nd	89.0
TNN-17a	Cu-Fe oxides (c1)	nd	13.0	nd	nd	39.9	45.9	nd	nd	nd	1.3	95.5
		Cu	S	Fe	O	total						
TNN-17a	sulphide edge (c2)	78.2	19.8	1.9	nd	84.6						
TNN-17a	copper prill (c3)	99.1	nd	nd	0.9	80.1						
		SiO <sub>2</sub>	P <sub>2</sub> O <sub>5</sub>	FeO	CuO	Cl	total					
TNN-17d	Cu-Fe oxides (d1)	8.3	nd	37.1	51.5	3.1	97.8					
TNN-17d	Cu-Fe oxides (d2)	4.0	0.7	45.2	50.2	nd	101.8					
		Cu	S	Fe	total							
TNN-17d	sulphide rim and prill (d3)	77.1	21.2	1.7	104.1							
		Al <sub>2</sub> O <sub>3</sub>	Cr <sub>2</sub> O <sub>3</sub>	MnO	FeO	CuO	total					
PB-31	corroded copper prill (e1)	1.6	0.9	0.8	90.3	6.4	65.8					
		Cu	S	Fe	total							
PB-31	sulphide rim (e2)	79.1	20.3	0.6	98.3							
		SiO <sub>2</sub>	FeO	CuO	total							
PB-26a	bright particles (f1)	0.6	48.8	50.6	91.3							
PB-26a	grey filling (f2)	1.9	95.4	2.7	76.9							

Table 33. Composition of the phases numbered in the Fig. 103, SEM-EDS results (wt%), normalised. Numbering of phases from the Fig. 77 presented in the brackets; for instance ‘c1’ – fig. 77c, phase 1.

## 6. Residual phases

Although the slag pieces examined are generally well reacted, in most of them, few admixtures which did not reach their melting points during the slag formation also occur. They are more commonly found in the irregular pieces of slag though they were also observed in the platy slag. The most abundant type of unreacted material is quartz. Individual grains of quartz often occur in the vicinity of the slag faces (Fig. 104a) which may indicate their mechanical incorporation to the melt when it was cooling and getting viscous. In the sample PB-24b a cluster of fine-grained quartz was noticed (Fig. 104b). It is closely associated with sulphide prills and may be interpreted as an unreacted component of a charge.

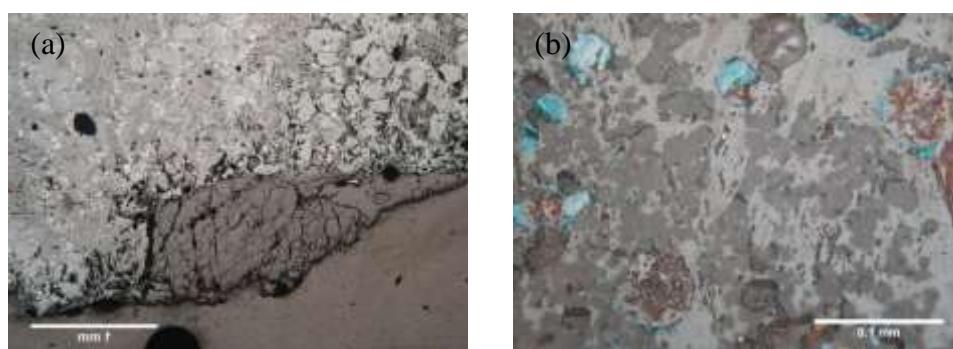


Fig. 104. Reflected light micrographs of unreacted quartz: (a) in the sample TNN-17d; (b) partially reacted quartz associated with sulphide prills in PB-24b.

Earthy material adhering to the bottom of the coarse plate slag is probably a residue of partly decomposed and trapped into the slag surface on which the silicate melt was freezing. In the sample PB-23 it is composed mainly of quartz in an iron and alumina rich siliceous matrix showing fine bloating pores. The minor presence of zircon and globular iron oxide grains was also noticed (Fig. 105a-b). The cluster of material of similar composition was observed inside the platy slag PB-31 (Fig. 105c).

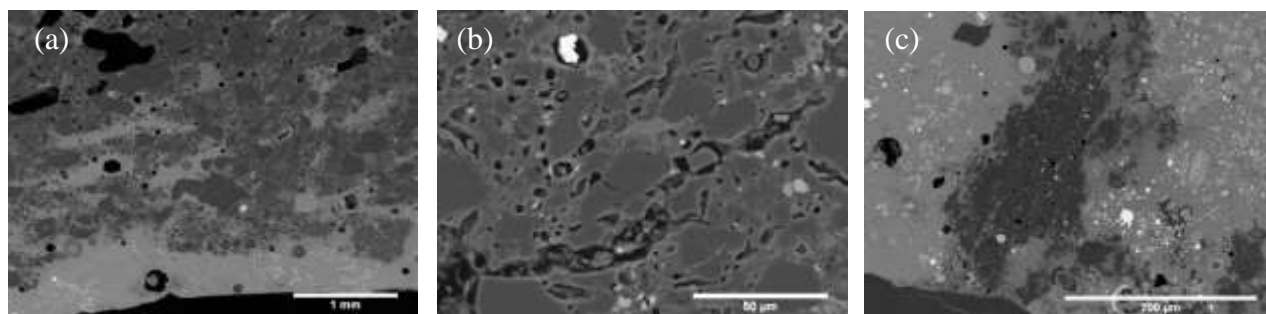


Fig. 105. Backscattered images of earthy material entrapped in the separate slag samples: (a-b) coarse plate slag PB-23; (b) residue within the sample PB-31. See their composition in Table 34.

A piece of ceramic incorporated in the lumpy slag TNN-17 has a similar composition to the crucible fabric. The fragmented structure is also visible (Fig. 106).

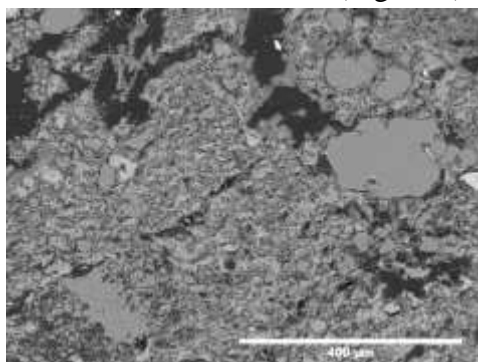


Fig. 106. Backscattered electron image of a piece of ceramic adhering to the sample TNN-17a. See its composition in Table 34.

All of the iron oxide crystals described above are newly-formed phases. In a few cases also partially reacted grains, thought to be residual component of a charge, were observed. In the lumpy slag PB-24a a cluster of iron oxide was recognised. It is lower in alumina than the primary euhedral magnetite crystals from the same sample and it contains sulphide prills.

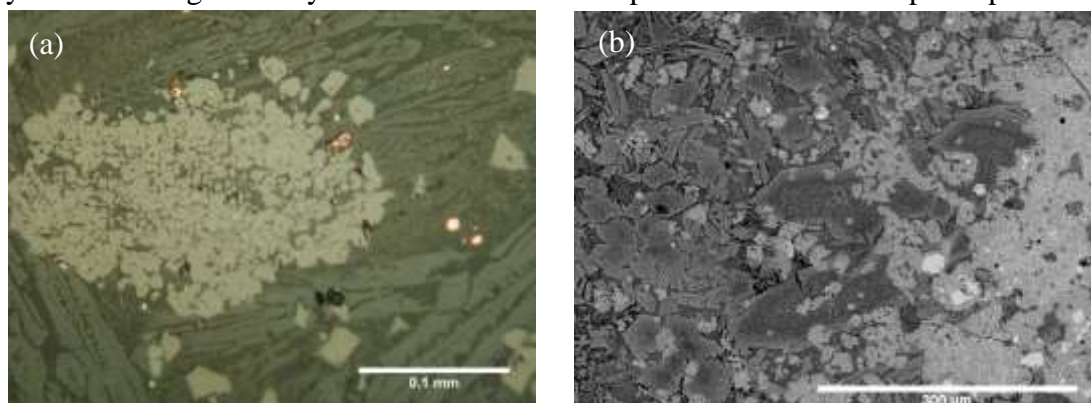


Fig. 107. Residual iron oxide in the separate slag sample: (a) Reflected light micrograph: light grey iron oxide in the centre; sample PB-26a; (b) Backscattered electron micrograph showing cluster of residual iron oxide on the right with white sulphides, PB-24a.

In the sample TNN-16a two phases associated with copper, sulphur and iron were observed (Fig. 108). It is unclear to which extent they are related to the original composition of a charge (unreacted ore minerals?) and to the post-depositional alteration of slag. Their compositions are presented in Table 34.

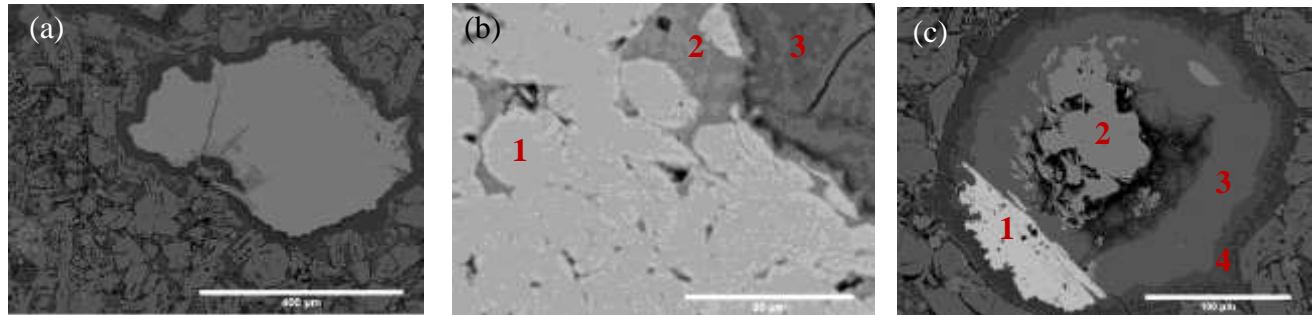


Fig. 108. Backscattered electron images of the phases of unclear origin in the sample TNN-16a: (a-b) Cu-Fe globules in botryoidal cluster; (c) barite (1) and unrecognised phases (2-3). See composition of the phases in Table 34

Sample	Description	MgO	Al <sub>2</sub> O <sub>3</sub>	SiO <sub>2</sub>	P <sub>2</sub> O <sub>5</sub>	K <sub>2</sub> O	CaO	TiO <sub>2</sub>	FeO	CuO	F	total
PB-23	bottom part bulk (fig. 105a)	nd	8.6	76.4	nd	0.3	nd	0.4	13.2	1.12	nd	99.8
PB-23	bottom part matrix (fig. 105b)	1.4	19.5	60.8	nd	2.9	1.6	1.2	12.6	nd	nd	105.4
TNN-17d	ceramic fr. bulk (fig. 106)	0.7	22.5	66.1	0.9	1.4	nd	0.7	7.7	nd	nd	69.1
TNN-17d	ceramic fr. matrix (fig. 106)	1.6	36.1	49.1	nd	4.2	nd	0.4	8.6	nd	nd	103.7
PB-31	earthy material (fig. 105c)	0.5	9.2	78.3	nd	2.1	nd	0.6	5.8	1.27	2.26	97.3
PB-24a	residual iron oxide (fig. 107b)	2.5	0.8	0.6	nd	nd	nd	nd	96.1	nd	nd	96.8
		O	Mg	S	Fe	Cu	total					
PB-24a	sulphide within residual iron oxide (fig. 107b)	1.2	0.1	14.6	9.3	74.9	99.7					
		Al <sub>2</sub> O <sub>3</sub>	SiO <sub>2</sub>	P <sub>2</sub> O <sub>5</sub>	SO <sub>3</sub>	FeO	CuO	ZnO	As <sub>2</sub> O <sub>3</sub>	BaO	total	total <sup>a</sup>
TNN-16a	Cu-Fe oxide (fig. 108b1)	nd	0.8	nd	nd	47.3	50.7	1.2	nd	nd	102.3	
TNN-16a	light grey inside (b2)	0.8	6.5	nd	1.2	85.6	3.9	1.9	nd	nd	78.4	96.3
TNN-16a	dark grey matrix around (b3)	13.7	27.6	1.3	nd	52.7	3.6	1.2	nd	nd	82.2	99.8
TNN-16a	barite (fig. 108c1)	nd	nd	nd	36.4	1.0	nd	nd	0.4	62.1	99.6	
TNN-16a	grey inside (c2)	nd	nd	nd	nd	48.7	51.3	nd	nd	nd	100.4	
TNN-16a	light grey around (c3)	nd	3.8	nd	nd	92.5	2.3	1.3	nd	nd	77.2	100.9
TNN-16a	dark grey around (c4)	13.0	20.5	2.2	2.3	58.3	3.6	nd	nd	nd	82	98.6

Table 34. Composition of the partially reacted phases discussed in the present section, SEM-EDS results (wt%), normalised. Numbering of phases from the Fig. 105-108 presented in the brackets. Total<sup>a</sup> - all elements measured.



## References

- Bachmann, H.-G. (1982). *The identification of slags from archaeological sites*. London: Institute of Archaeology.
- Baxter, K., Dreisinger, D., & Pratt, G. (online). The Sepon Copper Project: development of a flowsheet. In C. A. Young, A. M. Alfantazi, C. G. Anderson, D. B. Dreisinger, B. Harris, & A. James (Eds.), *Hydrometallurgy 2003 – Fifth International Conference in Honor of Professor Ian Ritchie – Volume 2: Electrometallurgy and Environmental Hydrometallurgy*. Retrieved from <http://www.bateman.com/papers/seponflowsheet.pdf>
- Bayley, J., & Rehren, T. (2007). Towards a functional and typological classification of crucibles. In S. La Niece, D. Hook, & P. Craddock (Eds.), *Metals and Mines*. London: Archetype Publications.
- Bennett, A. (1989). The contribution of metallurgical studies to South-East Asian archaeology. *World Archaeology*, 20(3), 329–351.
- Bourgarit, D., Mille, B., Burens, A., & Carozza, L. (2005). Smelting of Chalcopyrite During Chalcolithic Times: Some Have one It in Ceramic Pots as Vase-furnaces. In H. Kars & E. Burke (Eds.), *International Symposium on Archaeometry (33rd: 2002: Amsterdam, Netherlands): Proceedings of the 33rd international symposium on archaeometry, 22-26 April 2002, Amsterdam* (pp. 297–302). Amsterdam: Institute for Geo- and Bioarchaeology, Vrije Universiteit.
- Bourgarit, D., Rostan, P., Burger, E., Carozza, L., Mille, B., & Artioli, G. (2008). The beginning of copper mass production in the western Alps: the Saint-Véran mining area reconsidered. *Historical Metallurgy*, 42(1), 1–11.
- Bowen, N. L., & Schairer, J. F. (1935). The System, MgO-FeO-SiO<sub>2</sub>. *American Journal of Science*, 5(29), 197–217.
- Cawte, H. J. (unpublished). *Archaeometallurgical investigations at Puen Baolo and Dragon Field, Savannakhet Province, Laos: Stage one results and recommendations*.
- Chang. (unpublished). Preliminary Report on the Khanong A2 Pit Archaeological Excavation, April 2009.
- Chang. (unpublished 2). *A Very Short Report on the Peun Baolo V Archaeological Expedition*.
- Chang, & Sayavongkhamdy, T. (unpublished). The excavation of Dragon Field and Peun Baolo and associated investigation.
- Chang, Sayavongkhamdy, T., Cawte, H. J., & Souksavtdy, V. (unpublished). Peun Baolo & the Dragon Field - First evidence of a prehistoric metallurgical industry from the Lao PDR.
- Chirikure, S., Heimann, R. B., & Killick, D. (2010). The technology of tin smelting in the Rooiberg Valley, Limpopo Province, South Africa, ca. 1650–1850 CE. *Journal of Archaeological Science*, 37(7), 1656–1669.
- Ciliberto, E., & Spoto, G. (2000). *Modern analytical methods in art and archaeology*. New York: Wiley.

- Craddock, P. T. (1995). *Early metal mining and production*. Edinburgh: Edinburgh University Press.
- Craddock, P. T. (2001). From hearth to furnace: evidences for the earliest metal smelting technologies in the Eastern Mediterranean. *Paléorient*, 26(2), 151–165.
- Craddock, P. T., & Meeks, N. D. (1987). Iron in ancient copper. *Archaeometry*, 29(2), 187–204.
- Cromie, P. (2010). Abstract. *Geological setting, geochemistry and genesis of the Sepon gold and copper deposits, Laos, PhD thesis* (p. II–V). Retrieved from [http://eprints.utas.edu.au/10703/1/Paul\\_Cromie\\_984886\\_UTAS\\_PhD\\_thesis\\_\(title,\\_abstract\\_%26\\_conten.pdf](http://eprints.utas.edu.au/10703/1/Paul_Cromie_984886_UTAS_PhD_thesis_(title,_abstract_%26_conten.pdf)
- Donaldson, C. (1976). An Experimental Investigation of Olivine Morphology. *Contributions to Mineralogy and Petrology*, 57, 187–213.
- Doonan, R. (1994). Sweat, fire and Brimstone: Pre-treatment of copper ore and the effects on smelting techniques. *Historical Metallurgy*, 28(2), 84–97.
- Freestone, I. C., Meeks, N. D., & Middleton, A. P. (1985). RETENTION OF PHOSPHATE IN BURIED CERAMICS: AN ELECTRON MICROBEAM APPROACH. *Archaeometry*, 27(2), 161–177.
- Freestone, I. C., & Tite, M. S. (1986). Refractories in the Ancient and Preindustrial World. In W. D. Kingery (Ed.), *Ceramics and Civilisation, Volume 3. High-Technology Ceramics Past, Present and Future. The Nature of Innovation and Change in Ceramic Technology* (pp. 35–63). Westerville, Ohio: American Ceramic Society.
- Gale, N. H., Kayafa, M., & Stos-Gale, Z. A. (2009). Further evidence for Bronze Age production of copper from ores in the Lavrion Ore District, Attica, Greece. *Archaeometallurgy in Europe 2007* (pp. 158–177). Milano: Associazione Italiana di Metallurgia.
- Gale, N. H., Papastamaki, A., Stos-Gale, Z. A., & Leonis, K. (1985). Copper sources and copper metallurgy in the Aegean Bronze Age. In P. T. Craddock & M. J. Hughes (Eds.), *Furnaces and smelting technology in antiquity* (pp. 81–101). London: British Museum.
- Georgakopoulou, M., Bassiakos, Y., & Philaniotou, O. (2011). SERIPHOS SURFACES: A STUDY OF COPPER SLAG HEAPS AND COPPER SOURCES IN THE CONTEXT OF EARLY BRONZE AGE AEGEAN METAL PRODUCTION. *Archaeometry*, 53(1), 123–145.
- Hanks, B., & Doonan, R. (2009). From Scale to Practice: A New Agenda for the Study of Early Metallurgy on the Eurasian Steppe. *Journal of World Prehistory*, 22, 329–356.
- Hauptmann, A. (1989). In A. Hauptmann, E. Pernicka, & G. A. Wagner (Eds.), *Old World Archaeometallurgy* (pp. 119–135). Bochum: Deutschen Bergbau-Museum.
- Hauptmann, A., Maddin, R., & Prange, M. (2002). On the Structure and Composition of Copper and Tin Ingots Excavated from the Shipwreck of Ulubrun. *Bulletin of the American Schools of Oriental Research*, 328, 1–30.



- Hein, A., Kilikoglou, V., & Kassianidou, V. (2007). Chemical and mineralogical examination of metallurgical ceramics from a Late Bronze Age copper smelting site in Cyprus. *Journal of Archaeological Science*, 34(1), 141–154.
- Higham, C., & Higham, T. (2009). A new chronological framework for prehistoric Southeast Asia, based on a Bayesian model from Ban Non Wat. *Antiquity*, 83, 125–144.
- Humphris, J., Martín-Torres, M., Rehren, T., & Reid, A. (2009). Variability in single smelting episodes – a pilot study using iron slag from Uganda. *Journal of Archaeological Science*, 36(2), 359 – 369.
- Iles, L., & Martín-Torres, M. (2009). Pastoralist iron production on the Laikipia Plateau, Kenya: wider implications for archaeometallurgical studies. *Journal of Archaeological Science*, 36(10), 2314–2326.
- Ineson, P. R. (1989). *Introduction to practical ore microscopy*. Harlow: Longman Scientific & Technical.
- Keller, W. D. (1964). The origin of high-alumina clay minerals. In W. F. Bradlay (Ed.), *Clays and Clay Minerals : Proceedings of the Twelfth National Conference on Clays and Clay Minerals* (pp. 129–151). New York: Macmillan Company.
- Levin, E. M., McMurdie, H. F., & Hall, F. P. (1956). *Phase Diagrams for Ceramists*. Columbus: The American Ceramic Society.
- Lippi, M. M., Gonnelli, T., & Pallecchi, P. (2011). Rice chaff in ceramics from the archaeological site of Sumhuram (Dhofar, Southern Oman). *Journal of Archaeological Science*, 38(6), 1173 – 1179.
- Lutz, J., Pernicka, E., & Wagner, G. A. (1994). Chalkolitische Kupferhuetung in Murgul, Ostanatolien. In R. Wartke (Ed.), *Handwerk und Technologie im Alten Orient* (pp. 59–66). Mainz: Philo von Zabern.
- Maldonado, B., & Rehren, T. (2009). Early copper smelting at Itziparátzico, Mexico. *Journal of Archaeological Science*, 36(9), 1998–2006.
- Manini, T., & Albert, P. (online). Exploration and development of the Sepon gold and copper deposits, Laos. Retrieved from <http://www.smedg.org.au/Tiger/Sepon.htm>
- mindat. (2012). *Mineralogy Database*. Retrieved from <http://www.mindat.org/>
- Mongiatti, A., Rehren, T., Martín-Torres, M., & Cech, B. (2009). Smelting of gold and silver ores in Renaissance Austria. *Archaeometallurgy in Europe 2007* (pp. 60–67). Milano: Associazione Italiana di Metallurgia.
- Murillo-Barroso, M., Pryce, T. O., Bellina, B., & Martín-Torres, M. (2010). Khao Sam Kaeo – an archaeometallurgical crossroads for trans-asiatic technological traditions. *Journal of Archaeological Science*, 37(7), 1761 – 1772.
- Nesse, W. D. (2004). *Introduction to optical mineralogy*. Oxford: Oxford University Press.
- Park, H.-S., Park, S. S., & Sohn, I. (2011). The Viscous Behaviour of FeO-Al<sub>2</sub>O<sub>3</sub>-SiO<sub>2</sub> Copper Smelting Slag. *Metallurgical and Materials Transactions B*, 42b, 692–699.

- Pettijohn, F. J., Potter, P. E., & Siever, R. (1973). *Sand and Sandstone*. New York, Heidelberg, Berlin: Springer Verlag.
- Pigott, V. C., Natapintu, S., & Theetiparivatra, U. (1992). The Thailand Archaeometallurgy Project 1984-1985: research in the development of prehistoric metal use in Northeast Thailand. *Early metallurgy, trade and urban centres in Thailand and Southeast Asia* (pp. 47–52). Bangkok: White Lotus.
- Pigott, V. C., Weiss, D., & Natapintu, S. (1997). The Archaeology of Copper Production: Excavation in the Khao Wong Prachan Valley, Central Thailand. In R. Ciarla & F. Rispoli (Eds.), *South-East Asian Archaeology 1992* (pp. 119–157). Roma: Istituto italiano per l’Africa e l’Oriente.
- Pollard, A. M., & Heron, C. (1996). *Archaeological Chemistry*. Cambridge: Royal Society of Chemistry.
- Potts, P. J. (1992). *A Handbook of Silicate Rock Analysis*. London: Blackie Academic & Professional.
- Pryce, Brauns, M., Chang, N., Pernicka, E., Pollard, A. M., Ramsey, C., Rehren, T., et al. (2011). Isotopic and technological variation in prehistoric Southeast Asian primary copper production. *Journal of Archaeological Science*, 38(12), 3309 – 3322.
- Pryce, T. O., Pigott, V. C., Martín-Torres, M., & Rehren, T. (2010). Prehistoric copper production and technological reproduction in the Khao Wong Prachan Valley of Central Thailand. *Archaeological and Anthropological Sciences*, 2, 237–264.
- Radivojević, M., Rehren, T., Pernicka, E., Šljivar, D., Brauns, M., & Borić, D. (2010). On the origins of extractive metallurgy: new evidence from Europe. *Journal of Archaeological Science*, 37(11), 2775 – 2787.
- Rehren, Th., Charlton, M., Chirikure, S., Humphris, J., Ige, A., & Veldhuijzen, H. A. (2007). Decision set in slag: the human factor in African iron smelting. In S. La Niece, D. Hook, & P. Craddock (Eds.), *Metals and Mines* (pp. 211–218). London: Archetype Publications.
- Rehren, Thilo, Boscher, L., & Pernicka, E. (2012). Large scale smelting of speiss and arsenical copper at Early Bronze Age Arisman, Iran. *Journal of Archaeological Science*, 39(6), 1717 – 1727.
- Rice, P. M. (1987). *Pottery analysis. A sourcebook*. Chicago and London: The University of Chicago Press.
- Rostoker, W. (1975). Some experiments in prehistoric copper smelting. *Paléorient*, 3, 311–315.
- Rostoker, W., Pigott, V., & Dvorak, J. R. (1986). Direct reduction to copper metal by oxidesulfide mineral interaction. *Archeomaterials*, 3, 69–87.
- Rostoker, W., & Sadowski, M. (1980). The carbon reduction of fully oxidized chalcopyrite (copper) ores. *Historical Metallurgy*, 14(1), 38–42.
- Rothenberg, B. (1972). *Timna: valley of the Biblical copper mines*. London: Thames & Hudson.

- Sharp, W. E., & Mittwede, S. K. (2012). Medieval kirschsteinite-bearing iron slag of the Develi-Yahyali area (Kayseri), Turkey. In M. Broekmans (Ed.), *Proceedings of the 10th International Congress for Applied Mineralogy* (pp. 649–653). Heidelberg: Springer Verlag.
- Tite, M. S., Freestone, I. C., & Wood, N. (2012). AN INVESTIGATION INTO THE RELATIONSHIP BETWEEN THE RAW MATERIALS USED IN THE PRODUCTION OF CHINESE PORCELAIN AND STONEWARE BODIES AND THE RESULTING MICROSTRUCTURES\*. *Archaeometry*, 54(1), 37–55.
- Tomber, R., Cartwright, C., & Gupta, S. (2011). Rice temper: technological solutions and source identification in the Indian Ocean. *Journal of Archaeological Science*, 38(2), 360 – 366.
- Tylecote, R. F., & Boydell, P. J. (1978). *Chalcolithic copper smelting. Experiments on Copper Smelting*. London: Institute for Archaeo-Metallurgical Studies.
- Tylecote, R. F., Ghaznavi, H. A., & Boydell, P. J. (1977). Partitioning of trace elements between the ores, fluxes, slags and metal during the smelting of copper. *Journal of Archaeological Science*, 4(4), 305 – 333.
- Vincent, B. (2003). Rice in Pottery: New evidence for early rice cultivation in Thailand. *Bulletin of the Indo-Pacific Prehistory Association*, 23, 51–58.
- Weisgerber, G., & Yule, P. (2003). Al-Aqir near Bahla - an Early Bronze Age dam site with planconvex “copper” ingots. *Arabian Archaeology and Epigraphy*, 14, 24–53.
- Wells, R. G. (1954). Microscopic identification of wustite in presence of other oxides of iron. *Analytical Chemistry*, 26(4).
- Workman, D. R. (1997). Laos. In E. Moores & R. Fairbridge (Eds.), *Encyclopedia of European and Asian regional geology* (pp. 493–497). London: Chapman & Hall.
- Zhang, L., Zhang, L., Wang, M., & Sui, Z. (2005). Oxidation mechanism in CaO-FeO<sub>x</sub>-SiO<sub>2</sub> slag with high iron content. *Transactions of Nonferrous Metals Society of China*, 15(4), 938–943.